Matter

Article

Rational design and synthesis of zwitterionic liquid dielectrics

Graphical abstract

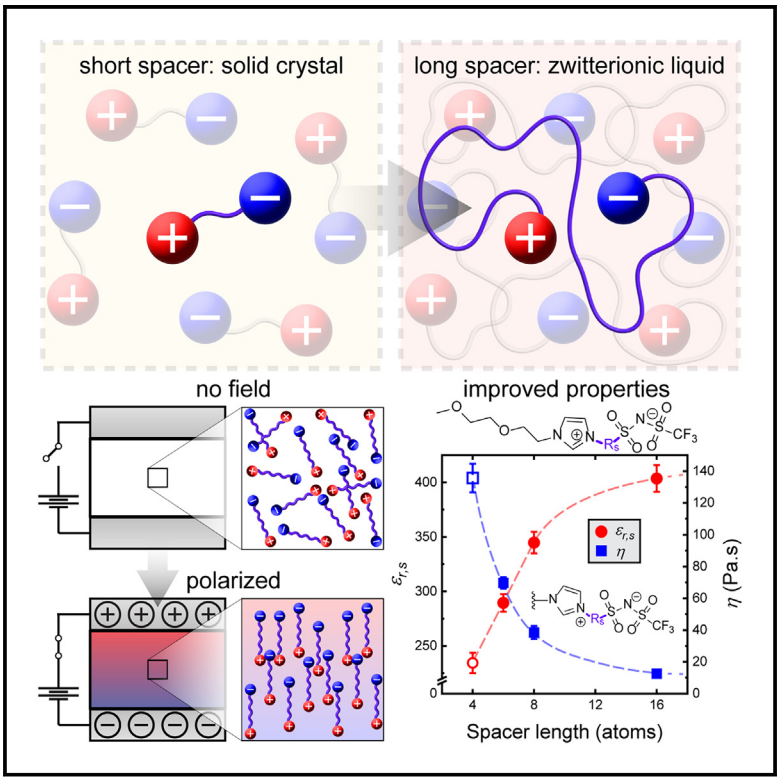

Highlights

- Entropy answers the decades-old problem of high melting points in zwitterions
- Our zwitterionic liquids are up to 500-fold less viscous than benchmark molecules
- They feature static dielectric constants up to 400

Authors

Dylan M. Barber, Michael D. Nelwood, Jennifer A. Lewis

Correspondence

dbarber@seas.harvard.edu (D.M.B.), jalewis@seas.harvard.edu (J.A.L.)

In brief

Stable zwitterionic liquids offer routes to polarizable soft matter, but known zwitterions are limited by high melting points and viscosities. We demonstrate that long, flexible inter-charge spacers suppress crystallization in small-molecule zwitterions, decrease viscosity up to 500-fold compared to an established benchmark, and achieve dielectric constants up to, and even exceeding, 400. These high-permittivity liquids provide a roadmap to polarizable soft matter, unlocking opportunities for high-sensitivity and tissue-compatible bioelectronics, all-soft transistors, and high-conductivity battery electrolytes.

Barber et al., 2025, Matter *8*, 102049
April 2, 2025
https://doi.org/10.1016/j.matt.2025.102049

CellPress

Matter

CellPress

Article

Rational design and synthesis of zwitterionic liquid dielectrics

Dylan M. Barber,[1,2,3,*] Michael D. Nelwood,[1,2] and Jennifer A. Lewis[1,2,*]
[1]John A. Paulson School of Engineering and Applied Sciences, Harvard University, Cambridge, MA 02138, USA
[2]Wyss Institute for Biologically Inspired Engineering, Harvard University, Boston, MA 02215, USA
[3]Lead contact
*Correspondence: dbarber@seas.harvard.edu (D.M.B.), jalewis@seas.harvard.edu (J.A.L.)
https://doi.org/10.1016/j.matt.2025.102049

PROGRESS AND POTENTIAL Next-generation soft electronics, robotics, and bioelectronics demand materials that combine high dielectric permittivity with mechanical softness. Zwitterionic liquids offer a potential solution by endowing extraordinary dipole moments with the freedom to bias in an electric field. Yet, the vast majority of zwitterions either melt above 150°C or are prohibitively viscous. In this work, we outline a strategy that increases the entropy of fusion to suppress the melting point in imidazolium-derived zwitterions, affording zwitterionic liquids. The resulting liquids are up to 500-fold less viscous than an established benchmark and feature dielectric constants up to, or even exceeding, 400 at room temperature, the largest reported to date for organic molecules. Downstream applications include soft, high-gain field-effect transistors, bioelectronic sensors, and high-conductivity liquid- or gel-state electrolytes for next-generation batteries.

SUMMARY

Zwitterions (ZIs) are emerging candidates for soft dielectrics but are limited by high melting points (T_m), glass transition temperatures (T_g), and viscosities (η) dramatically exceeding those of ionic liquids. To overcome these limitations, we synthesized 18 imidazolium-derived zwitterions with systematically varied composition at the (1) imidazolium tail (R_t), (2) imidazolium 2 position (R_2), (3) inter-charge spacer (R_s), and (4) anion (R_a). We found that long, flexible spacers yield stable zwitterionic liquids (ZILs), which we attribute to amplified entropy of fusion. Remarkably, stable ZILs with an elongated (6–16 atom length) inter-charge spacer, flexible tail, and a CF_3-sulfonimide anion are 100- to 500-fold less viscous at room temperature than a benchmark supercooled ZI with a 4-atom spacer and a sulfonate anion. Moreover, these previously unreported ZILs exhibit high permittivities ranging from $\varepsilon_{r,s}$ = 290 (6-atom spacers) to $\varepsilon_{r,s}$ = 404 (16-atom spacers), highlighting the promise of this class of polarizable soft matter.

INTRODUCTION

Soft functional materials are under development with potential applications spanning ion conduction,[1–5] ionoelastomer logic elements,[6] low-voltage electroadhesion,[7] wearable and implantable devices,[8–13] actuators,[14–22] and grippers.[23,24] Among these, soft dielectrics that exhibit strong polarization in an applied electric field, play a crucial role.[8,13,22,24–26] While their property requirements vary by application, they are unified by the need for mechanical compliance and high dielectric properties. Presently, few materials offer both high compliance and polarizability, necessitating compromises in device design. For example, implantable bioelectronic sensors are often mechanically mismatched with the surrounding tissue,[10–12] while the low static dielectric constant ($\varepsilon_{r,s}$ ~2–10) of most elastomers limits their practical utility.[14–21]

Embedding permanent dipoles in a soft medium enables both mechanical compliance and high permittivity. Both polar small molecules and tethered dipoles exhibit bulk polarization in an electric field.[27] Below their polarization volume overlap, static dielectric permittivity scales as $\varepsilon_{r,s} \sim \rho_d \mu^2$, where ρ_d is the number density of dipoles, and μ is dipole moment.[28–31] At higher concentrations, $\varepsilon_{r,s}$ undershoots this prediction yet still increases with μ.[30] Hence, μ represents the most effective route to achieve high permittivity in a dipolar system. This has been demonstrated using sulfonyl,[32] nitrile,[33] and amide[34] groups (μ ~3.7–4.5 Debye).[35–38] Even stronger dipoles have been reported recently by Mei et al., who prepared liquid, solvated, and supercooled zwitterions (ZIs) with dipole moments above 50 Debye and $\varepsilon_{r,s}$ up to 350, offering the first proof of concept of high permittivity in such materials.[30,31,39] ZIs, which consist of oppositely charged ions separated by a covalent spacer, exhibit superlative

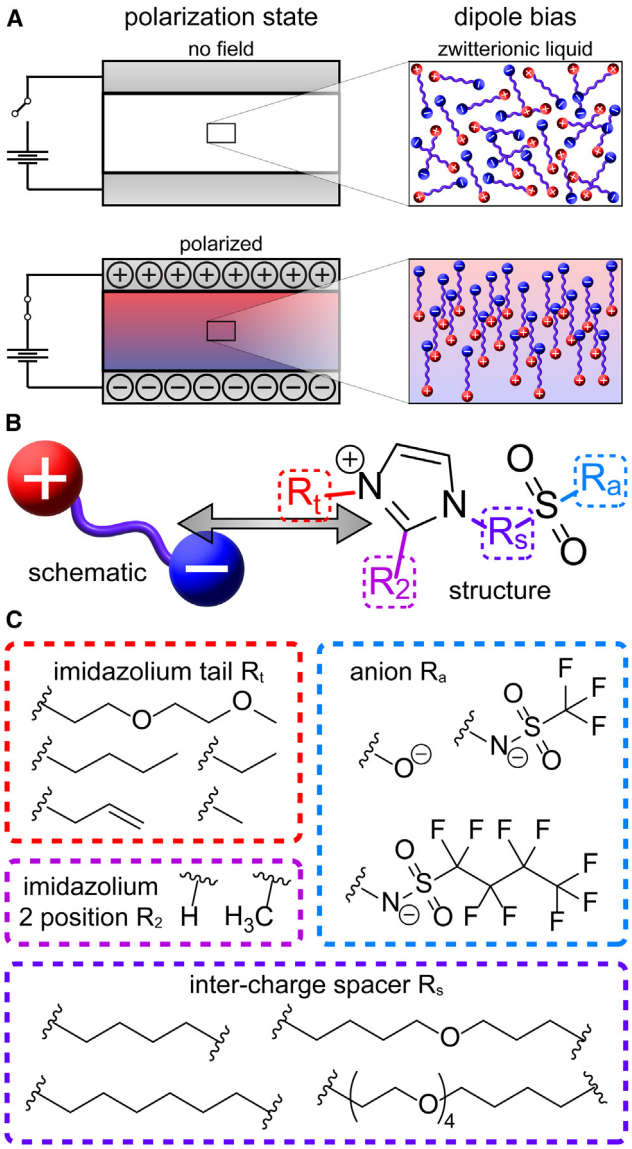

Figure 1. Soft polarizable materials composed of ZILs

(A) Schematic of a bulk material (left) composed of a ZIL (inset, right) in the absence (top) or presence (bottom) of an applied electric field.

(B) Schematics representing imidazolium sulfonyl ZIs synthesized to explore effects of R_t, 2-position R_2, inter-charge spacer (R_s), and anion R_a on thermal phase behavior, viscosity, and dielectric properties.

(C) Molecular structures of R_t, R_2, R_s, and R_a used to synthesize 18 ZIs.

dipole moments for two reasons. First, each pole carries a full charge (cation and anion), enabling a larger polarization amplitude compared to electronegativity- and delocalization-mediated dipoles. Second, they can be prepared with inter-charge spacers of arbitrary length to enable longer dipoles and, thus, higher μ.

Despite these promising attributes, most ZIs suffer from key limitations. First, they possess high melting points (T_m), with the vast majority melting above 150°C.[40] This poses a challenge, as arrested phases (i.e., crystal and glass) are stiff under ambient conditions, undermining their mechanical compliance. These arrested states also inhibit field-mediated dipole bias and bulk polarization and, hence, do not result in high permittivity. Second, zwitterionic liquids (ZILs) reported to date are extremely viscous. For example, Yoshizawa-Fujita et al. reported a supercooled imidazolium sulfonate with a viscosity that was too high to measure under ambient conditions.[41] Others acknowledged, without quantifying, the exceptional viscosity of their imidazolium carboxylate ZIs[42] or reported a viscosity of 1.5 Pa s at 70°C,[43] limiting practical use at room temperature.

Here, we report the rational design and synthesis of ZILs (Figures 1, 2, and 3) that exhibit excellent stability, low viscosity, and high permittivity under ambient conditions. Specifically, we create a library of 18 small-molecule ZIs (structures are shown in Figure 2, and synthesis pathways are shown in Figure 3) that include three previously reported ZIs (control molecules **1–3**) and another 15 as-yet unreported ZIs (molecules **4–18**). Next, their melting behavior, shear rate-dependent viscosity, and frequency-dependent dielectric behavior are characterized to reveal the distinct contributions of the (1) imidazolium tail (R_t), (2) imidazolium 2 position (R_2), (3) inter-charge spacer (R_s), and (4) anion (R_a) (Figure 1B) to determine compositional effects (Figure 1C) on these properties. First, the effects of each moiety on the enthalpy (ΔH_m) and entropy (ΔS_m) of fusion are quantified to understand their melting behavior. Next, by strategically employing functional groups designed to increase the entropy of fusion, including long, flexible spacers, six ZILs (molecules **13–18**) are synthesized that reside in the liquid state under ambient conditions. By replacing the sulfonate anion with sulfonimide, increasing R_s length, and using a long, ether-rich tail, these ZILs exhibit a 500-fold reduction in apparent viscosity (η = 13 Pa s) at room temperature compared to a supercooled ZI **3** (η = 6490 Pa s), which has been reported previously.[30,31,39] Last, we show that these ZILs exhibit static dielectric constants ranging from $\varepsilon_{r,s}$ = 290 for a 6-atom (ZIL **13**) to 404 for a 16-atom (ZIL **18**) R_s, approaching a 2-fold higher value than benchmark ZI **3**. Given their stability in the liquid state, low viscosity, and high permittivity under ambient conditions, these ZILs offer a route to polarizable soft matter for applications ranging from soft electronics to liquid electrolytes.

RESULTS

ZI synthesis

To create this zwitterionic library, we first prepare multi-gram quantities of the sulfonimide anion[5,31,44–47] with a functional handle to enable ZI synthesis. We achieve this goal by building around our target 4-, 6-, 8-, and 16-atom spacers. Specifically, we design and synthesize intermediate molecules **A**, **D**, **G**, and **J** (Figure 3), which all consist of a spacer terminated at one end by a strongly electrophilic sulfonyl chloride and at the other by a modestly electrophilic primary chloroalkane. These groups are advantageous because they can be installed simultaneously in a single step, shortening the pathway to the zwitterionic targets. Next, these α-chloro-ω-sulfonyl chlorides are combined with a CF_3- or C_4F_9-sulfonamide in the presence of a weak base (K_2CO_3) to generate the sulfonimide potassium salt (intermediates **B**, **E**, **H**, and **K**). Finally, the primary chloroalkyl groups are reacted with functional imidazoles to yield ZIs **4–18**. Their purity is confirmed

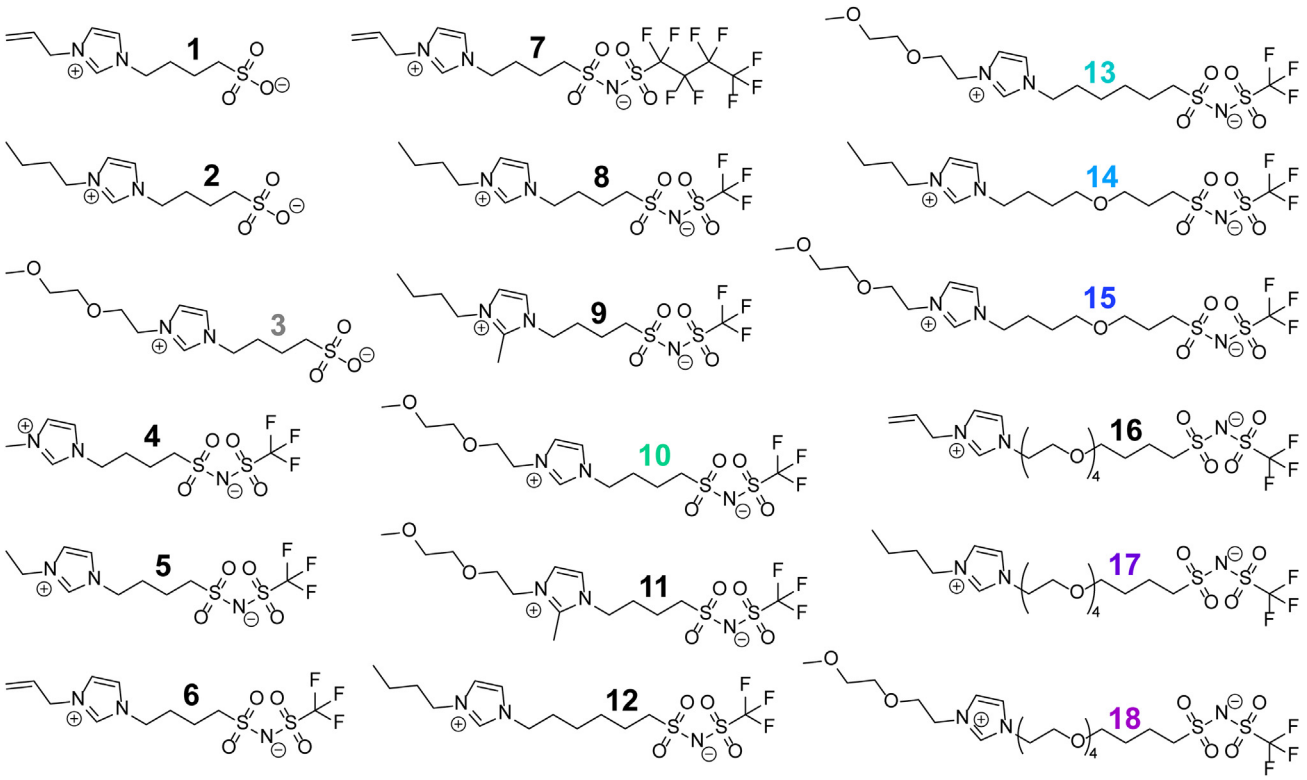

Figure 2. ZI library

ZIs **1–3** have been reported previously, while **4–18** have not.

by ^{1}H, ^{13}C, and ^{19}F NMR and by high-resolution mass spectrometry (see supplemental information or download our source data).

While the route from α-chloro-ω-sulfonyl chlorides to target ZIs is straightforward, the pathway to these intermediates varies by spacer length and composition. Of these, intermediate **A** (4-carbon spacer) is the most scalable. It is prepared by refluxing 1,4-butanesultone in neat thionyl chloride, which ring opens the sultone and chlorinates both the sulfonyl and alkyl termini in a single step. For longer spacers (6–16 atoms), the α-chloro-ω-sulfonyl chloride is prepared in two steps. First, α-hydroxy-ω-sulfonates are created by reacting 6-chlorohexanol with sodium sulfite (6-atom-spacer intermediate **D**), ring-opening 1,3-butanesultone with excess 1,4-butanediol in the presence of tert-butoxide (8-atom-spacer intermediate **G**), and ring-opening 1,4-butanesultone with excess tetraethylene glycol in the presence of hydroxide (16-atom-spacer intermediate **J**). Asymmetric syntheses (diol and sultone in the presence of base) required careful column chromatography to separate the monofunctional target from inevitable difunctional side products and excess starting diol (methods). The α-hydroxy-ω-sulfonates are then converted into α-chloro-ω-sulfonyl chlorides by refluxing in excess thionyl chloride in the presence of catalytic dimethylformamide.

ZI phase behavior

ZIs melt at higher temperatures than untethered salts composed of the same ion pair.[5,31,40,47,48] We hypothesize that this arises from an entropic penalty incurred by the zwitterionic linker R_s (Figures 4A–4C). To examine this hypothesis, we first consider the thermodynamics of melting in conventional ionic liquids.[46,49–55] Consider sodium chloride (NaCl), which melts at 800°C,[46,56] and the ionic liquid 1-butyl-3-methylimidazolium bis(trifluoromethylsulfonyl)imide (BT), which melts at −3°C (Figures 4D and 4E).[46,57] This extraordinary difference in T_m is driven almost exclusively by the entropy of fusion (ΔS_m(BT) = 3.4 × ΔS_m(NaCl)) combined with a small contribution from the enthalpy of fusion (ΔH_m(BT) = 0.85 × ΔH_m(NaCl) Figure 4F). To understand how this changes in the presence of a zwitterionic tether, we synthesize ZI **8**, which serves as a zwitterionic analog to BT (Figure 4D) with a 4-carbon spacer. ZI **8** melts at 73°C, which is far higher than BT. This difference is driven exclusively by a decrease in ΔS_m from 88.0 to 69.2 J mol^{-1} K^{-1} upon installing the inter-charge tether (Figures 4E and 4F). Next, ZI **12**, which features a 6-carbon spacer, is synthesized to interrogate the impact of spacer length on ΔH_m and ΔS_m. Interestingly, T_m increases to 103°C because, although ΔS_m increases to 89.8 J mol^{-1} K^{-1}, ΔH_m increases by a larger margin to 33.8 kJ mol^{-1}. Hence, although a longer spacer increases entropy of fusion, it only serves the goal of T_m suppression if a simultaneous increase in ΔH_m can be avoided. We therefore hypothesize that greater spacer flexibility might more selectively increase ΔS_m. We further note that polyethers, such as poly(ethylene oxide) (PEO), have shorter Kuhn lengths (b_{PEO} = 1.1 nm) than straight-chain alkanes, such as polyethylene (PE, b_{PE} = 1.4 nm), suggesting greater chain

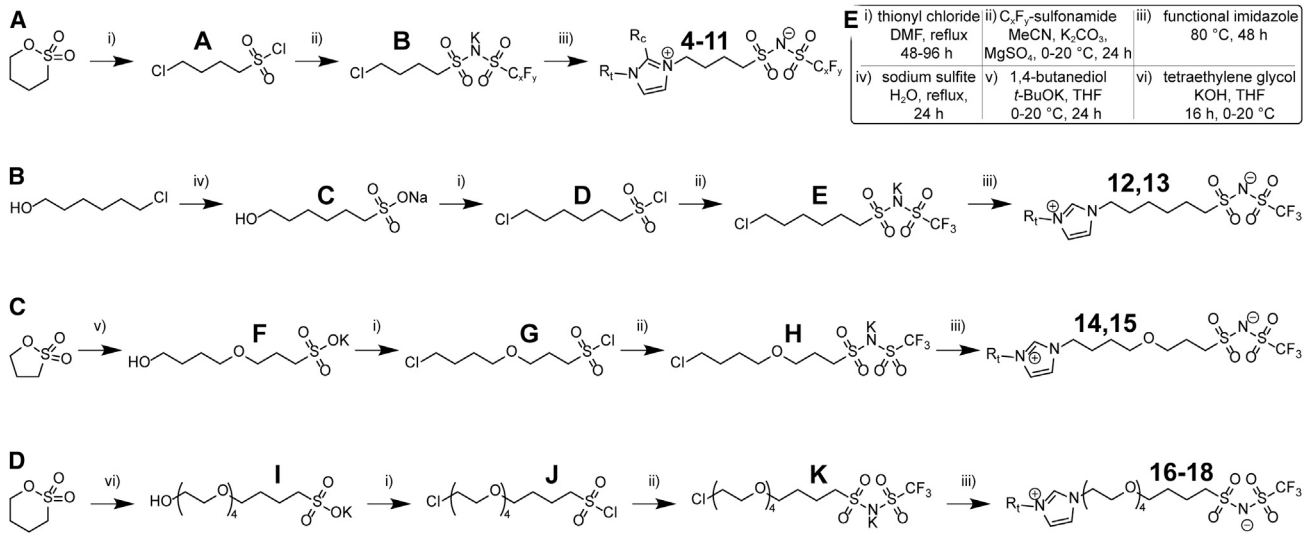

Figure 3. The synthetic pathway depends on spacer length

(A) The 4-atom spacer is synthesized by directly ring-opening 1,4-butanesultone in refluxing thionyl chloride to produce **A**.

(B) The 6-atom spacer is synthesized by reacting 6-chlorohexanol with sodium sulfite in aqueous solution to yield **C** and then chlorinated in refluxing thionyl chloride to produce **D**.

(C) The 8-atom spacer is synthesized by ring-opening 1,3-propanesultone with 1,4-butanediol in the presence of *tert*-butoxide, isolating **F**, then refluxing in thionyl chloride to yield **G**.

(D) The 16-atom spacer is synthesized by ring-opening 1,4-butanesultone with tetraethylene glycol in the presence of hydroxide, isolating **I**, then refluxing in thionyl chloride to yield **J**.

In all cases, the sulfonyl chloride is reacted with triflamide in the presence of K_2CO_3 to yield sulfonimides **B**, **E**, **H**, and **K** and then reacted with R_t-imidazole to generate ZIs **4**–**18**.

flexibility.[58] To enhance chain length and flexibility, we prepared ZIL **14** and ZIL **17**, which are composed of 8- and 16-atom spacers with 1 and 4 ether groups, respectively. Both are isolated as liquids at room temperature and remain stable under prolonged storage (>6 months at 22°C in a vacuum desiccator), suggesting good stability under ambient temperatures.

R_t is dominated by enthalpic contributions for tail lengths of 1–4 carbon atoms and by entropy for a longer, 7-atom tail, as determined by ZIs **4**, **5**, **6**, **8**, and **10** (Figure S1A). ZI **4**, with a methyl tail, is the highest-melting of the five, with T_m = 150°C (Figure S1B), arising from a large ΔH_m = 43.3 kJ mol^{-1} and ΔS_m = 102 J mol^{-1} K^{-1} (Figure S1C). Replacing the methyl tail with ethyl yields ZI **5**, whose lower T_m (126°C; Figure S1B) arises from a decrease in ΔH_m to 27.7 kJ mol^{-1} (Figure S1C). Incorporating an allyl tail produces ZI **6**, the lowest-melting species (T_m = 57°C) of this set of five, driven by a drop in ΔH_m to 18.5 J mol^{-1} K^{-1}. Incorporating a butyl tail leads to ZI **8**, which melts at 73°C (Figure S1B) with ΔH_m = 23.9 kJ mol^{-1} (Figure S1C). Finally, using a 2-(2-methoxyethoxy)ethyl (MEE) tail leads to ZI **10**, with T_m = 69°C (Figure S1B), accompanied by a striking increase in both ΔH_m (to 41.9 kJ mol^{-1}) and ΔS_m (to 122 J mol^{-1} K^{-1}). Next, the effects of the 2-position R_2 are elucidated by replacing the 2-proton in ZIs **8** and **10** with methyl groups to yield ZIs **9** and **11** (Figure S2A). This change primarily impacts ΔS_m. Compared to **8** (T_m = 73°C; Figure S2B), 2-methylated ZI **9** melts at 132°C, driven by a drop in ΔS_m from 69.2 to 45.1 J mol^{-1} K^{-1} and attenuated by a drop in ΔH_m from 23.9 to 18.2 kJ mol^{-1} (Figure S2C). A similar result is observed when comparing 2-H ZI **10** to 2-Me ZI **11**; 2-methyl substitution decreases ΔH_m from 41.9 to 28.6 kJ mol^{-1} and ΔS_m from 122 to 82.4 J mol^{-1} K^{-1} (Figure S2C) to raise T_m from 69°C to 74°C. Finally, we characterize R_a across three anions (Figure S3), including sulfonate (ZI **1**, R_a = O, T_m = 112°C), CF_3-sulfonimide (ZI **6**, R_a = NTf, T_m = 57°C), and C_4F_9-sulfonimide (ZI **7**, R_a = NNf, T_m = 114°C). The dramatic decrease of 55°C–57°C in T_m (**6**) compared to **1** and **7** is driven by a relatively lower ΔH_m (by ~9 kJ mol^{-1}) and attenuated by a decrease in ΔS_m (by ~15 J mol^{-1} K^{-1}). T_g, T_m, ΔH_m, and ΔS_m for all 18 ZIs are provided in Figure S4, while triplicate differential scanning calorimetry (DSC) traces are shown in the supplemental information.

Rheological properties

Shear-rate-dependent viscosity is measured for seven ZIs, including five of our six stable ZILs (**13**, **14**, **15**, **17**, and **18**) and two crystalline ZIs (**3** and **10**) that are first melted and supercooled prior to each measurement. ZI **3** serves as a control, as it is one of the most frequently reported ZILs.[30,31,39] Each ZI exhibits a low-shear plateau viscosity η at shear rates, $\dot{\gamma}$, below 10^1 s^{-1}, followed by a shear-thinning response at higher shear rates (Figure 5A). This effect is most pronounced for ZILs with higher viscosity, especially the ZI **3** control. Their η at $\dot{\gamma}$ = 1 s^{-1} is shown as a function of spacer length in Figure 5B, which reveals a more than 10-fold viscosity decrease as spacer length increases from four (ZI **10**) to 16 (ZIL **18**) atoms. Figure 5B also highlights the roles of tail R_t and anion R_a. For example, liquids **14** (η = 98 Pa s) and **17** (η = 25 Pa s) feature a butyl tail with 8- and 16-atom spacers, respectively. ZILs **15** (η = 38 Pa s) and

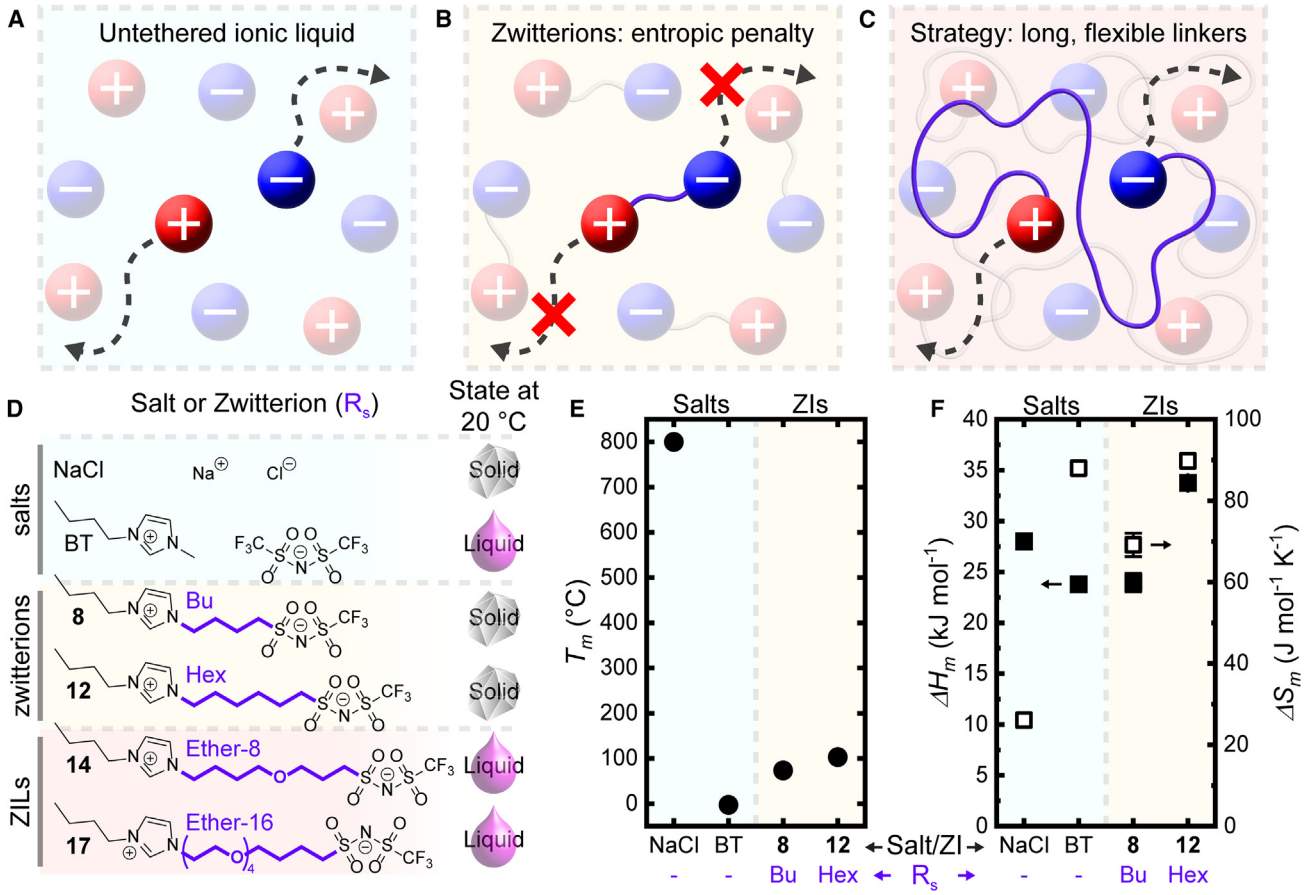

Figure 4. Zwitterionic spacer R_s governs melting behavior

(A) Schematic of a conventional ionic liquid in which dissociated ions can diffuse independently.

(B) Schematic of a ZIL in which individual ions are unable to diffuse independently, incurring an entropic penalty.

(C) We employ long, flexible R_s to depress T_m.

(D) Comparison of salts NaCl and BT with ZIs **8** and **12** and ZILs **14** and **17**.

(E and F) T_m (E) and enthalpy (ΔH_m) and entropy (ΔS_m) of fusion (F) of NaCl, BT, **8** and **12**. Data for NaCl and BT were taken from previous studies.[45,55,56] Data for **8** and **12** are represented as mean ± SD; n = 3.

18 (η = 13 Pa s) are identical to **14** and **17** but feature MEE tails, which decrease liquid viscosity by 2.5-fold (**15** versus **14**) or 2-fold (**18** versus **17**). The effect of R_a is even more pronounced. Supercooled benchmark **3** (η = 6490 Pa s) contains a sulfonate anion and is 48-fold more viscous than supercooled **10** (η = 136 Pa s), whose only difference is a CF_3-sulfonimide anion.

Dielectric spectroscopy

Dielectric relaxation spectroscopy measurements are conducted on the same set of seven ZIs and on silicone oil, an additional control, to understand how R_s, R_t, and R_a impact dielectric properties. The real (ε'; Figure 6A) and imaginary (ε''; Figure 6B) parts of the unitless complex permittivity are measured as a function of angular frequency $\omega = 2\pi\nu$ rad s^{-1}, where dielectric frequency ν = 20 Hz to 2 MHz. In this range, all seven ZIs exhibit a fast relaxation event that is attributed to electric field-mediated dipole bias, yielding the static dielectric constant $\varepsilon_{r,s}$ as a plateau in ε' and the dielectric relaxation timescale τ_{dr} at the local maximum in ε''.[30,39] At longer timescales, a larger polarization event is observed in ε' due to macroscopic electrode charging, and the onset of direct current conductivity is observed in ε''. The corresponding real (σ'; Figure S5A) and imaginary (σ''; Figure S5B) parts of conductivity are given by $\sigma^* = i\omega\varepsilon_0\varepsilon^*$ and are discussed alongside the dielectric loss tangent (Tan(δ); Figure S5C) in the supplemental information.[59]

The incorporation of longer spacers R_s leads to a monotonic increase in the polarization magnitude ($\varepsilon_{r,s}$; Figure 6C) and decrease in characteristic relaxation times τ_{dr}. For example, the MEE series of ZI **10**, ZIL **13**, ZIL **15**, and ZIL **18** possesses static dielectric constants of 234, 290, 345, and 404 and relaxation timescales of 10, 10, 4, and 2.5 μs, respectively. The R_t has a modest influence on relaxation timescales τ_{dr}, with a ~2.5-fold decrease upon replacing a butyl tail (τ_{dr}(**14**) = 10 μs and τ_{dr}(**17**) = 6.3 μs) with MEE (τ_{dr}(**15**) = 4 μs and τ_{dr}(**18**) = 2.5 μs), consistent with the apparent viscosity data for the same ZILs. Next, we characterize the effect of R_a by comparing ZIs **3**

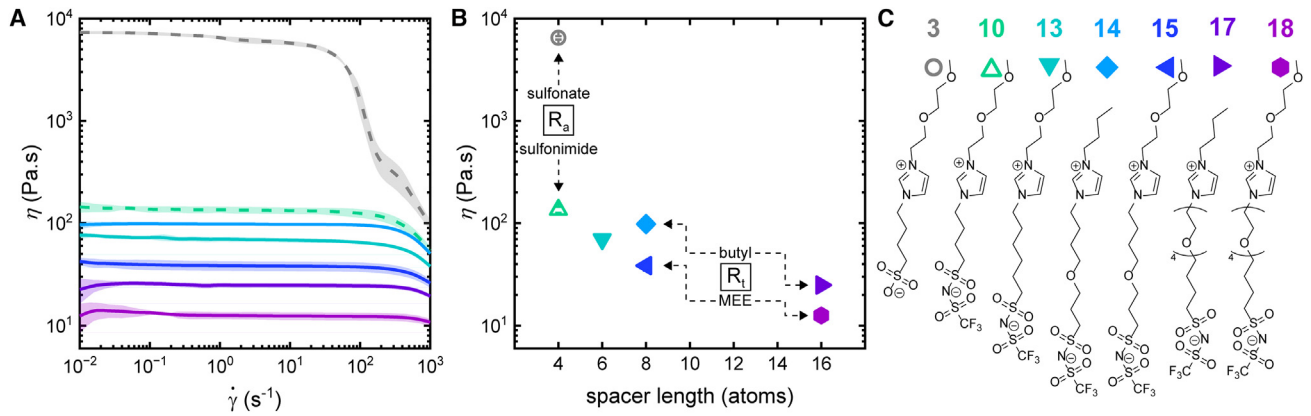

Figure 5. Apparent viscosity of ZILs

(A) Log-log plot of apparent viscosity as a function of shear rate.

(B and C) Semi-log plot (B) of apparent viscosity at a shear rate of 1 s^{-1} as a function of spacer length for (C) supercooled ZIs **3** and **10** and zwitterionic liquids (ZILs) **13**–**15**, **17**, and **18**.

Dashed lines and open data points denote supercooled liquids; solid lines and filled points denote ZILs. Data are shown as mean ± SD; n = 3.

(R_a = sulfonate) and **10** (R_a = CF_3-sulfonimide). Consistent with the 48-fold difference in viscosity, τ_{dr}(**3**) = 400 μs, while τ_{dr}(**10**) = 10 μs, confirming the importance of the anion in determining ZIL dynamics. Interestingly, this change in anion has a negligible impact on the static dielectric constant, $\varepsilon_{r,s}$(**3**) = 231 and $\varepsilon_{r,s}$(**10**) = 234 (Figure 6C), whose values are nearly the same as those reported previously for ZI **3** ($\varepsilon_{r,s}$ = 250).[30]

DISCUSSION

Spacer R_s: Length and flexibility enable stable ZILs, faster dynamics, and higher permittivity

It is well known that ZIs melt at higher temperatures than untethered ionic liquids (ILs) using the same ion pairs.[5,31,40,47,48] This phenomenon motivates the experiment shown in Figure 4, which presents the melting thermodynamics of NaCl,[56] ionic liquid BT,[57] ZI **8**, and ZI **12**. First, there is an extraordinary ΔT_m of 803°C between NaCl and BT. Strikingly, this melting point difference is dominated by entropy (Figures 4E and 4F), consistent with other ionic liquids and alkali halides.[46] ZIs **8** and **12** were designed to replicate the structure of BT as closely as possible to elucidate why ZIs melt at higher temperatures than their untethered IL counterparts. Importantly, ΔH_m for ZI **8** is identical to that of BT. Yet, the T_m of **8** is 76°C higher than that of BT due to a decrease in entropy of fusion. This result validates our hypothesis that ZIs melt at higher temperatures than ILs because their tethers incur an entropic penalty. To recover the lost entropy of fusion, we prepared ZI **12**, which is identical to **8** but replaces its 4-carbon spacer with a 6-carbon spacer whose two additional rotatable bonds should increase the molar entropy in the liquid state. Strikingly, **12** increases ΔS_m by 20 J mol^{-1} K^{-1} compared to **8**, roughly matching BT. Yet, **12** also melts 30°C higher than **8**

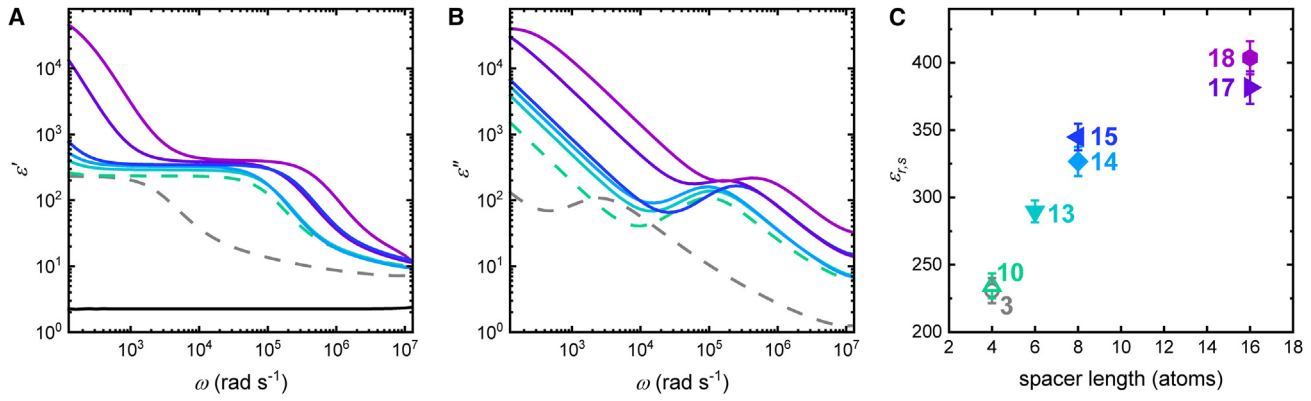

Figure 6. Dielectric properties of neat ZIs

(A and B) Relative (A) storage (ε′) and (B) loss (ε″) permittivity as a function of angular frequency ω at 25°C for supercooled ZIs **3** and **10** and ZILs **13**–**15**, **17**, and **18**.

(C) Static dielectric constant $\varepsilon_{r,s}$ of these ZIs as a function of spacer length.

Dashed lines and open data points denote supercooled liquids; solid lines and filled points denote stable liquids.

Data in (C) are shown as the flattest portion (**3**) or mean (**10**, **13**–**15**, **17**, **18**) ± SD of the plateau regions in (A).

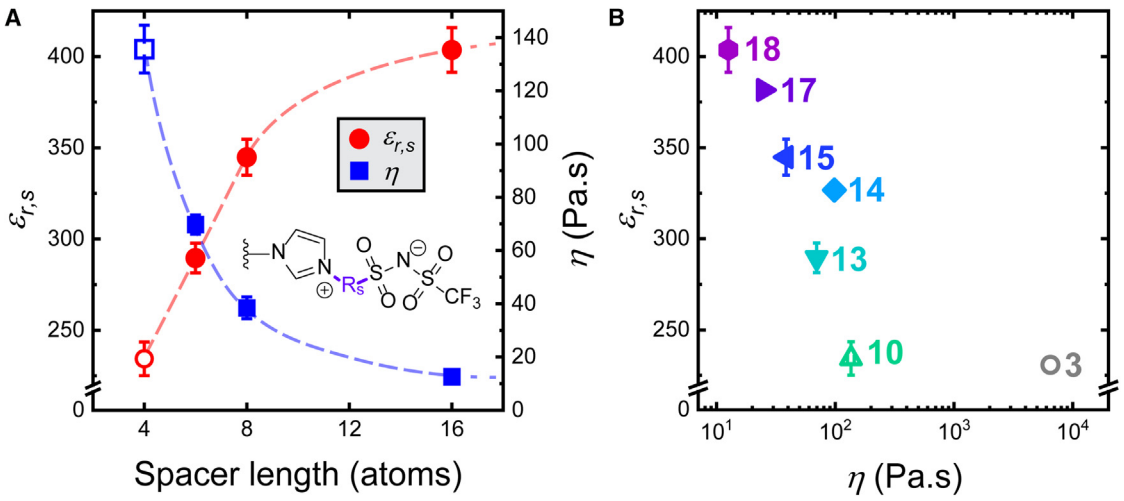

Figure 7. Comparison of ZIL static dielectric constant $\varepsilon_{r,s}$ and apparent viscosity η

(A) Orthogonal scaling of $\varepsilon_{r,s}$ (circles) and η (squares) as a function of spacer length for the MEE series of supercooled ZI **10** and ZILs **13**, **15**, and **18**.

(B) Semi-log plot of $\varepsilon_{r,s}$ as a function of η for supercooled ZIs **3** and **10** and ZILs **13**–**15**, **17**, and **18**.

Open data points denote supercooled liquids; filled points denote ZILs. Viscosity data are represented as mean ± SD; $n = 3$. Dielectric data are represented as the flattest portion (**3**) or mean (**10**, **13**–**15**, **17**, **18**) ± SD of the plateau regions in (Figure 6A).

due to a proportionally larger increase in ΔH_m. This suggests that, while a longer spacer increases ΔS_m, this alone is insufficient to suppress T_m. Rather, the entropy lost by introducing a zwitterionic tether must be recaptured without a concomitant increase in ΔH_m. This observation led us to introduce long and flexible linkers composed of ethers that offer greater flexibility than straight-chain alkanes.[58] The resulting ZILs **14** and **17** feature 8- and 16-atom spacers containing one and four ether groups, respectively. Both ZILs are stable liquids after drying and purification (>6 months dry storage at ambient temperatures). Moreover, synthesis of ZILs **15**, **16**, and **18**, featuring the same 8- and 16-atom ether-containing spacers, and ZIL **13**, whose hexyl spacer is combined with an ether-rich MEE tail, yielded four more stable ZILs. We verified that all six ZILs are pure and water free by ^{1}H, ^{13}C, and ^{19}F NMR (supplemental information), high-resolution mass spectrometry (supplemental information), thermogravimetric analysis (TGA; Figure S6; supplemental methods), and Fourier transform infrared (FTIR) spectroscopy (Figure S7; supplemental methods). Moreover, their viscosity does not change with prolonged storage (Figure S8), suggesting stable liquid structure over periods of at least 6–9 months. Additional η, T_g, spacer length, and molecular weight correlations are shown in Figures S9 and S10 and discussed in the supplemental methods.

To complement these thermodynamic effects, R_s greatly influences liquid viscosity and dielectric properties. Remarkably, dynamics grow faster as spacer length increases from 4 to 16 atoms. This is particularly pronounced for apparent viscosity, which decreases by more than 10-fold from a 4-carbon (ZI **10**) to a 16-atom (ZIL **18**) spacer. This trend is attributed to dilution of charge-charge interactions that likely dominate in these materials. However, τ_{dr} shows only a 4-fold decrease over the same interval. To understand this discrepancy, we note that timescale τ_{dr} describes dipole bias, which depends on displacement of charged end groups and should therefore correlate positively with spacer length. In other words, longer spacers simultaneously decrease the viscosity and increase the diffusion path length of charged end groups in an electric field.

The static dielectric constant $\varepsilon_{r,s}$ strongly correlates with spacer length. Interestingly, spacer length-dependent scaling of $\varepsilon_{r,s}$ is consistent across the 4-, 6-, and 8-atom spacers and then deviates upon elongation to a 16-atom spacer. Based on their structure, we estimate that the Kuhn lengths b_s of the two ether-containing spacers lie within the range of $b_{PEO} < b_s < b_{PE}$, where b_{PEO} = 1.1 nm and b_{PE} = 1.4 nm.[58] Thus, assuming C-C and C-O bond lengths of 1.54 and 1.42 Å, respectively,[60] we estimate that the 8-atom-spacer is roughly one Kuhn length, suggesting that scaling transitions for longer spacers coincide with a loss in bond-bond correlation. The spacer length dependence of both η and $\varepsilon_{r,s}$ for the MEE series of **10**, **13**, **15**, and **18** highlights the critical importance of R_s in determining ZIL properties (Figure 7A), which leads to a synergistic improvement in both η and $\varepsilon_{r,s}$ compared to benchmark **3** (Figure 7B).

Tail R_t: A long, flexible tail increases entropy of fusion and decreases viscosity

ZIs **4**, **5**, and **6** carry R_t = methyl, ethyl, and allyl, respectively, the shortest tail groups. Across this series, their decreasing T_m (T_m = 150°C, 126°C, and 57°C) are driven by decreasing enthalpy of fusion (43.3, 27.7, and 18.5 kJ mol^{-1}) that support the hypothesis that, in the limit of short tails, increasing steric hindrance around the cation disrupts intimate charge-charge packing. Finally, an MEE tail (ZI **10**) yields T_m = 69°C with strikingly large values for both ΔH_m and ΔS_m. Thus, MEE subverts the trend that larger tails decrease ΔH_m, possibly due to a different crystalline packing structure than observed for ZIs **4**, **5**, **6**, or **8**, or to a strong enthalpic contribution from the MEE tail itself. The large entropy of fusion is more intuitive. MEE adds three more rotatable

bonds than a butyl group, including two flexible ethers. This result supports our earlier argument that long and ether-rich moieties should increase the entropy of fusion compared to straight-chain alkanes, decreasing T_m. R_t also plays a meaningful role in determining viscosity, offering a roughly 2-fold decrease upon exchanging a butyl tail for MEE. The greater tail length of MEE is hypothesized to increase steric hindrance around the imidazolium cation relative to the butyl tail. Moreover, the ether groups, which coordinate cations,[41–43] may competitively interact with the imidazolium to decrease the strength and duration of charge-charge interactions and decrease bulk viscosity.

R_2: Methyl substitution decreases entropy of fusion

Exchanging the imidazolium 2-proton for a methyl group is instructive because imidazolium cations concentrate charge density at the 2 position.[61–63] As a result, the strongest Coulombic interactions occur at this position. Thus, increasing local steric bulk should weaken charge-charge interactions.[49–51] We replace the 2 proton in ZIs **8** and **10** with methyl groups to produce **9** and **11**. Although we observe the predicted decrease in ΔH_m, 2-methylation still increases T_m because ΔS_m decreases by an even larger margin. However, this effect varies dramatically: 2-methyl ZI **9** melts 49°C higher than 2-H ZI **8**, yet 2-methyl ZI **11** melts only 5°C above 2-H ZI **10**, suggesting that 2-position thermodynamic effects depend strongly on tail composition. Specifically, the MEE tail attenuates the effects of 2-substitution, possibly by increasing the entropy of the liquid with additional rotatable bonds.

R_a: CF_3-sulfonimide decreases enthalpy of fusion and viscosity compared to sulfonate

CF_3-sulfonimide ZI **10** melts 55°C–57°C lower than sulfonate ZI **1** or C_4F_9-sulfonimide ZI **7** because its enthalpy of fusion is 9 kJ mol^{-1} lower. Anion volume offers a potential explanation. Compared to sulfonate (71 $Å^3$),[31] structural analogs to CF_3-sulfonimide, including *N*-carboxytriflamide (173 $Å^3$)[31] and bis-triflimide (264 $Å^3$),[64] occupy larger volumes, suggesting a more diffuse charge that may diminish ΔH_m. By contrast, the structures of CF_3- and C_4F_9-sulfonimide are quite similar and only distinguished by the length of the perfluoroalkyl chain. The difference in ΔH_m cannot be explained in terms of electron-withdrawing strength, since the acid dissociation constants (pK_a) for the corresponding sulfonic acids are both ~0.7 in acetonitrile.[65,66] However, prior reports have described strong interactions between fluorine atoms in C_4F_9-sulfonimide and 1-ethyl-3-methylimidazolium cations, offering a potential explanation for the difference in ΔH_m observed here.[45] Finally, the viscosity η and dielectric relaxation time τ_{dr} for sulfonate **3** are 48- and 40-fold larger than for CF_3-sulfonimide **10**. Again, anion volume offers a possible explanation, as the higher charge density of **3** may create a deeper energy well for intimate ion pairs, slowing ion pair dynamics.

Conclusions

We synthesized a library of 18 ZIs, including three known and 15 previously unreported ZIs, to map their melting behavior, apparent viscosity, and dielectric properties across four functional positions. We find that the spacer R_s is the most important given the resulting liquid stability, faster dynamics, and increased permittivity. While a longer spacer increases the entropy of fusion, T_m suppression also demands avoiding a concomitant increase in enthalpy of fusion. We achieved this goal via ether-mediated chain flexibility, yet we anticipate that many alternative strategies may exist. In parallel, we showed that a long, flexible tail and a bulky, diffuse CF_3-sulfonimide anion decrease T_m and offer faster dynamics than shorter tails and a sulfonate anion. These insights guided the design and synthesis of six room temperature ZILs, which feature static dielectric constants as large as 404 and apparent viscosities 500-fold smaller than supercooled benchmark ZI **3** at room temperature. Together, our results provide the foundation for an emergent class of liquid dielectrics with potential applications in soft electronics and energy storage.

METHODS

Detailed methods can be found in the supplemental information.

RESOURCE AVAILABILITY

Lead contact

Requests for further information and resources should be directed to and will be fulfilled by the lead contact, Dylan M. Barber (dbarber@seas.harvard.edu).

Materials availability

There are restrictions to the availability of the ZIs and precursors reported in this work because of the lack of an external centralized repository for its distribution and our need to maintain the stock. Specific molecules may be made available upon negotiation of possible collaboration and a completed materials transfer agreement.

Data and code availability

Source data, including dielectric spectroscopy, differential scanning calorimetry, fourier transform infrared spectroscopy, nuclear magnetic resonance, mass spectrometry, rheology, and thermogravimetric analysis have been deposited at Zenodo and are publicly available as of the date of publication at Zenodo: https://doi.org/10.5281/zenodo.14510696 under the title: Source Data for "Rational Design and Synthesis of Zwitterionic Liquid Dielectrics." No new code was generated by this work.

ACKNOWLEDGMENTS

The authors gratefully acknowledge NSF DMR-2011754 (Harvard MRSEC), NSF DMR-2122195 (NTU PREM), the Harvard John A. Paulson School of Engineering and Applied Sciences post-baccalaureate program, and the Harvard Research Scholar Initiative. This work was performed in part at the Harvard University Center for Nanoscale Systems (CNS), a member of the National Nanotechnology Coordinated Infrastructure Network (NNCI), which is supported by the National Science Foundation under NSF award ECCS-2025158. Mass spectrometry data were collected at the Harvard Center for Mass Spectrometry. NMR data were collected at the Laukien-Purcell Instrumentation Center. The authors thank Dr. N. Colella, J. Sosa, and Dr. B. Paren for insightful discussions and guidance in materials characterization.

AUTHOR CONTRIBUTIONS

Conceptualization, D.M.B.; methodology, D.M.B., M.D.N., and J.A.L.; validation, D.M.B. and M.D.N.; formal analysis, D.M.B. and J.A.L.; investigation, D.M.B. and M.D.N.; resources, J.A.L.; data curation, D.M.B. and J.A.L.;

writing – original draft, D.M.B.; writing – review and editing, D.M.B. and J.A.L.; visualization, D.M.B.; supervision, J.A.L.; project administration, D.M.B. and J.A.L.; funding acquisition, J.A.L.

DECLARATION OF INTERESTS

This work has been filed under International Patent Application PCT/US2024/58135.

SUPPLEMENTAL INFORMATION

Supplemental information can be found online at https://doi.org/10.1016/j.matt.2025.102049.

Received: August 24, 2024
Revised: January 20, 2025
Accepted: February 19, 2025
Published: March 17, 2025

REFERENCES

1. Shin, H., Shin, J., Hayward, R.C., and Kim, H.J. (2023). Ionoelastomers at Electrified Interfaces: Differential Electric Double-Layer Capacitances of Cross-Linked Polymeric Ions and Mobile Counterions. Macromolecules *56*, 7827–7836. https://doi.org/10.1021/acs.macromol.3c01092.
2. Ahmed, M.D., Zhu, Z., Khamzin, A., Paddison, S.J., Sokolov, A.P., and Popov, I. (2023). Effect of Ion Mass on Dynamic Correlations in Ionic Liquids. J. Phys. Chem. B *127*, 10411–10421. https://doi.org/10.1021/acs.jpcb.3c05568.
3. Shen, C., Kabbani, M., and Evans, C.M. (2021). Solid-State, Single-Anion-Conducting Networks for Flexible and Stable Supercapacitor Electrolytes. ACS Appl. Polym. Mater. *3*, 4168–4176. https://doi.org/10.1021/acsapm.1c00613.
4. Chen, C., Mei, B., Zhou, J., Schweizer, K.S., Evans, C.M., and Braun, P.V. (2024). Coupling of Ethylene-Oxide-Based Polymeric Network Structure and Counterion Chemistry to Ionic Conductivity and Ion Selectivity. Macromolecules *57*, 6779–6788. https://doi.org/10.1021/acs.macromol.4c00539.
5. Jones, S.D., Nguyen, H., Richardson, P.M., Chen, Y.Q., Wyckoff, K.E., Hawker, C.J., Clément, R.J., Fredrickson, G.H., and Segalman, R.A. (2022). Design of Polymeric Zwitterionic Solid Electrolytes with Superionic Lithium Transport. ACS Cent. Sci. *8*, 169–175. https://doi.org/10.1021/acscentsci.1c01260.
6. Kim, H.J., Chen, B., Suo, Z., and Hayward, R.C. (2020). Ionoelastomer junctions between polymer networks of fixed anions and cations. Science *367*, 773–776. https://doi.org/10.1126/science.aay8467.
7. Kim, H.J., Paquin, L., Barney, C.W., So, S., Chen, B., Suo, Z., Crosby, A.J., and Hayward, R.C. (2020). Low-Voltage Reversible Electroadhesion of Ionoelastomer Junctions. Adv. Mater. *32*, e2000600. https://doi.org/10.1002/adma.202000600.
8. Kim, Y.J., Lee, J., Hwang, J.H., Chung, Y., Park, B.J., Kim, J., Kim, S.H., Mun, J., Yoon, H.J., Park, S.M., and Kim, S.W. (2024). High-Performing and Capacitive-Matched Triboelectric Implants Driven by Ultrasound. Adv. Mater. *36*, e2307194. https://doi.org/10.1002/adma.202307194.
9. Liu, Y., Li, J., Song, S., Kang, J., Tsao, Y., Chen, S., Mottini, V., McConnell, K., Xu, W., Zheng, Y.Q., et al. (2020). Morphing electronics enable neuromodulation in growing tissue. Nat. Biotechnol. *38*, 1031–1036. https://doi.org/10.1038/s41587-020-0495-2.
10. Xu, H., Hirschberg, A.W., Scholten, K., Berger, T.W., Song, D., and Meng, E. (2018). Acute in vivo testing of a conformal polymer microelectrode array for multi-region hippocampal recordings. J. Neural. Eng. *15*, 016017. https://doi.org/10.1088/1741-2552/aa9451.
11. Lebedev, M.A., and Nicolelis, M.A.L. (2006). Brain-machine interfaces: past, present and future. Trends Neurosci. *29*, 536–546. https://doi.org/10.1016/j.tins.2006.07.004.
12. Robinson, J.T., Pohlmeyer, E., Gather, M.C., Kemere, C., Kitching, J.E., Malliaras, G.G., Marblestone, A., Shepard, K.L., Stieglitz, T., and Xie, C. (2019). Developing Next-Generation Brain Sensing Technologies - A Review. IEEE Sens. J. *19*, 10163–10175. https://doi.org/10.1109/JSEN.2019.2931159.
13. Li, H., Shi, W., Song, J., Jang, H.J., Dailey, J., Yu, J., and Katz, H.E. (2019). Chemical and Biomolecule Sensing with Organic Field-Effect Transistors. Chem. Rev. *119*, 3–35. https://doi.org/10.1021/acs.chemrev.8b00016.
14. Chortos, A., Mao, J., Mueller, J., Hajiesmaili, E., Lewis, J.A., and Clarke, D.R. (2021). Printing Reconfigurable Bundles of Dielectric Elastomer Fibers. Adv. Funct. Mater. *31*, 1–10. https://doi.org/10.1002/adfm.202010643.
15. Larson, N.M., Mueller, J., Chortos, A., Davidson, Z.S., Clarke, D.R., and Lewis, J.A. (2023). Rotational multimaterial printing of filaments with sub-voxel control. Nature *613*, 682–688. https://doi.org/10.1038/s41586-022-05490-7.
16. Chortos, A., Hajiesmaili, E., Morales, J., Clarke, D.R., and Lewis, J.A. (2020). 3D Printing of Interdigitated Dielectric Elastomer Actuators. Adv. Funct. Mater. *30*, 1–10. https://doi.org/10.1002/adfm.201907375.
17. Hajiesmaili, E., Khare, E., Chortos, A., Lewis, J., and Clarke, D.R. (2019). Voltage-controlled morphing of dielectric elastomer circular sheets into conical surfaces. Extreme Mech. Lett. *30*, 100504. https://doi.org/10.1016/j.eml.2019.100504.
18. Duduta, M., Clarke, D.R., and Wood, R.J. (2017). A high speed soft robot based on dielectric elastomer actuators. In IEEE International Conference on Robotics and Automation, pp. 4346–4351. https://doi.org/10.1109/ICRA.2017.7989501.
19. Cohen, A.J., Kollosche, M., Yuen, M.C., Lee, D.Y., Clarke, D.R., and Wood, R.J. (2022). Batch-Sprayed and Stamp-Transferred Electrodes: A New Paradigm for Scalable Fabrication of Multilayer Dielectric Elastomer Actuators. Adv. Funct. Mater. *32*, 1–11. https://doi.org/10.1002/adfm.202205394.
20. Duduta, M., Hajiesmaili, E., Zhao, H., Wood, R.J., and Clarke, D.R. (2019). Realizing the potential of dielectric elastomer artificial muscles. Proc. Natl. Acad. Sci. USA *116*, 2476–2481. https://doi.org/10.1073/pnas.1815053116.
21. Zhao, H., Hussain, A.M., Israr, A., Vogt, D.M., Duduta, M., Clarke, D.R., and Wood, R.J. (2020). A Wearable Soft Haptic Communicator Based on Dielectric Elastomer Actuators. Soft Robot. *7*, 451–461. https://doi.org/10.1089/soro.2019.0113.
22. El-Atab, N., Mishra, R.B., Al-Modaf, F., Joharji, L., Alsharif, A.A., Alamoudi, H., Diaz, M., Qaiser, N., and Hussain, M.M. (2020). Soft Actuators for Soft Robotic Applications: A Review. Adv. Intell. Syst. *2*. https://doi.org/10.1002/aisy.202000128.
23. Acome, E., Mitchell, S.K., Morrissey, T.G., Emmett, M.B., Benjamin, C., King, M., Radakovitz, M., and Keplinger, C. (2018). Hydraulically amplified self-healing electrostatic actuators with muscle-like performance. Science *359*, 61–65. https://doi.org/10.1126/science.aao6139.
24. Shintake, J., Cacucciolo, V., Floreano, D., and Shea, H. (2018). Soft Robotic Grippers. Adv. Mater. *30*, e1707035. https://doi.org/10.1002/adma.201707035.
25. Sokolov, A.N., Tee, B.C.-K., Bettinger, C.J., Tok, J.B.H., and Bao, Z. (2012). Chemical and Engineering Approaches To Enable Organic Field-Effect Transistors for Electronic Skin Applications. Acc. Chem. Res. *45*, 361–371.
26. Zhao, D., Zhu, Y., Cheng, W., Chen, W., Wu, Y., and Yu, H. (2021). Cellulose-Based Flexible Functional Materials for Emerging Intelligent Electronics. Adv. Mater. *33*, e2000619. https://doi.org/10.1002/adma.202000619.

27. Zhu, L., and Wang, Q. (2012). Novel ferroelectric polymers for high energy density and low loss dielectrics. Macromolecules *45*, 2937–2954. https://doi.org/10.1021/ma2024057.

28. Chen, K., Liu, Z., Zheng, W., Liu, S., Chi, Z., Xu, J., and Zhang, Y. (2023). Research progress of intrinsic polymer dielectrics with high permittivity. IET Nanodielectrics *6*, 182–211. https://doi.org/10.1049/nde2.12054.

29. Onsager, L. (1936). Electric Moments of Molecules in Liquids. J. Am. Chem. Soc. *58*, 1486–1493. https://doi.org/10.1021/ja01299a050.

30. Mei, W., Rothenberger, A.J., Bostwick, J.E., Rinehart, J.M., Hickey, R.J., and Colby, R.H. (2021). Zwitterions Raise the Dielectric Constant of Soft Materials. Phys. Rev. Lett. *127*, 228001. https://doi.org/10.1103/PhysRevLett.127.228001.

31. Mei, W., Colby, R.H., and Hickey, R.J. (2024). Enhancing the dielectric constant of zwitterionic liquids via dipole moment and anion chemistry. J. Chem. Phys. *161*, 014506. https://doi.org/10.1063/5.0213612.

32. Xu, Y., Lu, S., Wei, Z., and Feng, S. (2023). Supramolecular Elastomers with Excellent Dielectric Properties and High Recyclability Based on the Coordinative Bond. Macromol. Rapid Commun. *44*, e2200766. https://doi.org/10.1002/marc.202200766.

33. von Szczepanski, J., Wolf, J., Hu, W.H., Schneider, R., Danner, P.M., Kupferschmid, A., Jenatsch, S., Hany, R., Nüesch, F.A., and Opris, D.M. (2024). High-Permittivity Polysiloxanes for Bright, Stretchable Electroluminescent Devices. Adv. Opt. Mater. *12*, 1–9. https://doi.org/10.1002/adom.202400132.

34. Sheima, Y., Von Szczepanski, J., Danner, P.M., Künniger, T., Remhof, A., Frauenrath, H., and Opris, D.M. (2022). Transient Elastomers with High Dielectric Permittivity for Actuators, Sensors, and beyond. ACS Appl. Mater. Interfaces *14*, 40257–40265. https://doi.org/10.1021/acsami.2c05631.

35. Kurland, R.J., and Wilson, E.B., Jr. (1957). Microwave spectrum, structure, dipole moment, and quadrupole coupling constants of formamide. J. Chem. Phys. *27*, 585–590. https://doi.org/10.1063/1.1743775.

36. Beers, Y., and Russell, T.W. (1966). Evaluation of a Stark Voltmeter. IEEE Trans. Instrum. Meas. *15*, 380–388.

37. Coop, I.E., and Sutton, L.E. (1939). The vapour-phase electric dipole moments of thionyl chloride, sulphuryl chloride, dimethyl sulphone, and thiophosgene. Trans. Faraday Soc. *35*, 505–511. https://doi.org/10.1039/tf9393500505.

38. Sheima, Y., Yuts, Y., Frauenrath, H., and Opris, D.M. (2021). Polysiloxanes Modified with Different Types and Contents of Polar Groups: Synthesis, Structure, and Thermal and Dielectric Properties. Macromolecules *54*, 5737–5749. https://doi.org/10.1021/acs.macromol.1c00362.

39. Mei, W., Han, A., Hickey, R.J., and Colby, R.H. (2021). Effect of chemical substituents attached to the zwitterion cation on dielectric constant. J. Chem. Phys. *155*, 244505. https://doi.org/10.1063/5.0074100.

40. Yoshizawa, M., Narita, A., and Ohno, H. (2004). Design of ionic liquids for electrochemical applications. Aust. J. Chem. *57*, 139–144. https://doi.org/10.1071/CH03240.

41. Yoshizawa-Fujita, M., Tamura, T., Takeoka, Y., and Rikukawa, M. (2011). Low-melting zwitterion: Effect of oxyethylene units on thermal properties and conductivity. Chem. Commun. *47*, 2345–2347. https://doi.org/10.1039/c0cc03754k.

42. Jadhav, S., Ganvir, V., Singh, M.K., and Shanmuganathan, K. (2023). Synthesis of N-oxyethylene substituted imidazolium-based zwitterions as a recyclable solvent for cellulose dissolution. Cellulose *30*, 87–109. https://doi.org/10.1007/s10570-022-04883-1.

43. Kuroda, K., Satria, H., Miyamura, K., Tsuge, Y., Ninomiya, K., and Takahashi, K. (2017). Design of Wall-Destructive but Membrane-Compatible Solvents. J. Am. Chem. Soc. *139*, 16052–16055. https://doi.org/10.1021/jacs.7b08914.

44. Yoshizawa-Fujita, M., and Ohno, H. (2023). Applications of Zwitterions and Zwitterionic Polymers for Li-Ion Batteries. Chem. Rec. *23*, e202200287. https://doi.org/10.1002/tcr.202200287.

45. Lee, O.A., McBride, M.K., Ticknor, M., Sharpes, J., and Hayward, R.C. (2023). Pendent Sulfonylimide Ionic Liquid Monomers and Ionoelastomers via SuFEx Click Chemistry. Chem. Mater. *35*, 10030–10040. https://doi.org/10.1021/acs.chemmater.3c02038.

46. Endo, T., Sunada, K., Sumida, H., and Kimura, Y. (2022). Origin of low melting point of ionic liquids: dominant role of entropy. Chem. Sci. *13*, 7560–7565. https://doi.org/10.1039/d2sc02342c.

47. Yoshizawa, M., Hirao, M., Ito-Akita, K., and Ohno, H. (2001). Ion conduction in zwitterionic-type molten salts and their polymers. J. Mater. Chem. *11*, 1057–1062. https://doi.org/10.1039/b101079o.

48. Ohno, H., Yoshizawa-Fujita, M., and Kohno, Y. (2018). Design and properties of functional zwitterions derived from ionic liquids. Phys. Chem. Chem. Phys. *20*, 10978–10991. https://doi.org/10.1039/c7cp08592c.

49. Hunt, P.A. (2007). Why does a reduction in hydrogen bonding lead to an increase in viscosity for the 1-Butyl-2,3-dimethyl-imidazolium-based ionic liquids? J. Phys. Chem. B *111*, 4844–4853. https://doi.org/10.1021/jp067182p.

50. Zhang, Y., and Maginn, E.J. (2012). The effect of C2 substitution on melting point and liquid phase dynamics of imidazolium based-ionic liquids: Insights from molecular dynamics simulations. Phys. Chem. Chem. Phys. *14*, 12157–12164. https://doi.org/10.1039/c2cp41964e.

51. Endo, T., Kato, T., and Nishikawa, K. (2010). Effects of methylation at the 2 position of the cation ring on phase behaviors and conformational structures of imidazolium-based ionic liquids. J. Phys. Chem. B *114*, 9201–9208. https://doi.org/10.1021/jp104123v.

52. Zhang, Y., and Maginn, E.J. (2014). Molecular dynamics study of the effect of alkyl chain length on melting points of [CnMIM] [PF6] ionic liquids. Phys. Chem. Chem. Phys. *16*, 13489–13499. https://doi.org/10.1039/c4cp01048e.

53. Serra, P.B., Ribeiro, F.M., Rocha, M.A., Fulem, M., Růžička, K., Coutinho, J.A., and Santos, L.M. (2017). Solid-liquid equilibrium and heat capacity trend in the alkylimidazolium PF6 series. J. Mol. Liq. *248*, 678–687. https://doi.org/10.1016/j.molliq.2017.10.042.

54. Lobo Ferreira, A.I.M.C., Rodrigues, A.S.M.C., Villas, M., Tojo, E., Rebelo, L.P.N., and Santos, L.M.N.B.F. (2019). Crystallization and Glass-Forming Ability of Ionic Liquids: Novel Insights into Their Thermal Behavior. ACS Sustain. Chem. Eng. *7*, 2989–2997. https://doi.org/10.1021/acssuschemeng.8b04343.

55. Serra, P.B., Ribeiro, F.M., Rocha, M.A., Fulem, M., Růžička, K., and Santos, L.M. (2016). Phase behavior and heat capacities of the 1-benzyl-3-methylimidazolium ionic liquids. J. Chem. Thermodyn. *100*, 124–130. https://doi.org/10.1016/j.jct.2016.04.009.

56. Janz, G. (1967). Molten Salts Handbook (Academic Press).

57. Shimizu, Y., Ohte, Y., Yamamura, Y., and Saito, K. (2007). Effects of thermal history on thermal anomaly in solid of ionic liquid compound, [C4mim][Tf2N]. Chem. Lett. *36*, 1484–1485. https://doi.org/10.1246/cl.2007.1484.

58. Rubinstein, M., and Colby, R.H. (2003). Polymer Physics (Oxford University Press, Inc.).

59. Kremer, F., and Schönhals, A. (2003). Broadband Dielectric Spectroscopy (Springer-Verlag Berlin Heidelberg GmbH). https://doi.org/10.1016/b978-0-12-823518-8.00001-3.

60. Glockler, G. (1958). Carbon-oxygen bond energies and bond distances. J. Phys. Chem. *62*, 1049–1054. https://doi.org/10.1021/j150567a006.

61. Dymek, C.J., Grossie, D.A., Fratini, A.V., and Wade Adams, W. (1989). Evidence for the presence of hydrogen-bonded ion-ion interactions in the molten salt precursor, 1-methyl-3-ethylimidazolium chloride. J. Mol. Struct. *213*, 25–34. https://doi.org/10.1016/0022-2860(89)85103-8.

62. Dong, K., Zhang, S., Wang, D., and Yao, X. (2006). Hydrogen bonds in imidazolium ionic liquids. J. Phys. Chem. A *110*, 9775–9782. https://doi.org/10.1021/jp054054c.

63. Hardacre, C., Holbrey, J.D., McMath, S.E.J., Bowron, D.T., and Soper, A.K. (2003). Structure of molten 1,3-dimethylimidazolium chloride using

neutron diffraction. J. Chem. Phys. *118*, 273–278. https://doi.org/10.1063/1.1523917.

64. Smith, G.D., Borodin, O., Magda, J.J., Boyd, R.H., Wang, Y., Bara, J.E., Miller, S., Gin, D.L., and Noble, R.D. (2010). A comparison of fluoroalkyl-derivatized imidazolium: TFSI and alkyl-derivatized imidazolium: TFSI ionic liquids: A molecular dynamics simulation study. Phys. Chem. Chem. Phys. *12*, 7064–7076. https://doi.org/10.1039/c001387k.

65. Raamat, E., Kaupmees, K., Ovsjannikov, G., Trummal, A., Kütt, A., Saame, J., Koppel, I., Kaljurand, I., Lipping, L., Rodima, T., et al. (2013). Acidities of strong neutral Brønsted acids in different media. J. Phys. Org. Chem. *26*, 162–170. https://doi.org/10.1002/poc.2946.

66. Kondo, H., Hatsuda, K., Tano, N., and Baghel, P. (2017). Ionic Liquid, Lubricant, and Magnetic Recording Medium.

Matter, Volume *8*

Supplemental information

Rational design and synthesis of zwitterionic liquid dielectrics

Dylan M. Barber, Michael D. Nelwood, and Jennifer A. Lewis

Supplemental Methods

Materials. Dichloromethane (99.9 %) (Avantor Performance Material LLC), 1-methylimidazole (99.0 %), 1-ethylimidazole (98.0 %) (TCI America), toluene (anhydrous, 99.5 %), 2,2,2-trifluoroethanol (99%) (BeanTown Chemical), Tetrahydrofuran (THF, 99%, stabilized ACS), Hexane (98.5 %, mixture of isomers, ACS), Acetonitrile (99.9%, anhydrous, Hi PerSolv CHROMANORM® super gradient grade for HPLC), Acetone (99.5 %), Diethyl ether (Et_2O, 98%, stabilized), Ethyl acetate (EtOAc, 99.5% ACS), Glacial acetic acid (AcOH, 99.7-100.5 % ACS), Methanol (MeOH, 99.8 % ACS, used for workups) (VWR Chemicals BDH®), KOH (85%, Reagent Grade), Sodium sulfite (anhydrous ACS) (VWR), HPLC-grade methanol (99.9%, used for mass spectrometry), 1,4-butanesultone (98%), 1,3-propanesultone (98%), 1-Butylimidazole (98%), Imidazole (99%, ReagentPlus®), 2-methylimidazole (99%), Magnesium sulfate ($MgSO_4$, anhydrous, ReagentPlus®, 99.5%), Sodium sulfate (99.0 %, anhydrous, granular), Potassium carbonate (K_2CO_3, anhydrous, free-flowing, Redi-Dri™, ACS reagent, 99%), Silica gel (technical grade, pore size 60 Å, 40-63 μm particle size), 1-Bromobutane (99%, ReagentPlus®), Thionyl chloride (99%, ReagentPlus®), N,N-Dimethylformamide (DMF, 99.8%, Anhydrous), 1,4-butanediol (99% ReagentPlus®), Potassium *tert*-butoxide (*t*-BuOK, 1.0 M in THF), Lithium bis(trimethylsilyl)amide solution (Li-HMDS, 1.0 M in THF), Tetraethylene glycol (TetrEG, 99 %), Butylated hydroxytoluene (BHT, 99 %) (Millipore Sigma), DMSO-d_6 (99.9 % D, AcroSeal™), 6-chloro-1-hexanol (97 %), Celite® 535 (Thermo Scientific Chemicals), High purity argon (AR HP300) (Airgas), 1-Bromo-2-(2-methoxyethoxy)ethane (MEE-Br, 97 %) (Combi-Blocks), 1-allylimidazole (97%), Activated charcoal (DARCO® 4-12 mesh) (Avantor), Trifluoromethanesulfonamide (triflamide, 98%), and Perfluorobutanesulfonyl fluoride (95%) (Oakwood Chemical) were used as received without further purification unless otherwise noted.

Instrumentation.^{1}H NMR (400.2 MHz), ^{13}C NMR (100.6 MHz), and ^{19}F NMR (376.5 MHz) were collected using a 400 MHz Bruker AVANCE NEO NMR spectrometer equipped with a 5 mm RT double resonance broad banded iProbe. Products were dissolved (20 μM) in HPLC-grade MeOH and measured via positive ion (zwitterions, **L**, **N**) and negative ion (sulfonate, sulfonimide, and C_4F_9-sulfonamide intermediates) electrospray ionization on a Bruker Impact II q-TOF mass spectrometer equipped with an Agilent 1260 HPLC system using flow injection analysis. The samples were introduced into the mass spectrometer using 60% acetonitrile with 0.1% formic acid through the HPLC system. The mass scale was internally calibrated using sodium formate clusters which were introduced at the end of each run to achieve high mass accuracy. Differential scanning calorimetry (DSC) was conducted on a TA instruments Discovery 250 calorimeter. All zwitterions were dried for 24 h at 115 °C in a vacuum oven, stored under high purity argon, and quickly transferred to aluminum pans and hermetically sealed for characterization. Room-temperature solids were subjected to heat-cool-heat cycles, and liquids to cool-heat cycles (all ramp rates 10 °C min^{-1}, with equilibration and 5-minute isotherms at each maximum and minimum) followed by a ramp to 25 °C at 20 °C min^{-1}. T_m was defined as the onset of the melting endotherm to limit variability with scanning rate and sample mass. ΔS_m was calculated by $\Delta S_m = \Delta H_m / T_m$. T_g was determined by taking the mean from the cooling and subsequent heating cycles. ΔC_g was determined as the difference between extrapolated liquid and glass heat capacities at T_g during heating. Rheology was conducted on a TA Instruments Discovery Hybrid HR20 rheometer with an 8 mm parallel plate geometry and a 400 μm gap. All liquids were dried for 24 h at 115 °C in a vacuum oven, then immediately transferred to the rheometer for measurement. Dielectric spectroscopy was conducted on a TA Instruments Discovery Hybrid HR20 rheometer with 25 mm custom dielectric parallel plate geometries equipped with a Keysight E4980A LCR meter and operating with 100 mV oscillation amplitude and a 100 μm gap. All molecules were dried for 24 h at 115 °C in a vacuum oven, then stored under high purity argon and transferred to the rheometer for measurement. Molecules **3** and **10** were placed on the bottom electrode as dry powders and heated to 150 °C for 5 minutes. Then, the top electrode was lowered into place and the apparatus quenched to 25 °C before measuring. Thermogravimetric analysis (TGA) was run on a TA Instruments Discovery TGA 550; samples were heated to 600 °C with a ramp rate of 20 °C min^{-1} under a pure N_2 atmosphere and mass change recorded as a function of time and temperature. FTIR measurements were conducted on a Nicolet iS50 FTIR spectrometer. A background spectrum was collected in the absence of any sample, then samples were

placed on the ATR crystal, and, in the case of crystalline **10**, compressed under the attached metal piston before measuring. FTIR data was processed by applying an Asymmetric Least Squares (AsLS) baseline correction with AsLS Log(lambda) = 6 and AsLS asymmetry = 0.000001, then normalized. Water uptake was characterized by drying ZI **10** and ZILs **15** and **18** in a vacuum oven at 115 °C for 24 h before TGA and FTIR measurements. 500 mg samples of each were then sealed in a container with an open cup of deionized water (100% relative humidity) for 1 week before repeating FTIR, TGA, viscosity, and dielectric spectroscopy measurements.

An important note regarding safety with refluxing thionyl chloride. All reactions using refluxing thionyl chloride should be run and quenched with care as thionyl chloride reacts violently with water to produce concentrated hydrochloric acid and sulfur dioxide vapor. This vapor is caustic, toxic, and can damage infrastructure, including the downstream ductwork of a fume hood. To prevent large-scale release of concentrated acid and sulfur dioxide vapor during reaction and quenching, evolved gas should be routed through a vacuum trap to prevent back-suck, followed by a gas scrubber composed of a glass sparger and concentrated aqueous base; we used a stirring, 5 L bath of 5 M KOH. While quenching with ice pellets, it is important to maintain a high stirring rate because liquid water is immiscible with the crude product mixture. A low stirring rate enables formation of a reservoir of liquid water, which can lead to a violent runaway reaction. To avoid this, we maintain a high stirring rate and incremental addition of ice pellets while keeping the reaction vessel at 0 °C. This note applies to the synthesis of sulfonyl chloride intermediates **A**, **D**, **G**, and **J**.

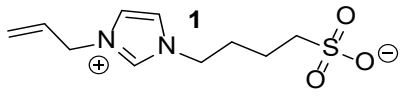

*Synthesis of **1**.* 4.411 g (40.8 mmoles) 1-allylimidazole was combined with 5.138 g (37.7 mmoles) 1,4-butanesultone and 41 mg (0.19 mmoles) in a 20 mL scintillation vial and heated to 80 °C with stirring for 43.5 hours, then stopped by removing from heat. The solid pellet of product was collected by breaking the vial, separating glass fragments, grinding the product in a mortar and pestle, washing with 3x40 mL of acetone, and drying under reduced pressure to afford **1** as a white powder in 7.531 g (82 %) yield. ^{1}H NMR (400.2 MHz, DMSO-d_6, δ): 9.41-9.29 (s, 1H), 7.92-7.85 (s, 1H), 7.82-7.75 (s, 1H), 6.15-5.98 (m, 1H), 5.41-5.24 (m, 2H), 4.94-4.81 (d, 2H), 4.31-4.14 (t, 2H), 2.58-2.42 (t, 2H), 2.00-1.81 (m, 2H), 1.66-1.46 (m, 2H). ^{13}C NMR (100.6 MHz, DMSO-d_6, δ): 136.30 (s, 1C), 131.85 (s, 1C), 122.68 (s, 1C), 122.50 (s, 1C), 120.23 (s, 1C), 50.79 (s, 1C), 50.55 (s, 1C), 48.63 (s, 1C), 28.64 (s, 1C), 21.82 (s, 1C). ESI (m/z): 245.0965 ($C_{10}H_{17}N_2O_3S^+$, calculated 245.0954).

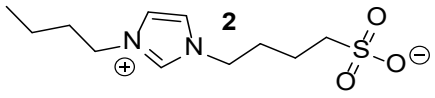

*Synthesis of **2**.* 118.2 g (952 mmoles) 1-butylimidazole was combined with 121.0 g (889 mmoles) 1,4-butanesultone in a 500 mL round-bottom flask, then heated to 80 °C with stirring for 24 h to afford a white, solid hemisphere in the bottom of the flask. The flask was broken, glass fragments removed, and the solids ground in a mortar and pestle under acetone, then isolated and washed with 3 x 500 mL acetone to afford **2** as a white powder in 230.95 (99.8 %) yield. ^{1}H NMR (400.2 MHz, DMSO-d_6, δ): 9.41-9.34 (s, 1H), 7.90-7.83 (m, 2H), 4.28-4.14 (m, 4H), 2.55-2.45 (t, 2H), 1.97-1.84 (m, 2H), 1.84-1.72 (m, 2H), 1.64-1.49 (m, 2H), 1.34-1.17 (m, 2H), 0.97-0.83 (t, 3H). ^{13}C NMR (100.6 MHz, DMSO-d_6, δ): 136.19 (s, 1C), 122.52 (s, 1C),

122.43 (s, 1C), 50.53 (s, 1C), 48.54 (s, 1C), 48.50 (s, 1C), 31.31 (s, 1C), 28.64 (s, 1C), 21.81 (s, 1C), 18.78 (s, 1C), 13.26 (s, 1C). ESI (m/z): 261.1268 ($C_{11}H_{21}N_2O_3S^+$, calculated 261.1267).

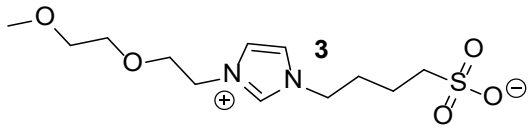

*Synthesis of **3**.* 1.254 g (7.37 mmoles) **L** was combined with 1.010 g (7.42 mmoles) 1,4-butanesultone and 7 mL acetone in a 20 mL scintillation vial and heated to 50 °C with stirring for 120 hours, then returned to room temperature and precipitated in 12 mL Et_2O. The dense phase was 5x (diluted to 2 mL in MeOH and precipitated in 12 mL EtOAc) followed by 3x (dilute to 2 mL in MeOH and precipitate in 12 mL Et_2O). The viscous liquid was then sonicated in 15 mL Et_2O to induce crystallization, Et_2O was decanted, the solid pellet broken into a powder, and sonicated in 15 mL additional Et_2O before centrifuging, decanting, and leaving at reduced pressure for 24 h to remove residual Et_2O to afford **3** as a white powder in 1.26 g (56 %) yield. ^{1}H NMR (400.2 MHz, DMSO-*d*$_6$, δ): 9.26-9.19 (s, 1H), 7.86-7.80 (m, 1H), 7.80-7.74 (m, 1H), 4.43-4.28 (m, 2H), 4.28-4.15 (m, 2H), 3.83-3.72 (m, 2H), 3.60-3.49 (m, 2H), 3.46-3.37 (m, 2H), 3.27-3.16 (s, 3H), 2.49-2.43 (m, 2H), 1.96-1.82 (m, 2H), 1.62-1.48 (m, 2H). ^{13}C NMR (100.6 MHz, DMSO-*d*$_6$, δ): 136.46 (s, 1C), 122.75 (s, 1C), 122.29 (s, 1C), 71.07 (s, 1C), 69.35 (s, 1C), 68.08 (s, 1C), 58.08 (s, 1C), 50.46 (s, 1C), 48.78 (s, 1C), 48.58 (s, 1C), 28.70 (s, 1C), 21.78 (s, 1C). ESI (m/z): 307.1337 ($C_{12}H_{23}N_2O_5S^+$, calculated 307.1322).

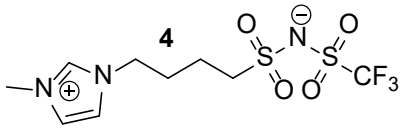

*Synthesis of **4**.* 1.019 g (3.36 mmoles) **B-CF$_3$** (as conjugate acid), 2.709 g (33.0 mmoles) 1-methylimidazole, 1.053 g (7.62 mmoles) K_2CO_3, and 415 mg (3.45 mmoles) $MgSO_4$ were combined in a 20 mL scintillation vial and heated to 80 °C for 48 h, returned to room temperature, centrifuged to remove solids, then precipitated into acetone. Then, the resulting solids were 3x (diluted into 10 mL trifluoroethanol and precipitated into 150 mL Et_2O) afford **4** as a white, crystalline solid in 1.07 g (91 %) yield. ^{1}H NMR (400.2 MHz, DMSO-*d*$_6$, δ): 9.15-9.09 (s, 1H), 7.79-7.74 (m, 1H), 7.73-7.68 (m, 1H), 4.26-4.15 (m, 2H), 3.90-3.80 (s, 3H), 3.06-2.98 (m, 2H), 1.98-1.85 (m, 2H), 1.71-1.58 (m, 2H). ^{13}C NMR (100.6 MHz, DMSO-*d*$_6$, δ): 136.61 (s, 1C), 124.93-115.26 (q, 1C), 123.68 (s, 1C), 122.25 (s, 1C), 53.60 (s, 1C), 48.24 (s, 1C), 35.75 (s, 1C), 28.02 (s, 1C), 20.46 (s, 1C). ^{19}F NMR (376.5 MHz, DMSO-*d*$_6$, δ): -77.51 (s, 3F). ESI (m/z): 350.0454 ($C_9H_{15}F_3N_3O_4S_2^+$, calculated 350.0451).

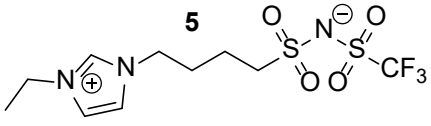

*Synthesis of **5**.* 1.031 g (3.39 mmoles) **B-CF$_3$** (as conjugate acid), 3.184 g (33.1 mmoles) 1-ethylimidazole, 1.017 g (7.36 mmoles) K_2CO_3, and 415 mg (3.45 mmoles) $MgSO_4$ were combined in a 20 mL scintillation vial and heated to 80 °C for 48 h, returned to room temperature, centrifuged to remove solids, then precipitated into acetone. Then, the resulting solids were 3x (diluted into 10 mL trifluoroethanol and precipitated into 150 mL Et_2O) to afford **5** as a white, crystalline solid in 960 mg (78 %) yield. ^{1}H NMR (400.2 MHz, DMSO-*d*$_6$, δ): 9.22-9.15 (s, 1H), 7.84-7.75 (m, 2H), 4.27-4.12 (m, 4H), 3.09-2.97 (m, 2H), 2.00-1.85

(m, 2H), 1.73-1.58 (m, 2H), 1.48-1.37 (t, 3H). ^{13}C NMR (100.6 MHz, DMSO-*d*$_6$, δ): 135.73 (s, 1C), 124.93-115.26 (q, 1C), 122.39 (s, 1C), 122.21 (s, 1C), 53.57 (s, 1C), 48.30 (s, 1C), 44.25 (s, 1C), 27.96 (s, 1C), 20.49 (s, 1C), 14.91 (s, 1C). ^{19}F NMR (376.5 MHz, DMSO-*d*$_6$, δ): -77.52 (s, 3F) ESI (m/z): 364.0610 ($C_{10}H_{17}F_3N_3O_4S_2^+$, calculated 364.0607)

6

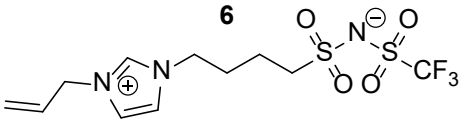

*Synthesis of **6**.* 1.082 g (3.56 mmoles) **B-CF$_3$** (as conjugate acid), 1.857 g (17.2 mmoles) 1-allylimidazole, 969 mg (7.01 mmoles) K_2CO_3, and 414 mg (3.44 mmoles) $MgSO_4$ were combined in a 20 mL scintillation vial and heated to 80 °C for 24 h, then returned to 20 °C, diluted to 20 mL in acetone, and centrifuged to remove solids before precipitating into 100 mL of Et_2O. The resulting viscous brown oil was 2x (dissolved to 20 mL in acetone and precipitated in 100 mL of Et_2O) and placed under low vac to afford **6** as a tan, crystalline solid (1.1 g, 82 %). ^{1}H NMR (400.2 MHz, DMSO-*d*$_6$, δ): 9.25-9.11 (s, 1H), 7.89-7.68 (m, 2H), 6.15-5.95 (m, 1H), 5.45-5.23 (m, 2H), 4.92-4.77 (m, 2H), 4.33-4.14 (t, 2H), 3.08-2.98 (t, 2H), 2.03-1.85 (m, 2H), 1.74-1.58 (m, 2H). ^{13}C NMR (100.6 MHz, DMSO-*d*$_6$, δ): 136.15 (s, 1C), 131.61 (s, 1C), 124.94-115.26 (q, 1C), 122.62 (s, 1C), 122.59 (s, 1C), 120.32 (s, 1C), 53.60 (s, 1C), 50.94 (s, 1C), 48.41 (s, 1C), 28.00 (s, 1C), 20.49 (s, 1C). ^{19}F NMR (376.5 MHz, DMSO-*d*$_6$, δ): -77.53 (s, 3F). ESI (m/z): 376.0614 ($C_{11}H_{17}F_3N_3O_4S_2^+$, calculated 376.0607).

7

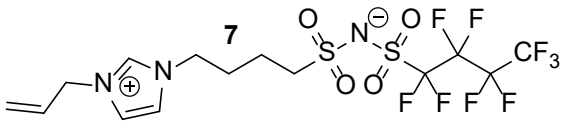

*Synthesis of **7**.* 5.007 g (10.2 mmoles) **B-C$_4$F$_9$** was combined with 1.107 g (10.2 mmoles) allylimidazole, 26 mg (0.12 mmoles) BHT, and 2 mL acetonitrile in a 20 mL scintillation vial, then heated to 80 °C with stirring for 24 h. Solids were removed by centrifugation, then the supernatant was combined with an equal volume of reverse osmosis water to induce crystallization and solvent was removed via air stream at 50 °C to afford a yellow solid. This was washed 2x with reverse osmosis water and the resulting solid dried via vacuum oven to afford **7** as a white, crystalline solid (3.54 g, 77%). ^{1}H NMR (400.2 MHz, DMSO-*d*$_6$, δ): 9.22-9.15 (s, 1H), 7.86-7.77 (m, 1H), 7.77-7.70 (m, 1H), 6.16-5.94 (m, 1H), 5.45-5.21 (m, 2H), 4.94-4.76 (m, 2H), 4.35-4.13 (t, 2H), 3.10-2.99 (t, 2H), 2.07-1.83 (m, 2H), 1.79-1.57 (m, 2H). ^{13}C NMR (100.6 MHz, DMSO-*d*$_6$, δ): 136.19 (s, 1C), 131.62 (s, 1C), 122.62 (s, 1C), 122.59 (s, 1C), 121.34-108.25 (br m, 4C, fluorinated), 120.26 (s, 1C), 53.86 (s, 1C), 50.95 (s, 1C), 48.41 (s, 1C), 28.00 (s, 1C), 20.48 (s, 1C). ^{19}F NMR (376.5 MHz, DMSO-*d*$_6$, δ) -80.52 (m, 3F), -112.88 (m, 2F), -121.02 (m, 2F), -125.74 (m, 2F). ESI (m/z): 526.0491 ($C_{14}H_{17}F_9N_3O_4S_2^+$, calculated 526.0511).

8

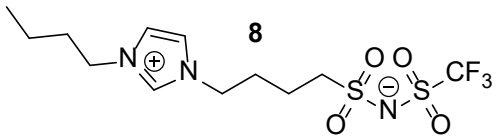

*Synthesis of **8**.* 1.044 g (3.44 mmoles) **B-CF$_3$** (as conjugate acid), 2.131 g (17.2 mmoles) 1-butylimidazole, 963 mg (6.97 mmoles) K_2CO_3, and 412 mg (3.42 mmoles) $MgSO_4$ were combined in a 20 mL scintillation vial and heated to 80 °C for 24 h, then returned to 20 °C, diluted to 20 mL in acetone, and centrifuged to remove solids before precipitating into 100 mL of Et_2O. The resulting viscous brown oil was 2x (dissolved to 20 mL in acetone and precipitated in 100 mL of Et_2O) and placed under low vac to afford **8** as a tan,

crystalline solid (1.1 g, 82 %). ^{1}H NMR (400.2 MHz, DMSO-d_6, δ): 9.27-9.11 (s, 1H), 7.87-7.72 (m, 2H), 4.33-4.05 (m, 4H), 3.08-2.98 (t, 2H), 2.00-1.87 (m, 2H), 1.84-1.72 (m, 2H), 1.72-1.59 (m, 2H), 1.33-1.19 (m, 2H), 0.95-0.84 (t, 3H). ^{13}C NMR (100.6 MHz, DMSO-d_6, δ): 136.00 (s, 1C), 124.94-115.27 (q, 1C), 122.52 (s, 1C), 122.43 (s, 1C), 53.60 (s, 1C), 48.65 (s, 1C), 48.35 (s, 1C), 31.25 (s, 1C), 27.97 (s, 1C), 20.48 (s, 1C), 18.80 (s, 1C), 13.20 (s, 1C). ^{19}F NMR (376.5 MHz, DMSO-d_6, δ): -77.60 (s, 3F). ESI (m/z): 392.0924 ($C_{12}H_{21}F_3N_3O_4S_2^+$, calculated 392.0920).

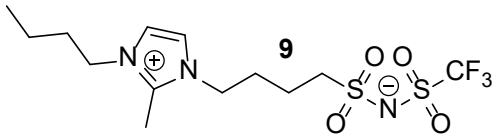

*Synthesis of **9**.* 1.007 g (3.32 mmoles) **B-CF$_3$** (as conjugate acid), 2.301 g (16.6 mmoles) **N**, 927 mg (6.71 mmoles) K_2CO_3, and 398 mg (3.31 mmoles) $MgSO_4$ were combined in a 20 mL scintillation vial and heated to 80 °C for 48 h, then returned to 20 °C, diluted to 15 mL in acetone, and centrifuged to remove solids before precipitating into 120 mL of Et_2O. The resulting tan solid was washed with 3x 40 mL Et_2O before placing under low vac to afford **9** as a tan powder in 716 mg (53 %) yield. ^{1}H NMR (400.2 MHz, DMSO-d_6, δ): 7.74-7.64 (m, 2H), 4.23-4.01 (m, 4H), 3.08-2.97 (t, 2H), 2.70-2.56 (s, 3H), 1.96-1.79 (m, 2H), 1.79-1.62 (m, 4H), 1.39-1.20 (m, 2H), 1.01-0.83 (t, 3H). ^{13}C NMR (100.6 MHz, DMSO-d_6, δ): 143.76 (s, 1C), 124.94-115.27 (q, 1C), 121.28 (s, 2C), 53.68 (s, 1C), 47.31 (s, 1C), 46.99 (s, 1C), 31.03 (s, 1C), 27.54 (s, 1C), 20.55 (s, 1C), 18.92 (s, 1C), 13.37 (s, 1C), 9.09 (s, 1C). ^{19}F NMR (376.5 MHz, DMSO-d_6, δ): -7.51 (s, 3F). ESI (m/z): 406.1081 ($C_{13}H_{23}F_3N_3O_4S_2^+$, calculated 406.1077).

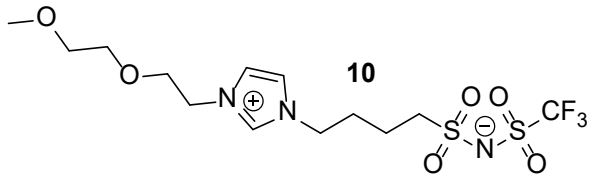

*Synthesis of **10**.* 5.009 g (14.7 mmoles) **B-CF$_3$** was combined with 17.494 g (103 mmoles) **L**, and 410 mg (2.97 mmoles) K_2CO_3, and 884 mg (7.34 mmoles) $MgSO_4$ under an argon atmosphere, sealed, and heated to 80 °C for 48 hours. The mixture was returned to 20 °C, centrifuged (5 minutes, 4500 RPM) to remove solids, then the solids were washed with 3x10 mL acetone. The crude product and acetone washes were combined and left under reduced pressure for 24 h to remove acetone. Then, the crude product mixture was washed with 10 x 20 mL Et_2O and purified by flash column chromatography (silica gel stationary phase, gradient eluent EtOAc → 2:1 EtOAc:acetone) and concentrated under reduced pressure to afford **10** as an amber crystalline solid in 4.895 g (76 %) yield. ^{1}H NMR (400.2 MHz, DMSO-d_6, δ): 9.15-9.10 (s, 1H), 7.81-7.72 (m, 2H), 4.39-4.31 (t, 2H), 4.28-4.19 (t, 2H), 3.81-3.73 (m, 2H), 3.59-3.50 (m, 2H), 3.45-3.38 (m, 2H), 3.26-3.18 (s, 3H), 3.09-2.99 (t, 2H), 2.00-1.87 (m, 2H), 1.73-1.61 (m, 2H). ^{13}C NMR (100.6 MHz, DMSO-d_6, δ): 136.42 (s, 1C), 124.97-115.30 (q, 1C), 122.86 (s, 1C), 122.20 (s, 1C), 71.09 (s, 1C), 69.41 (s, 1C), 68.06 (s, 1C), 58.05 (s, 1C), 53.63 (s, 1C), 48.91 (s, 1C), 48.35 (s, 1C), 28.11 (s, 1C), 20.49 (s, 1C). ^{19}F NMR (376.5 MHz, DMSO-d_6, δ): -77.57 (s, 3F). ESI (m/z): 438.0978 ($C_{13}H_{23}F_3N_3O_6S_2^+$, calculated 438.0975).

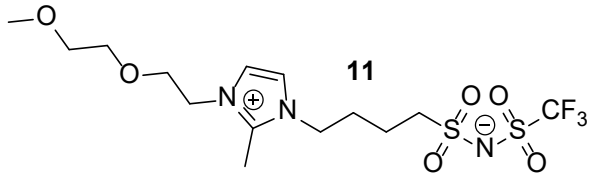

*Synthesis of **11**.* 349 mg (1.15 mmoles) **B-CF$_3$** (as conjugate acid) was combined with 1.02 g (5.54 mmoles) **O**, 319 mg (2.31 mmoles) K_2CO_3, and 141 mg (1.17 mmoles) $MgSO_4$ in a 20 mL scintillation vial and heated to 80 °C for 48 h with stirring before returning to room temperature, removing solids by centrifugation, and washing the resulting brown oil with 3 x 12 mL Et_2O to afford **11** as a tan solid (392 mg, 76 %). ^{1}H NMR (400.2 MHz, DMSO-*d*$_6$, δ): 7.77-7.57 (m, 2H), 4.38-4.24 (t, 2H), 4.24-4.10 (t, 2H), 3.79-3.67 (m, 2H), 3.56-3.46 (m, 2H), 3.44-3.35 (m, 2H), 3.25-3.16 (s, 3H), 3.09-2.97 (m, 2H), 2.69-2.58 (s, 3H), 1.93-1.78 (m, 2H), 1.77-1.63 (m, 2H). ^{13}C NMR (100.6 MHz, DMSO-*d*$_6$, δ): 144.53 (s, 1C), 124.96-115.28 (q, 1C), 121.61 (s, 1C), 121.19 (s, 1C), 71.12 (s, 1C), 69.55 (s, 1C), 68.42 (s, 1C), 58.05 (s, 1C), 53.69 (s, 1C), 47.62 (s, 1C), 47.03 (s, 1C), 27.67 (s, 1C), 20.55 (s, 1C), 9.33 (s, 1C). ^{19}F NMR (376.5 MHz, DMSO-*d*$_6$, δ): -77.50 (s, 3F). ESI (m/z): 452.1140 ($C_{14}H_{25}F_3N_3O_6S_2^+$, calculated 452.1131).

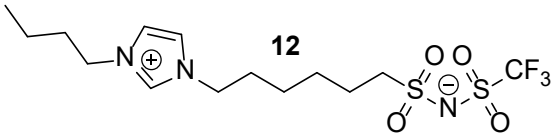

*Synthesis of **12**.* 613 mg (1.66 mmoles) **E** was combined with 1.23 g (9.91 mmoles) 1-butylimidazole, 246 mg (1.78 mmoles) K_2CO_3, and 126 mg (1.04 mmoles) $MgSO_4$, in a 20 mL scintillation vial, then heated to 80 °C with stirring for 48 h. Solids were removed by centrifugation, then the product was washed with 5 x 12 mL Et_2O to afford **12** as a tan powder (625 mg, 90 %). ^{1}H NMR (400.2 MHz, DMSO-*d*$_6$, δ): 9.23-9.13 (s, 1H), 7.85-7.73 (m, 2H), 4.23-4.09 (m, 4H), 3.01-2.89 (t, 2H), 1.87-1.72 (m, 4H), 1.72-1.60 (m, 2H), 1.45-1.32 (m, 2 H), 1.32-1.18 (m, 4H), 0.96-0.85 (t, 3H). ^{13}C NMR (100.6 MHz, DMSO-*d*$_6$, δ): 135.93 (s, 1C), 124.97-115.30 (q, 1C), 122.47 (s, 1C), 122.44 (s, 1C), 54.25 (s, 1C), 48.75 (s, 1C), 48.60 (s, 1C), 31.23 (s, 1C), 29.01 (s, 1C), 26.88 (s, 1C), 25.03 (s, 1C), 23.44 (s, 1C), 18.78 (s, 1C), 13.21 (s, 1C). ^{19}F NMR (376.5 MHz, DMSO-*d*$_6$, δ): -77.52 (s, 3F). ESI (m/z): 420.1238 ($C_{14}H_{25}F_3N_3O_4S_2^+$, calculated 420.1233).

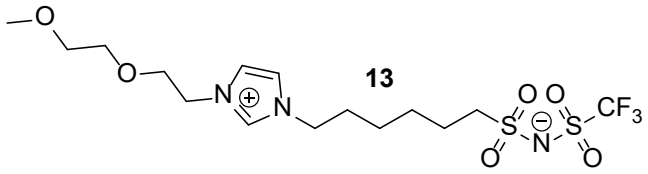

*Synthesis of **13**.* 1.02 g (2.76 mmoles) **E**, 2.98 g (17.5 mmoles) **L**, 387 mg (2.80 mmoles) K_2CO_3, and 178 mg (1.48 mmoles) $MgSO_4$ were combined in a 20 mL scintillation vial and stirred at 80 °C for 50 h. The crude reaction mixture was cooled to 20 °C, then washed with 3 x 12 mL Et_2O and purified by flash column chromatography (29.8 g silica, acetone eluent) to afford **13** as a viscous brown oil (817 mg, 64 %). ^{1}H NMR (400.2 MHz, DMSO-*d*$_6$, δ): 9.21-9.05 (s, 1H), 7.87-7.67 (m, 2H), 4.41-4.29 (t, 2H), 4.25-4.13 (t, 2H), 3.85-3.71 (m, 2H), 3.61-3.49 (m, 2H), 3.47-3.36 (m, 2H), 3.24-3.18 (s, 3H), 3.01-2.91 (t, 2H), 1.88-1.73 (m, 2H), 1.73-1.61 (m, 2H), 1.47-1.32 (m, 2H), 1.32-1.17 (m, 2H). ^{13}C NMR (100.6 MHz, DMSO-*d*$_6$, δ): 136.35 (s, 1C), 124.99-115.32 (q, 1C), 122.78 (s, 1C), 122.20 (s, 1C), 71.08 (s, 1C), 69.37 (s, 1C), 68.04 (s, 1C), 58.06 (s, 1C), 54.30 (s, 1C), 48.86 (s, 1C), 48.76 (s, 1C), 29.14 (s, 1C), 26.95 (s, 1C), 25.05 (s, 1C), 23.47 (s,

1C). ^{19}F NMR (376.5 MHz, DMSO-*d*$_6$, δ): -77.55 (s, 3F). ESI (m/z): 488.1115 ($C_{15}H_{27}F_3N_3O_6S_2^+$, calculated 488.1107).

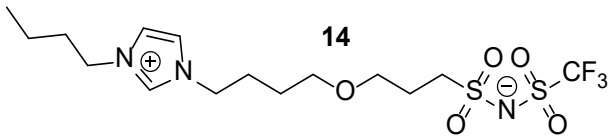

*Synthesis of **14**.* 5.67 g (14.2 mmoles) **H** was combined with 17.13 g (138 mmoles) 1-butylimidazole, 2.29 g, (16.6 mmoles) K_2CO_3, and 2.13 g (17.7 mmoles) $MgSO_4$ and heated to 80 °C with stirring for 48 h, then returned to room temperature and washed with 3x40 mL hexanes before purifying by flash column chromatography (135 g silica, mixed eluent starting with EtOAc, then switching to a gradient 1:1 acetone:hexanes → pure acetone) and concentrated under reduced pressure to afford **14** as a viscous brown oil in 5.79 g (91 %) yield. ^{1}H NMR (400.2 MHz, DMSO-*d*$_6$, δ): 9.24-9.07 (s, 1H), 7.88-7.69 (m, 2H), 4.29-4.08 (m, 4H), 3.53-3.28 (m, 4H), 3.13-2.92 (t, 2H), 2.02-1.68 (m, 6H), 1.61-1.39 (m, 2H), 1.38-1.15 (m, 2H), 1.01-0.80 (t, 3H). ^{13}C NMR (100.6 MHz, DMSO-*d*$_6$, δ): 135.90 (s, 1C), 124.96-115.29 (q, 1C), 122.44 (s, 1C), 122.42 (s, 1C), 69.07 (s, 1C), 68.12 (s, 1C), 51.79 (s, 1C), 48.76 (s, 1C), 48.63 (s, 1C), 31.27 (s, 1C), 26.57 (s, 1C), 25.75 (s, 1C), 24.26 (s, 1C), 18.78 (s, 1C), 13.17 (s, 1C). ^{19}F NMR (376.5 MHz, DMSO-*d*$_6$, δ): -77.65 (s, 3F). ESI (m/z): 472.1174 ($C_{15}H_{27}F_3N_3O_5S_2^+$, calculated 472.1158).

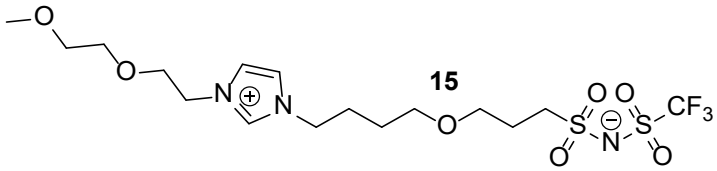

*Synthesis of **15**.* 1 g (2.5 mmoles) **H** was combined with 3.02 g (17.7 mmoles) **L**, 361 mg (2.6 mmoles) K_2CO_3, and 162 mg (1.3 mmoles) $MgSO_4$ and heated to 80 °C for 48 h, returned to room temperature, and washed with 3x40 mL Et_2O and concentrated under reduced pressure to afford **15** as a viscous brown oil in 1.27 g (100 %) yield. ^{1}H NMR (400.2 MHz, DMSO-*d*$_6$, δ): 9.15-9.07 (s, 1H), 7.82-7.70 (m, 2H), 4.40-4.29 (t, 2H), 4.27-4.17 (t, 2H), 3.83-3.72 (m, 2H), 3.59-3.50 (m, 2H), 3.49-3.35 (m, 6H), 3.24-3.19 (s, 3H), 3.06-2.99 (t, 2H), 1.96-1.79 (m, 4H), 1.55-1.42 (m, 2H). ^{13}C NMR (100.6 MHz, DMSO-*d*$_6$, δ): 136.36 (s, 1C), 124.98-115.30 (q, 1C), 122.78 (s, 1C), 122.19 (s, 1C), 71.08 (s, 1C), 69.37 (s, 1C), 69.07 (s, 1C), 68.16 (s, 1C), 68.03 (s, 1C), 58.04 (s, 1C), 51.79 (s, 1C), 48.85 (s, 1C), 48.74 (s, 1C), 26.62 (s, 1C), 25.74 (s, 1C), 24.27 (s, 1C). ^{19}F NMR (376.5 MHz, DMSO-*d*$_6$, δ): -77.59 (s, 3F). ESI (m/z): 518.1238 ($C_{16}H_{29}F_3N_3O_7S_2^+$, calculated 518.1213).

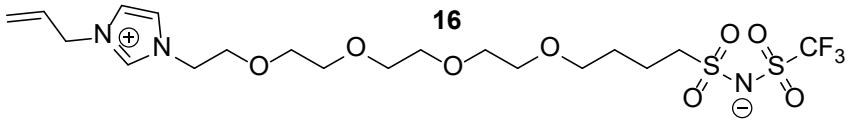

*Synthesis of **16**.* 7.089 g (13.7 mmol) of **K** was combined with 1.487 g (13.8 mmol) of 1-allylimidazole and a stir bar under an argon atmosphere in a 20 mL scintillation vial, then stirred at 80 °C for 72 h. The reaction was stopped by removing from heat, then ran 3x (diluted to 12.5 mL in acetone, precipitated into 35 mL of Et_2O, shaken vigorously, centrifuged 4500 RPM for 120 s, decanted the buoyant phase). The product was

purified by silica gel column chromatography using a gradient eluent (EtOAc → 3:1 EtOAc:acetone), concentrated under reduced pressure, dried over $MgSO_4$, then transferred to a vacuum oven for 24 h at 115 °C to afford **16** as an amber oil (5.6 g, 74 %). ^{1}H NMR (400.2 MHz, DMSO-d_6, δ): 9.15-9.05 (s, 1H), 7.81-7.74 (s, 1H), 7.74-7.66 (s, 1H), 6.13-5.98 (m, 1H), 5.41-5.33 (dd, 1H), 5.33-5.24 (dd, 1H), 4.92-4.82 (d, 2H), 4.43-4.32 (t, 2H), 3.85, 3.75 (t, 2H), 3.62-3.43 (br m, 12 H), 3.43-3.34 (t, 2H), 3.04-2.93 (t, 2H), 1.77-1.65, (m, 2H), 1.62-1.51, (m, 2H). ^{13}C NMR (100.6 MHz, DMSO-d_6, δ): 136.44 (s, 1C), 131.69 (s, 2C overlapping), 125.01-115.33 (q, 1C, $\underline{C}F_3$), 123.02 (s, 1C), 122.25 (s, 1C), 120.12 (s, 1C), 69.82 (s, 2C overlapping), 69.79 (s, 1C), 69.72 (s, 1C), 69.61 (s, 1C), 69.56 (s, 1C), 69.51 (s, 1C), 68.06 (s, 1C), 54.39 (s, 1C), 50.87 (s, 1C), 48.93 (s, 1C), 27.87 (s, 1C), 20.81 (s, 1C). ^{19}F NMR (376.5 MHz, DMSO-d_6, δ): -77.59 (s, 3F). ESI (m/z): 552.1666 ($C_{19}H_{33}F_3N_3O_8S_2^+$, calculated 552.1656).

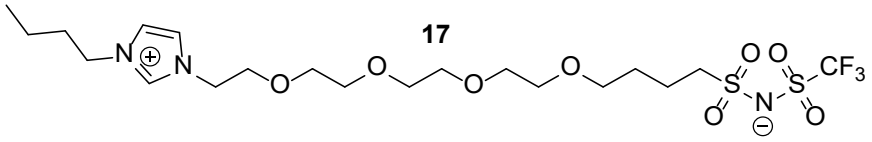

*Synthesis of **17**.* **K** (334 mg, 0.645 mmoles) was combined with 1-butylimidazole (1.22 g, 9.83 mmoles) K_2CO_3 (111 mg, 0.803 mmoles), and $MgSO_4$ (22 mg, 0.183 mmoles) under argon in a 20 mL scintillation vial. The mixture was sealed and heated to 80 °C while stirring for 48 h. Solids were removed by centrifugation and washed with acetone. Then, the crude liquid phase and acetone washes were combined, solvent was removed *in vacuo*, then the mixture washed with 3x10 mL hexanes. Then, the crude product was purified by flash column chromatography (10 g silica, gradient eluent EtOAc → acetone) and concentrated under vacuum to afford 380 mg **17** (100 %) as an amber oil. ^{1}H NMR (400.2 MHz, DMSO-d_6, δ): 9.15-9.08 (s, 1H), 7.82-7.72 (s+s, 2H overlapping), 4.40-4.29 (t, 2H), 4.25-4.14 (t, 2H), 3.84-3.73 (t, 2H), 3.62-3.43 (br m, 12H), 3.43-3.34 (t, 2H), 3.01-2.94 (t, 2H), 1.84-1.64 (br m, 4H), 1.63-1.50 (m, 2H), 1.33-1.19 (m, 2H), 0.96-0.84 (t, 3H). ^{13}C NMR (100.6 MHz, DMSO-d_6, δ): 136.30 (s, 1C), 124.99-115.31 (q, 1C, CF_3), 122.83 (s, 1C), 122.16 (s, 1C), 69.81 (s, 2C overlapping), 69.78 (s, 1C), 69.71 (s, 1C), 69.61 (s, 1C), 69.54 (s, 1C), 69.51 (s, 1C), 68.06 (s, 1C), 54.36 (s, 1C), 48.85 (s, 1C), 48.57 (s, 1C), 31.36 (s, 1C), 27.87 (s, 1C), 20.79 (s, 1C), 18.75 (s, 1C), 13.21 (s, 1C). ^{19}F NMR (376.5 MHz, DMSO-d_6, δ): -77.54 (s 3F). ESI (m/z): 568.1989 ($C_{20}H_{37}F_3N_3O_8S_2^+$, calculated 568.1969).

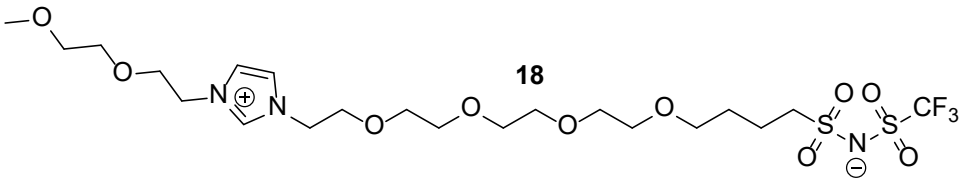

*Synthesis of **18**.* 6.898 g (13.3 mmol) **K** was combined with 2.304 g (13.5 mmol) **L** in a 20 mL scintillation vial under argon, then sealed and stirred at 80 °C for 88 h, then removed from heat and ran 8x (dilute to 10 mL in acetone, precipitate in 35 mL Et_2O, centrifuge, decant buoyant phase). Then, added 12.5 g silica gel, stirred for 12 h in EtOAc to encourage adsorption, added the crude product-silica slurry to a column packed in EtOAc, and purified by silica gel column chromatography using a gradient EtOAc → 3:1 EtOAc:acetone eluent, removed most solvent via rotary evaporator, dried over $MgSO_4$, then removed remaining solvent via vacuum oven (115 °C) to afford **18** as an amber oil in 3.48 g (42 %) yield. ^{1}H NMR (400.2 MHz, DMSO-d_6, δ): 9.11-9.02 (m, 1H), 7.79-7.69 (m, 2H), 4.43-4.32 (t, 4H), 3.83-3.74 (q, 4H), 3.59-3.44 (br m, 14H), 3.44-3.35 (br m, 4H), 3.25-3.19 (s, 3H), 3.02-2.94 (m, 2H), 1.77-1.65 (m, 2H), 1.63-1.51 (m, 2H). ^{13}C NMR (100.6 MHz, DMSO-d_6, δ): 136.66 (s, 1C, aromatic), 125.01-115.33 (q, 1C, CF_3), 122.63 (s, 1C, aromatic), 122.49 (s, 1C, aromatic), 71.09 (s, 1C), 69.83 (s, 2C overlapping), 69.79 (s, 1C), 69.73 (s, 1C), 69.63 (s, 1C), 69.57

(s, 1C), 69.52 (s, 1C), 69.40 (s, 1C), 68.14 (s, 2C overlapping), 58.05 (s, 1C), 54.38 (s, 1C), 48.87 (s, 1C), 48.85 (s, 1C), 27.88 (s, 1C), 20.81 (s, 1C). ^{19}F NMR (376.5 MHz, DMSO-*d*$_6$, δ): -77.55 (s, 3F). ESI (m/z): 614.2044 ($C_{21}H_{39}F_3N_3O_{10}S_2^+$, calculated 614.2023)

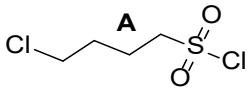

*Synthesis of **A**.* 197.6 g (1.45 moles) 1,4-butanesultone was combined with15 mL (194 mmoles) DMF, and 500 mL (6.85 moles) thionyl chloride in a 3 L round-bottom flask fitted with a reflux condenser, a vacuum trap, and a gas scrubber to neutralize the evolved acidic vapor. and heated to reflux for 1 week. Then, the reaction was cooled to 0 °C and quenched by incrementally adding ice while stirring vigorously. When gas stopped evolving, the mixture was returned to 20 °C and washed with 4 x 750 mL reverse osmosis water, dried over $MgSO_4$, and concentrated under reduced pressure to afford **A** (218.9, 69 %) as a yellow oil. ^{1}H NMR (400.2 MHz, DMSO-*d*$_6$, δ): 3.63-3.52 (t, 2H), 2.71-2.61 (t, 2H), 1.82-1.62 (m, 4H). ^{13}C NMR (100.6 MHz, DMSO-*d*$_6$, δ) 50.89 (s, 1C), 45.56 (s, 1C), 31.38 (s, 1C), 22.50 (s, 1C).

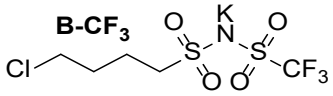

*Synthesis of **B-CF$_3$**.* 218.7 g (1.14 moles) **A** was combined with 206.7 g (1.39 moles) triflamide, 1 L acetonitrile and 36.4 g (302 mmoles) magnesium sulfate, and stirred until triflamide was fully solvated, then cooled to 0 °C while stirring. Then, 675.8 g (4.89 moles) K_2CO_3 was added incrementally over 2.5 h while maintaining a temperature of 0 °C. The mixture was allowed return to room temperature while stirring for 64 h, then stopped by filtering out solids and blowing off solvent via air stream. The resulting brown paste was washed with 3 x 500 mL Et_2O, then acidified with 800 mL (14 moles) acetic acid and diluted with an additional 800 mL of acetone. The mixture was stirred until all visible solid pieces dissolved, then concentrated under air stream to afford a tan paste. This was washed with 3 x 1.5 L Et_2O, then taken up in 1.5 L acetone, basified with 569 g (4.12 moles) K_2CO_3, and stirred vigorously for 19 hours before filtering out solids and concentrating the filtrate via air stream. The resulting solid was washed with 1 L Et_2O and placed under reduced pressure to afford **B-CF$_3$** as a white, crystalline powder (257.5 g, 66 %). ^{1}H NMR (400.2 MHz, DMSO-*d*$_6$, δ): 3.71-3.59 (t, 2H), 3.06-2.94 (t, 2H), 1.88-1.73 (m, 4H). ^{13}C NMR (100.6 MHz, DMSO-*d*$_6$, δ): 124.97-115.30 (q, 1C), 53.69 (s, 1C), 44.97 (s, 1C), 30.63 (s, 1C), 21.31 (s, 1C). ^{19}F NMR (376.5 MHz, DMSO-*d*$_6$, δ): -77.49 (s, 3F). ESI (m/z): 301.9545 ($C_5H_8ClF_3NO_4S_2^-$, calculated 301.9530).

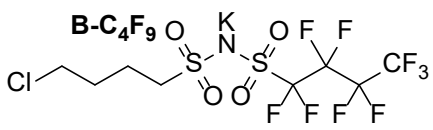

*Synthesis of **B-C$_4$F$_9$**.* **A** (40 g of 86 wt % solution in acetonitrile, 180 mmoles) was combined with 30.374 g (102 mmoles) **M** and 100 mL acetonitrile, then stirred until **M** was solvated. Then, the reaction was cooled to 0 °C under argon and 60.8 g (440 mmoles) K_2CO_3 was added. The reaction was allowed to return to room temperature while stirring for 96 h, then the solids were removed by filtration. The filtrate was concentrated under air stream, washed with 4x100 mL of dichloromethane, and placed under vacuum to afford **B-C$_4$F$_9$** as a tan powder (40.6 g, 88 %). ^{1}H NMR (400.2 MHz, DMSO-*d*$_6$, δ): 3.70-3.60 (t, 2H), 3.06-

2.95 (t, 2H), 1.89-1.75 (m, 4H). ^{13}C NMR (100.6 MHz, DMSO-*d*$_6$, δ): 120-105 (br m, 4C, fluorinated), 53.97 (s, 1C), 44.95 (s, 1C), 30.65 (s, 1C), 21.32 (s, 1C). ^{19}F NMR (376.5 MHz, DMSO-*d*$_6$, δ): -80.49 (m, 3F), -112.90 (m, 2F), -120.99 (m, 2F), -125.72 (m, 2F). ESI (m/z): 451.9455 ($C_8H_8ClF_9NO_4S_2^-$, calculated 451.9434).

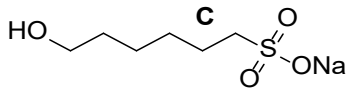

Synthesis of ***C****.* 10.00 g (73.2 mmoles) 6-chloro-1-hexanol was combined with 10.45 g (82.9 mmoles) sodium sulfite and deionized water (56.35 g) and refluxed at 120 °C for 24 h before removing water via air stream at 90 °C and washing the resulting white powder with 4 x 40 mL MeOH. MeOH was removed from the combined washes via air stream, then the resulting white solid was crushed and placed under reduced pressure to afford **C** as a white powder in 11.3 g (76 %) yield. ^{1}H NMR (400.2 MHz, DMSO-*d*$_6$, δ): 3.40-3.32 (t, 2H), 2.47-2.39 (m, 2H), 1.62-1.49 (m, 2H), 1.45-1.34 (m, 2H), 1.34-1.19 (m, 4H). ^{13}C NMR (100.6 MHz, DMSO-*d*$_6$, δ): 60.77 (s, 1C), 51.49 (s, 1C), 32.47 (s, 1C), 28.38 (s, 1C), 25.43 (s, 1C), 25.11 (s, 1C). ESI (m/z): 181.0541 ($C_6H_{13}O_4S^-$, calculated 181.0529).

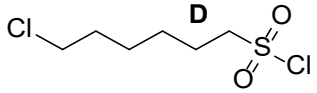

Synthesis of ***D****.* 16.9 g (82.8 mmoles) **C** was dried via azeotropic distillation of toluene (100 mL), then combined with dry DMF (8.5 mL, 110 mmoles) and thionyl chloride (60 mL, 823 mmoles) under argon in a 500 mL round-bottom flask fitted with a reflux condenser, a vacuum trap, and a gas scrubber to neutralize the evolved acidic vapor. Then, the mixture was stirred at 20 °C for 15 minutes before heating to reflux. After 27 h, an additional 60 mL (823 mmoles) of thionyl chloride was added and the reflux continued for another 21 h before returning to room temperature, cooling to 0 °C, and quenching excess thionyl chloride by incremental addition of ice with vigorous stirring. The mixture was returned to 20 °C and extracted into 3 x 100 mL of Et_2O, then the combined organic washes were dried over $MgSO_4$ and concentrated under vacuum to afford crude **D** as a yellow oil (22.4 g, exceeding theoretical yield due to impurities). ^{1}H NMR (400.2 MHz, DMSO-*d*$_6$, δ): 3.60-3.50 (t, 2H), 2.70-2.60 (m, 2H), 1.72-1.50 (m, 4H), 1.42-1.24 (m, 4H). ^{13}C NMR (100.6 MHz, DMSO-*d*$_6$, δ): 51.57 (s, 1C), 45.63 (s, 1C), 32.29 (s, 1C), 27.60 (s, 1C), 26.35 (s, 1C), 24.63 (s, 1C).

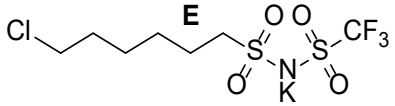

Synthesis of ***E****.* 22.4 g (102 mmoles) crude **D** was combined with triflamide (18.3 g, 123 mmoles), 4.02 g (33.3 mmoles) $MgSO_4$, and 100 mL acetonitrile in a 500 mL round-bottom flask. Then, the reaction was started by adding 59.3 (429 mmoles) of K_2CO_3. After stirring at 20 °C for 24 h, the solids were removed by filtration and solvent evaporated via air stream. Then, the mixture was washed with 3 x 100 mL of Et_2O, re-diluted to 200 mL in acetone, and acidified by adding 17.5 mL (306 mmoles) glacial acetic acid. The solvent was then evaporated via air stream and the crude mixture washed with another 3 x 100 mL Et_2O, re-dissolved in acetone, filtered to remove solid precipitate, and basified with 34.6 g (250 mmoles) of K_2CO_3. The mixture was stirred vigorously for 18 h, then solids were removed by filtration and concentrated via air stream to afford **E** as a tan powder (20.82 g, 55 %). ^{1}H NMR (400.2 MHz, DMSO-*d*$_6$, δ): 3.67-3.58 (t, 2H),

3.00-2.90 (m, 2H), 1.77-1.59 (m, 4H), 1.44-1.31 (m, 4H). ^{13}C NMR (100.6 MHz, DMSO-d_6, δ): 124.99-115.32 (q, 1C), 54.38 (s, 1C), 45.28 (s, 1C), 31.82 (s, 1C), 26.91 (s, 1C), 25.89 (s, 1C), 23.54 (s, 1C). ^{19}F NMR (376.5 MHz, DMSO-d_6, δ): -77.53 (s, 3F). ESI (m/z): 329.9856 ($C_7H_{12}ClF_3NO_4S_2^-$, calculated 329.9843).

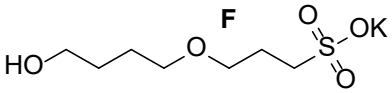

*Synthesis of **F**.* 22.6 g (251 mmoles) 1,4-butanediol was added to a dry, 250 mL round-bottom flask under argon atmosphere and dried by azeotropic distillation with toluene. Then, 50 mL (50 mmoles) 1M *t*-BuOK in THF was added dropwise over 20 minutes, followed by 1,3-butanesultone (7.10 g, 58.1 mmoles). The reaction was allowed to stir for 2 h at room temperature before diluting in 150 mL acetone and filtering to collect solids. These were washed with 2x100 mL acetone, then placed under vacuum to remove trace solvent to afford 11.4 g (91 %) of **F** as a powdery white solid. ^{1}H NMR (400.2 MHz, DMSO-d_6, δ): 4.43-4.38 (t, 1H), 3.42-3.29 (m, 6H), 2.59-2.43 (m, 2H), 1.88-1.71 (m, 2H), 1.60-1.34 (m, 4H). ^{13}C NMR (100.6 MHz, DMSO-d_6, δ): 69.93 (s, 1C), 69.23 (s, 1C), 60.68 (s, 1C), 48.50 (s, 1C), 29.36 (s, 1C), 26.00 (s, 1C), 25.69 (s, 1C). ESI (m/z): 211.0647 ($C_7H_{15}O_5S^-$, calculated 211.0635).

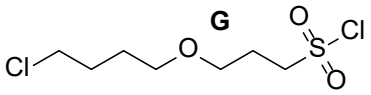

*Synthesis of **G**.* 11.1 g (44.3 mmoles) **F** was azeotropically distilled with toluene in a 250 mL round-bottom flask fitted with a reflux condenser, a vacuum trap, and a gas scrubber to neutralize acidic vapor. Then, thionyl chloride (64 mL, 877 mmoles) and DMF (4.5 mL, 58.1 mmoles) were added and the solution refluxed at 80 °C for 48 h before cooling to 0 °C and quenching by gradual addition of ice pellets. Crude product was extracted into 3x50 mL of diethyl ether, and the combined organic washes were dried over $MgSO_4$ and concentrated under vacuum to afford crude **G** as a yellow oil in 12.6 g (100%) crude yield. ^{1}H NMR (400.2 MHz, DMSO-d_6, δ): 3.65-3.57 (t, 2H), 3.44-3.29 (m, 4H), 2.69-2.60 (m, 2H), 1.86-1.67 (m, 4H),1.62-1.52 (m, 2H). ^{13}C NMR (100.6 MHz, DMSO-d_6, δ): 69.34 (s, 1C), 68.83 (s, 1C), 48.63 (s, 1C), 45.54 (s, 1C), 29.40 (s, 1C), 26.82 (s, 1C), 25.35 (s, 1C).

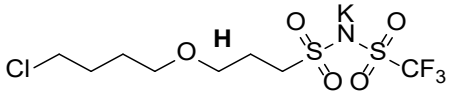

*Synthesis of **H**.* 12.6 g (50.6 mmoles) crude **G** was combined with 53 mL acetonitrile, 3.255 g (27.0 mmoles) $MgSO_4$, and 9.45 g (63.4 mmoles) triflamide in a 250 mL round-bottom flask and stirred until a homogeneous white dispersion. Then, K_2CO_3 was incrementally added and then the mixture was allowed to stir for 24 h at 20 °C. The solids were removed by filtration and washed with acetone. The filtrate and acetone washes were combined, and solvent was removed via air stream. The resulting tan solid was washed with hexanes and passed over a plug of silica (40 g silica, acetone eluent), then combined with 7.4 mL (129 mmoles) acetic acid, concentrated via air stream, and washed with 3x50 mL Et_2O. The product was purified by flash column chromatography (silica gel stationary phase, EtOAc eluent) and concentrated under reduced pressure to afford **H** (8.5 g, 42 %) as a soft brown solid. ^{1}H NMR (400.2 MHz, DMSO-d_6, δ): 3.68-3.61 (t, 2H), 3.47-3.40 (t, 2H), 3.40-2.94 (t, 2H), 3.03-2.94 (m, 2H), 1.93-1.82 (m, 2H), 1.82-1.71 (m, 2H), 1.66-1.55 (m, 2H). ^{13}C NMR (100.6 MHz, DMSO-d_6, δ): 124.97-115.29 (q, 1C), 69.04 (s, 1C), 68.14 (s,

1C), 51.78 (s, 1C), 45.31 (s, 1C), 29.10 (s, 1C), 26.53 (s, 1C), 24.29 (s, 1C). ^{19}F NMR (376.5 MHz, DMSO-d_6, δ): -77.53 (s, 3F). ESI (m/z): 359.9980 ($C_8H_{14}ClF_3NO_5S_2^-$, calculated 359.9949).

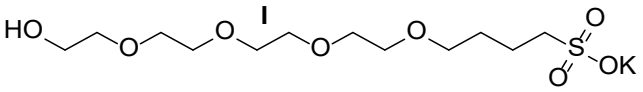

I

*Synthesis of **I**.* 430.6 g (2.22 moles) TetrEG, 60.2 g (442 mmoles) 1,4-butanesultone, and 440 mL THF were combined in a 3 L round-bottom flask and stirred until homogeneous. The mixture was cooled to 0 °C under argon and the reaction was started by adding 75.3 g (1.34 moles) KOH. The reaction was allowed to return to 20 °C over 24 h, then cooled again to 0 °C and quenched by adding 83.2 g (1.39 moles) glacial acetic acid. The crude product mixture was washed with 2x1 L hexanes and 3x1 L EtOAc before purifying via flash column chromatography (gradient eluent THF → 2:1 EtOAc:acetone) and concentrating via rotovap and then vacuum oven (100 °C) to afford **I** as a faintly amber solid in 133.5g (82 %) yield. ^{1}H NMR (400.2 MHz, DMSO-d_6, δ): 3.63-3.30 (m, 18H), 2.62-2.52 (m, 2H), 1.68-1.48 (m, 4H). ^{13}C NMR (100.6 MHz, DMSO-d_6, δ): 72.37 (s, 1C), 70.09-69.52 (m, 7C), 60.25 (s, 1C), 51.20 (s, 1C), 28.34 (s, 1C), 21.70 (s, 1C). ESI (m/z): 329.1281 ($C_{12}H_{25}O_8S$, calculated 329.1265).

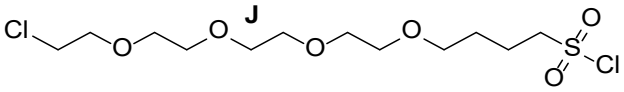

J

*Synthesis of **J**.* 133.5 g (362 mmoles) **I** was combined with 22 mL (284 mmoles) DMF in a 3 L round-bottom flask under argon. The flask was fitted with a reflux condenser with a gas outlet routed through a vacuum trap and a gas scrubber composed of a glass sparger submerged in 5 L of 5M KOH to prevent release of concentrated acid vapor. Then, 500 mL (5.5 moles) thionyl chloride was added. After the reaction finished bubbling, it was heated to reflux for 72 h before returning to room temperature and quenching by incremental addition of ice pellets with vigorous stirring. After complete quenching of residual thionyl chloride, another 100 mL of water was added and the mixture was stirred vigorously for 20 minutes before extracting with 3x 500 mL Et_2O. The extracted organic phase was transferred to a 3L round-bottom flask with 51 g (42.4 mmoles) $MgSO_4$ and concentrated under reduced pressure before purifying via silica gel column chromatography (silica gel stationary phase, gradient eluent hexanes → 4:1 Et_2O:hexanes) and concentrating under reduced pressure to afford **J** in 64.2 g (48 %) yield. ^{1}H NMR (400.2 MHz, DMSO-d_6, δ): 3.74-3.61 (m, 4H), 3.61-3.41 (m, 12H), 3.41-3.31 (m, 2H), 2.68-2.57 (m, 2H), 1.69-1.49 (m, 4H). ^{13}C NMR (100.6 MHz, DMSO-d_6, δ): 70.61 (s, 1C), 70.05-69.55 (q, 7C), 51.20 (s, 1C), 43.65 (s, 1C), 28.27 (s, 1C), 21.58 (s, 1C).

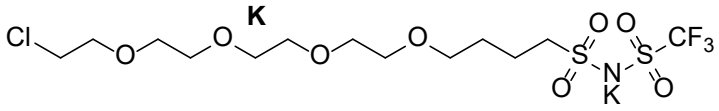

K

*Synthesis of **K**.* 64.2 g (175 mmoles) **J** was combined with 31.35 g (210 mmoles) triflamide, 30.8 g (256 mmoles) $MgSO_4$, and 174 mL acetonitrile under argon. The mixture was stirred until triflamide was solvated, then cooled to 0 °C and 101.5 g (735 mmoles) K_2CO_3 was added to start the reaction. The mixture was allowed to return to room temperature over 24 hours, then stirring stopped to allow the mixture to settle. Then, the liquid phase was decanted through a vacuum filtration apparatus and the solids washed with acetone until the wash solution came away colorless. The combined liquid phase and acetone washes were acidified with 36 mL (630 mmoles) AcOH and concentrated under reduced pressure. Then the mixture was

washed with 3x300 mL hexanes and 5x300 mLEt_2O. Due to product precipitation during the Et_2O washes, we ran them by stirring vigorously in a round-bottom flask (rather than shaking in a separatory funnel), then stopping the stir bar to allow phase separation, and decanting the buoyant phase. The crude product was then dissolved in EtOAc, then 164 g silica gel was added and the mixture stirred for 12 h before adding the slurry to the top of a silica gel column and purifying with a gradient eluent (EtOAc → acetone). The product fractions were concentrated under reduced pressure and basified by adding 25.3 g (183 mmoles) K_2CO_3 and 2.23 g (19 mmoles) $MgSO_4$ and stirring vigorously for 12 hours before filtering out solids, washing solids with acetone, combining product solution and acetone washes, concentrating under reduced pressure, and precipitating in Et_2O to afford **K** as a tan powder in 42.8 g (47 %) yield. ^{1}H NMR (400.2 MHz, DMSO-d_6, δ): 3.75-3.63 (m, 4H), 3.61-3.43 (m, 12H), 3.43-3.34 (t, 2H), 3.02-2.91 (m, 2H), 1.77-1.63 (m, 2H), 1.63-1.52 (m, 2H). ^{13}C NMR (100.6 MHz, DMSO-d_6, δ): 125.46-115.78 (q, 1C), 70.99-69.95 (m, 8C), 54.81 (s, 1C), 44.03 (s, 1C), 28.35 (s, 1C), 21.21 (s, 1C). ^{19}F NMR (376.5 MHz, DMSO-d_6, δ): -77.50 (s, 3F). ESI (m/z): 478.0601 ($C_{13}H_{24}ClF_3NO_8S_2^-$, calculated 478.0578).

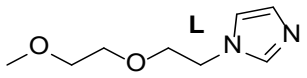

*Synthesis of **L**.* 10.059 g (148 mmoles) imidazole was stirred in 125 mL acetonitrile until fully dissolved, affording a clear, colorless solution. Then, 41.289 g (736 mmoles) KOH was added and allowed to stir for 25 minutes, affording a colorless, opaque mixture., followed by 30.832 g (168 mmoles) MEE-Br was added dropwise over 5 minutes to start the reaction. The mixture was allowed to stir for 24 h at 20 °C before decanting the yellow product solution, concentrating via air stream while stirring over $MgSO_4$, and then purified by flash column chromatography (silica gel stationary phase, gradient EtOAc → 6:1 EtOAc:MeOH eluent) and concentrated under reduced pressure to afford **L** as an amber oil in 23.232 g (92 %) yield. ^{1}H NMR (400.2 MHz, DMSO-d_6, δ): 7.62-7.56 (s, 1H), 7.18-7.13 (m, 1H), 6.89-6.84 (m, 1H), 4.13-4.07 (t, 2H), 3.69-3.63 (t, 2H), 3.53-3.48 (m, 2H), 3.44-3.38 (m, 2H), 3.25-3.20 (s, 3H).^{13}C NMR (100.6 MHz, DMSO-d_6, δ): 137.47 (s, 1C), 128.12 (s, 1C), 119.60 (s, 1C), 71.19 (s, 1C), 69.81 (s, 1C), 69.44 (s, 1C), 58.08 (s, 1C), 45.95 (s, 1C).ESI (m/z): 171.1147 ($C_8H_{15}N_2O_2^+$, calculated 171.1128).

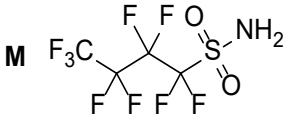

*Synthesis of **M**.* 254.55 g (843 mmoles) perfluorobutanesulfonyl fluoride was added to a 3 L round-bottom flask. Then, 1 L of 1 M Li-HMDS in THF was added by cannula transfer with vigorous stirring over 6 h and allowed to stir for 24 h before reducing the volume to ~500 mL via air stream. Then, 700 mL of 6 N HCl was added over the course of 1 day. The organic phase was collected, then the aqueous phase washed with 4x 75 mL of Et_2O; the organic phase and Et_2O washes were combined and stirred over anhydrous sodium sulfate and activated charcoal, stirred for 24 h, and passed over a plug of celite and concentrated by stirring under reduced pressure to afford **M** as a tacky brown-orange powder in 233 g (92 %) yield. ^{1}H NMR (400.2 MHz, DMSO-d_6, δ): 9.26-8.99 (s, 2H). ^{13}C NMR (100.6 MHz, DMSO-d_6, δ): 121.6-104.6 (br m, 4C). ^{19}F NMR (376.5 MHz, DMSO-d_6, δ): -80.56 (m, 3F), -114.18 (m, 2F), -121.28 (m, 2F), -125.89 (m, 2F). ESI (m/z): 297.9594 ($C_4HF_9NO_2S^-$, calculated 297.9579).

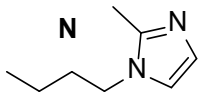

*Synthesis of **N**.* 13.075 g (159 mmoles) 2-methylimidazole, 23.958 g (175 mmoles) 1-bromobutane, and 80 mL THF were combined in a 250 mL round-bottom flask and stirred until homogeneous. 22.632 g (403 mmoles) KOH was added to start the reaction, the mixture was stirred for 17 h at 20 °C, and the solvent removed via forced air stream over 3 h. The resulting red oil was decanted and the remaining solids washed with 4 x 30 mL Et_2O. The decanted oil and Et_2O washes were combined and dried over $MgSO_4$, then centrifuged, decanted, and concentrated under reduced pressure. The resulting brown oil was extracted into 4x70 mL hexanes and concentrated under reduced pressure to afford **N** as a brown oil in 18.541 g (37 %) yield. ^{1}H NMR (400.2 MHz, DMSO-d_6, δ): 7.04-6.97 (d, 1H), 6.75-6.67 (d, 1H), 3.89-3.78 (t, 2H), 2.30-2.21 (s, 3H), 1.67-1.55 (m, 2H), 1.32-1.19 (m, 2H), 0.94-0.83 (t, 3H). ^{13}C NMR (100.6 MHz, DMSO-d_6, δ): 143.90 (s, 1C), 126.57 (s, 1C), 119.89 (s, 1C), 45.32 (s, 1C), 32.80 (s, 1C), 19.68 (s, 1C), 13.91 (s, 1C), 13.02 (s, 1C). ESI (m/z): 139.1236 ($C_8H_{15}N_2^+$, calculated 139.1230).

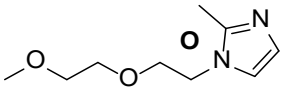

*Synthesis of **O**.* 1.012 g (12.3 mmoles) 2-methylimidazole was combined with 2.488 g (13.6 mmoles) MEE-Br and 12.2 mL acetonitrile and stirred until homogeneous. The reaction was started by adding 1.860 g (33.1 mmoles) KOH and allowed to stir at 20 °C for 18 h before centrifuging to remove solids, concentrating under reduced pressure, washing with 3x2 mL hexanes, and extracting into 5x3 mL Et_2O to afford **O** as a brown oil in 1.1 g (48 %) yield. ^{1}H NMR (400.2 MHz, DMSO-d_6, δ): 7.05-7.01 (d, 1H), 6.73-6.68 (d, 1H), 4.05-3.97 (t, 2H), 3.68-3.60 (t, 2H), 3.51-3.46 (m, 2H), 3.44-3.37 (m, 2H), 3.24-3.19 (s, 3H), 2.29-2.25 (s, 3H). ^{13}C NMR (100.6 MHz, DMSO-d_6, δ): 144.07 (s, 1C), 126.02 (s, 1C), 119.78 (s, 1C), 71.24 (s, 1C), 69.86 (s, 1C), 69.61 (s, 1C), 58.10 (s, 1C), 45.23 (s, 1C), 12.66 (s, 1C). ESI (m/z): 185.1288 ($C_9H_{17}N_2O_2^+$, calculated 185.1285).

Supplemental Notes

DC conductivity, electrode polarization, and Tan(δ). Complex conductivity was calculated according to $\sigma^* = i\omega\varepsilon_0\varepsilon^*$ and is shown in **Fig S5**.[1] The lower frequency range captures the onset of apparent DC conductivity (σ_{DC}), shown in **Fig 6b** as a straight, negative-sloping line and in **Fig S5a** as a low-frequency plateau. The exception is control ZI **3**, which does not fully plateau before the lowest frequency (ν = 20 Hz, ω = 126 rad s^{-1}) accessible to our instrument. Molecules **17** and **18** have sufficiently fast dynamics that we fully visualize the entire plateau before electrode charging begins to dominate, shown by a positive slope in **Fig S5a** for ω(**18**) < 1000 rad s^{-1} and ω(**17**) < 300 rad s^{-1}. For ZI **10** and ZILs **13**, **14**, and **15**, the accessible frequency range captured enough of the plateau region to confidently estimate σ_{DC} but did not capture the transition from conductivity-dominated to electrode charging-dominated behavior. Among the six molecules for which this plateau is visible, σ_{DC} varied dramatically from 1.7 (ZI **10**) to 120 μS m^{-1} (ZIL **18**). However, we emphasize, in agreement with a previous report on solvated and supercooled imidazolium sulfonate zwitterions, that this does not imply long-range ion transport in these systems.[2] Rather, because the molecules are net-charge-neutral, this value captures the aggregate contribution of a series of enormous dipoles, which, when driven to align in an electric field, afford a large *apparent* conductivity on the timescales of dipole alignment. For completeness, the imaginary part of $\sigma^*(\omega)$ is shown in **Fig S5b**.

The dielectric loss tangent Tan(δ) is shown in **Fig S5c**. For all molecules but control ZI **3**, it shows two maxima that we attribute to bulk polarization by dipole alignment (high frequency) and the onset of apparent DC conductivity (low frequency). The low-frequency peak is not fully resolved for molecules **10**, **13**, **14**, and **15**, and only a tail is visible for control ZI **3** due to its slow dynamics. At the high-frequency range, **18** shows the shoulder of an additional peak that is not fully resolved in the accessible frequency range but suggests an additional relaxation event that is also partially visible in the real permittivity of **Fig 6a**. Such complex behavior is unsurprising given the length and flexibility of the dipole in **18**, which likely samples a wide distribution of conformational modes and dipole lengths, in addition to carrying smaller local dipoles throughout the molecule, including within each charged end-group.[3,4]

Water uptake from ambient humidity. To quantify water uptake in a humid environment, samples of crystalline ZI **10** and ZILs **15** and **18** were first dried in a vacuum oven at 115 °C, then characterized by Fourier transform infrared (FTIR) spectroscopy and thermogravimetric analysis (TGA). Then, 500 mg of each molecule was equilibrated at 100% relative humidity for 1 week before repeating FTIR, TGA, and (for liquids **15** and **18**) dielectric relaxation spectroscopy and viscosity measurements. To maximize the surface area of solid **10**, the sample was ground to a fine powder in a mortar and pestle before humidifying.

Water uptake was quantified by TGA (**Fig S6**). Thermograms of samples dried in a vacuum oven showed negligible weight change below 300 °C (**Fig S6a**). By contrast, the humidified samples (**Fig S6b**) showed large variability in behavior. Humidified powder **10** afforded a nearly identical thermogram to the dried sample (*i.e.*, negligible mass loss below 300 °C), suggesting no water uptake. By contrast, humidified ZILs **15** and **18** showed considerable mass loss below 150 °C that we attribute to absorbed water. This difference in behavior between crystalline and liquid materials suggests that crystallinity of **10** stabilizes the material against water uptake, while the liquids are far more susceptible to environmental humidity. **Fig S6c** tabulates the remaining weight percent of each material at 100, 200, and 300 °C in the "dried" and "humidified" states. By 200 °C, dried molecules **10**, **15**, and **18** have lost 0.6, 0.5, and 0.5 weight percent of their original mass, respectively. This suggests a quite small amount of residual volatiles, including water, after drying in the vacuum oven. At the same temperature, the humidified samples have lost 0.5, 16.3, and 22.1 weight percent of their initial mass, respectively, supporting the idea that the liquids adsorb water in humid environments.

FTIR spectroscopically confirms negligible water content in all three molecules after 24 h at 115 °C, and that **15** and **18** readily adsorb atmospheric moisture, while crystalline **10** does not (**Fig S7**). For all three molecules, the dried "as synthesized" samples show a negligible O-H stretch at ~3400 wavenumbers. For **10**, this remains unchanged after 1 week at 100% relative humidity, but strong O-H stretches emerge for both **15** and **18**.

Fig S8 shows shear-rate-dependent viscosity of ZILs **15** and **18** i) "as synthesized," immediately after their original synthesis and purification, ii) after 9 (ZIL **15**) and 6 (ZIL **18**) months of storage in a vacuum desiccator, and iii) after 1 week in 100% relative humidity. After humidification, both samples exhibit a viscosity decrease of ~2 orders of magnitude compared to the "as synthesized" and "storage" samples, suggesting considerable water uptake.

NMR further supports negligible water content after drying in the vacuum oven. Our NMR spectra were all run in DMSO-d_6. Even dry DMSO kept in a desiccator and used under argon inevitably contributes a small amount of water, increasing the apparent water content. Despite this, the water peaks at ~3.3 ppm in the ^{1}H NMR spectra of all 18 zwitterions, particularly ZILs **13**-**18**, are negligible compared to the product peaks. This suggests, consistent with our TGA and FTIR results, that the water content after drying in a vacuum oven is negligible.

Finally, we replicated dielectric spectroscopy experiments with humidified **15** and **18**. The low-frequency end of the spectrum was dominated by electrode charging as characterized by $\varepsilon' > 10{,}000$, while at high frequencies, ε' and ε'' were both negative. This suggests sufficiently low impedance that inductive effects from the coaxial cables dominated the measurement.[1,5] As a result, these measurements reflect

artifacts of the measurement apparatus rather than material properties. Hence, we have not prepared a supplemental figure with this data.

Correlations in Viscosity, T_g, heat capacity, spacer length, and molecular weight. Several thermal and dynamic parameters showed interdependent behaviors and spacer-length-dependent trends. These are shown in **Figs S9-10** and discussed in this section.

Fig S9a shows that T_g correlates negatively with spacer length, decreasing by 11-21 °C as the spacer grows from four to sixteen atoms. To better understand this and the ZIL energy landscape, we quantified the change in heat capacity (ΔC_g) at T_g.[6-8] For each DSC scan, we estimated the liquid ($C_{g,liq}$) and glass ($C_{g,gl}$) heat capacities at T_g by extrapolating the linear regions of the thermogram on either side of the transition. We then calculated $\Delta C_g = C_{g,liq} - C_{g,gl}$ on both specific ($\Delta C_{g,s}$, **Fig S9b**) and molar ($\Delta C_{g,m}$, **Fig S9c**) bases and found that ΔC_g shows a strong positive relationship with length and flexibility for both the *spacer* R_s and the *tail* R_t. This is intuitive on a molar basis, because a molecule with more rotatable bonds can access a broader range of structural and vibrational modes.[9] However, it is striking that this trend holds on a specific basis, since it implies a net gain in available states despite fewer molecules per unit mass. This observation supports the hypothesis that, when transitioning from arrested to melt states, the magnitude of entropy gain *increases* with spacer length. **Fig S9d** shows a negative correlation between $\Delta C_{g,m}$ and T_g, as predicted by spacer length and an MEE tail. This trend suggests that T_g might be suppressed further by designing zwitterions with more rotatable bonds that unlock additional conformational entropy in the liquid state. Finally, viscosity at 22 °C correlates positively with T_g (**Fig S9e**) and negatively with $\Delta C_{g,m}$ (**Fig S9f**).

Fig S10 shows T_g (**Fig S10a**), $\Delta C_{g,m}$ (**Fig S10b**), and η (**Fig S10c**) as a function of zwitterion molecular weight. **Figs S10a-b** show data for sixteen of our eighteen zwitterions; we were unable to determine T_g for ZIs **4** and **9** because they recrystallized too quickly during the cooling cycle to trap them in the amorphous state (see DSC data at the end of this document or download our source data). The general trends are that T_g correlates negatively with molecular weight, while $\Delta C_{g,m}$ correlates positively. ZI **7** is an outlier in both data sets, with a larger T_g and a smaller $\Delta C_{g,m}$ than predicted by the trend of the other fifteen molecules. This outlier is instructive. Most of the molecular weight distribution across these 16 molecules can be attributed to changes in the tail or spacer length, which add a rotatable bond for every additional 14 (-CH_2-) or 16 (-O-) g mol^{-1}. By contrast, increasing the size of the perfluoroalkyl tail on the sulfonimide anion adds another 50 g mol^{-1} (-CF_2-) for every rotatable bond. Moreover, we expect that the larger steric bulk of -CF_2- compared to -O- or -CH_2- will afford larger barriers to bond rotation, suggesting a smaller contribution to the conformational entropy and liquid heat capacity than methylene or ether groups. Finally, liquid viscosity correlates negatively with molecular weight for supercooled **3** and **10**, and ZILs **13**, **14**, **15**, **17**, and **18** (**Fig S10c**), supporting the idea that, in the context of ZILs, increasing molecular size via long, flexible tails and spacers can decrease viscosity.

Supplemental references

1. Kremer, F., and Schönhals, A. (2003). Broadband Dielectric Spectroscopy (Springer-Verlag Berlin Heidelberg GmbH) https://doi.org/10.1016/b978-0-12-823518-8.00001-3.

2. Mei, W., Rothenberger, A.J., Bostwick, J.E., Rinehart, J.M., Hickey, R.J., and Colby, R.H. (2021). Zwitterions Raise the Dielectric Constant of Soft Materials. Phys. Rev. Lett. *127*, 1–6. https://doi.org/10.1103/PhysRevLett.127.228001.

3. Hunger, J., Stoppa, A., Buchner, R., and Hefter, G. (2009). Dipole correlations in the ionic liquid 1-N-ethyl-3-N-methylimidazolium ethylsulfate and its binary mixtures with dichloromethane. J. Phys. Chem. B *113*, 9527–9537. https://doi.org/10.1021/jp9024574.

4. Hunger, J., Stoppa, A., Schrödle, S., Hefter, G., and Buchner, R. (2009). Temperature dependence of the dielectric properties and dynamics of ionic liquids. ChemPhysChem *10*, 723–733. https://doi.org/10.1002/cphc.200800483.

5. Woodward, W.H.H. (2021). Broadband Dielectric Spectroscopy - A Practical Guide. ACS Symp. Ser. *1375*, 3–59. https://doi.org/10.1021/bk-2021-1375.ch001.

6. Adam, G., and Gibbs, J.H. (1965). On the temperature dependence of cooperative relaxation properties in glass-forming liquids. J. Chem. Phys. *43*, 139–146. https://doi.org/10.1063/1.1696442.

7. Dyre, J.C. (2006). Colloquium: The glass transition and elastic models of glass-forming liquids. Rev. Mod. Phys. *78*, 953–972. https://doi.org/10.1103/RevModPhys.78.953.

8. Trachenko, K., and Brazhkin, V. V. (2011). Heat capacity at the glass transition. Phys. Rev. B - Condens. Matter Mater. Phys. *83*, 1–6. https://doi.org/10.1103/PhysRevB.83.014201.

9. Tu, W., Li, X., Chen, Z., Liu, Y.D., Labardi, M., Capaccioli, S., Paluch, M., and Wang, L.M. (2016). Glass formability in medium-sized molecular systems/pharmaceuticals. I. Thermodynamics vs. kinetics. J. Chem. Phys. *144*. https://doi.org/10.1063/1.4947476.

Supplemental Figures

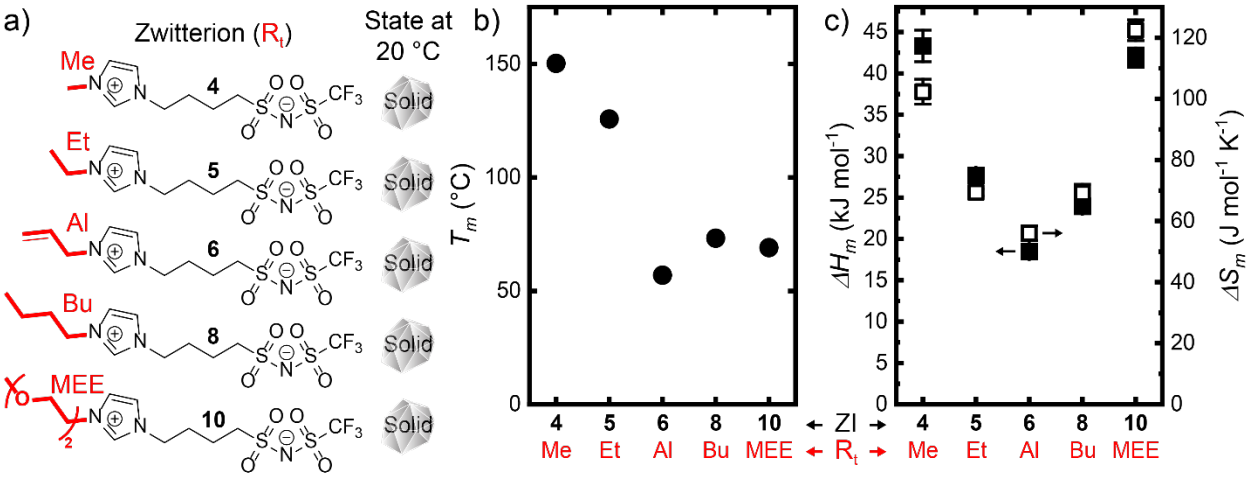

Figure S1. Imidazolium tail R_t impacts melting behavior of zwitterions. a) zwitterions **4**, **5**, **6**, **8**, and **10** were used to compare methyl (Me), ethyl (Et), allyl (Al), *n*-butyl (Bu) and (2-(2-methoxy)-ethoxy)-ethyl (MEE) tail groups to highlight their impact on (b) T_m ,and (c) ΔH_m and ΔS_m. Data are represented as mean ± SD, N = 3.

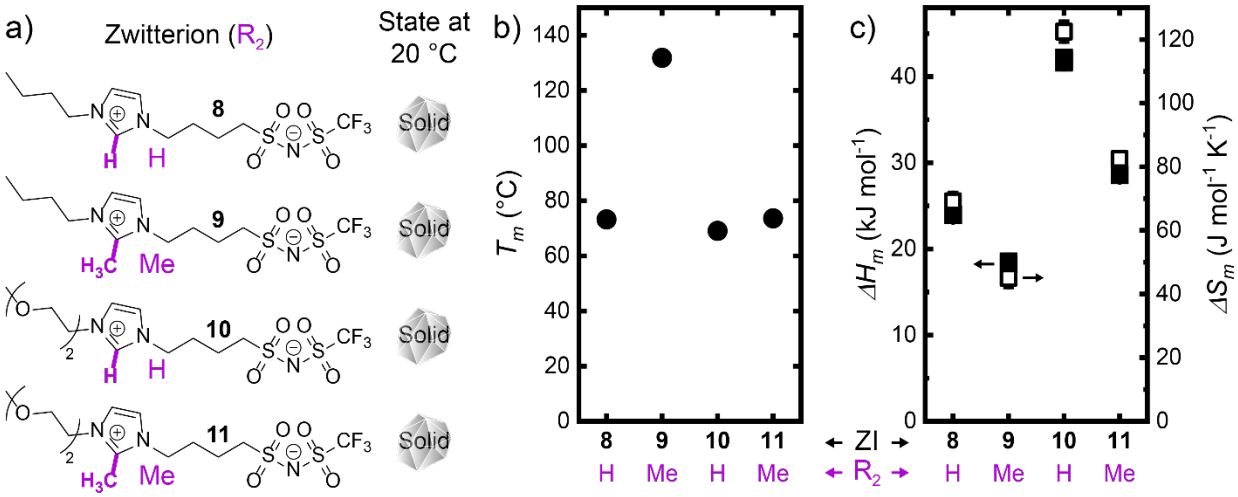

Figure S2. Imidazolium 2 position R_2 impacts melting behavior of zwitterions. a) zwitterions **8**, **9**, **10**, and **11** were used to compare proton (H) versus methyl (Me) at the 2 position on the imidazolium cation to highlight their impact on (b) T_m, and (c) ΔH_m and ΔS_m. Data are represented as mean ± SD, N = 3.

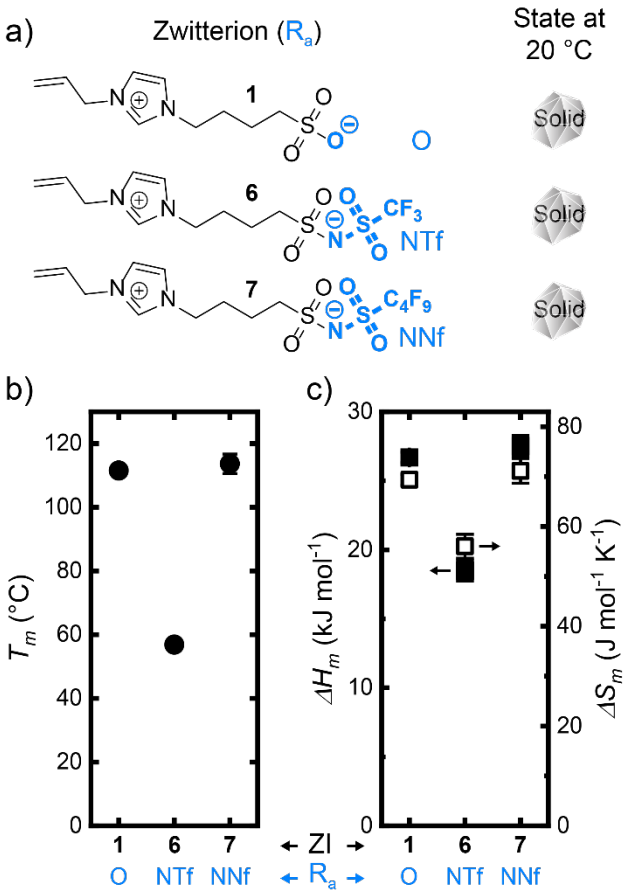

Figure S3. Anion R_a impacts melting behavior of zwitterions. a) zwitterions **1**, **6**, and **7** were used to compare sulfonate (O) triflimide (NTf), and nonaflimide (NNf), anions to highlight their impact on (b) T_m ,and (c) ΔH_m and ΔS_m. Data are represented as mean ± SD, N = 3.

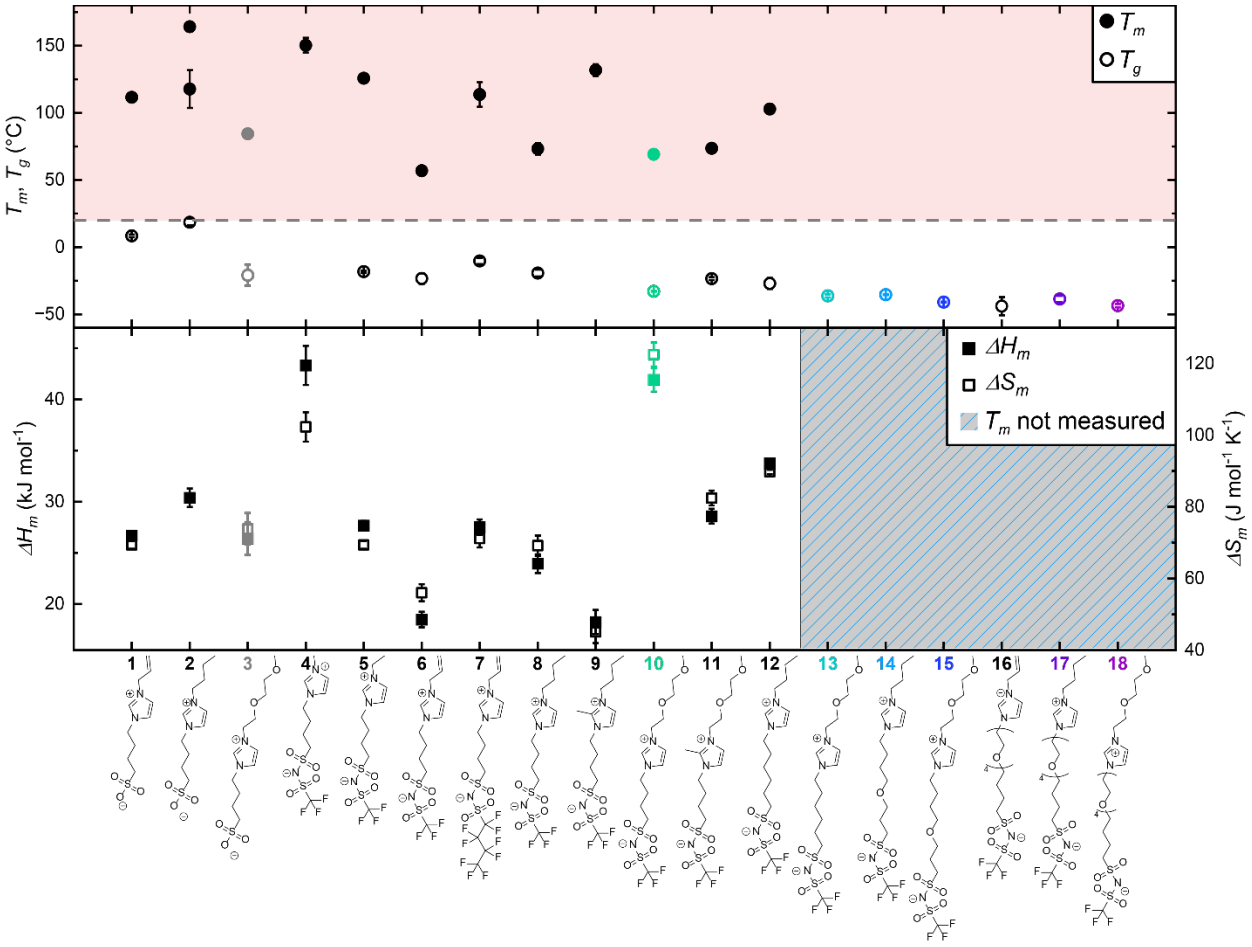

Figure S4. Thermal characterization of synthetic library of zwitterions. T_m, T_g (top) and ΔH_m, ΔS_m (bottom) of the eighteen molecules studied in this work. The dashed line represents 20 °C; molecules **1**-**12** exhibit T_m > 20 °C and reach thermodynamic minima as crystalline solids at room temperature. Molecules **13**-**18** were isolated as liquids and exhibited no crystallization when cycled to -90 °C at 10 °C min^{-1} or when stored at 22 °C in a vacuum desiccator for at least 4 months. Data are represented as mean ± SD, N = 3. Color-coding of molecules **3**, **10**, **13**, **14**, **15**, **17**, and **18** corresponds to **Figs 5-6**.

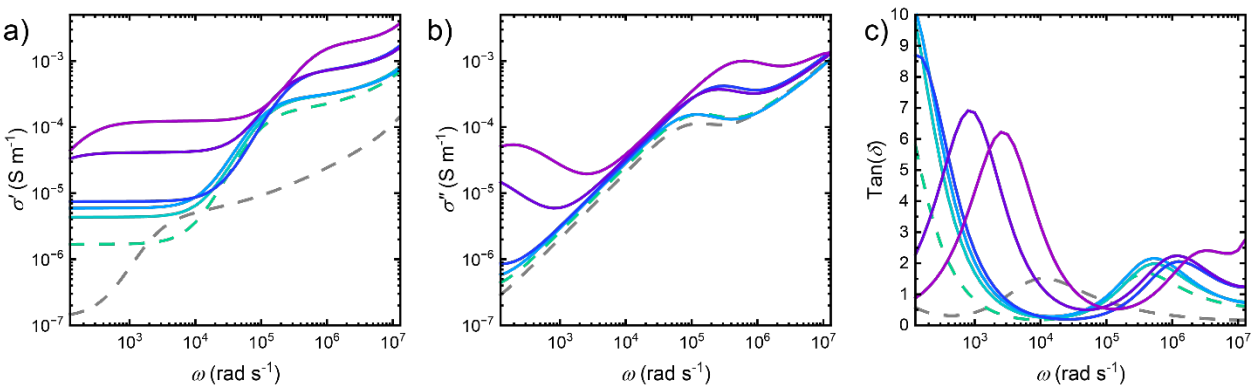

Figure S5. Additional electrical properties of neat zwitterions. (a) real σ' and (b) imaginary σ'' parts of conductivity at 25 °C for supercooled zwitterions: **3** and **10** and ZILs: **13-15**, **17**, and **18**; (c) dielectric loss tangent tan(δ) as a function of angular frequency ω. Dashed lines denote supercooled liquids; solid lines denote stable liquids. Color-coding is consistent with **Figs 5-6**.

a)

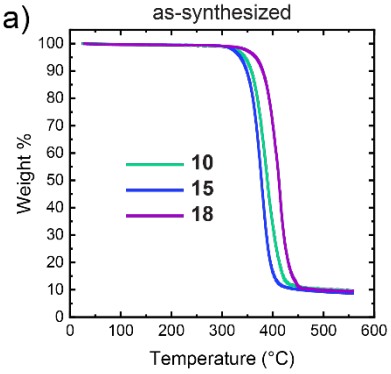

b)

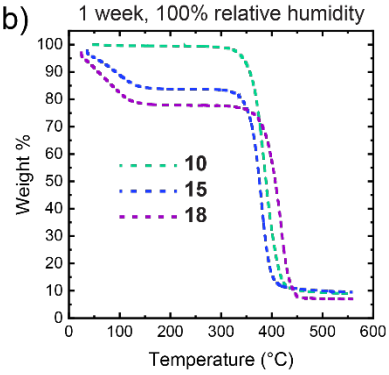

c)

	wt% 100 °C	wt% 200 °C	wt% 300 °C
10 (dry)	99.6	99.4	99.0
10 (humidified)	99.6	99.5	99.0
15 (dry)	99.6	99.5	99.1
15 (humidified)	88.9	83.7	83.5
18 (dry)	99.6	99.5	99.1
18 (humidified)	82.5	77.9	77.6

Figure S6. Thermogravimetric analysis of ZI **10** and ZILs **15** and **18.** a) as-synthesized after 24 h at 115 °C in a vacuum oven; b) after equilibrating for 1 week in 100% relative humidity; c) tabulated data for all 3 molecules in the dry and humidified state at 100, 200, and 300 °C.

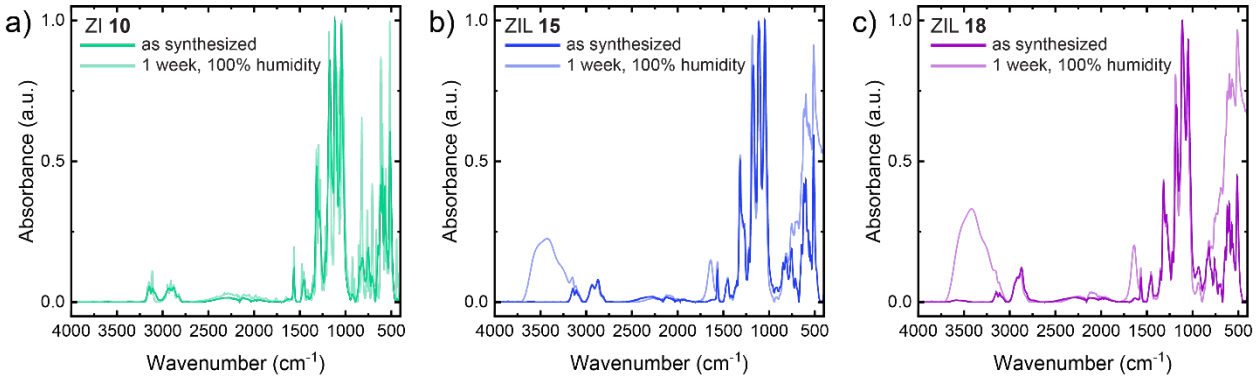

Figure S7. FTIR spectra of (a) ZI **10** and ZILs (b) **15** and (c) **18** as synthesized after 24 h at 115 °C in a vacuum oven (dark lines) and after 1 week in 100% relative humidity (light lines).

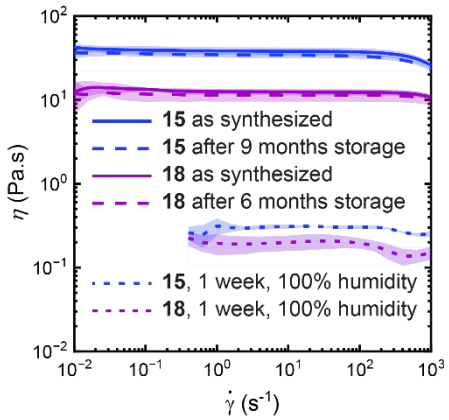

Figure S8. Apparent viscosity of **15** and **18** immediately after synthesis and purification (solid lines), after 9 (ZIL **15**) and 6 (ZIL **18**) months of storage (dashed line), and after equilibrating for 1 week in 100% relative humidity (dotted line). Data are shown as mean ± SD, N = 3.

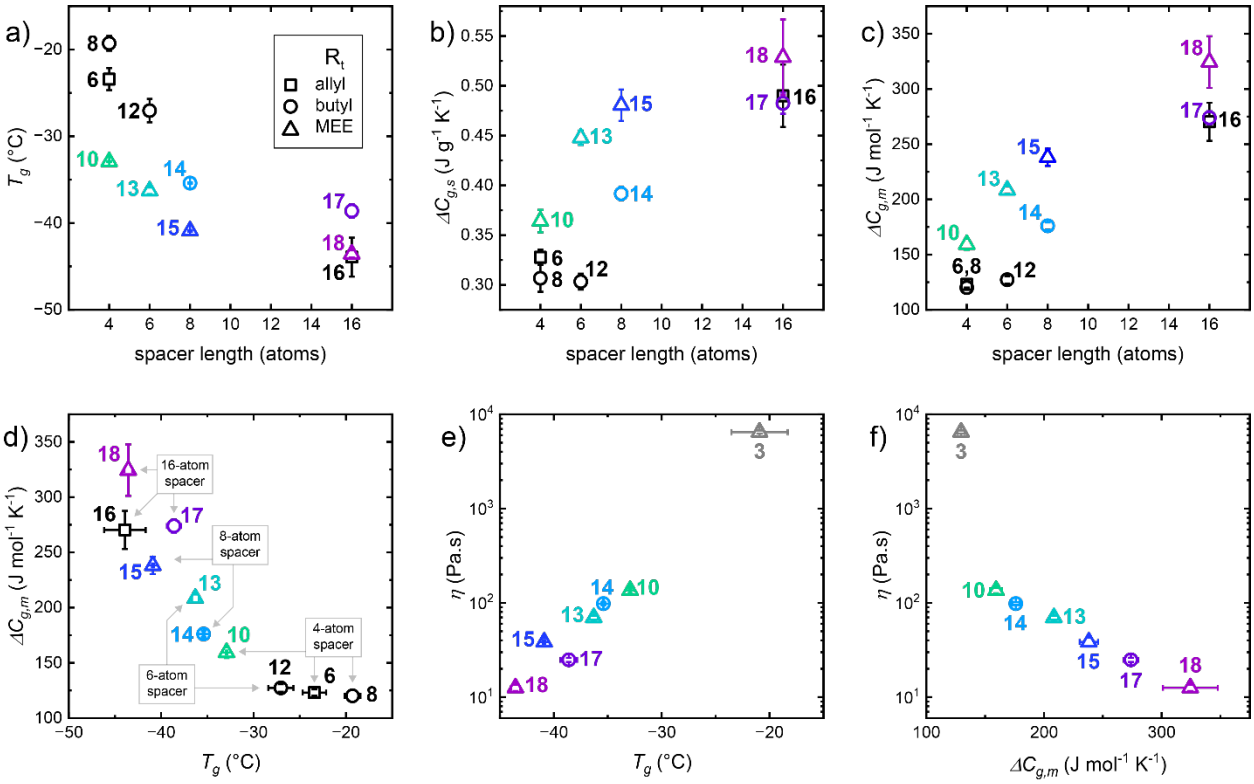

Figure S9. Viscosity, T_g, and spacer length correlations in reported zwitterions. a) T_g as a function of spacer length for zwitterions with R_t = allyl, butyl, and MEE; b) specific ($\Delta C_{g,s}$) and c) molar ($\Delta C_{g,m}$) heat capacity jump at T_g as a function of spacer length. d) $\Delta C_{g,m}$ as a function of T_g. Semilog plots of apparent viscosity at a shear rate of 1 s^{-1} as a function of e) T_g, and f) $\Delta C_{g,m}$. Data are shown as mean ± SD, n = 3. Color-coding of molecules **3**, **10**, **13**, **14**, **15**, **17**, and **18** corresponds to **Figs 5-6**.

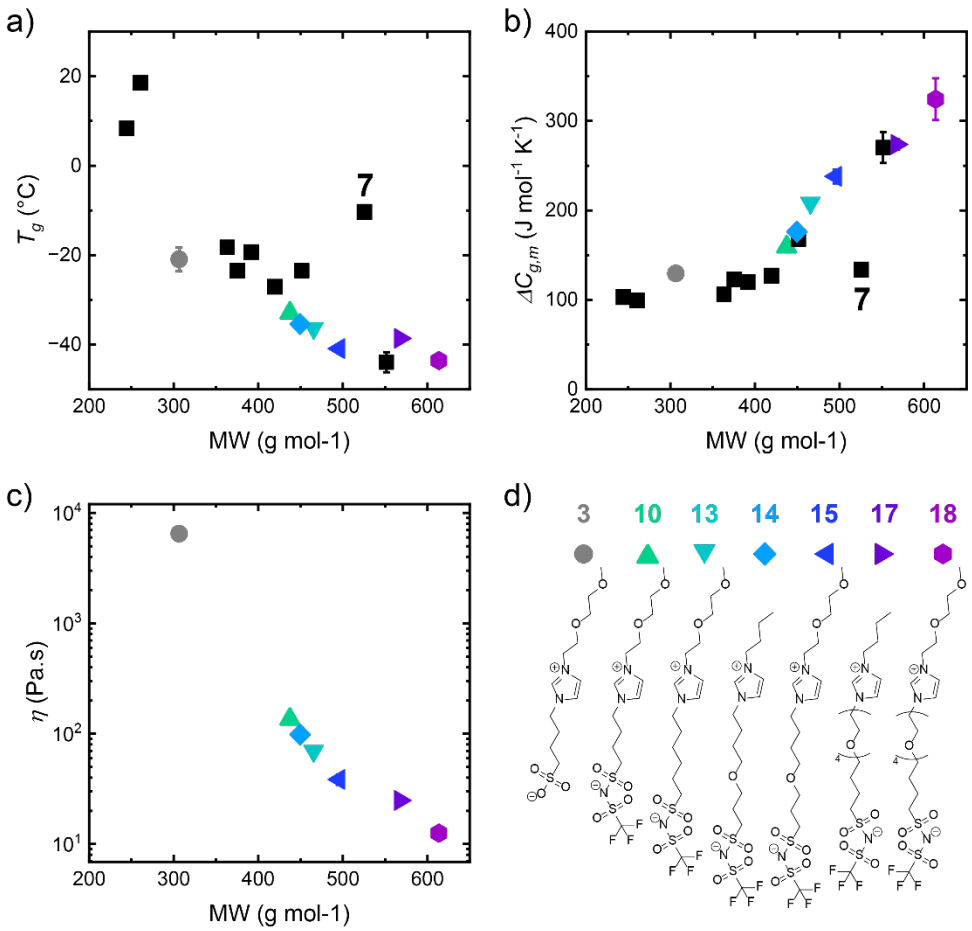

Figure S10. Molecular weight-dependence of thermal and kinetic behavior. a) T_g, b) $\Delta C_{g,m}$, and c) η as a function of molecular weight. d) supercooled zwitterions: **3** and **10** and zwitterionic liquids (ZILs): **13**-**15**, **17**, and **18**. Data are represented as mean ± SD, N = 3. Molecule **7** is highlighted as an outlier in a) and b). Color-coding of molecules **3**, **10**, **13**, **14**, **15**, **17**, and **18** corresponds to **Figs 5-6**.

Data S1: Nuclear magnetic resonance of zwitterions and intermediates

Molecule **1**

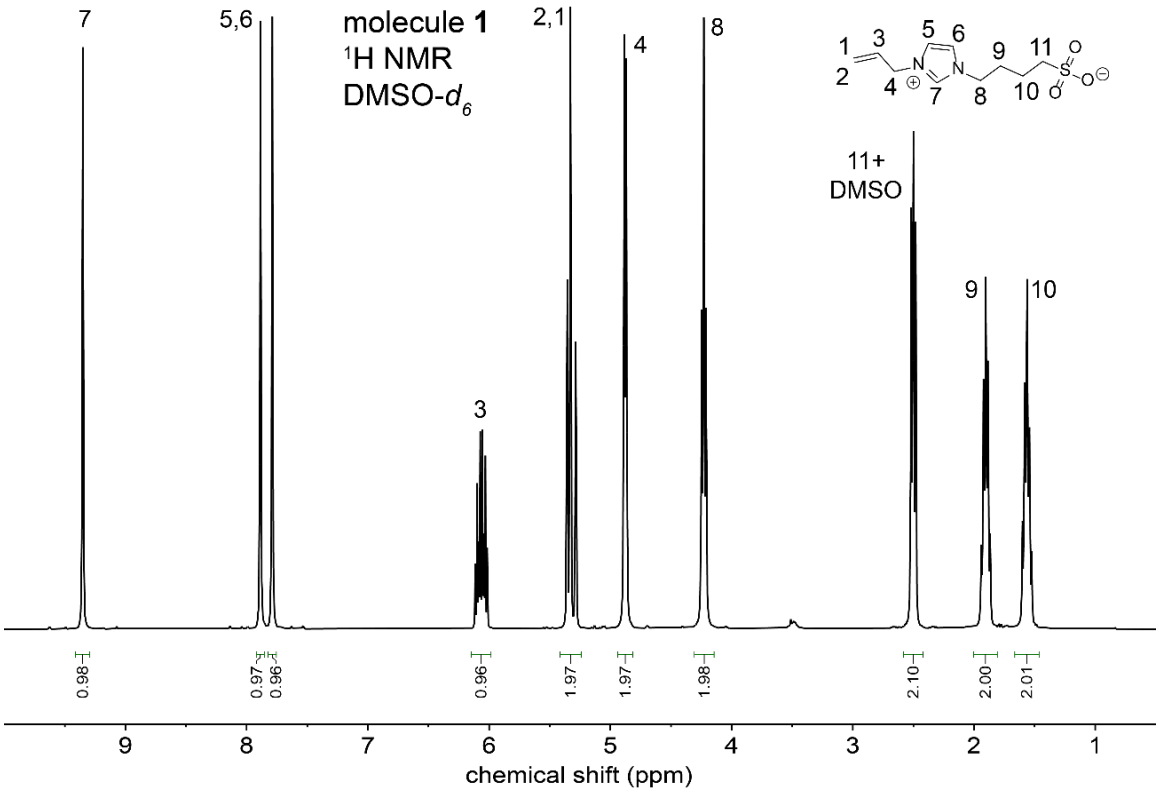

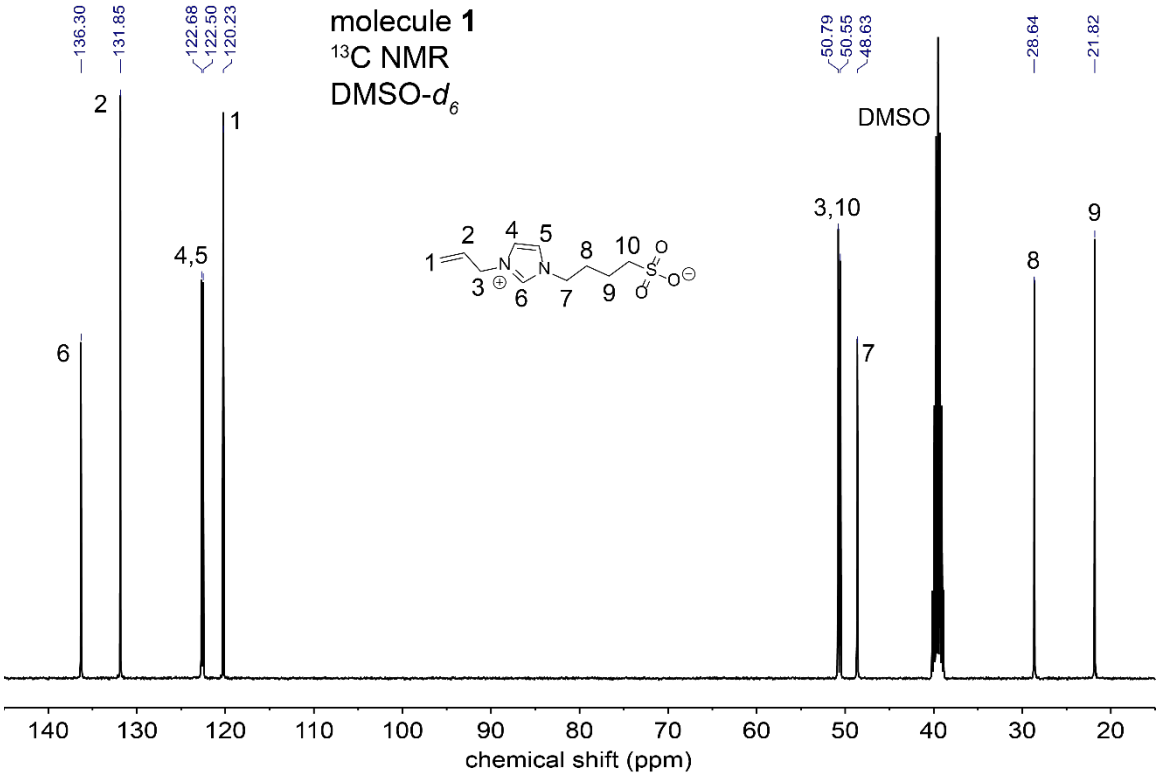

Molecule **2**

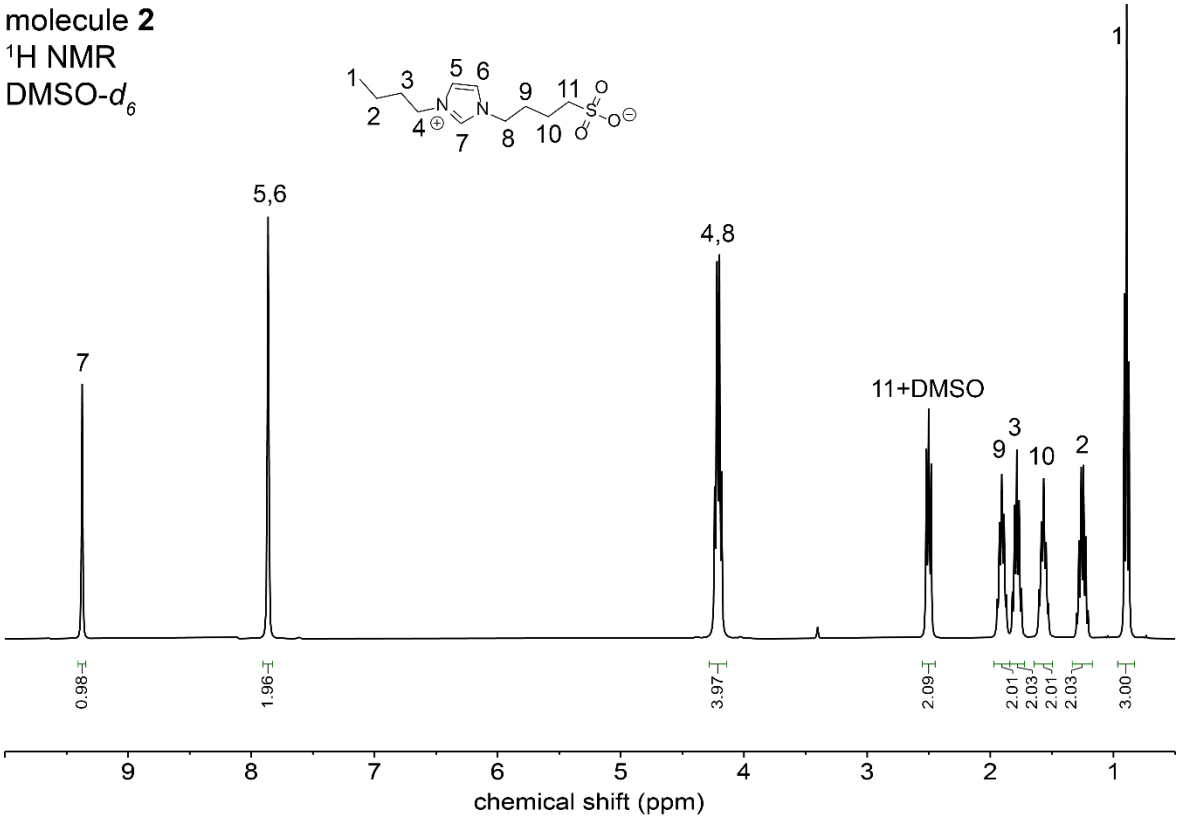
molecule **2**
^{1}H NMR
DMSO-d_6
7
5,6
4,8
11+DMSO
9
3
10
2
1
0.98
1.96
3.97
2.09
2.01
2.03
2.01
2.03
3.00
chemical shift (ppm)

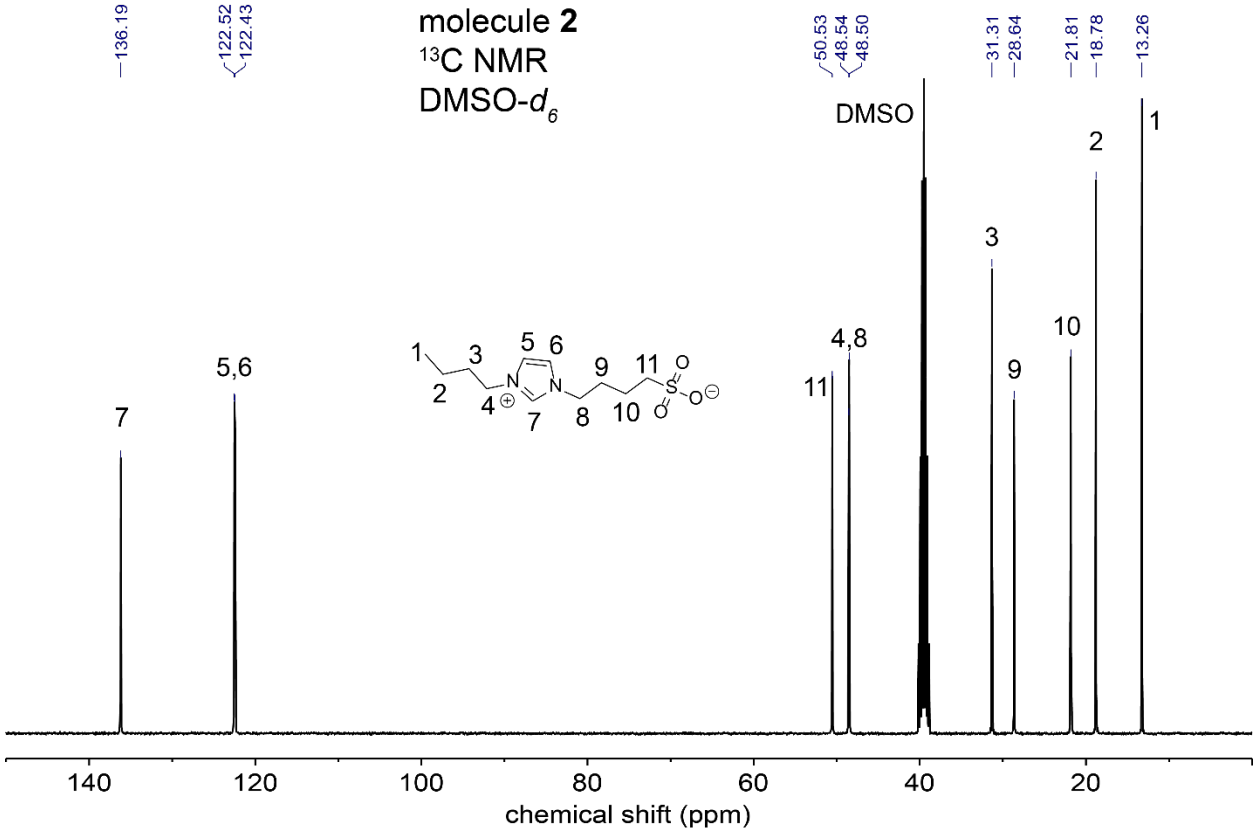
136.19
122.52
122.43
50.53
48.54
48.50
31.31
28.64
21.81
18.78
13.26
molecule **2**
^{13}C NMR
DMSO-d_6
DMSO
7
5,6
11
4,8
9
3
10
2
1
chemical shift (ppm)

Molecule **3**

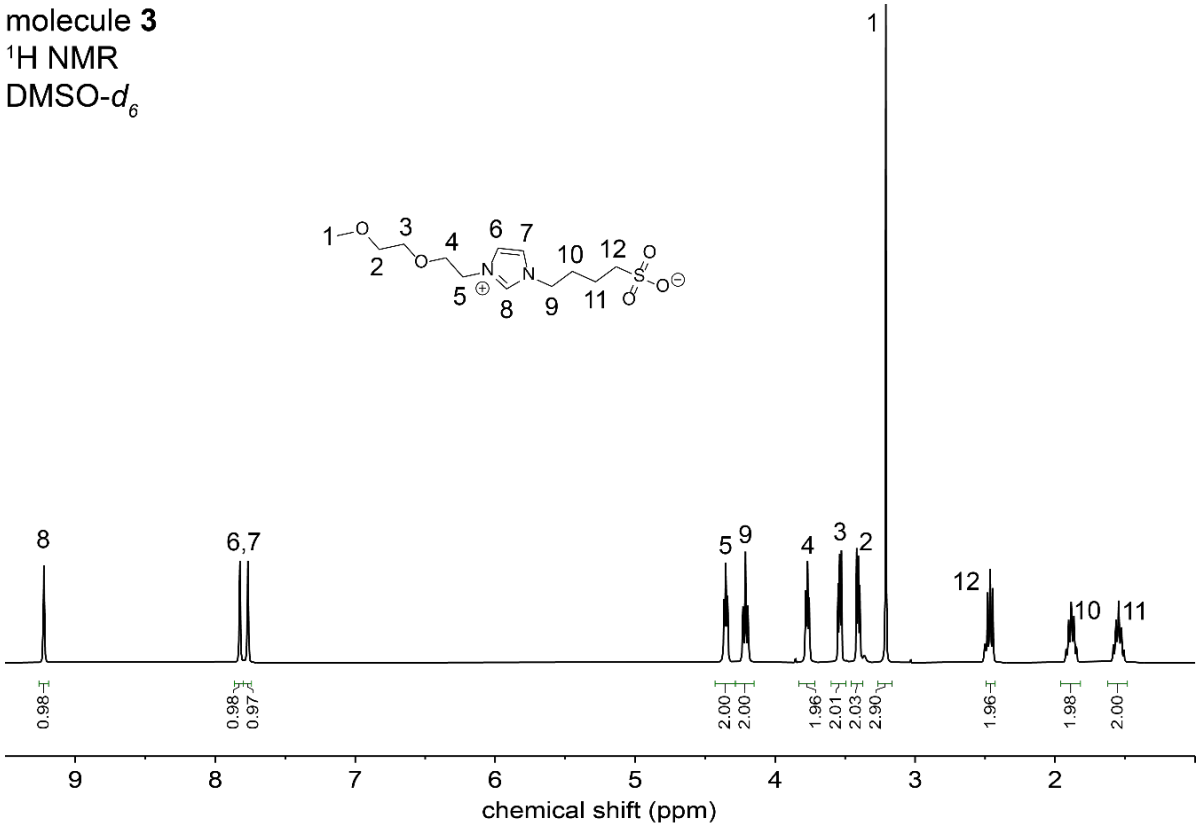
molecule **3**
^{1}H NMR
DMSO-d_6
chemical shift (ppm)

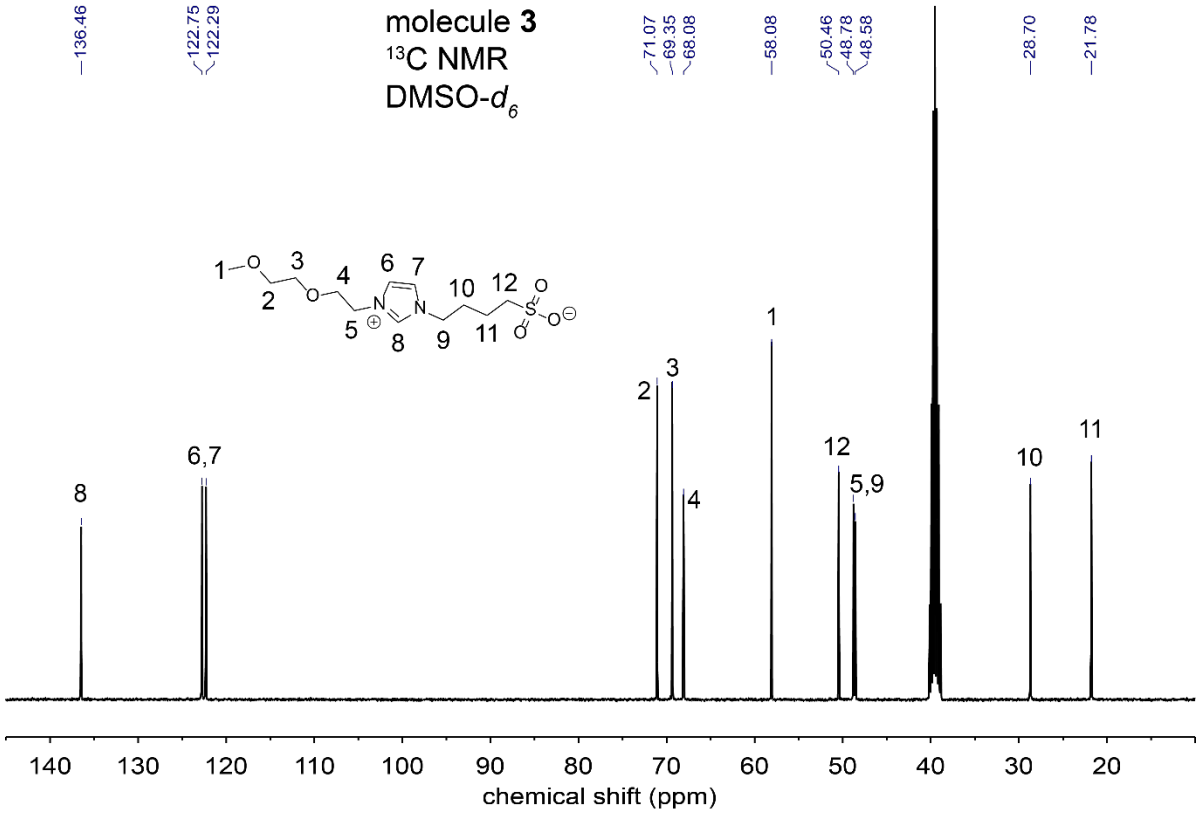
molecule **3**
^{13}C NMR
DMSO-d_6
chemical shift (ppm)

Molecule **4**

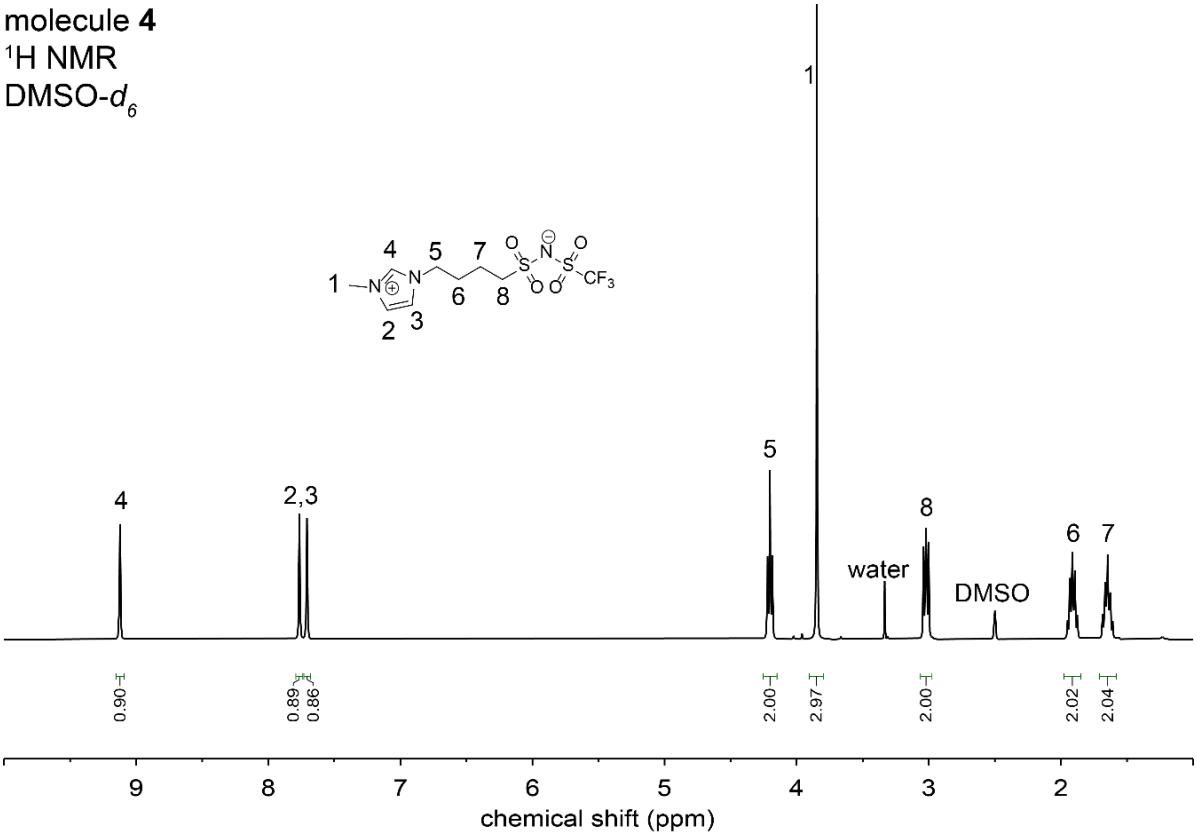
molecule **4**
^{1}H NMR
DMSO-d_6
1
5
4
2,3
8
6 7
water
DMSO
0.90
0.89
0.86
2.00
2.97
2.00
2.02
2.04
9 8 7 6 5 4 3 2
chemical shift (ppm)

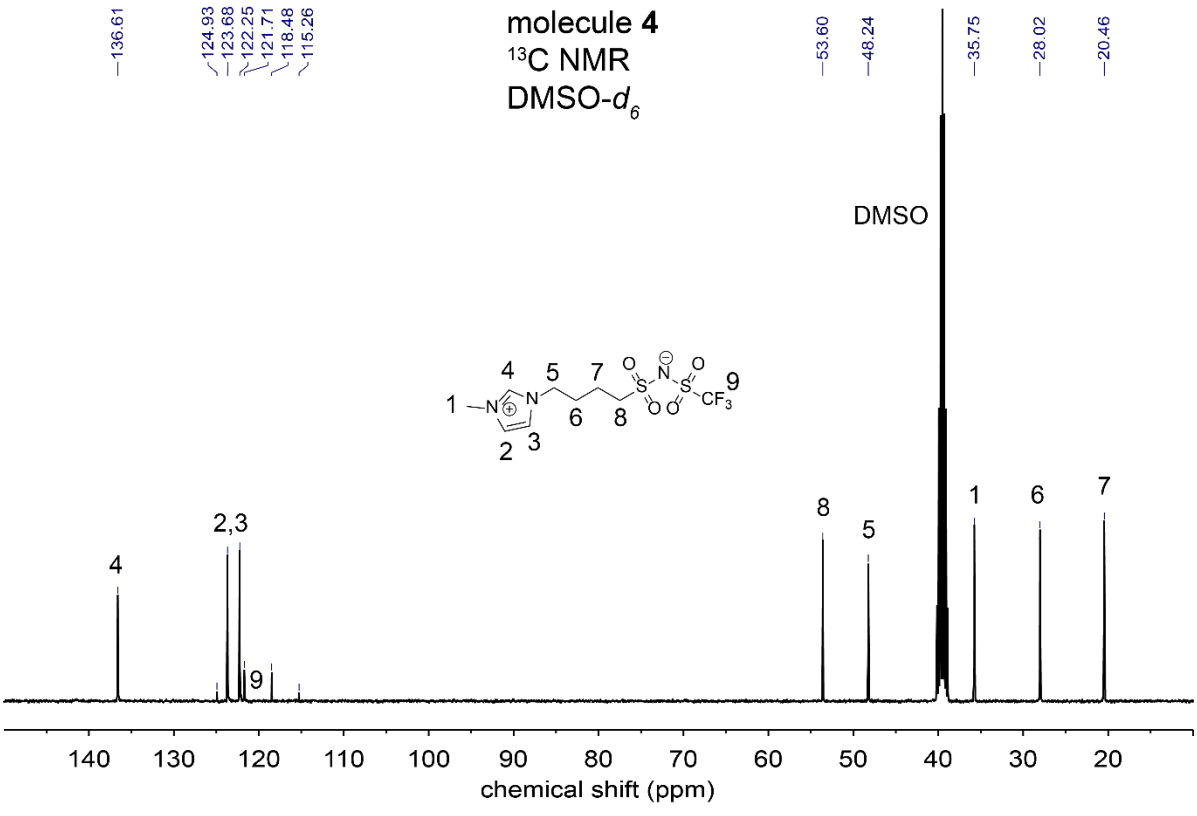
136.61
124.93
123.68
122.25
121.71
118.48
115.26
53.60
48.24
35.75
28.02
20.46
molecule **4**
^{13}C NMR
DMSO-d_6
DMSO
4
2,3
9
8
5
1
6
7
140 130 120 110 100 90 80 70 60 50 40 30 20
chemical shift (ppm)

molecule **4**
^{19}F NMR
DMSO-d_6

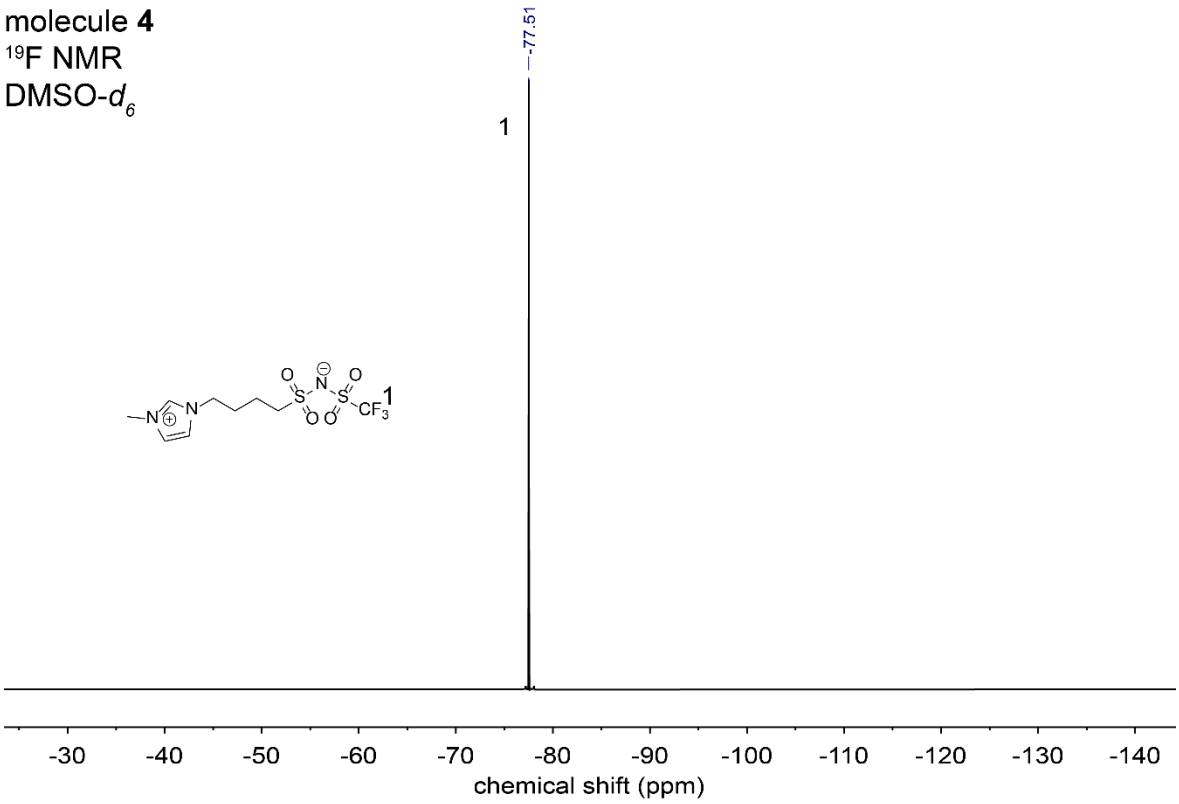

Molecule **5**

molecule **5**
^{1}H NMR
DMSO-d_6

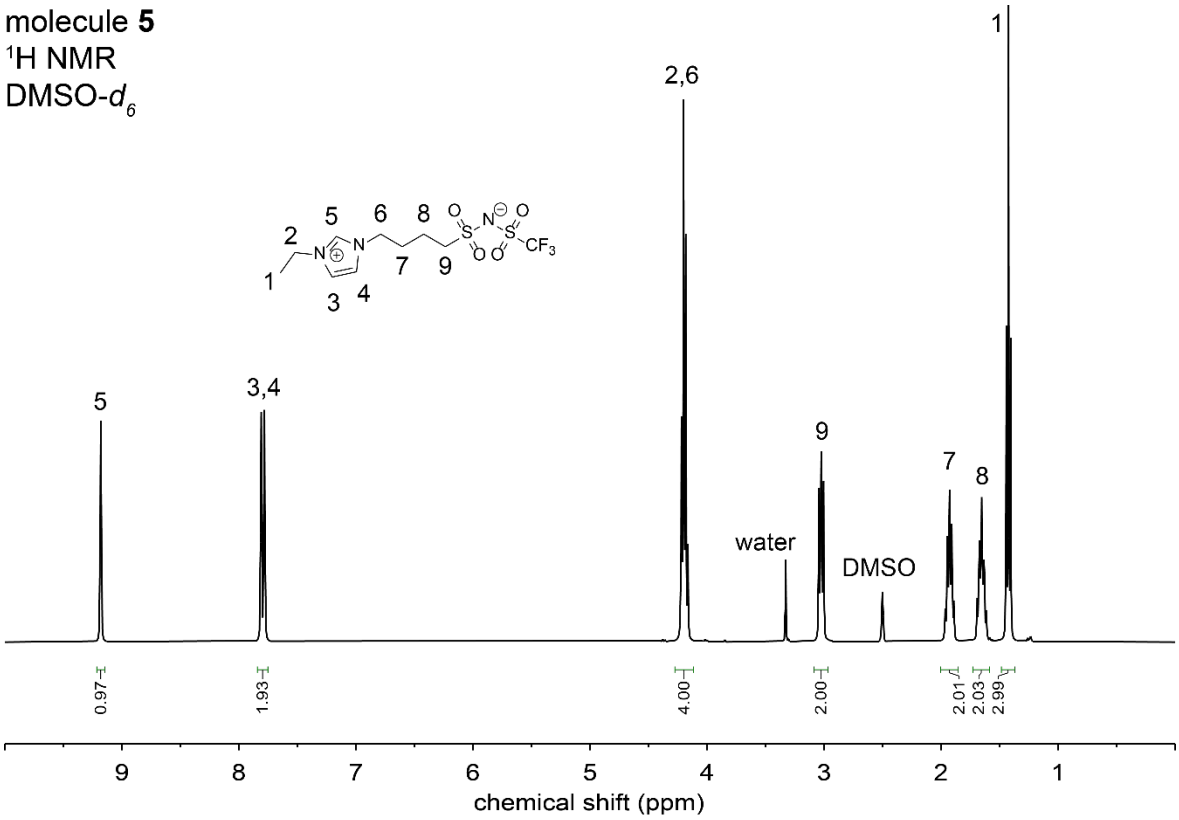

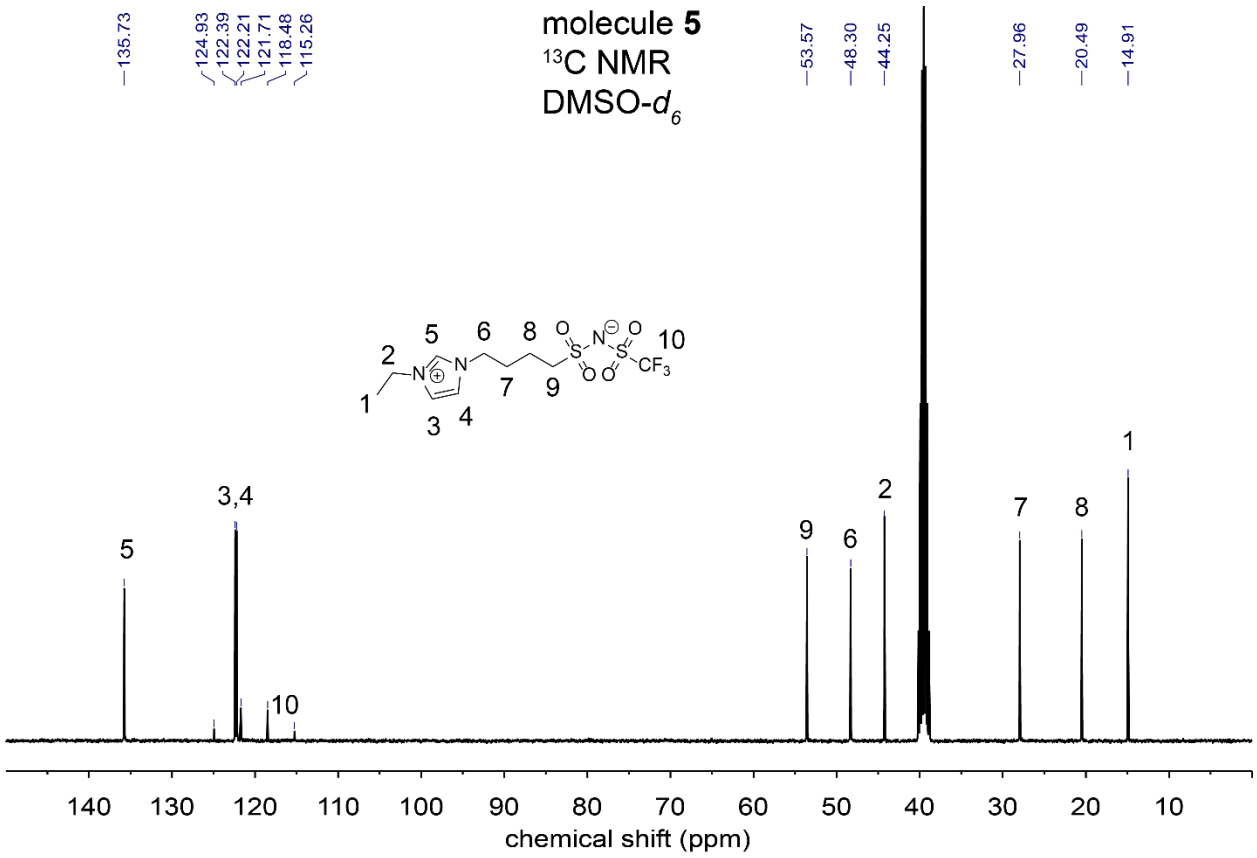
molecule **5**
^{13}C NMR
DMSO-d_6
135.73
124.93
122.39
122.21
121.71
118.48
115.26
53.57
48.30
44.25
27.96
20.49
14.91
5
3,4
10
9
6
2
7
8
1
chemical shift (ppm)

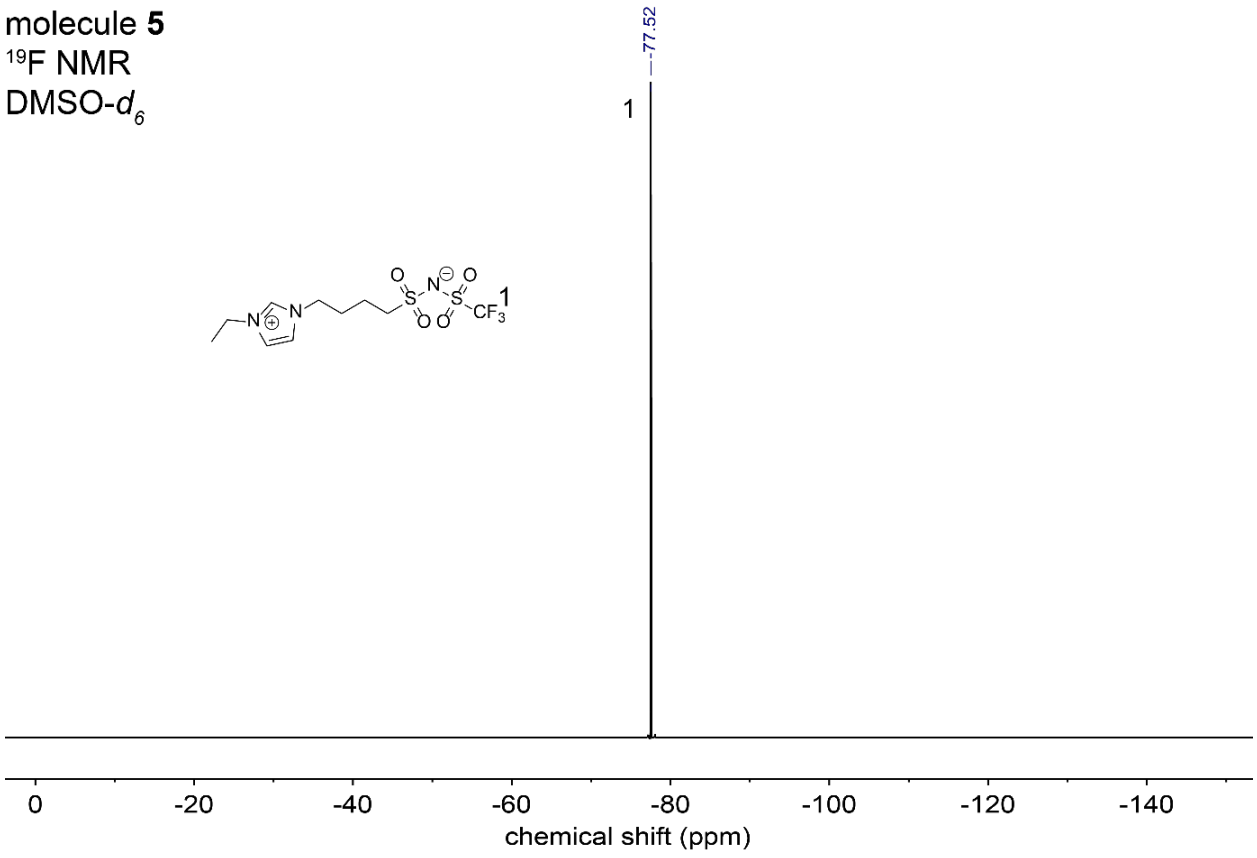
molecule **5**
^{19}F NMR
DMSO-d_6
-77.52
1
chemical shift (ppm)

Molecule **6**

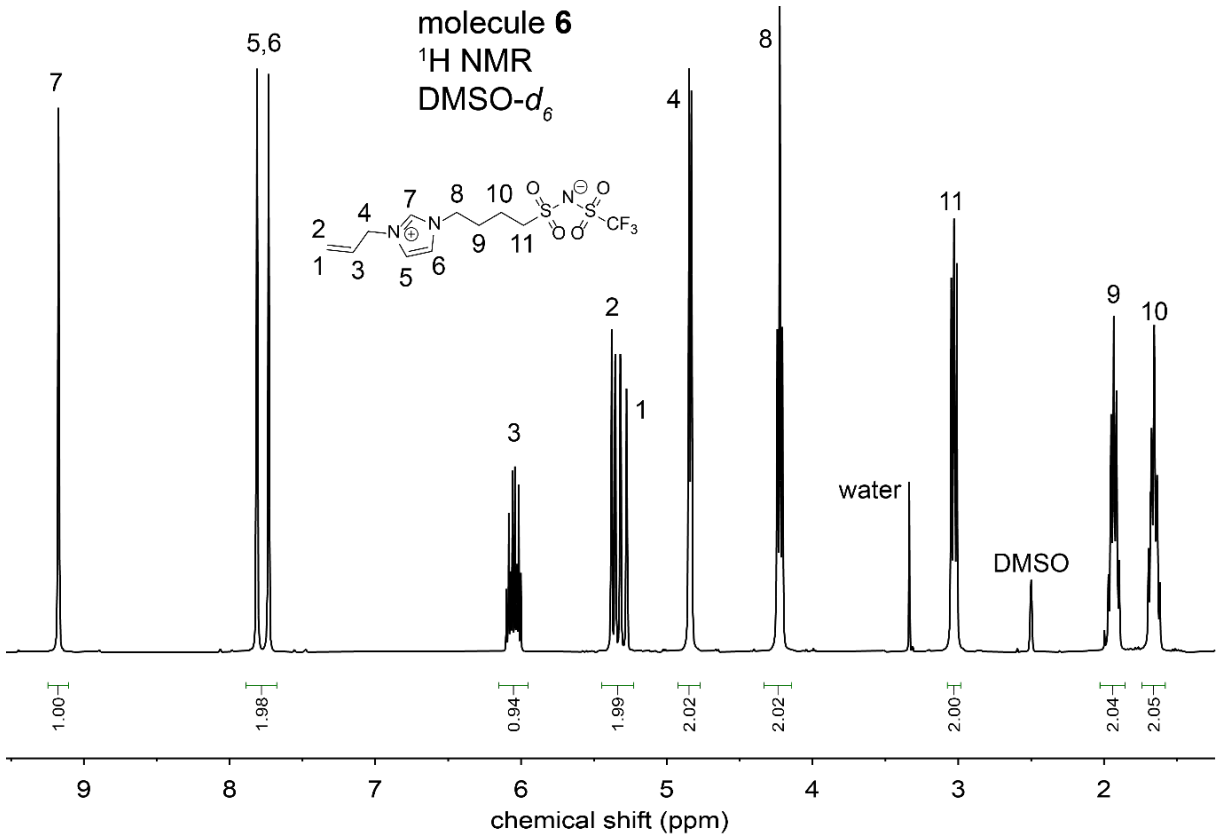
molecule **6**
^{1}H NMR
DMSO-d_6
7
5,6
4
8
2
1
3
11
9
10
water
DMSO
1.00
1.98
0.94
1.99
2.02
2.02
2.00
2.04
2.05
chemical shift (ppm)

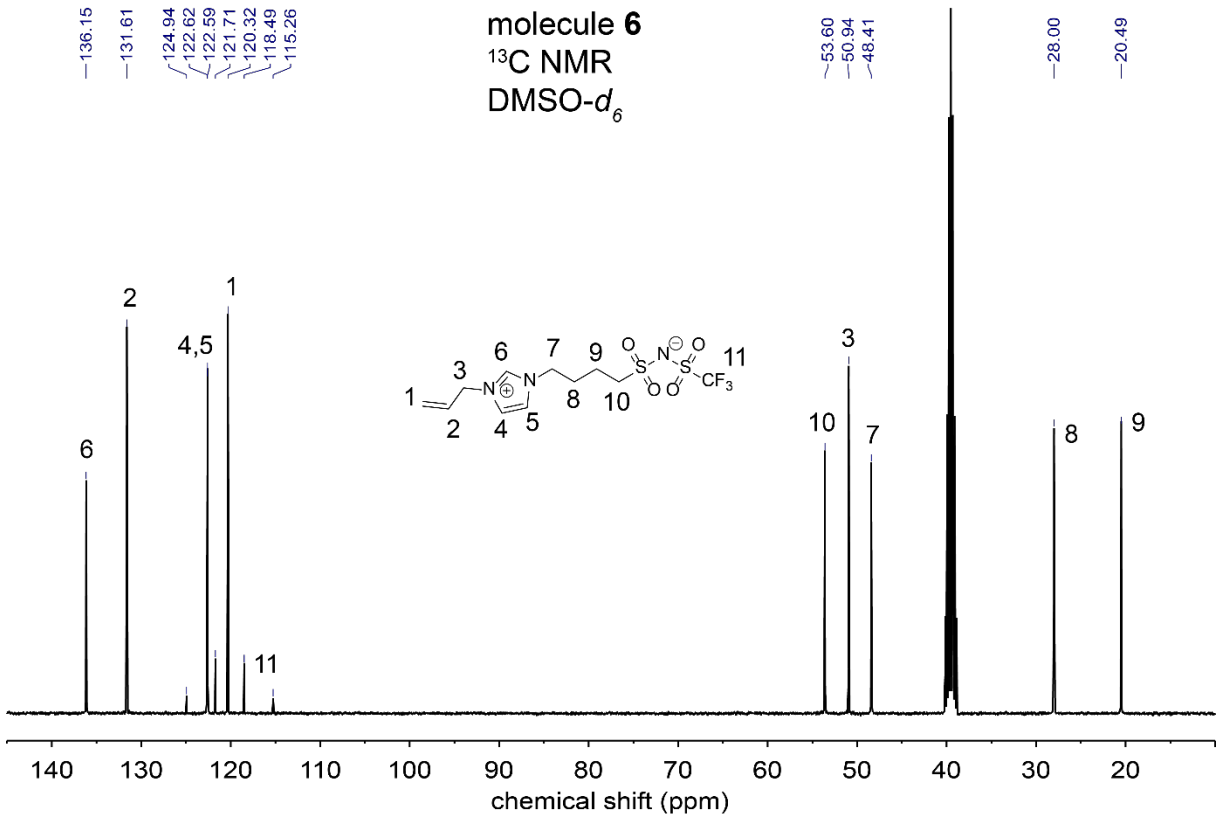
136.15
131.61
124.94
122.62
122.59
121.71
120.32
118.49
115.26
53.60
50.94
48.41
28.00
20.49
molecule **6**
^{13}C NMR
DMSO-d_6
6
2
4,5
1
11
10
3
7
8
9
chemical shift (ppm)

molecule **6**
^{19}F NMR
DMSO-d_6

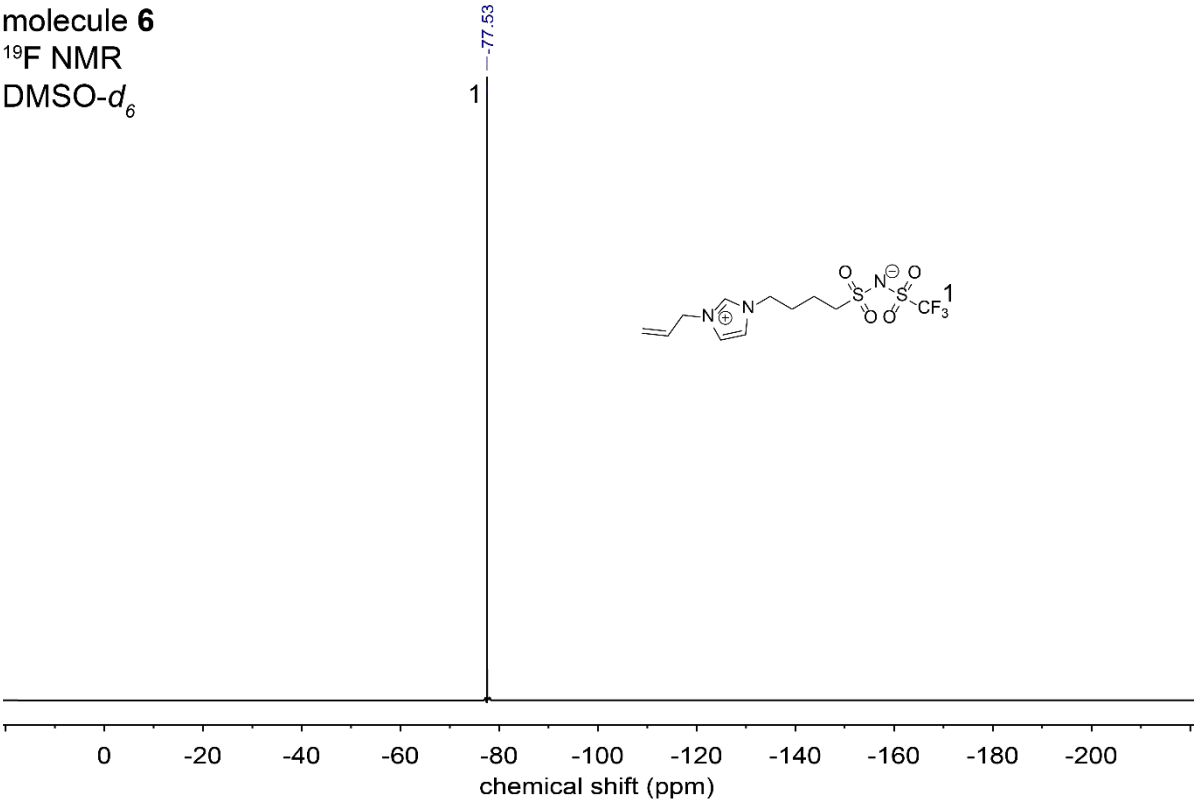

Molecule **7**

molecule **7**
^{1}H NMR
DMSO-d_6

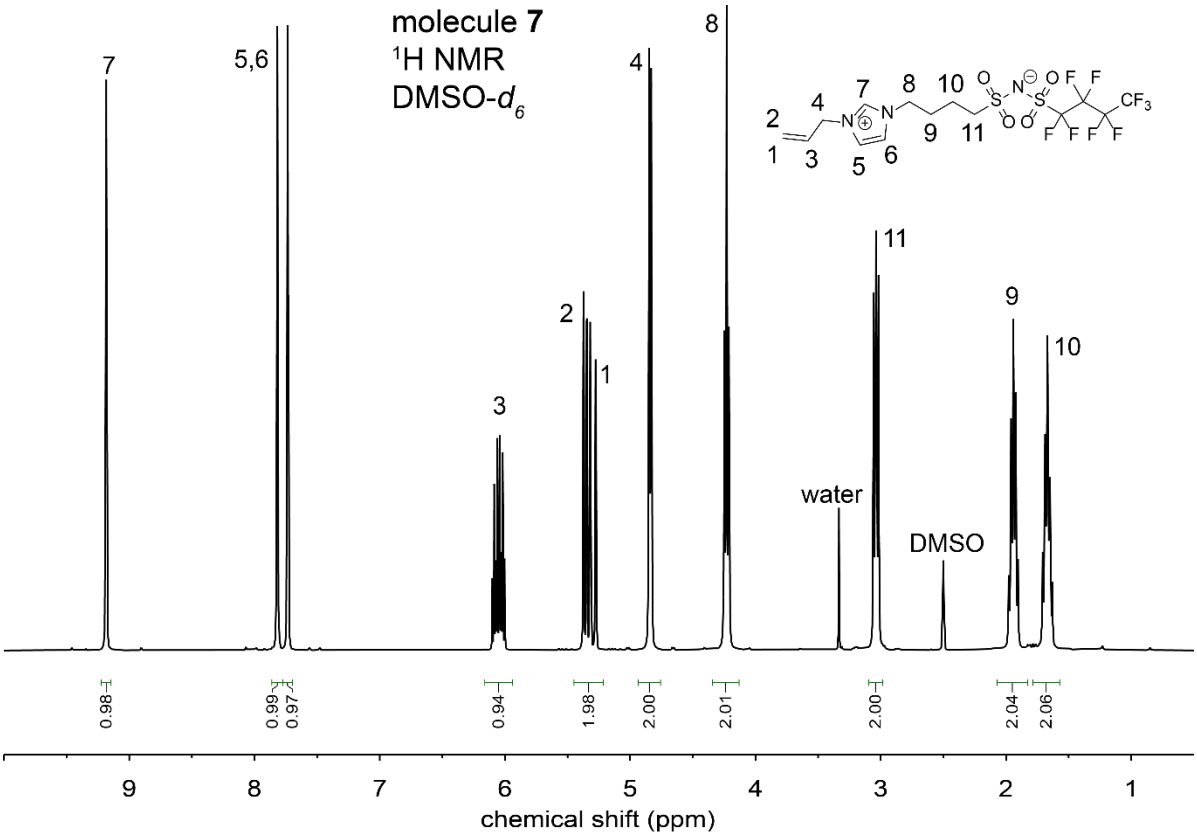

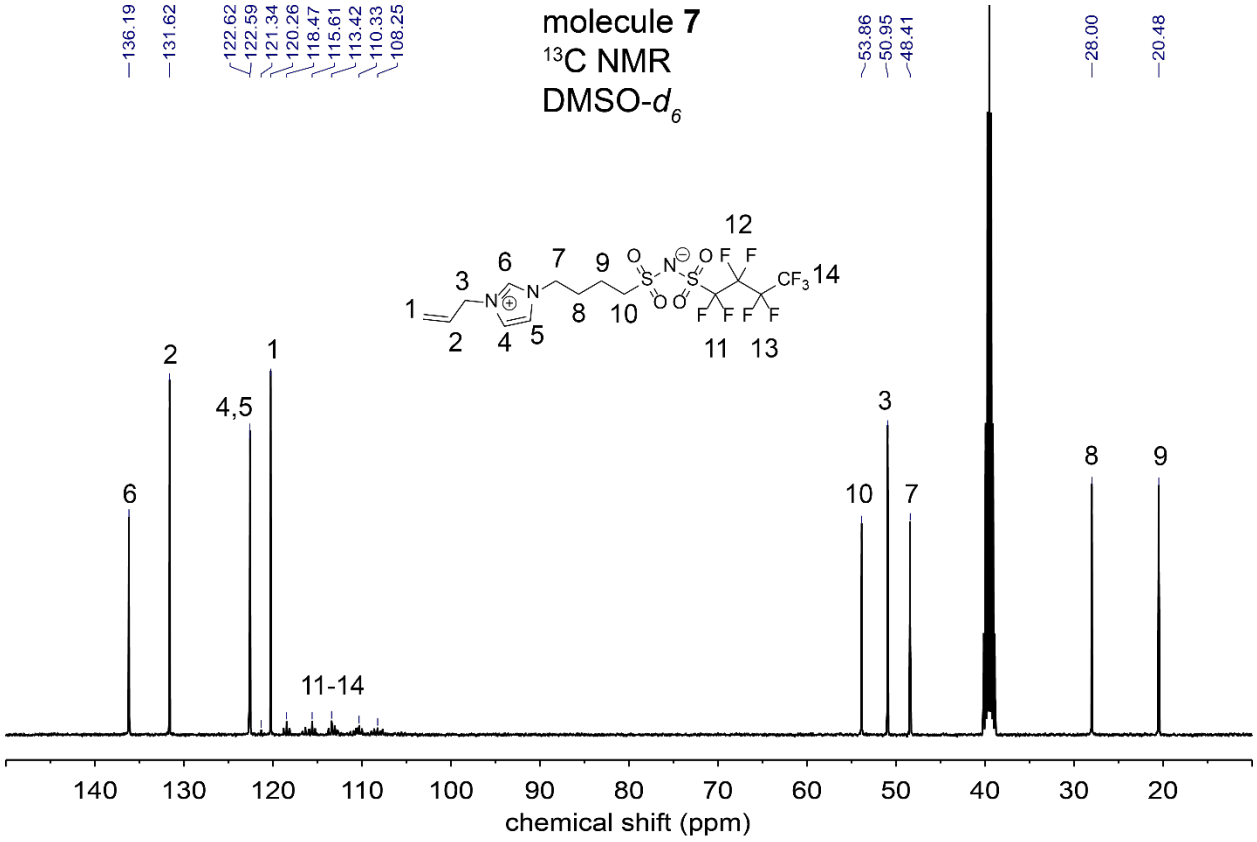
molecule 7
13C NMR
DMSO-d6
136.19
131.62
122.62
122.59
121.34
120.26
118.47
115.61
113.42
110.33
108.25
53.86
50.95
48.41
28.00
20.48
6
2
4,5
1
11-14
10
3
7
8
9
chemical shift (ppm)

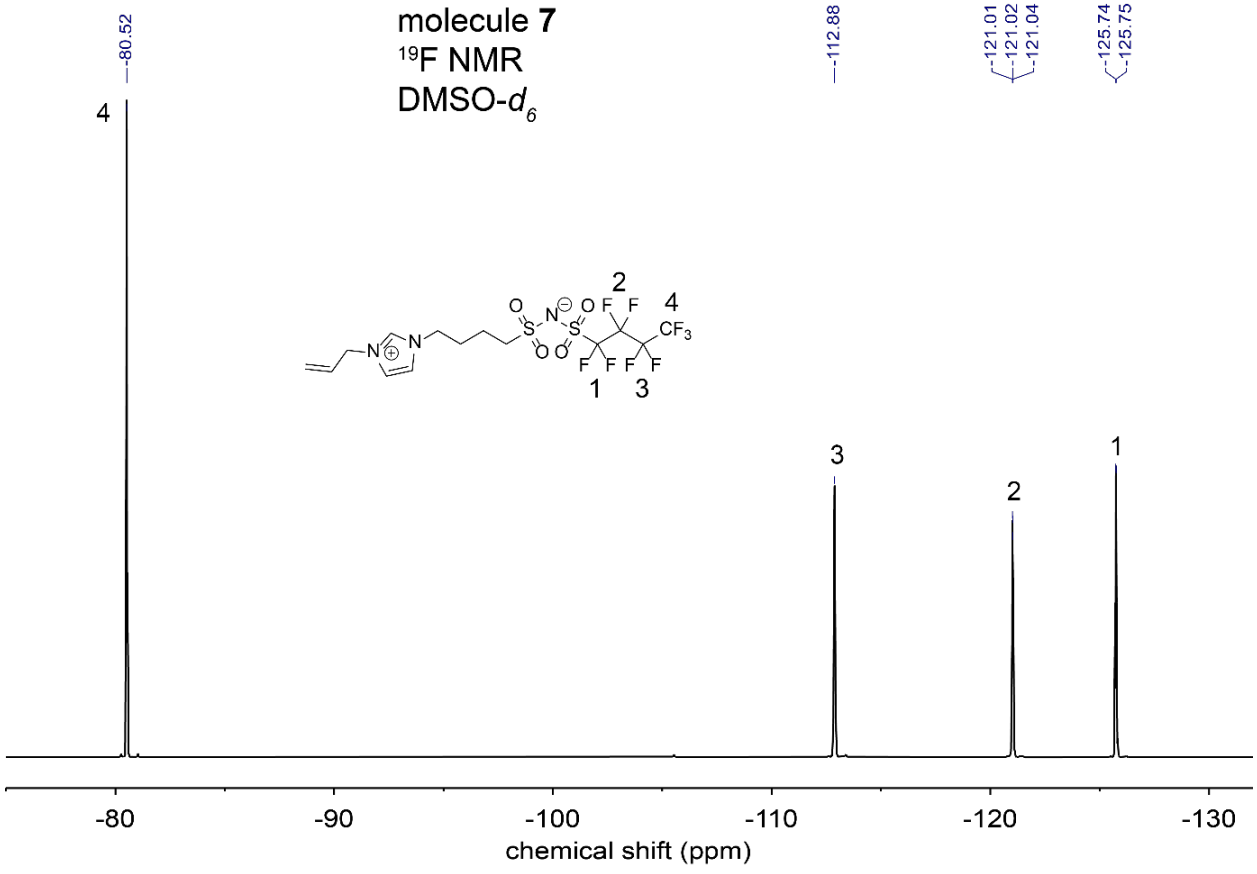
molecule 7
19F NMR
DMSO-d6
80.52
112.88
121.01
121.02
121.04
125.74
125.75
4
3
2
1
chemical shift (ppm)

Molecule **8**

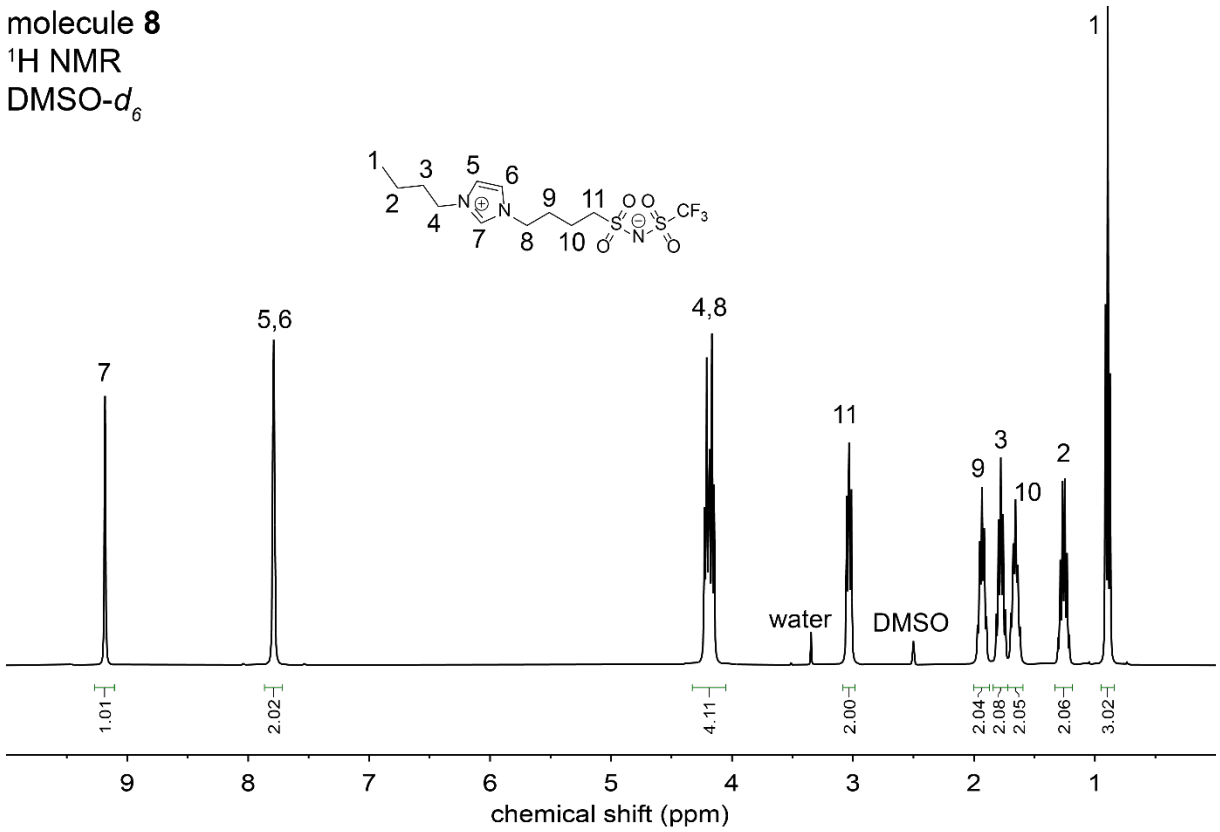
molecule **8**
^{1}H NMR
DMSO-d_6
1
2
3
4
5
6
7
8
9
10
11
CF3
7
5,6
4,8
11
9
3
10
2
1
water
DMSO
1.01
2.02
4.11
2.00
2.04
2.08
2.05
2.06
3.02
9
8
7
6
5
4
3
2
1
chemical shift (ppm)

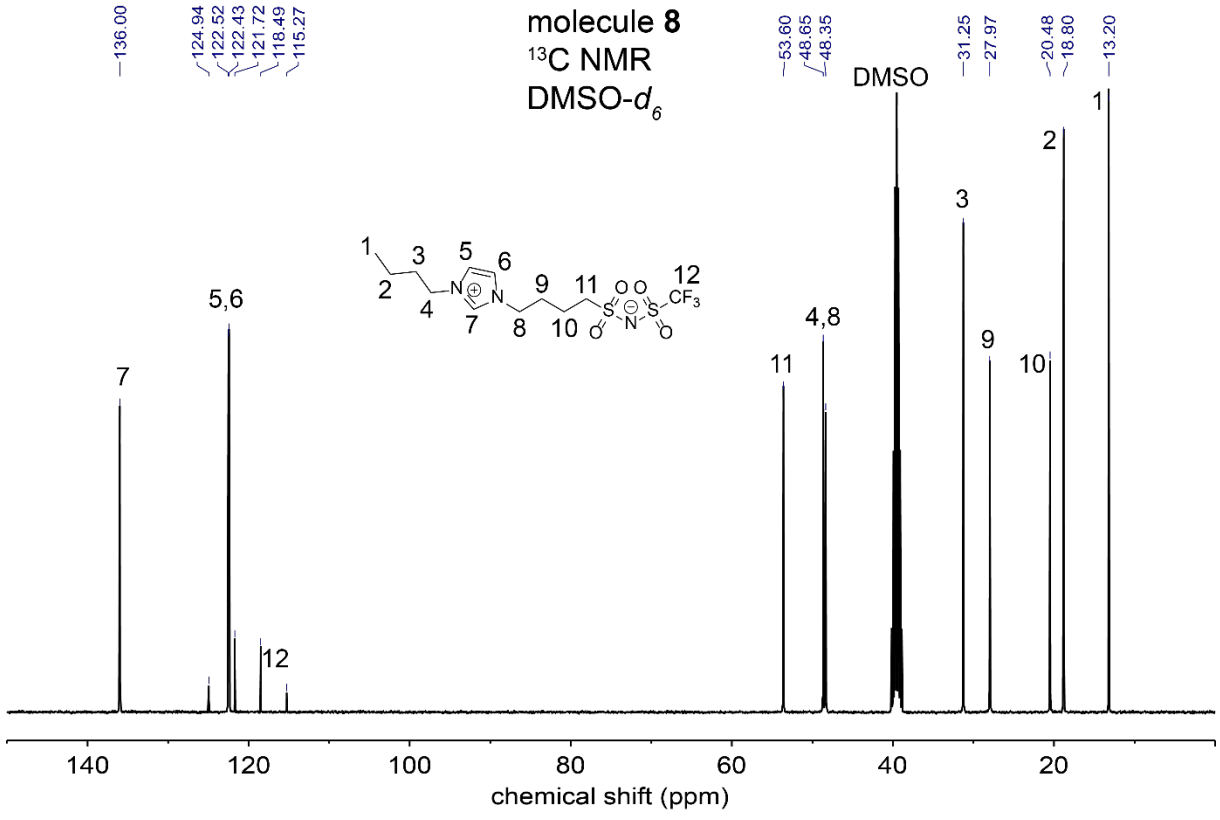
molecule **8**
^{13}C NMR
DMSO-d_6
136.00
124.94
122.52
122.43
121.72
118.49
115.27
53.60
48.65
48.35
31.25
27.97
20.48
18.80
13.20
DMSO
1
2
3
4
5
6
7
8
9
10
11
12
CF3
7
5,6
12
11
4,8
9
10
140
120
100
80
60
40
20
chemical shift (ppm)

molecule **8**
^{19}F NMR
DMSO-d_6

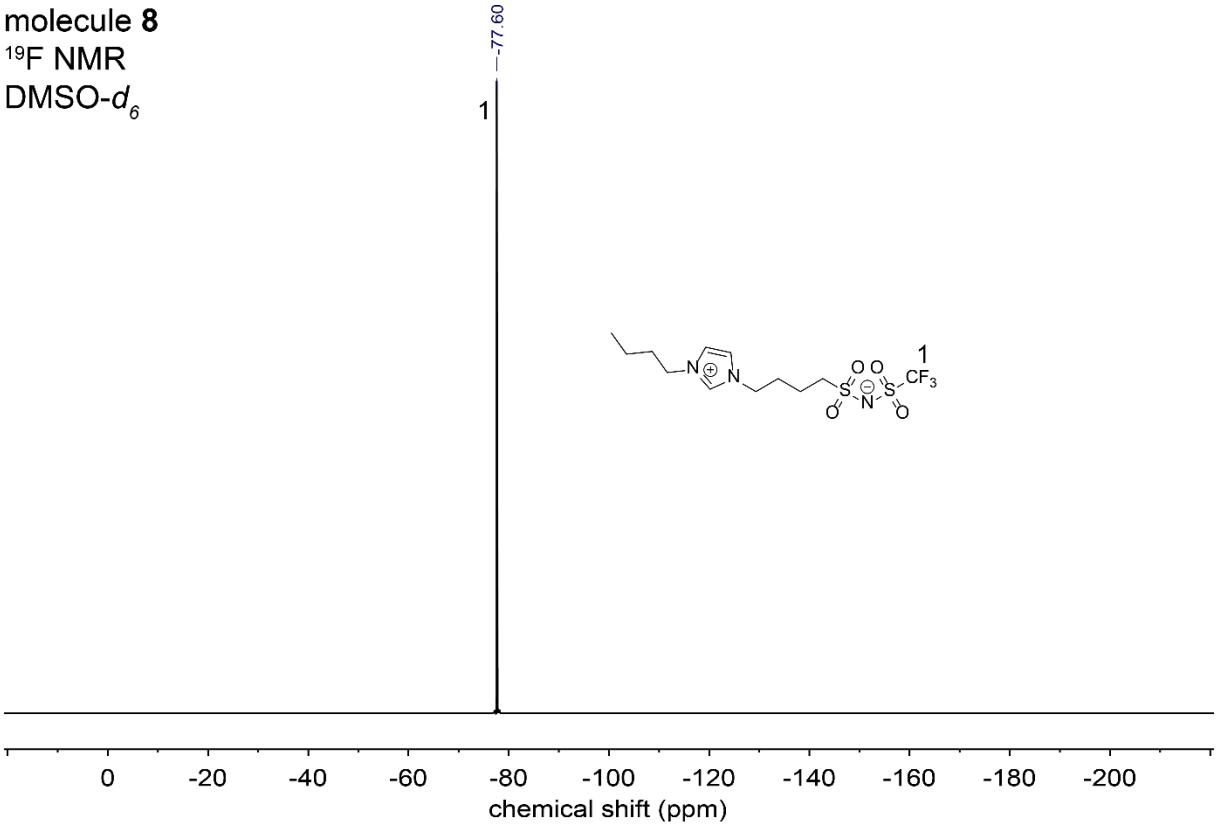

Molecule **9**

molecule **9**
^{1}H NMR
DMSO-d_6

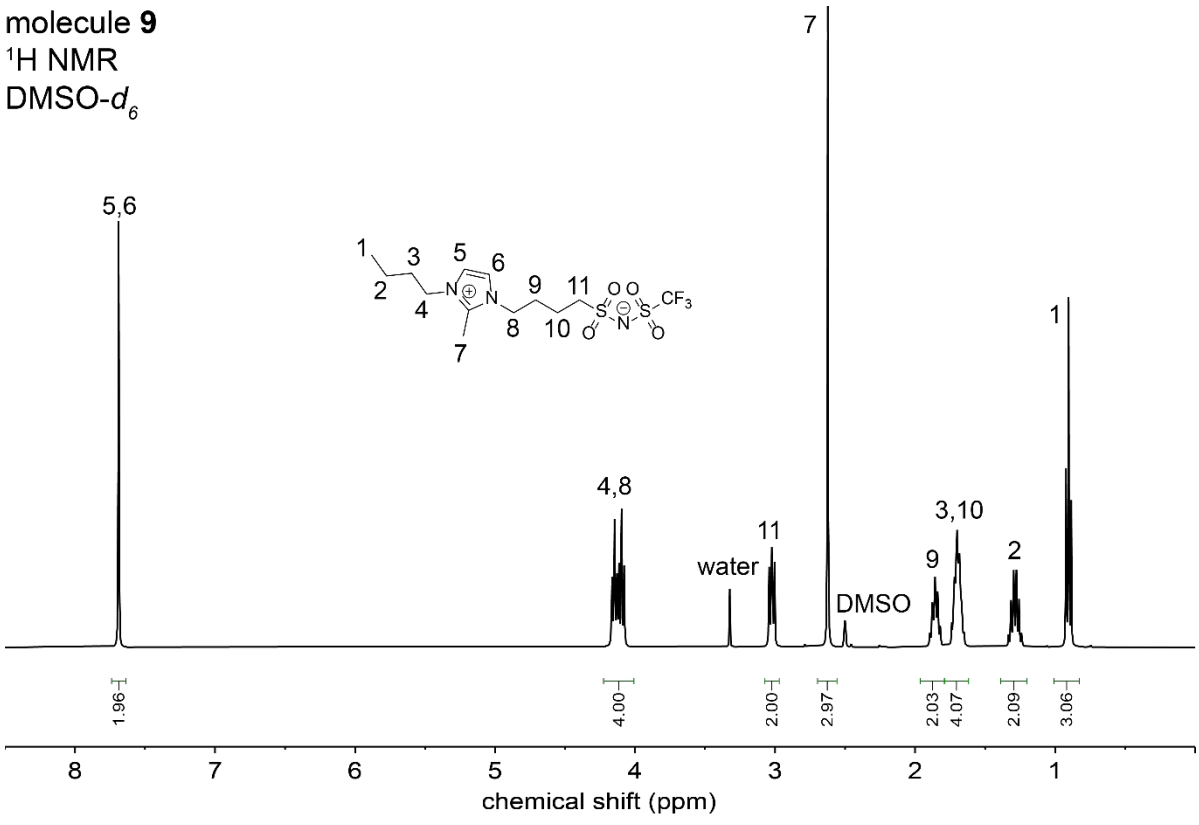

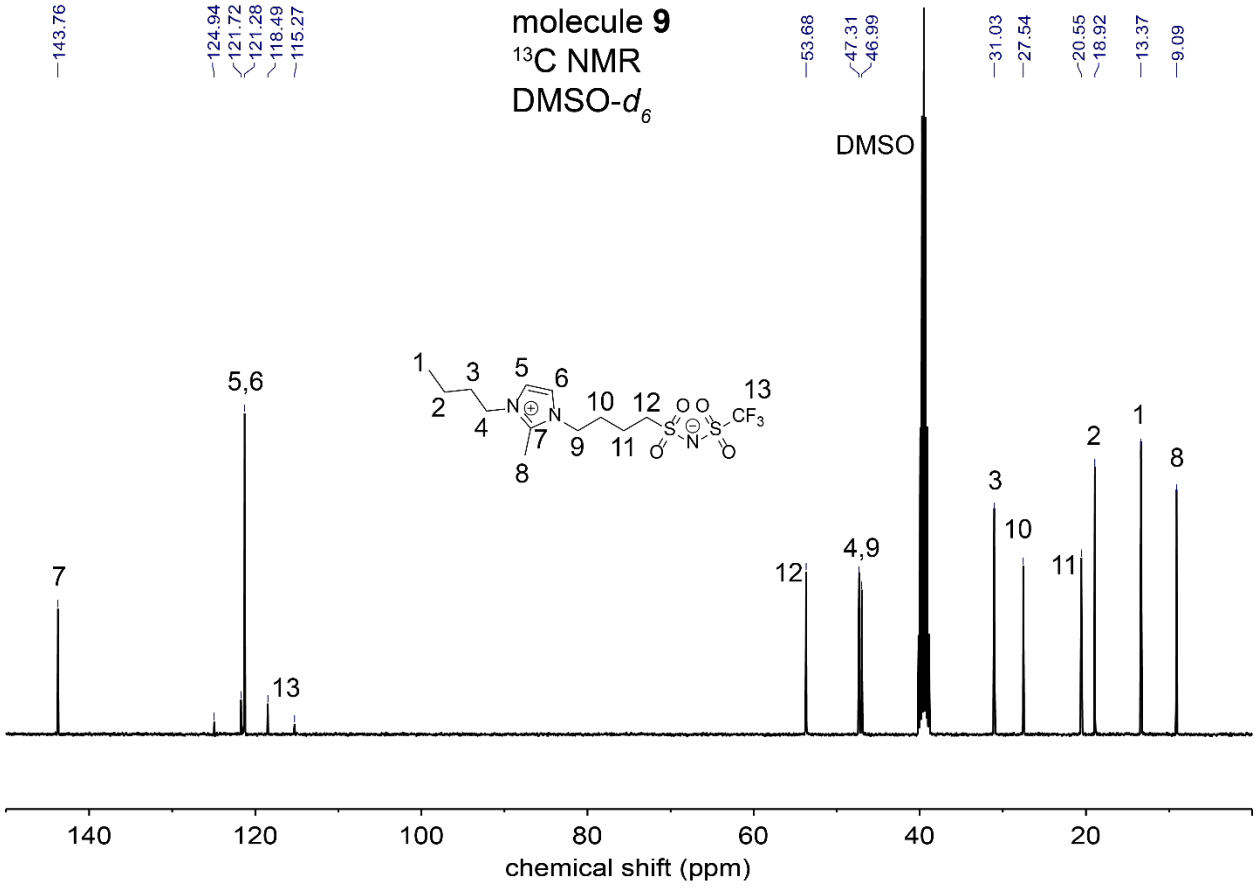
molecule **9**
^{13}C NMR
DMSO-d_6
143.76
124.94
121.72
121.28
118.49
115.27
53.68
47.31
46.99
31.03
27.54
20.55
18.92
13.37
9.09
DMSO
5,6
7
13
12
4,9
3
10
11
2
1
8
140
120
100
80
60
40
20
chemical shift (ppm)

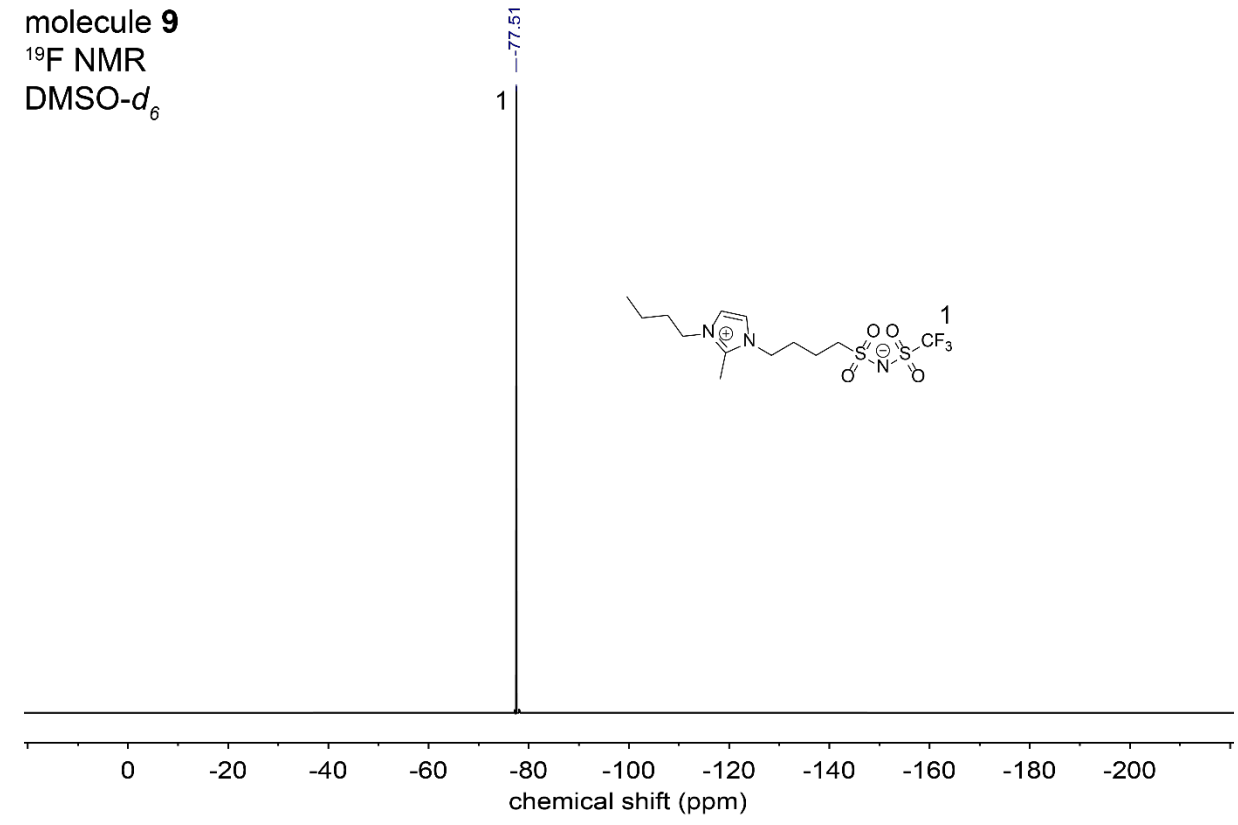
molecule **9**
^{19}F NMR
DMSO-d_6
-77.51
1
0
-20
-40
-60
-80
-100
-120
-140
-160
-180
-200
chemical shift (ppm)

Molecule **10**

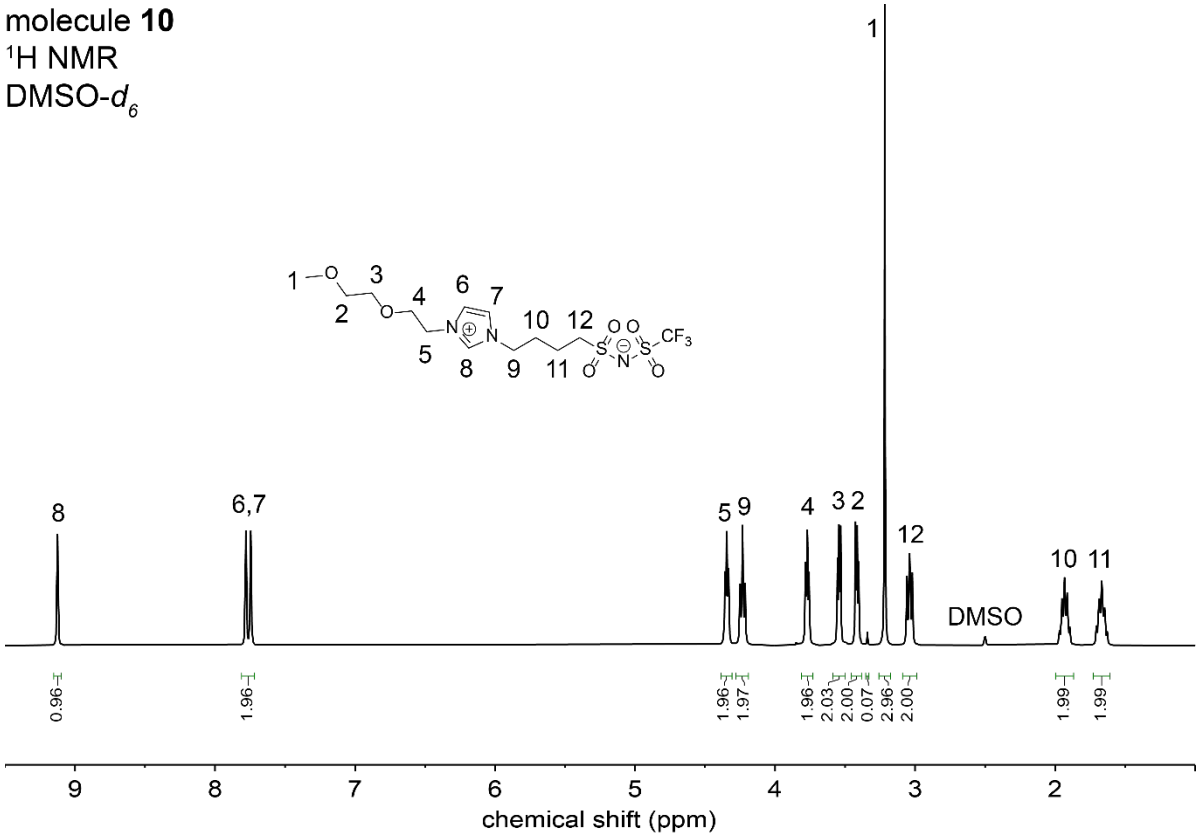
molecule **10**
^{1}H NMR
DMSO-d_6
1
8
6,7
5 9
4
3 2
12
10 11
DMSO
0.96
1.96
1.96
1.97
1.96
2.03
2.00
0.07
2.96
2.00
1.99
1.99
9
8
7
6
5
4
3
2
chemical shift (ppm)

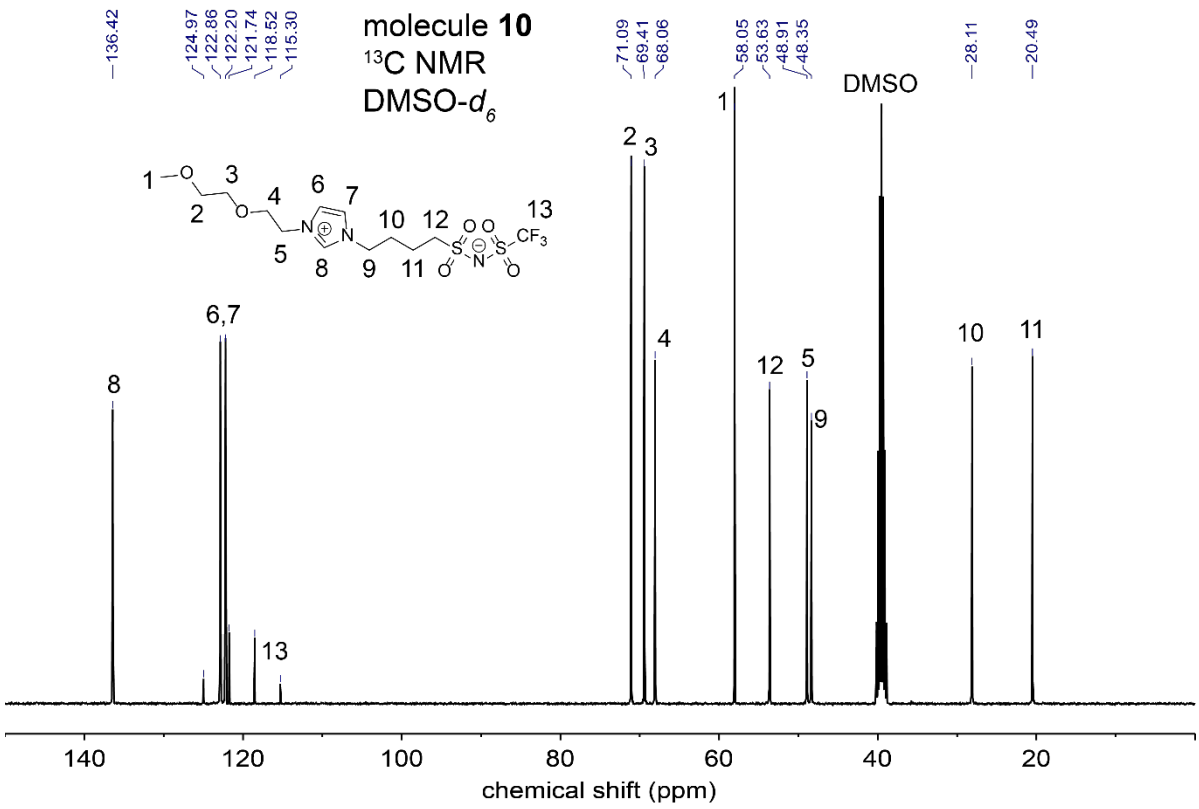
molecule **10**
^{13}C NMR
DMSO-d_6
136.42
124.97
122.86
122.20
121.74
118.52
115.30
71.09
69.41
68.06
58.05
53.63
48.91
48.35
28.11
20.49
DMSO
8
6,7
13
2
3
4
1
12
5
9
10
11
140
120
100
80
60
40
20
chemical shift (ppm)

molecule **10**
^{19}F NMR
DMSO-d_6

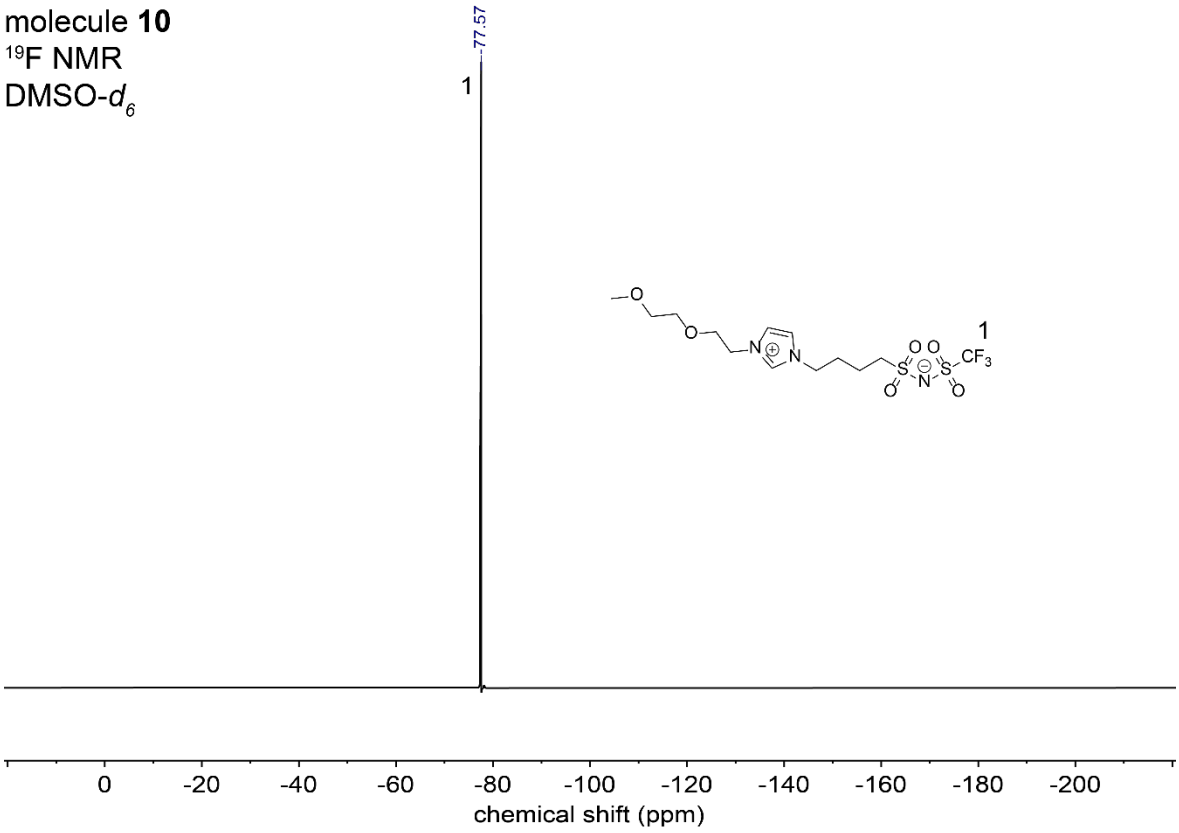

Molecule **11**

molecule **11**
^{1}H NMR
DMSO-d_6

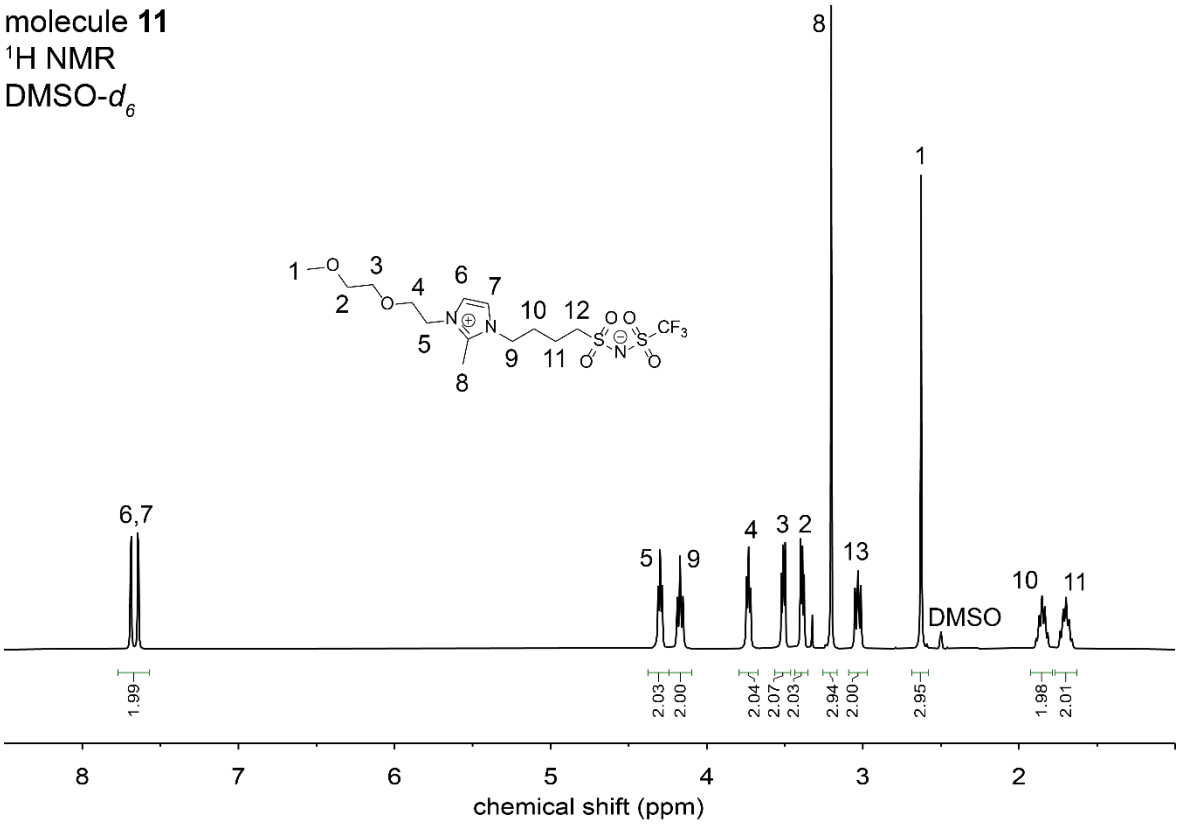

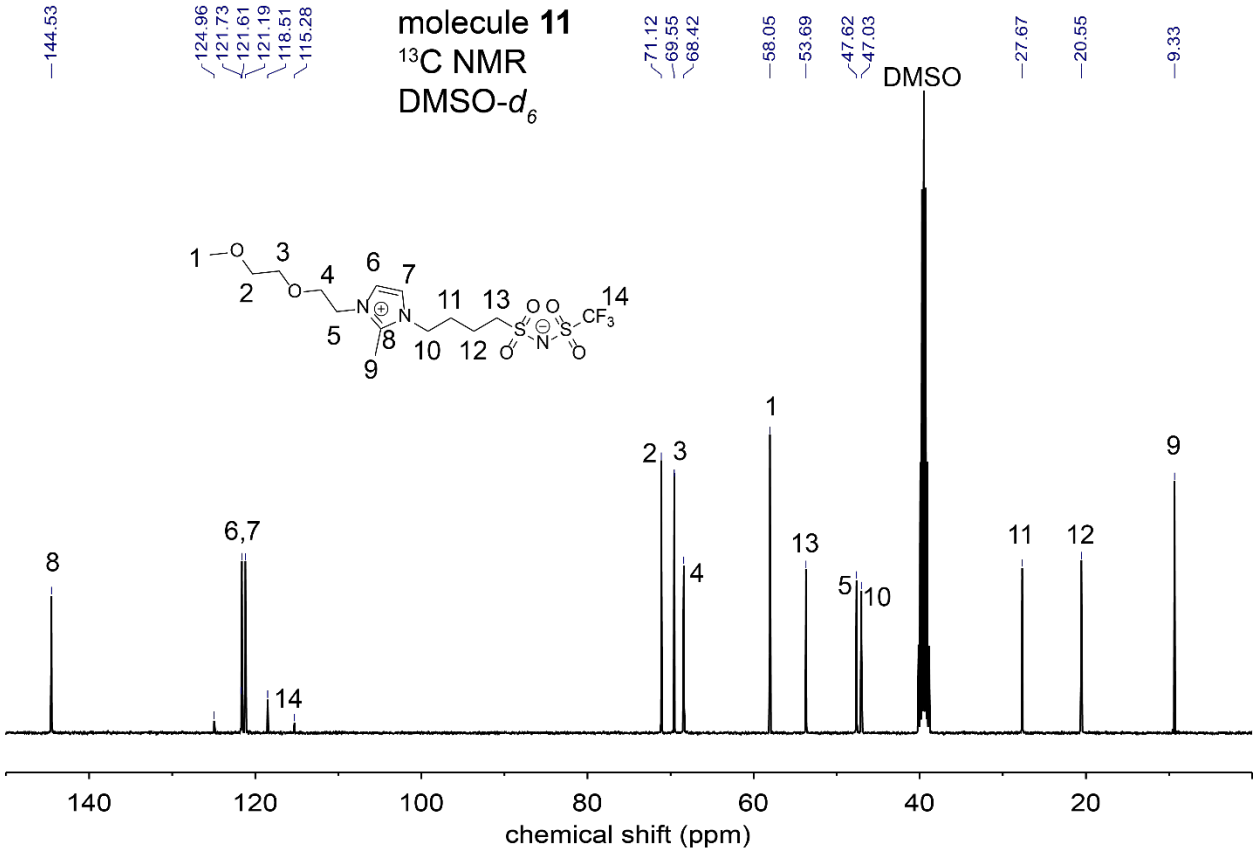
molecule **11**
^{13}C NMR
DMSO-d_6
144.53
124.96
121.73
121.61
121.19
118.51
115.28
71.12
69.55
68.42
58.05
53.69
47.62
47.03
DMSO
27.67
20.55
9.33
chemical shift (ppm)

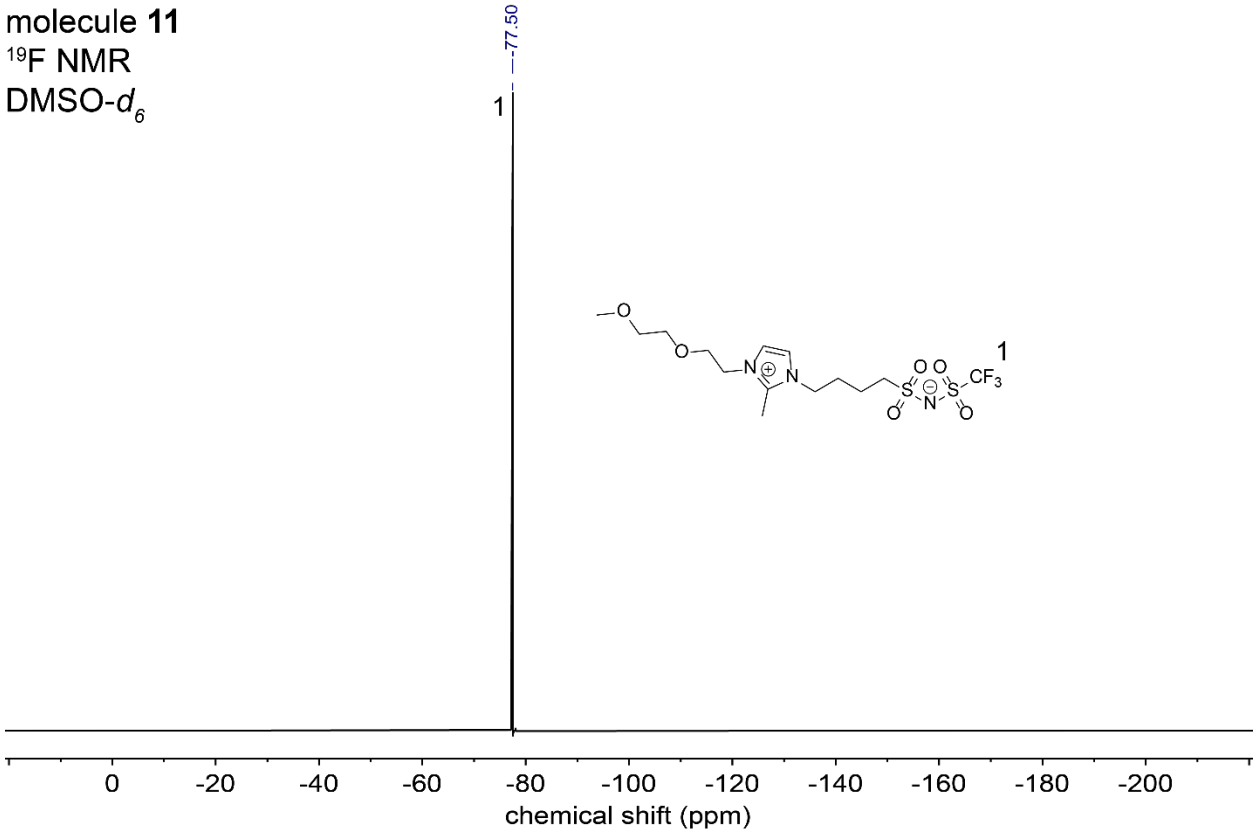
molecule **11**
^{19}F NMR
DMSO-d_6
-77.50
chemical shift (ppm)

Molecule **12**

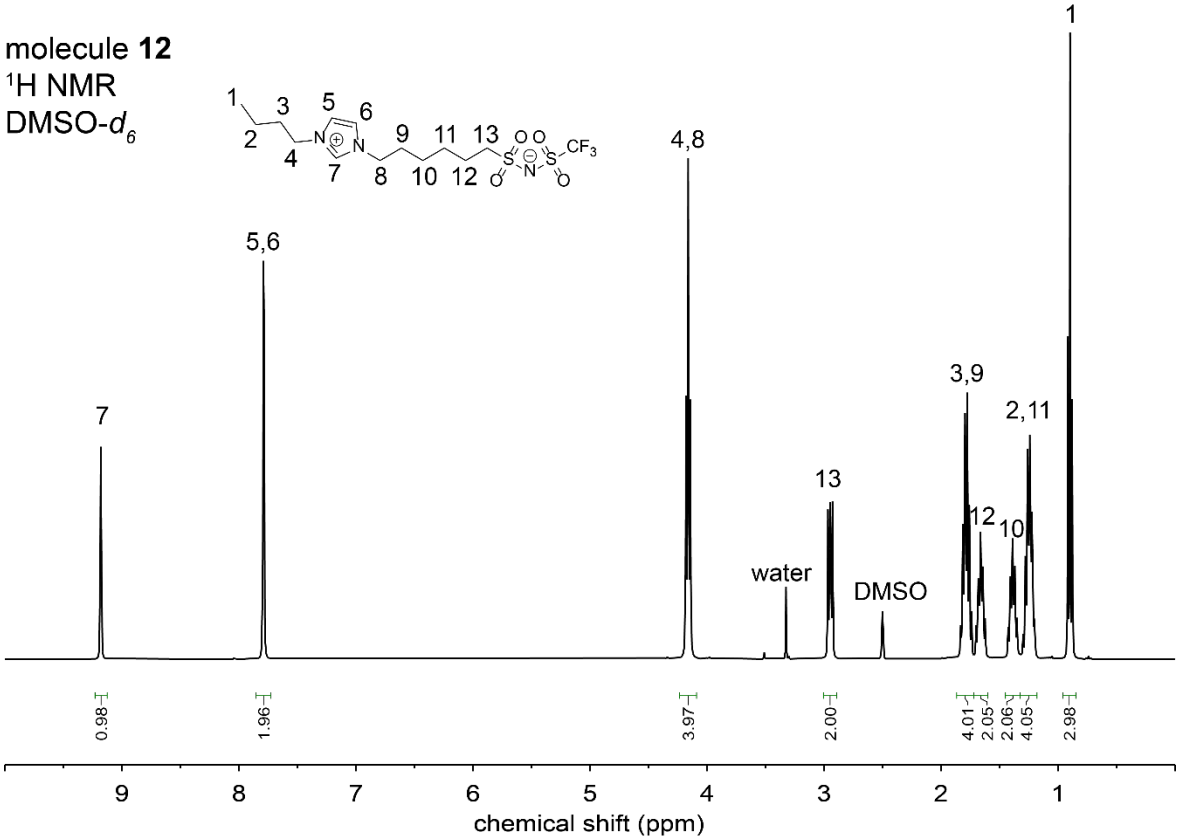
molecule **12**
^{1}H NMR
DMSO-d_6
1
2
3
4
5
6
7
8
9
10
11
12
13
4,8
5,6
7
3,9
2,11
13
12
10
water
DMSO
0.98
1.96
3.97
2.00
4.01
2.05
2.06
4.05
2.98
chemical shift (ppm)

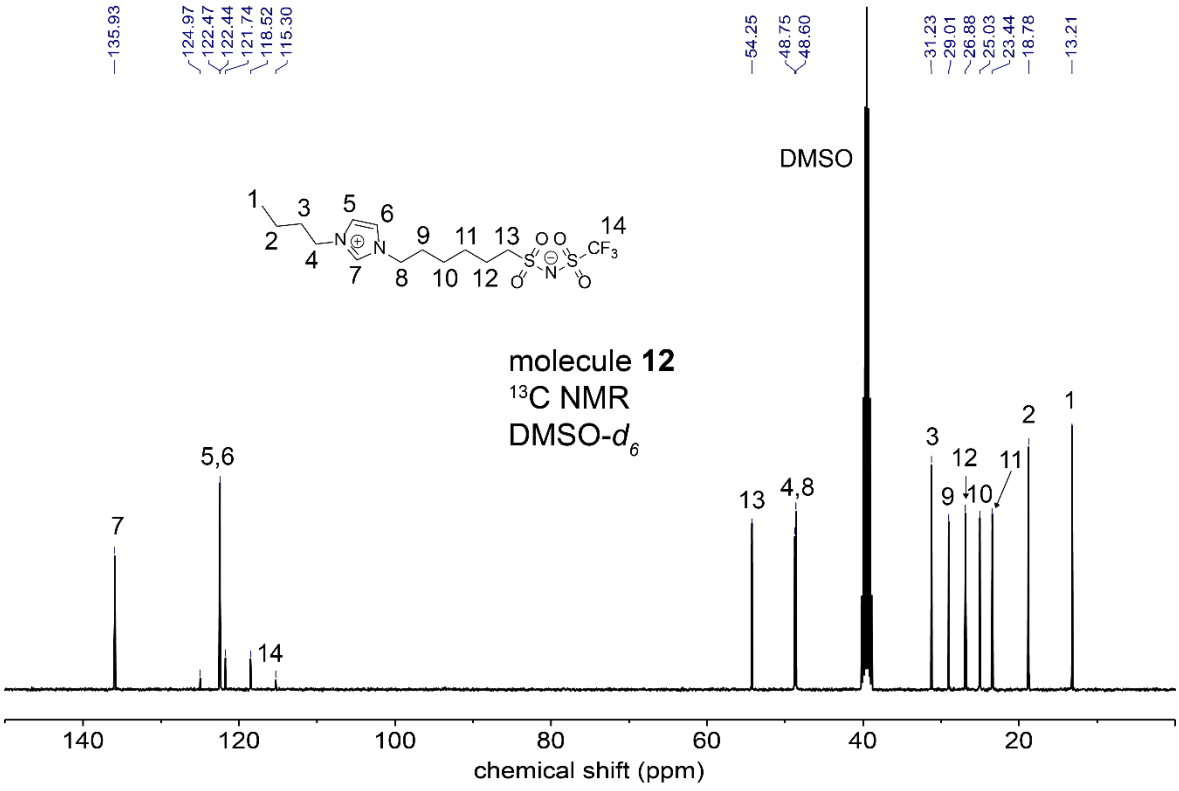
135.93
124.97
122.47
122.44
121.74
118.52
115.30
54.25
48.75
48.60
31.23
29.01
26.88
25.03
23.44
18.78
13.21
DMSO
molecule **12**
^{13}C NMR
DMSO-d_6
7
5,6
14
13
4,8
3
9
12
10
11
2
1
chemical shift (ppm)

molecule **12**
^{19}F NMR
DMSO-d_6

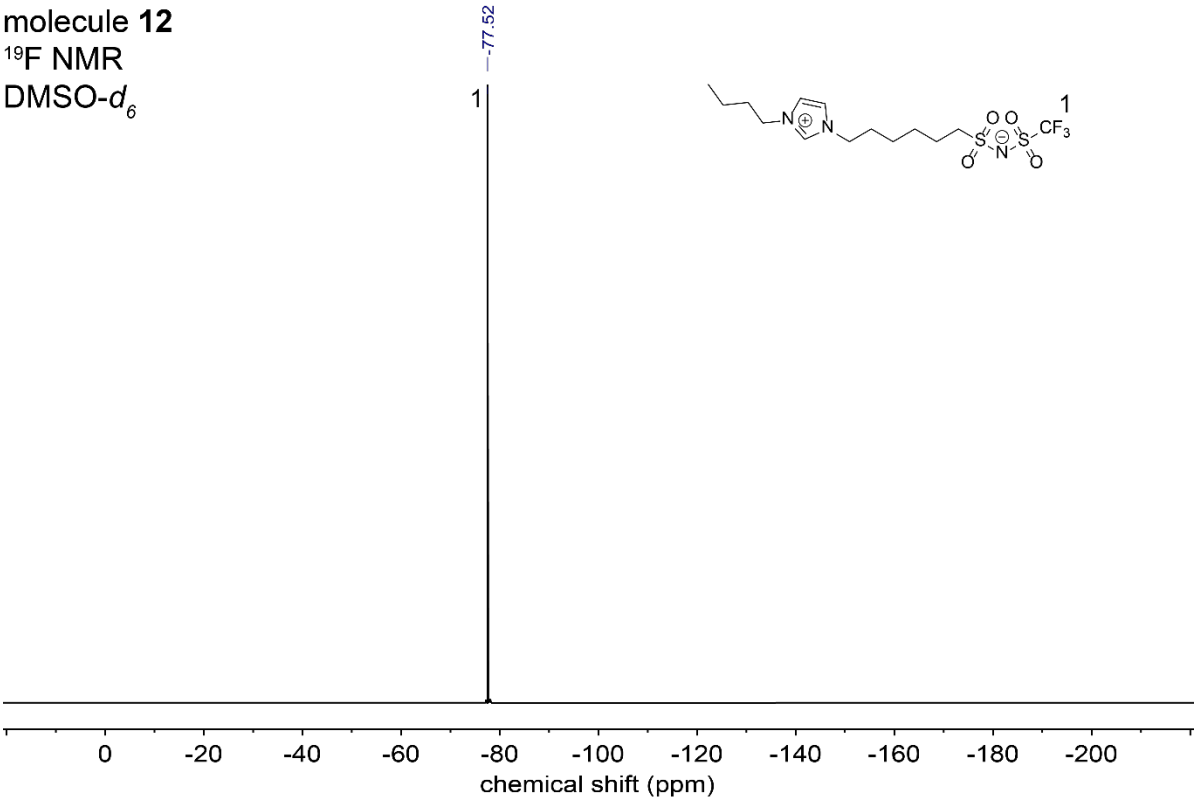

Molecule **13**

molecule **13**
^{1}H NMR
DMSO-d_6

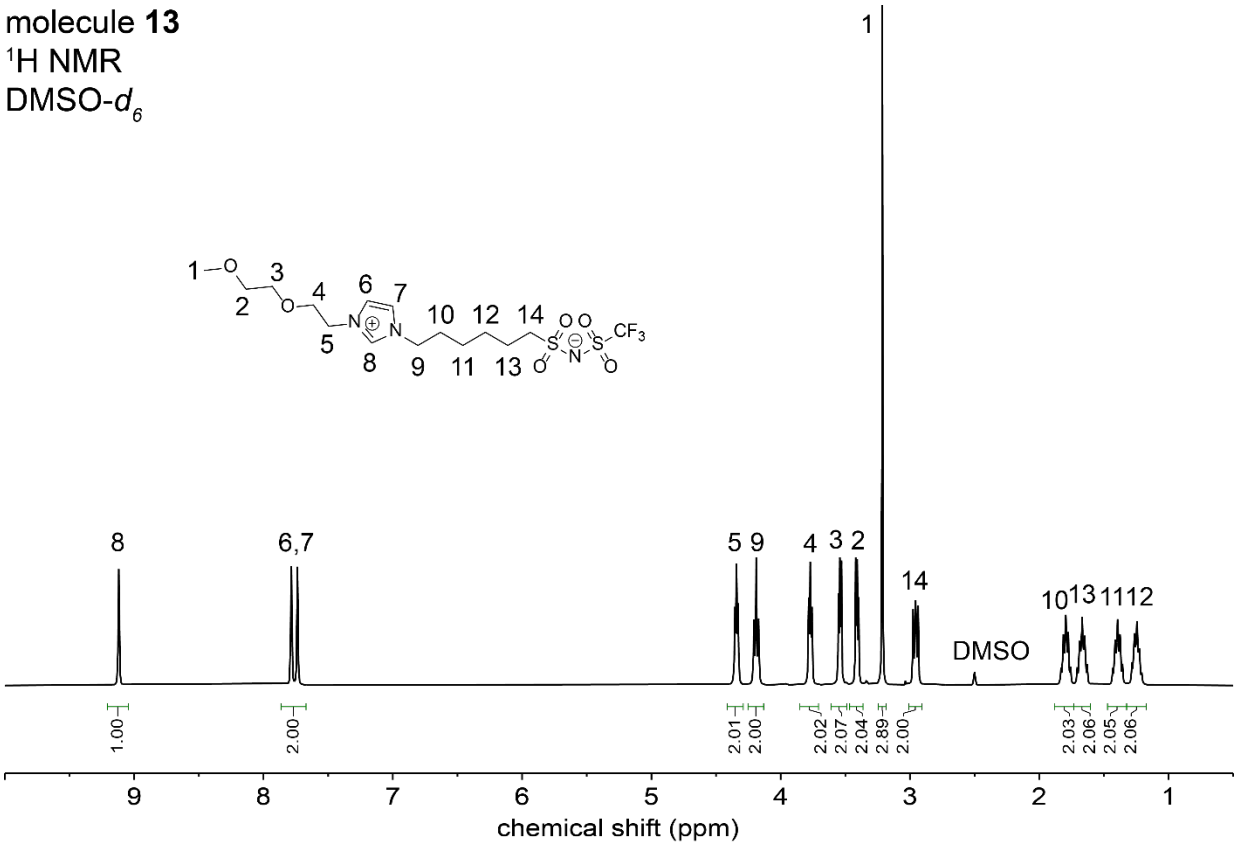

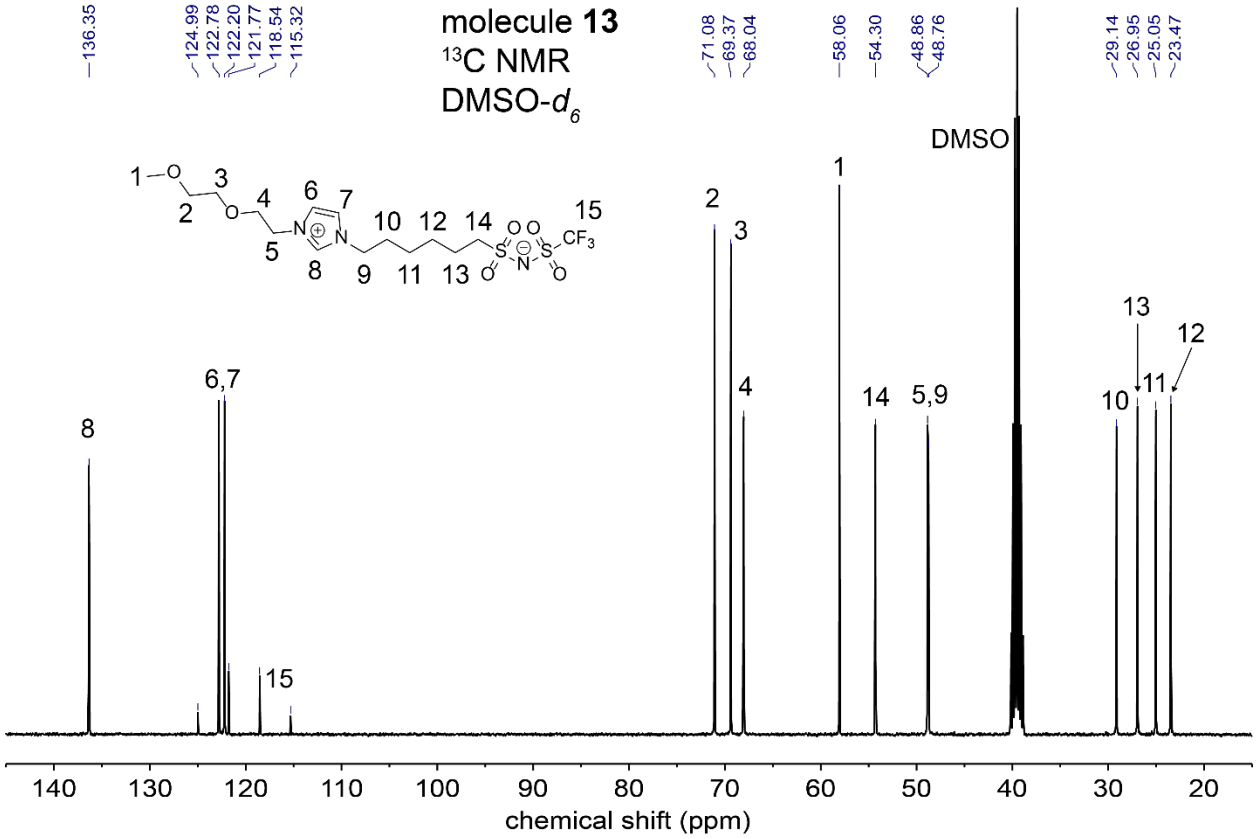
molecule **13**
^{13}C NMR
DMSO-d_6
136.35
124.99
122.78
122.20
121.77
118.54
115.32
71.08
69.37
68.04
58.06
54.30
48.86
48.76
29.14
26.95
25.05
23.47
DMSO
chemical shift (ppm)

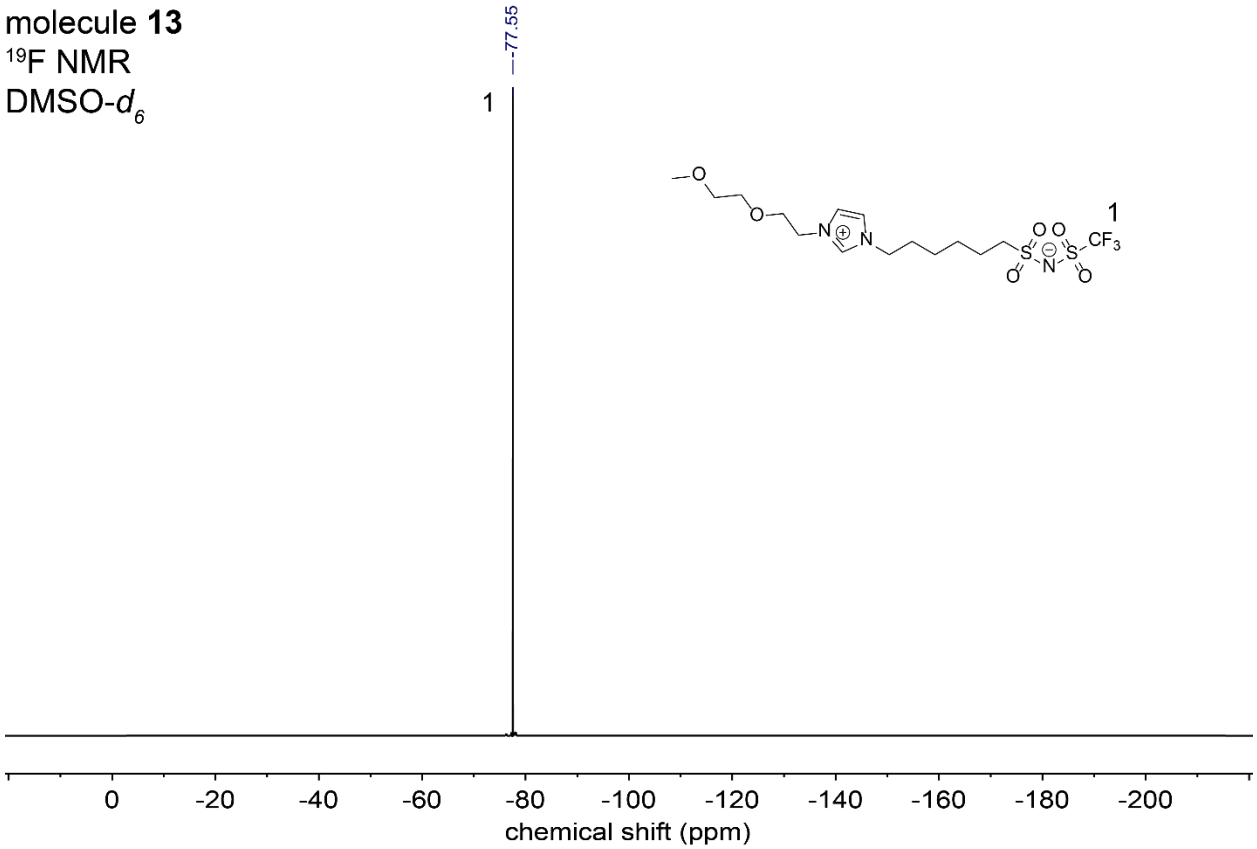
molecule **13**
^{19}F NMR
DMSO-d_6
-77.55
chemical shift (ppm)

Molecule **14**

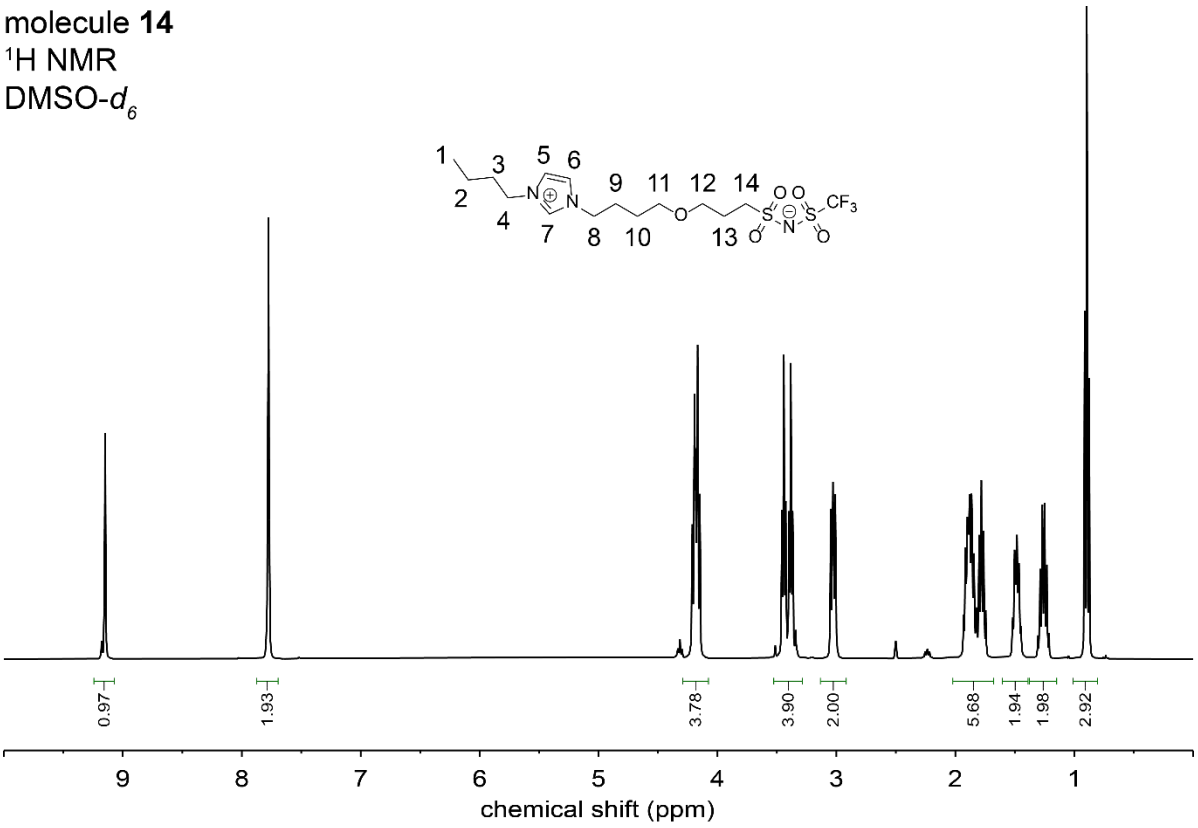
molecule **14**
^{1}H NMR
DMSO-d_6
0.97
1.93
3.78
3.90
2.00
5.68
1.94
1.98
2.92
chemical shift (ppm)

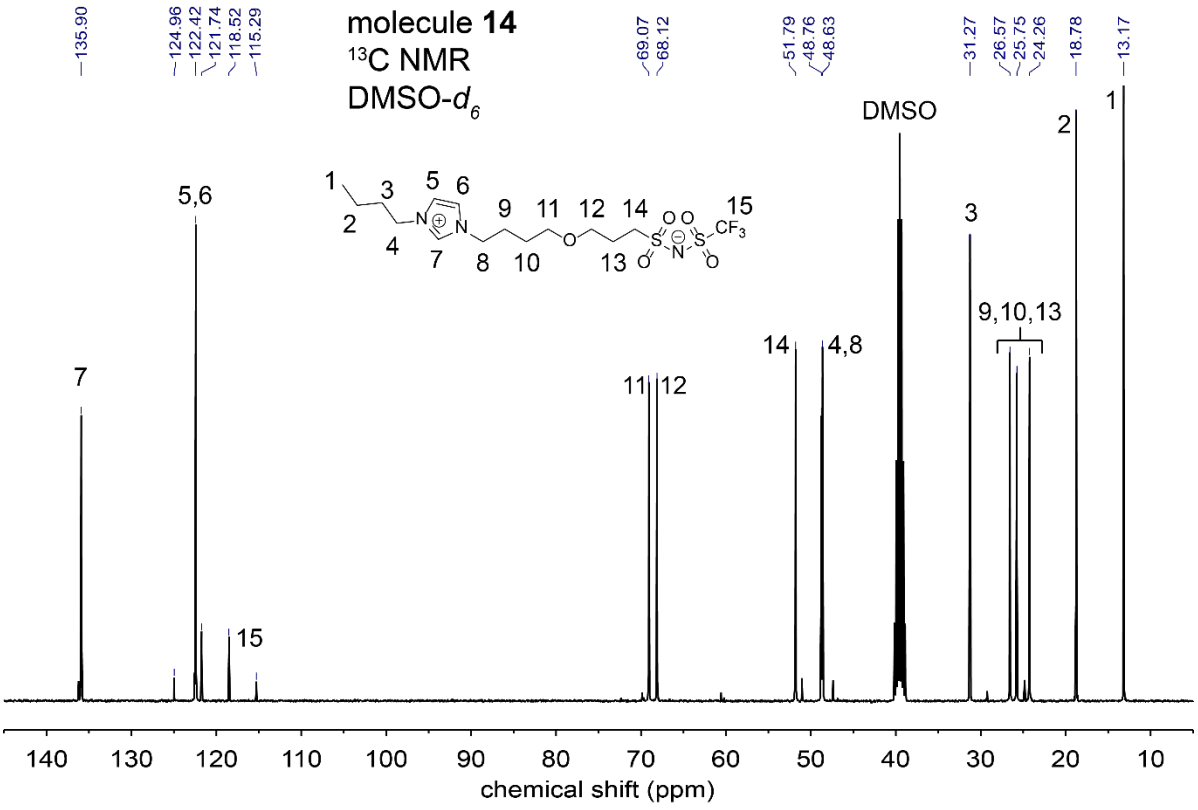
molecule **14**
^{13}C NMR
DMSO-d_6
135.90
124.96
122.42
121.74
118.52
115.29
69.07
68.12
51.79
48.76
48.63
31.27
26.57
25.75
24.26
18.78
13.17
DMSO
chemical shift (ppm)

molecule **14**
^{19}F NMR
DMSO-d_6

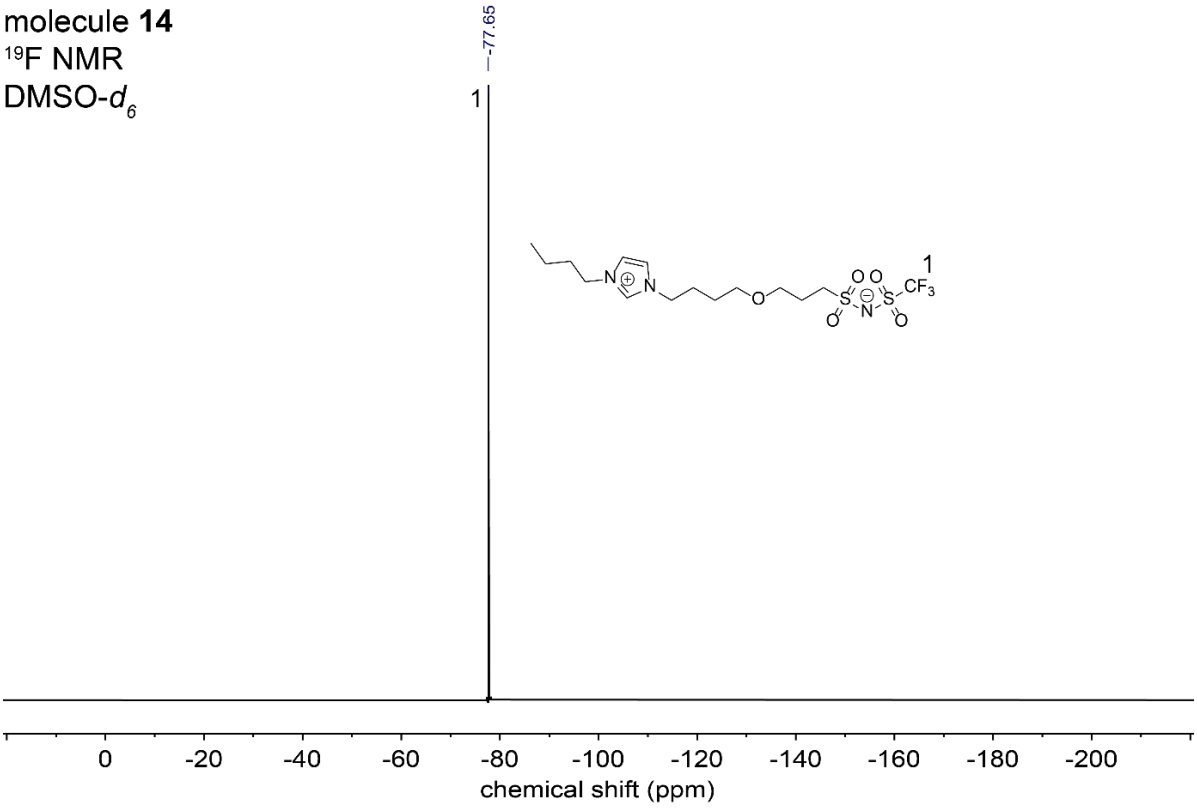

Molecule **15**

molecule **15**
^{1}H NMR
DMSO-d_6

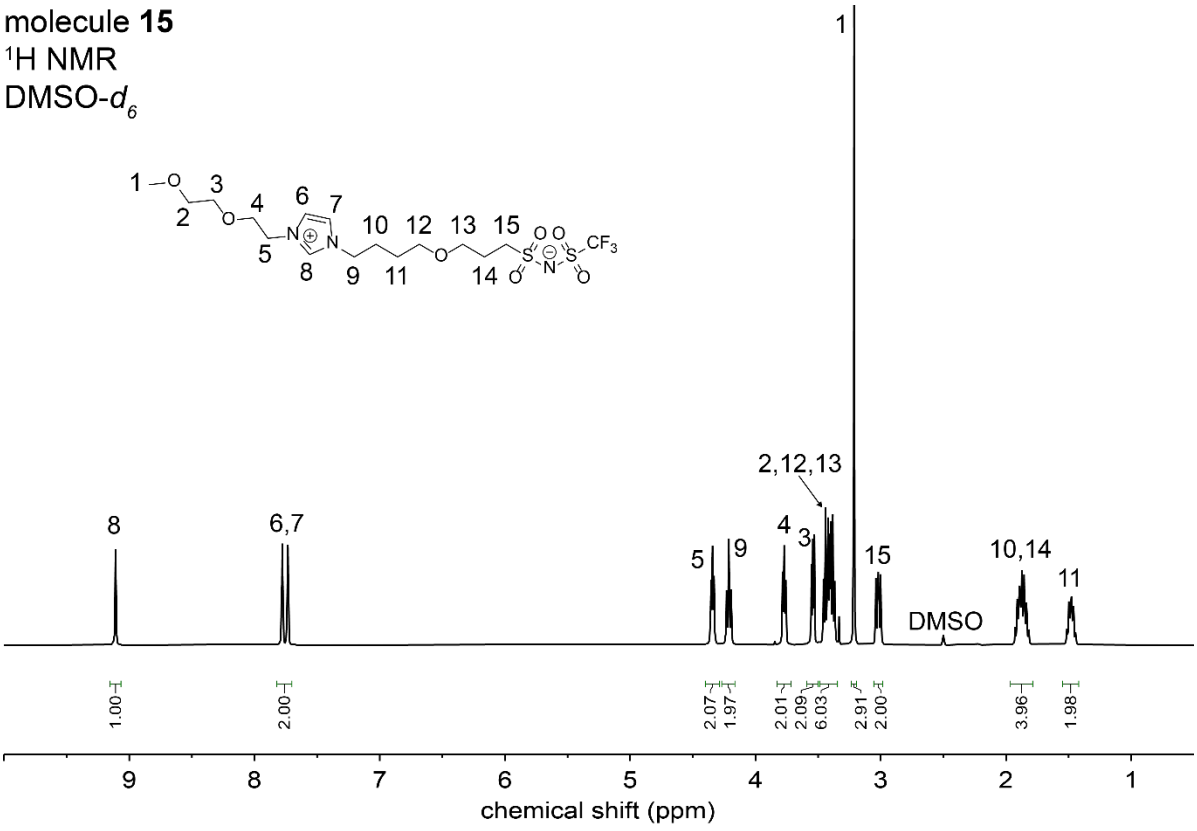

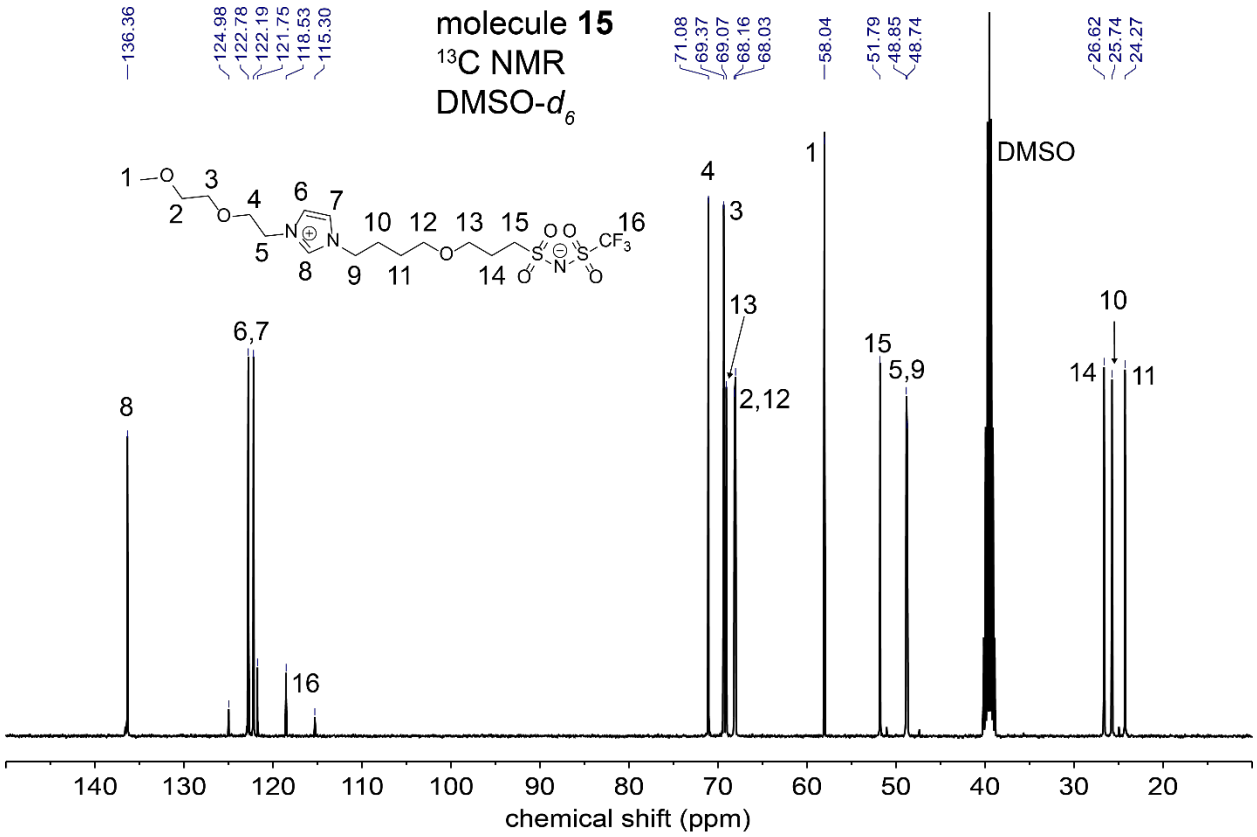
molecule **15**
^{13}C NMR
DMSO-d_6
136.36
124.98
122.78
122.19
121.75
118.53
115.30
71.08
69.37
69.07
68.16
68.03
58.04
51.79
48.85
48.74
26.62
25.74
24.27
DMSO
8
6,7
16
4
3
13
2,12
1
15
5,9
10
14
11
chemical shift (ppm)

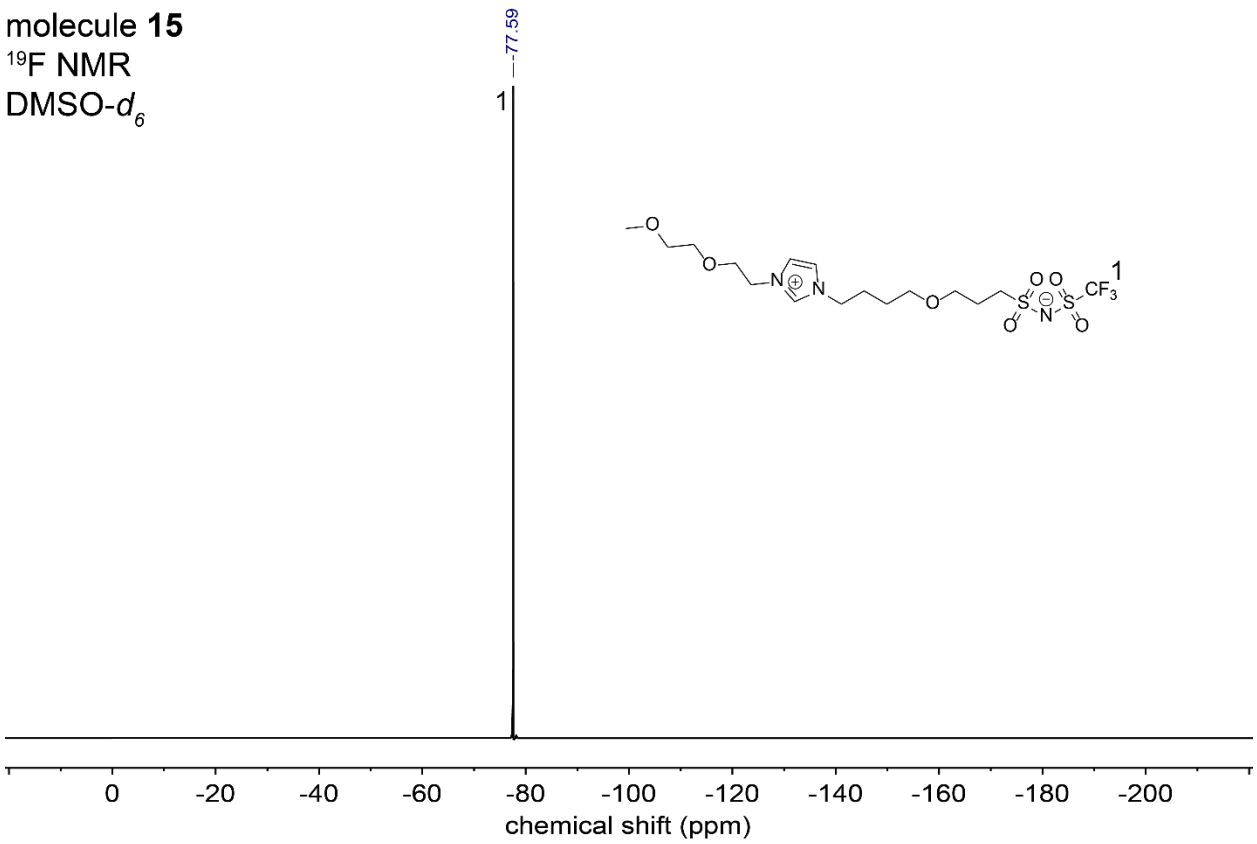
molecule **15**
^{19}F NMR
DMSO-d_6
77.59
1
chemical shift (ppm)

Molecule **16**

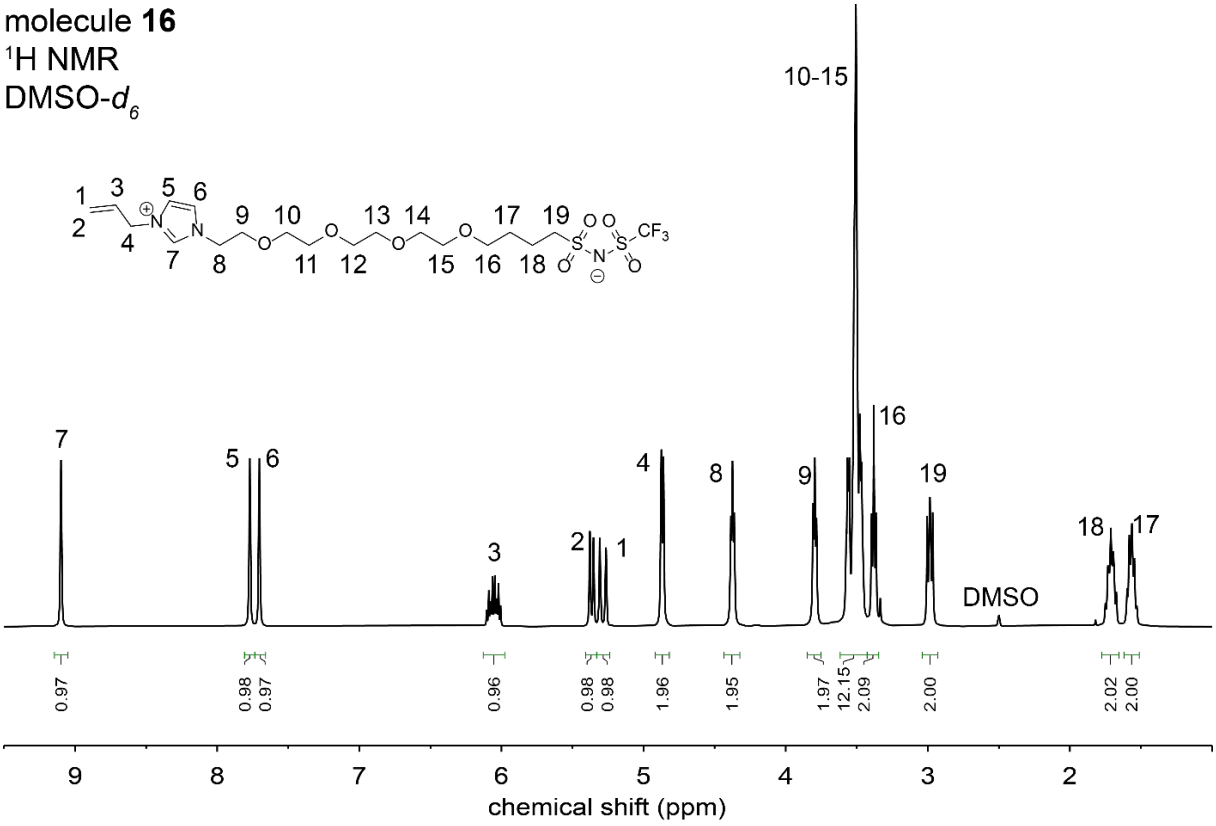
molecule **16**
^{1}H NMR
DMSO-d_6
10-15
16
7
5
6
4
8
9
19
18
17
3
2
1
DMSO
0.97
0.98
0.97
0.96
0.98
0.98
1.96
1.95
1.97
12.15
2.09
2.00
2.02
2.00
chemical shift (ppm)

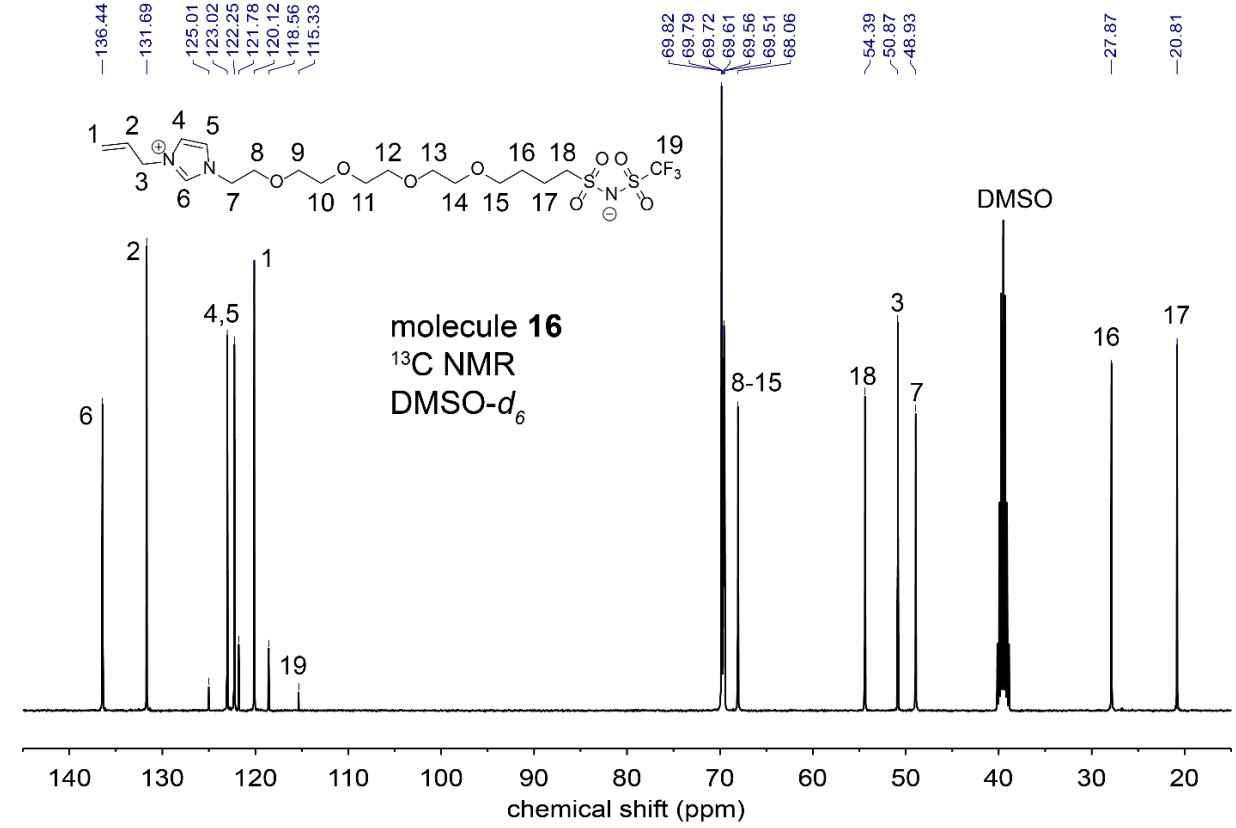
136.44
131.69
125.01
123.02
122.25
121.78
120.12
118.56
115.33
69.82
69.79
69.72
69.61
69.56
69.51
68.06
54.39
50.87
48.93
27.87
20.81
DMSO
molecule **16**
^{13}C NMR
DMSO-d_6
2
1
4,5
6
8-15
18
3
7
16
17
19
chemical shift (ppm)

molecule **16**
^{19}F NMR
DMSO-d_6

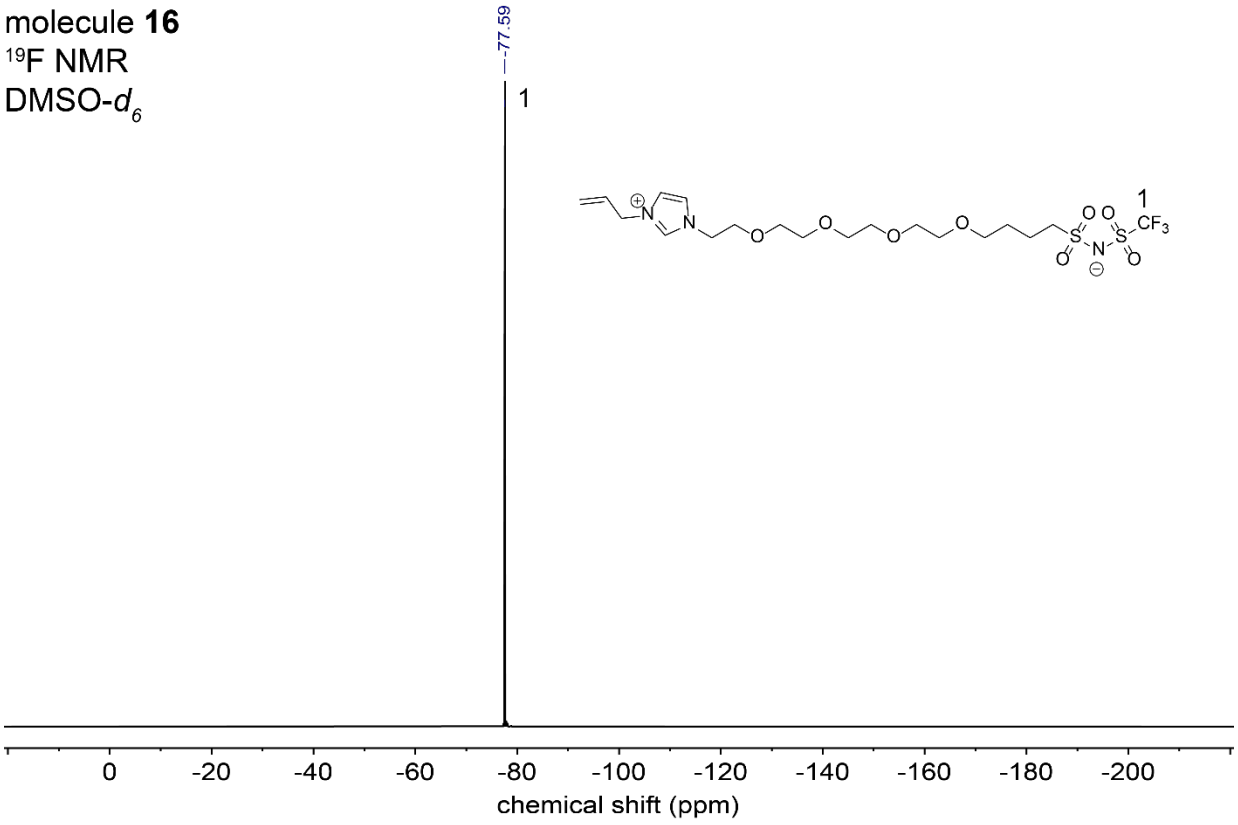

Molecule **17**

molecule **17**
^{1}H NMR
DMSO-d_6

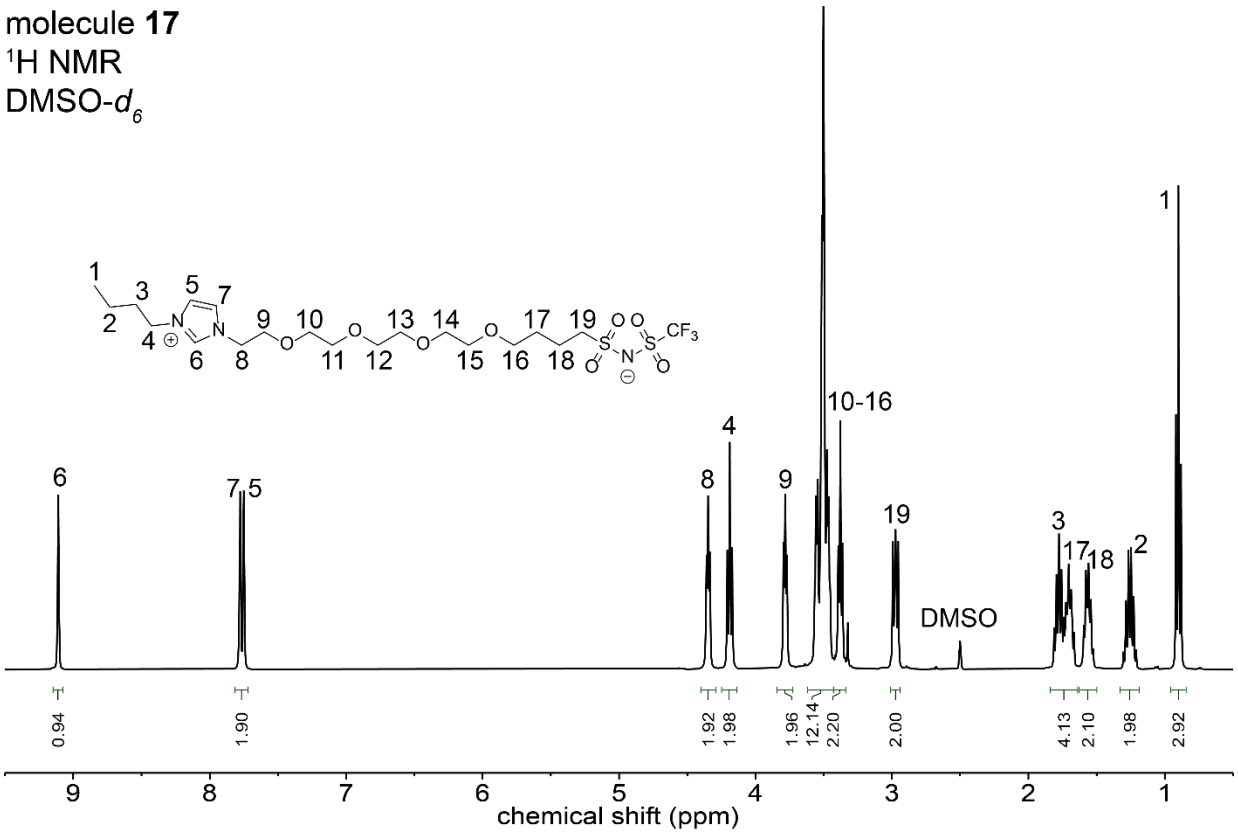

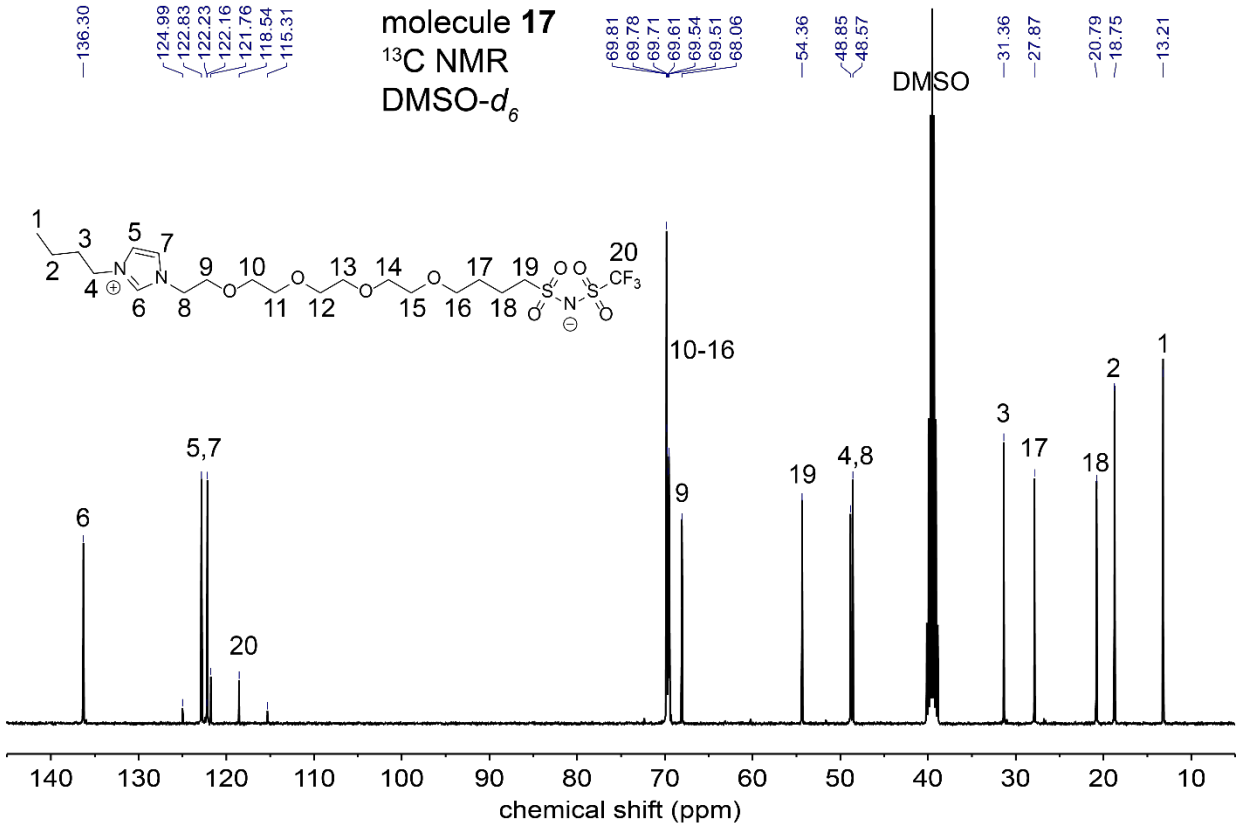
molecule **17**
^{13}C NMR
DMSO-d_6
136.30
124.99
122.83
122.23
122.16
121.76
118.54
115.31
69.81
69.78
69.71
69.61
69.54
69.51
68.06
54.36
48.85
48.57
DMSO
31.36
27.87
20.79
18.75
13.21
10-16
5,7
6
20
9
19
4,8
3
17
18
2
1
chemical shift (ppm)

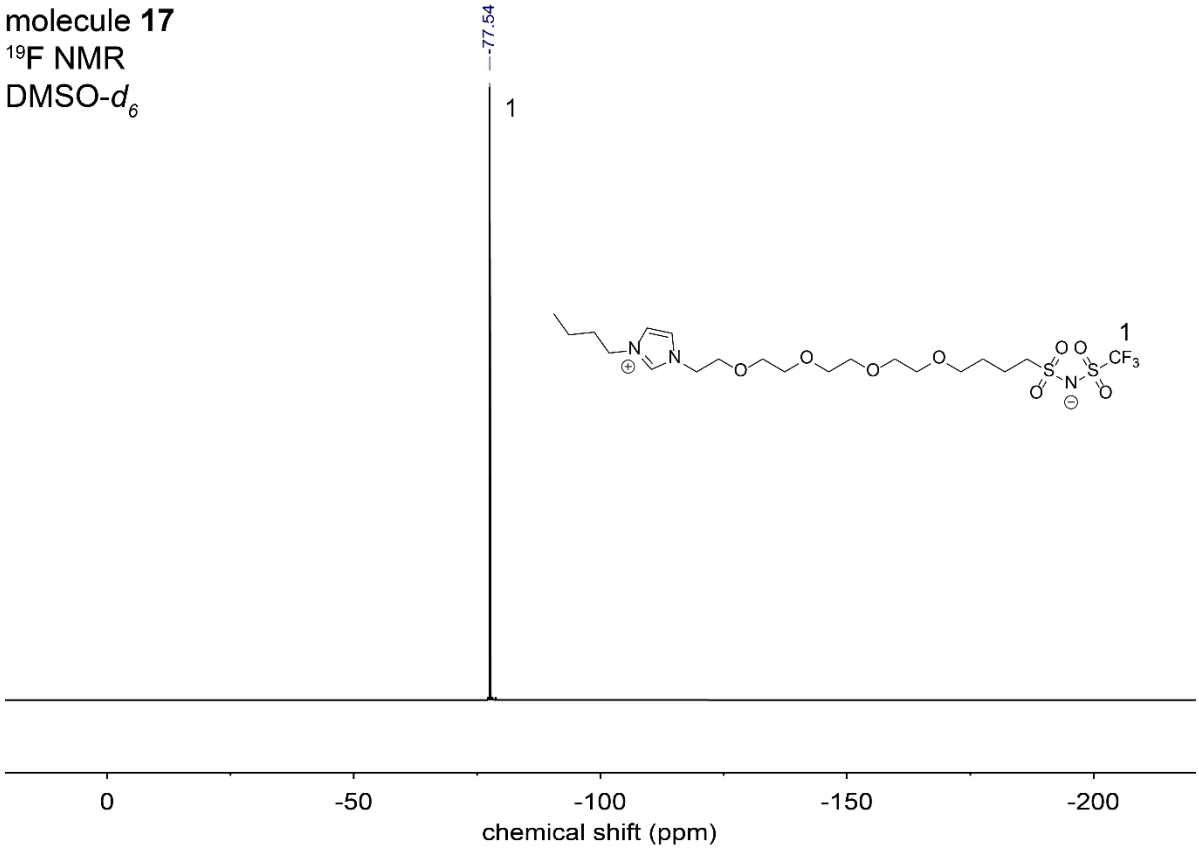
molecule **17**
^{19}F NMR
DMSO-d_6
-77.54
1
chemical shift (ppm)

Molecule **18**

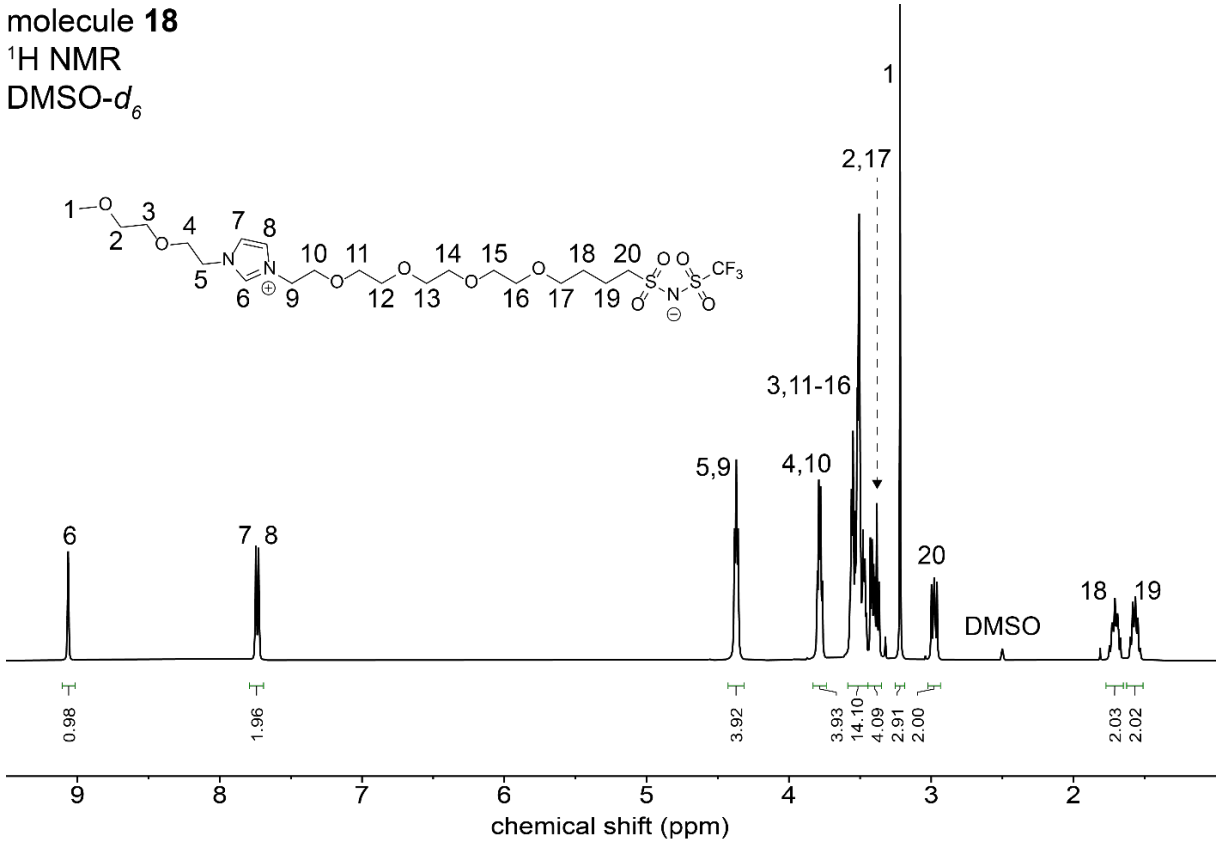
molecule **18**
^{1}H NMR
DMSO-d_6
1
2,17
3,11-16
5,9
4,10
6
7 8
20
18
19
DMSO
0.98
1.96
3.92
3.93
14.10
4.09
2.91
2.00
2.03
2.02
chemical shift (ppm)

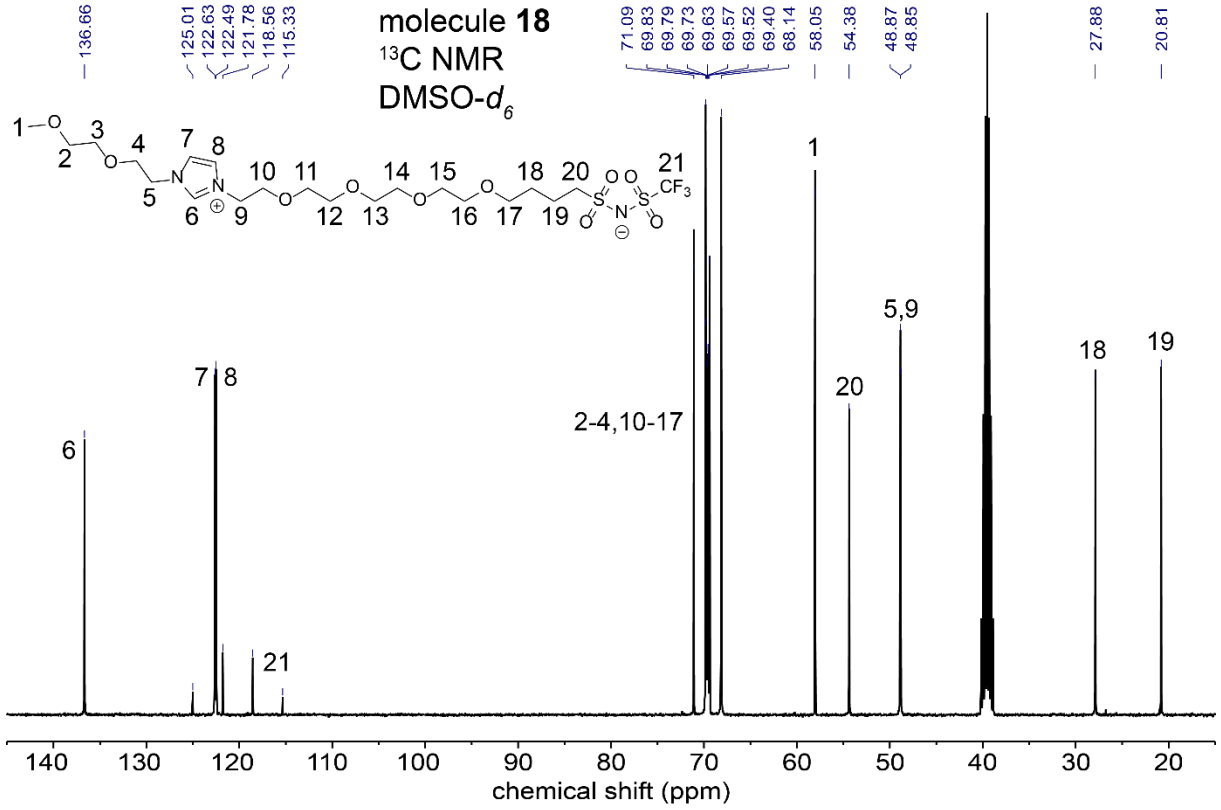
molecule **18**
^{13}C NMR
DMSO-d_6
136.66
125.01
122.63
122.49
121.78
118.56
115.33
71.09
69.83
69.79
69.73
69.63
69.57
69.52
69.40
68.14
58.05
54.38
48.87
48.85
27.88
20.81
1
5,9
18
19
20
7 8
6
2-4,10-17
21
chemical shift (ppm)

molecule **18**
^{19}F NMR
DMSO-d_6

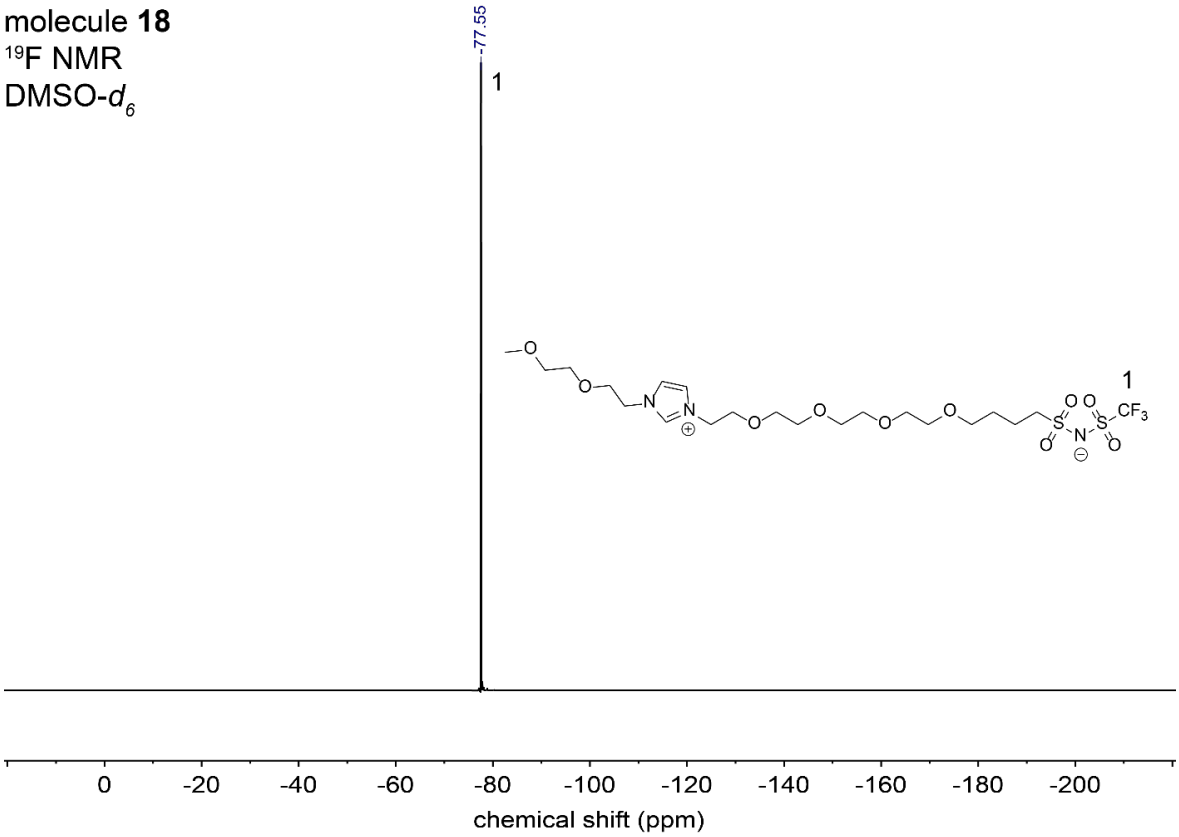

Molecule **A**

molecule **A**
^{1}H NMR
DMSO-d_6

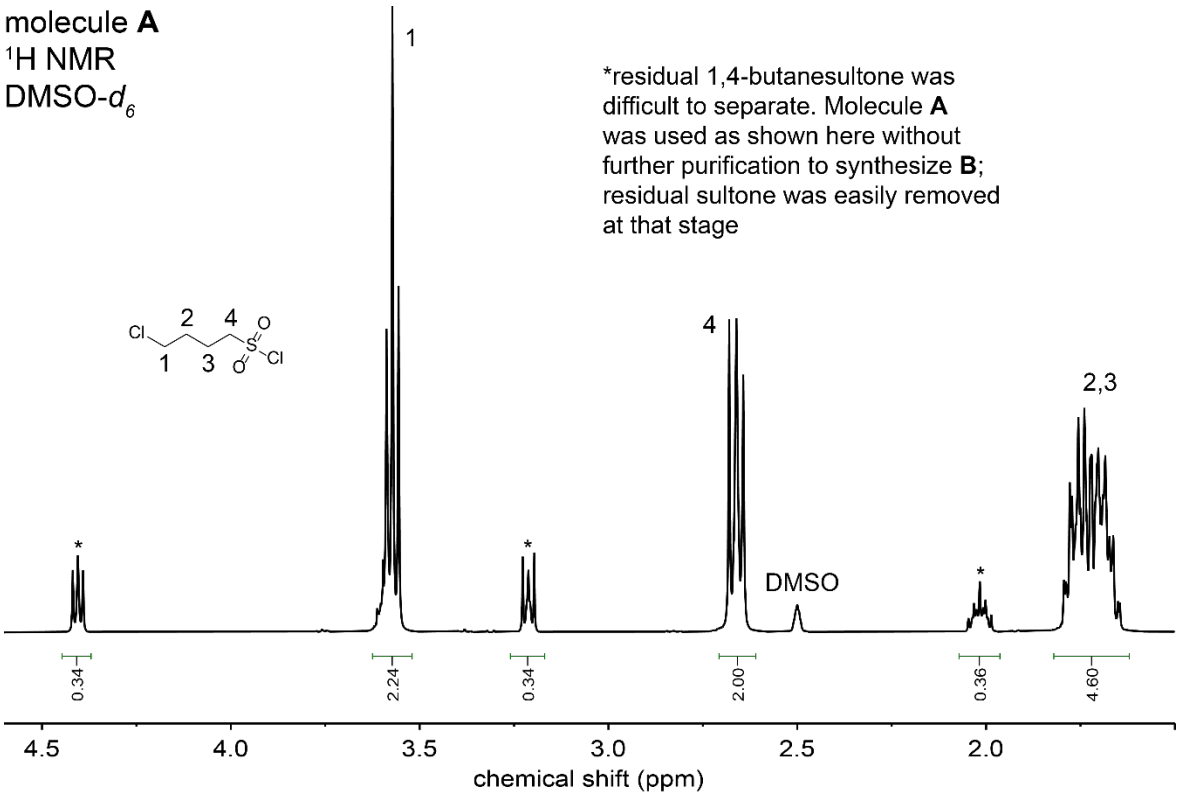

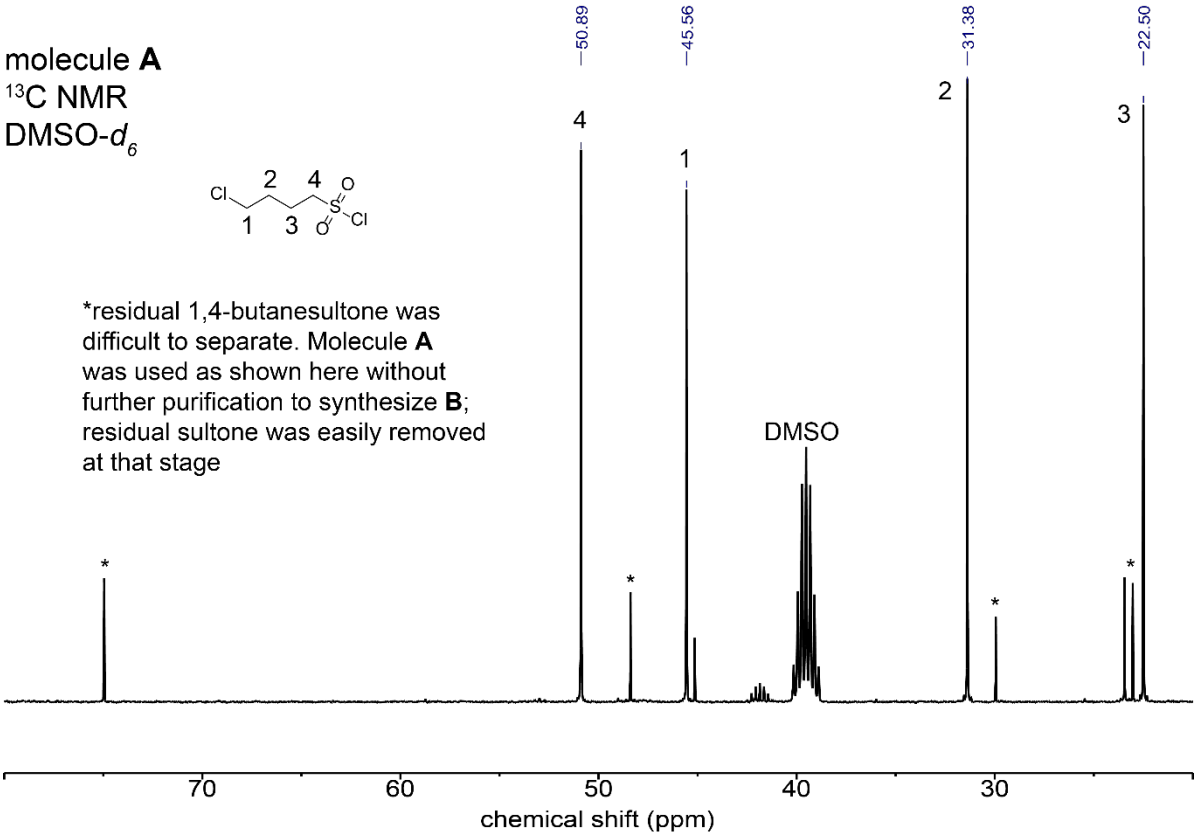

Molecule **B-CF$_3$**

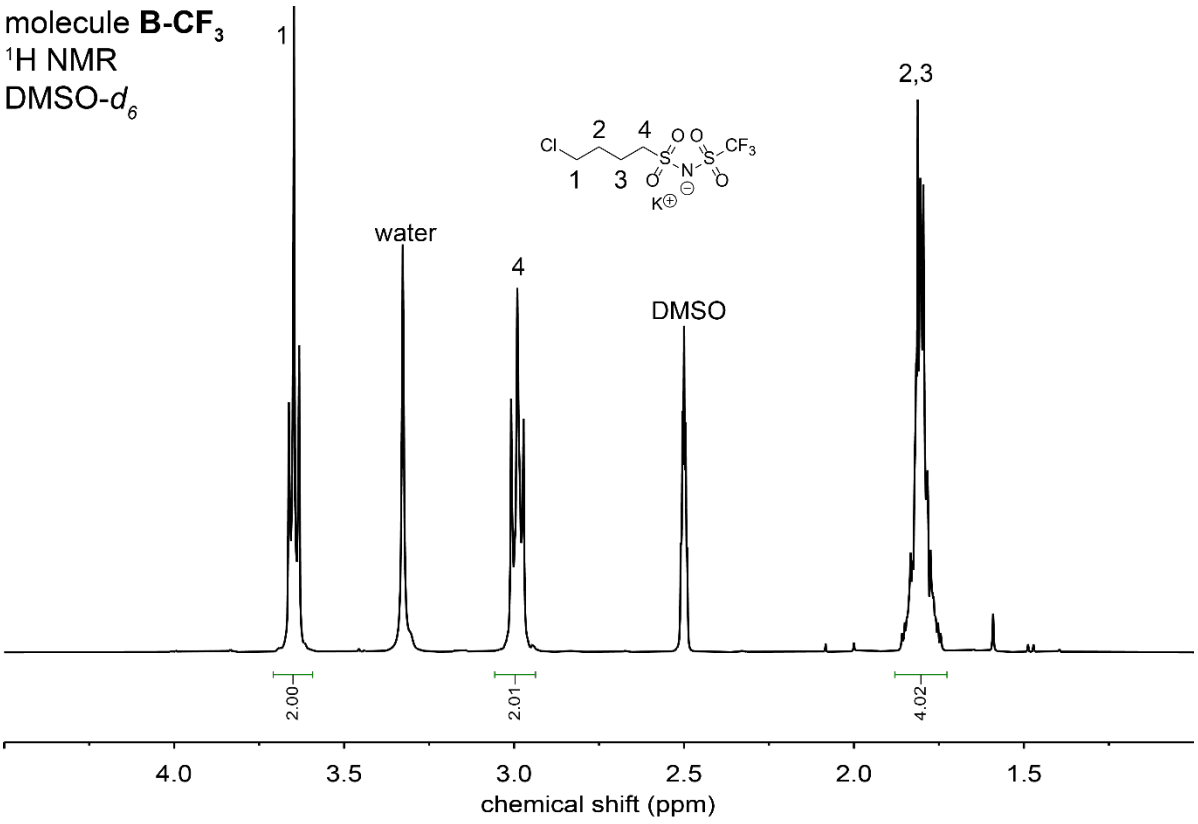

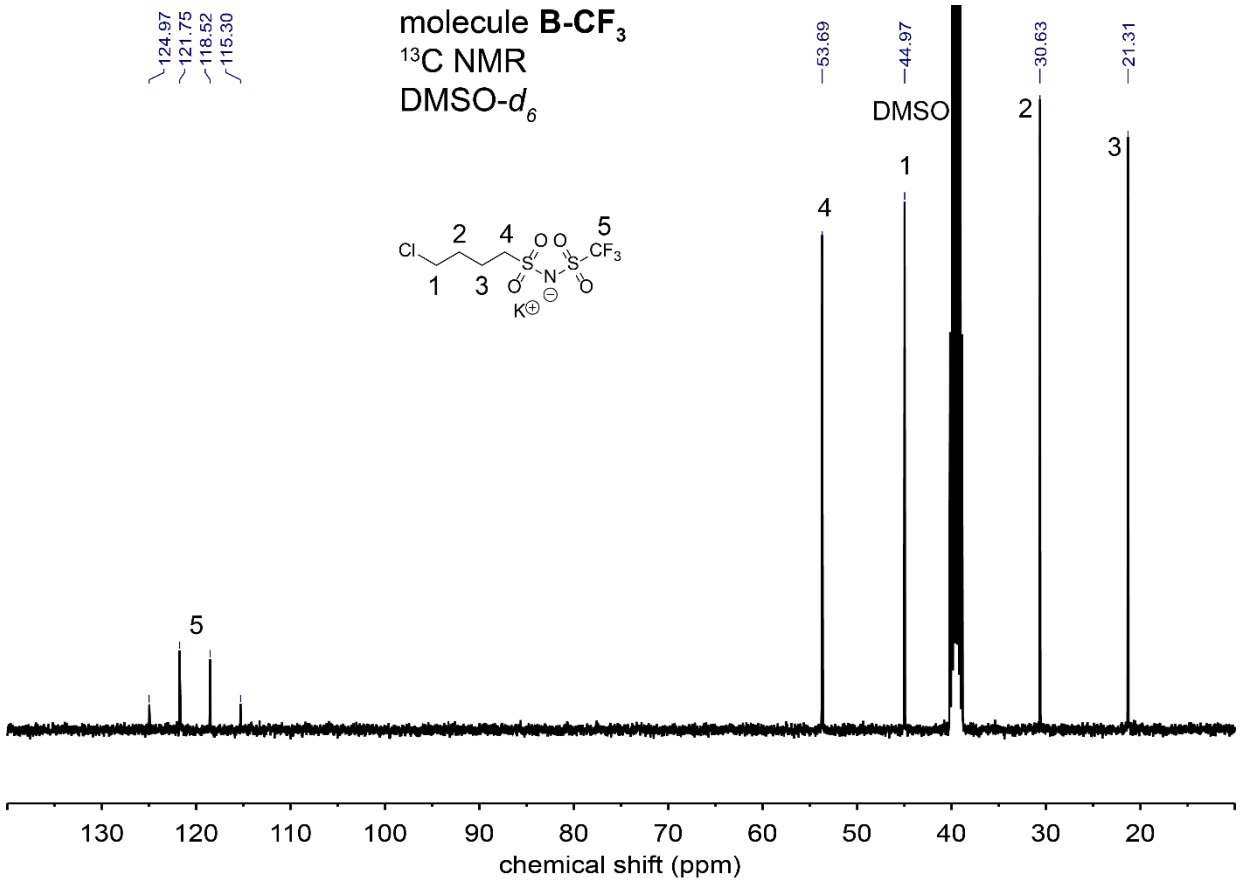
molecule B-CF3
13C NMR
DMSO-d6
124.97
121.75
118.52
115.30
53.69
44.97
30.63
21.31
DMSO
1
2
3
4
5
Cl
CF3
K
130
120
110
100
90
80
70
60
50
40
30
20
chemical shift (ppm)

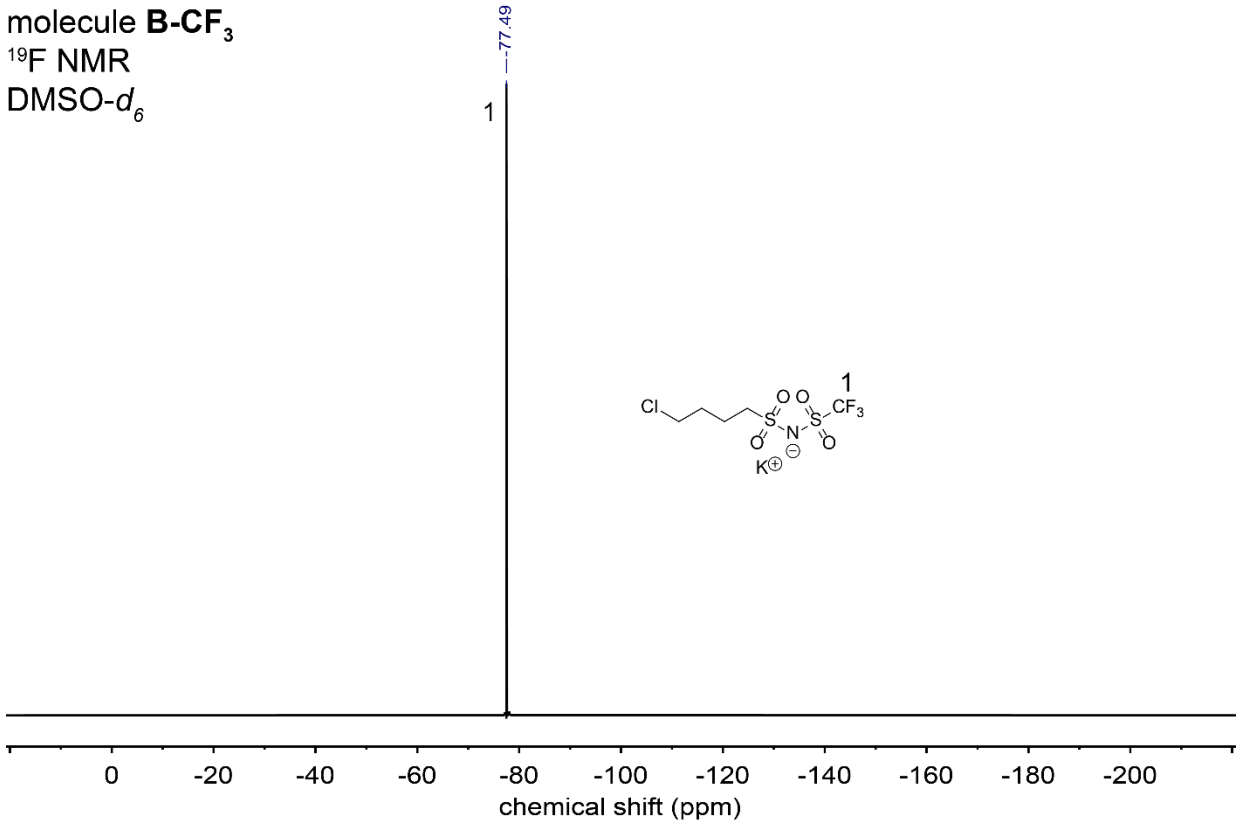
molecule B-CF3
19F NMR
DMSO-d6
-77.49
1
Cl
CF3
K
0
-20
-40
-60
-80
-100
-120
-140
-160
-180
-200
chemical shift (ppm)

Molecule **B-C$_4$F$_9$**

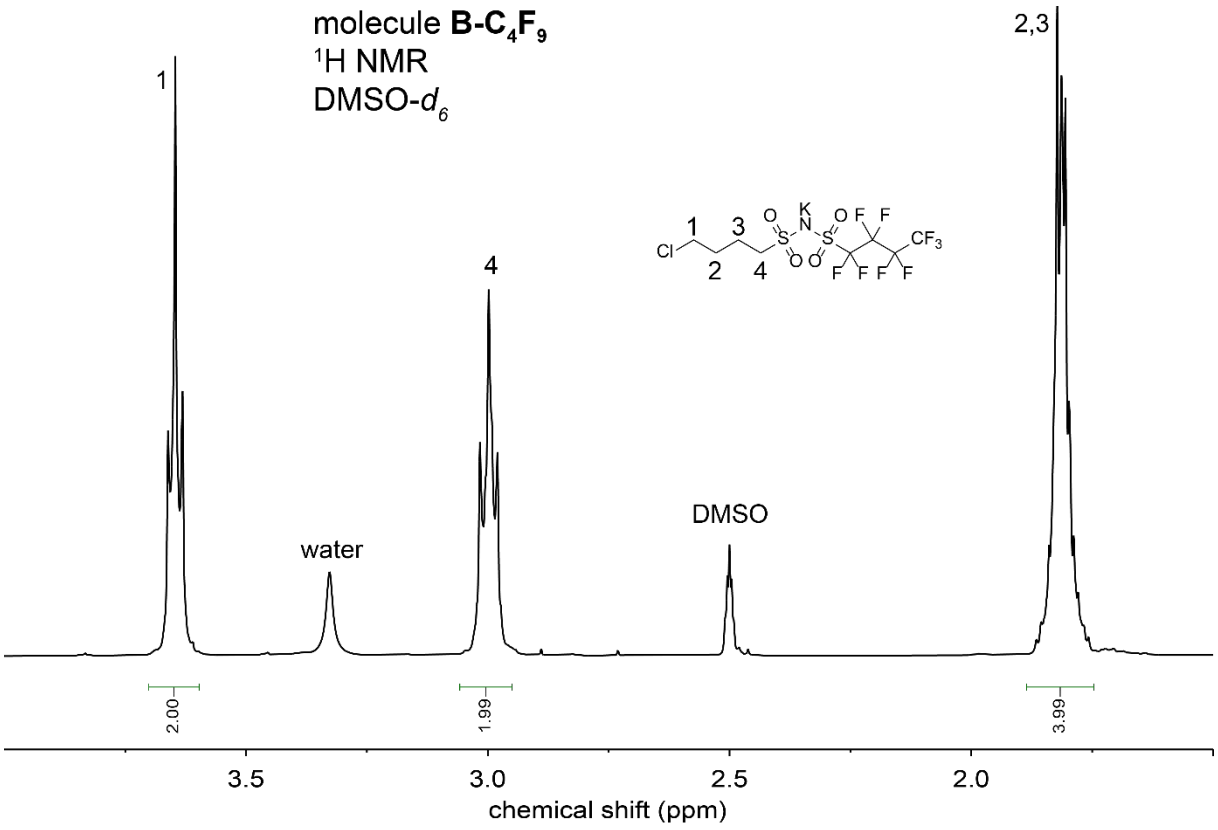

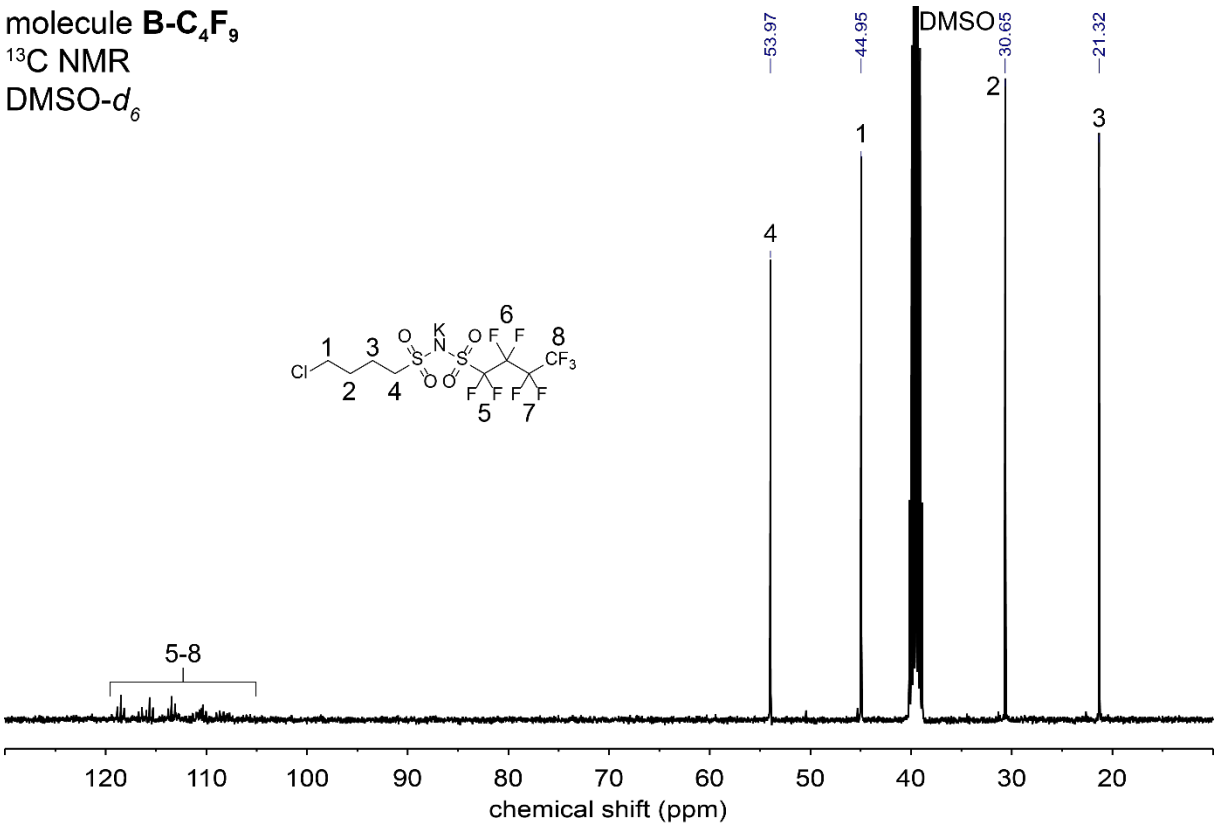

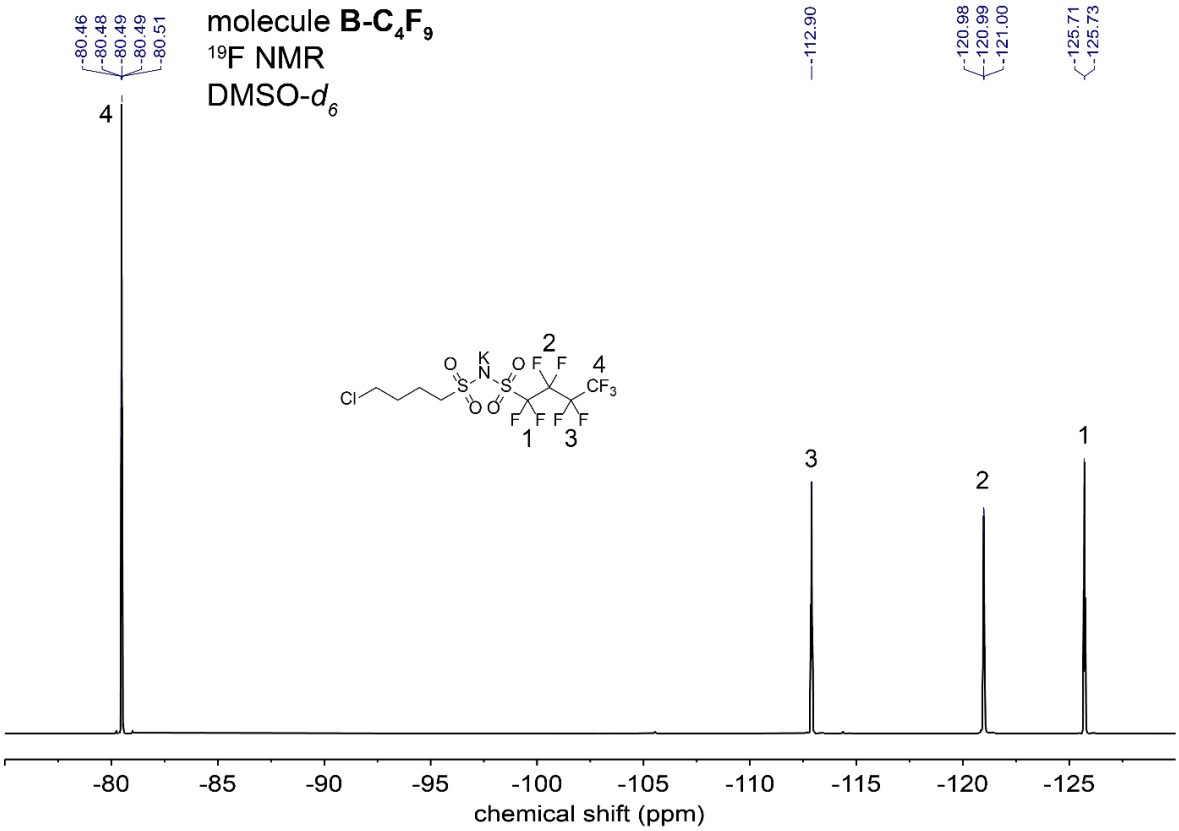
molecule B-C4F9
19F NMR
DMSO-d6
-80.46
-80.48
-80.49
-80.49
-80.51
-112.90
-120.98
-120.99
-121.00
-125.71
-125.73
4
3
2
1
chemical shift (ppm)

Molecule **C**

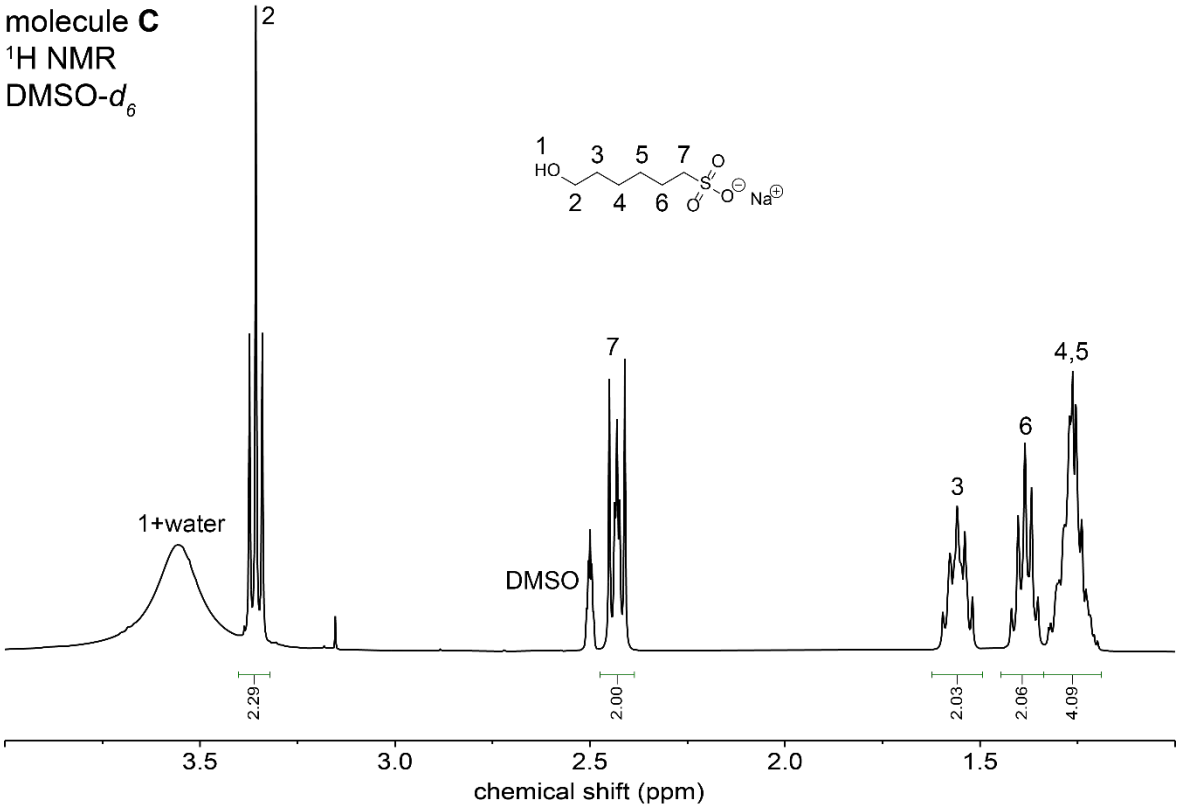
molecule C
1H NMR
DMSO-d6
1+water
DMSO
2.29
2.00
2.03
2.06
4.09
chemical shift (ppm)

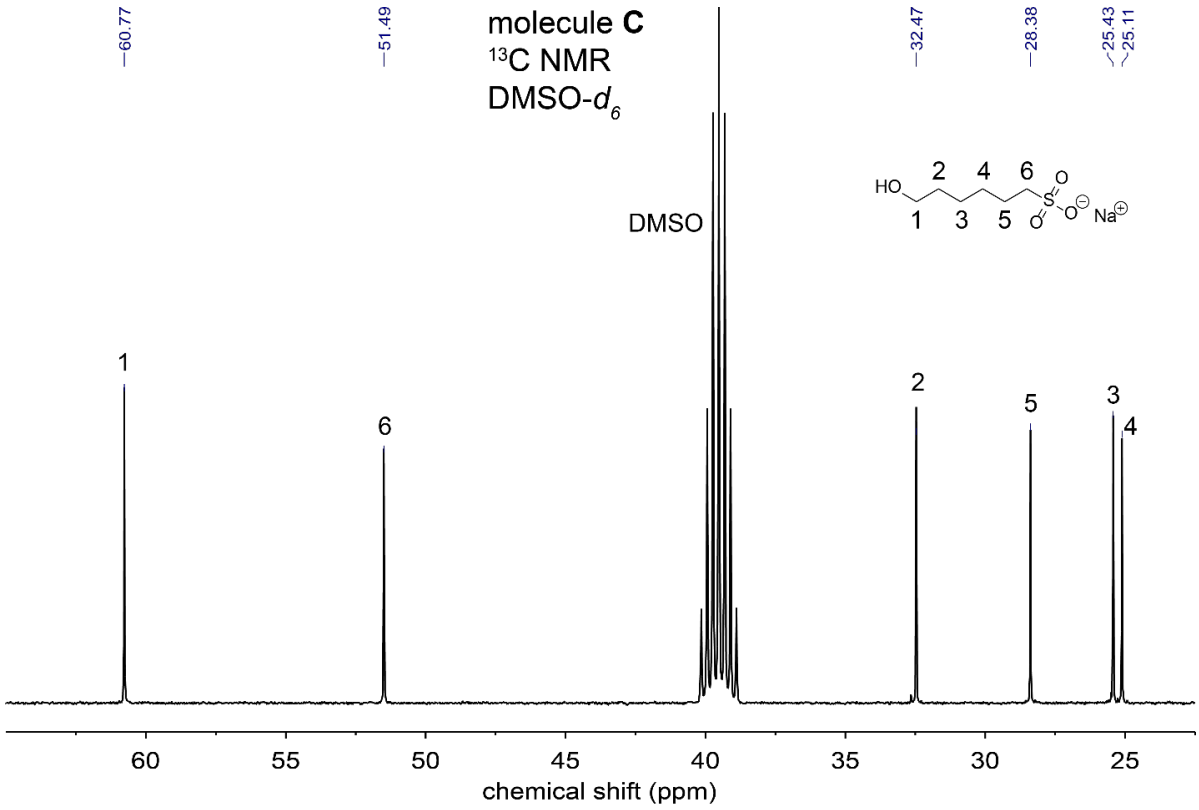
molecule **C**
^{13}C NMR
DMSO-d_6
60.77
51.49
32.47
28.38
25.43
25.11
DMSO
1
6
2
5
3
4
HO
Na
60
55
50
45
40
35
30
25
chemical shift (ppm)

Molecule **D**

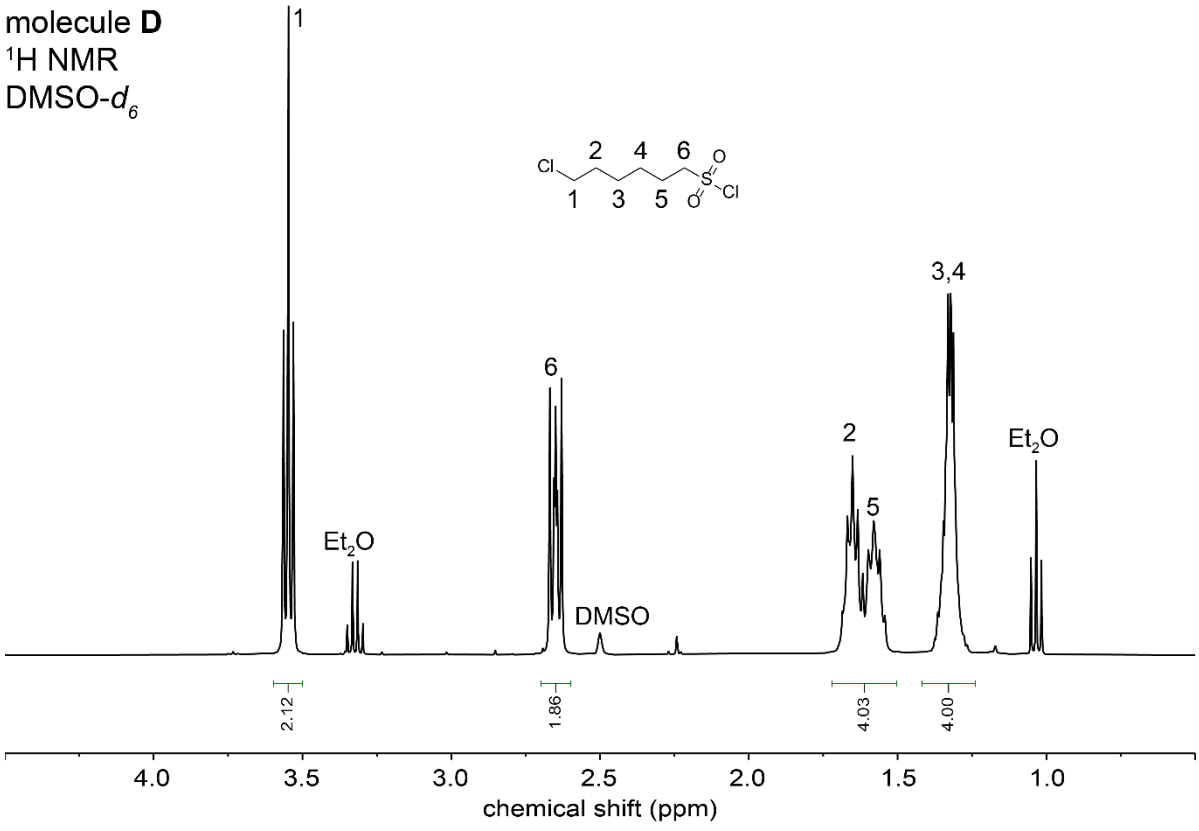
molecule **D**
^{1}H NMR
DMSO-d_6
Cl
Cl
1
6
2
5
3,4
Et_2O
Et_2O
DMSO
2.12
1.86
4.03
4.00
4.0
3.5
3.0
2.5
2.0
1.5
1.0
chemical shift (ppm)

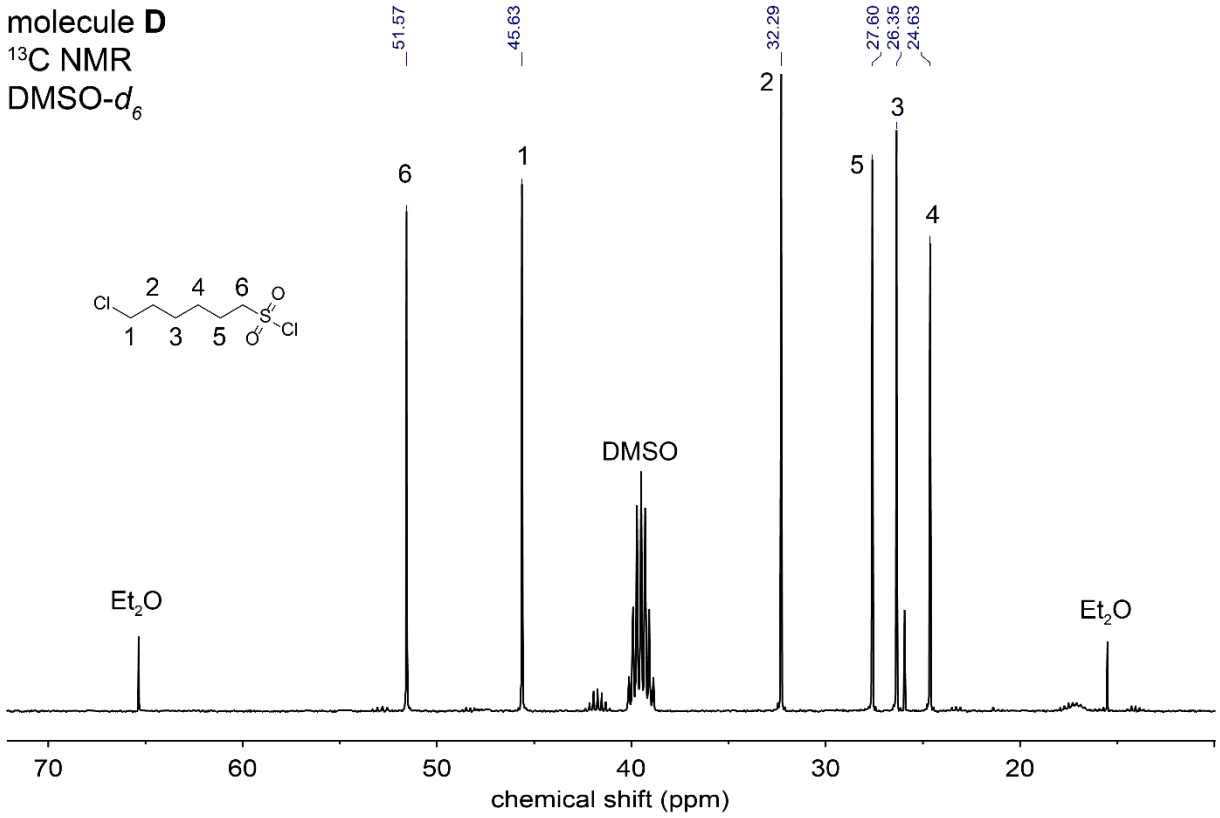
molecule **D**
^{13}C NMR
DMSO-d_6
51.57
45.63
32.29
27.60
26.35
24.63
6
1
2
3
5
4
DMSO
Et$_2$O
Et$_2$O
70
60
50
40
30
20
chemical shift (ppm)

Molecule **E**

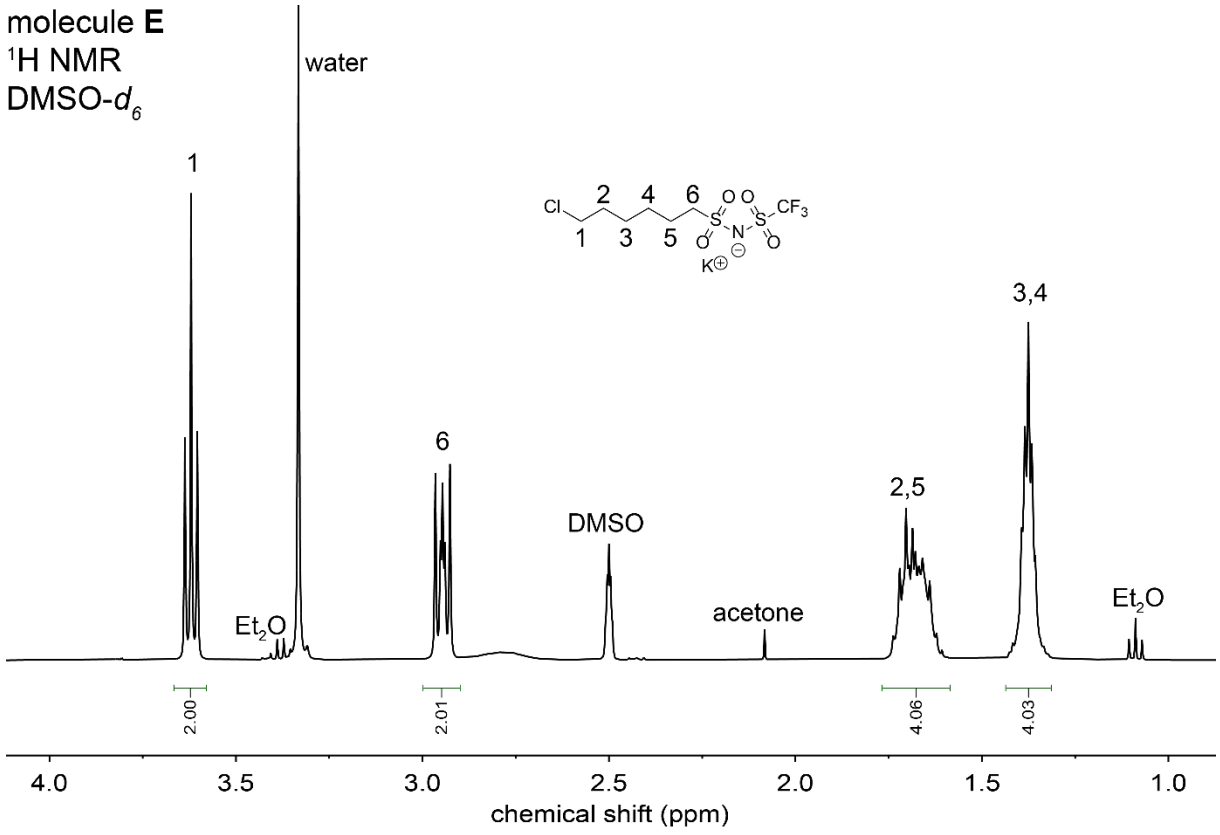
molecule **E**
^{1}H NMR
DMSO-d_6
water
1
6
DMSO
2,5
3,4
acetone
Et$_2$O
Et$_2$O
2.00
2.01
4.06
4.03
4.0
3.5
3.0
2.5
2.0
1.5
1.0
chemical shift (ppm)

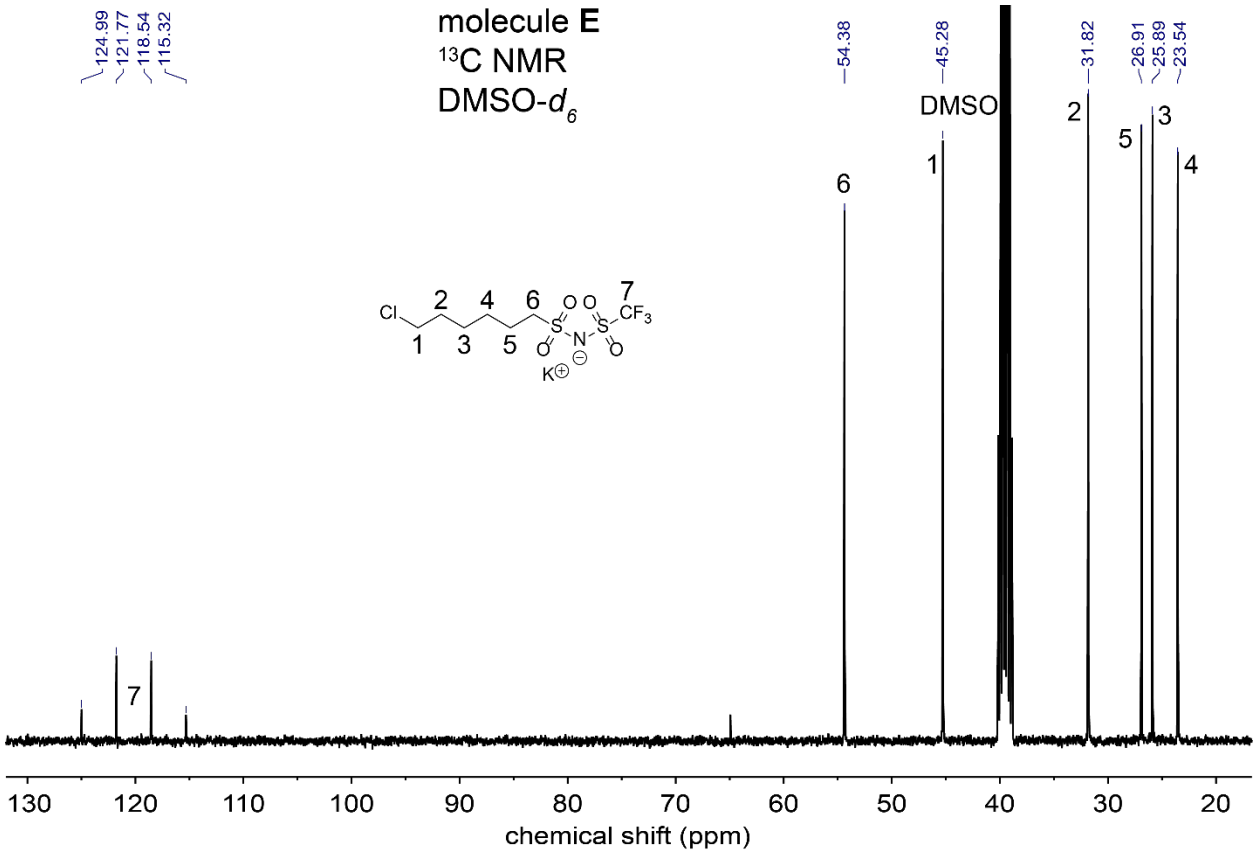
molecule **E**
^{13}C NMR
DMSO-d_6
124.99
121.77
118.54
115.32
54.38
45.28
31.82
26.91
25.89
23.54
DMSO
1
2
3
4
5
6
7
Cl
CF3
K
130
120
110
100
90
80
70
60
50
40
30
20
chemical shift (ppm)

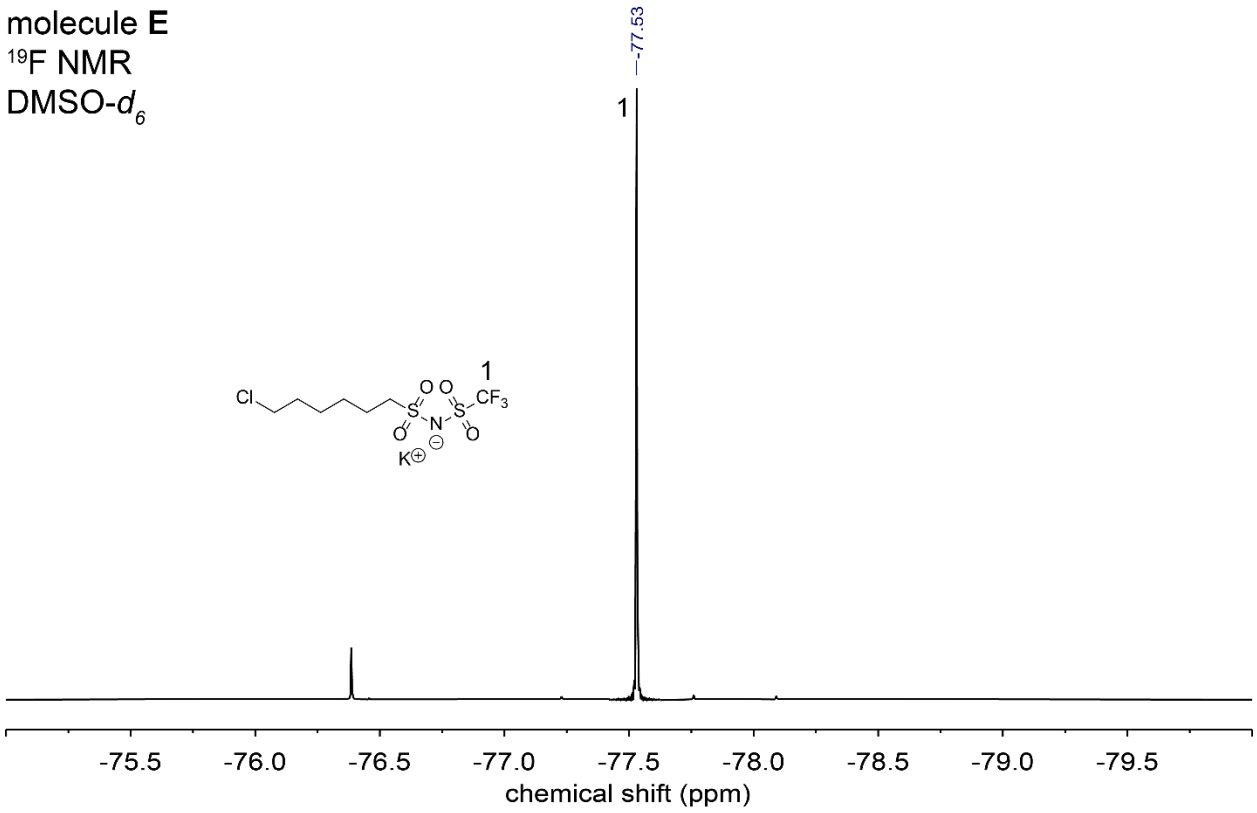
molecule **E**
^{19}F NMR
DMSO-d_6
-77.53
1
Cl
CF3
K
-75.5
-76.0
-76.5
-77.0
-77.5
-78.0
-78.5
-79.0
-79.5
chemical shift (ppm)

Molecule **F**

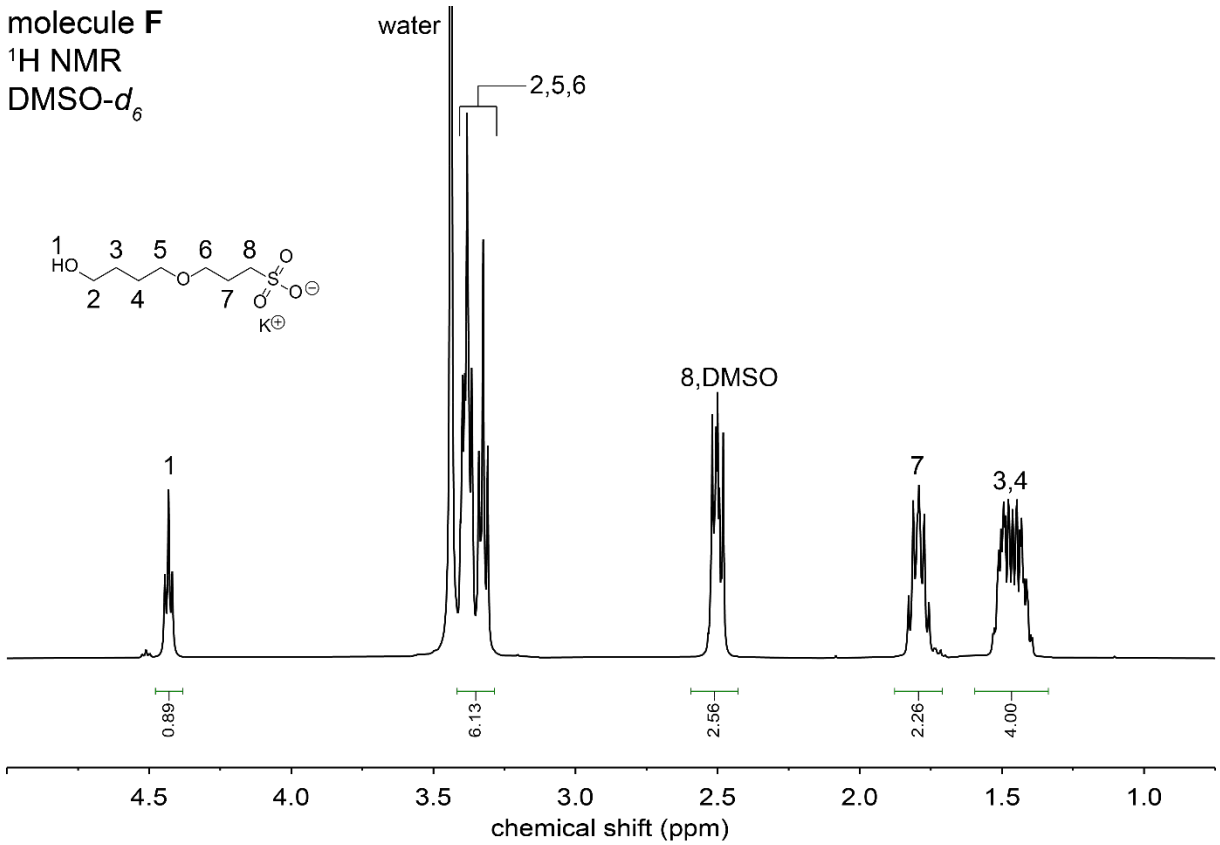
molecule **F**
^{1}H NMR
DMSO-d_6
water
2,5,6
8,DMSO
1
7
3,4
0.89
6.13
2.56
2.26
4.00
4.5
4.0
3.5
3.0
2.5
2.0
1.5
1.0
chemical shift (ppm)

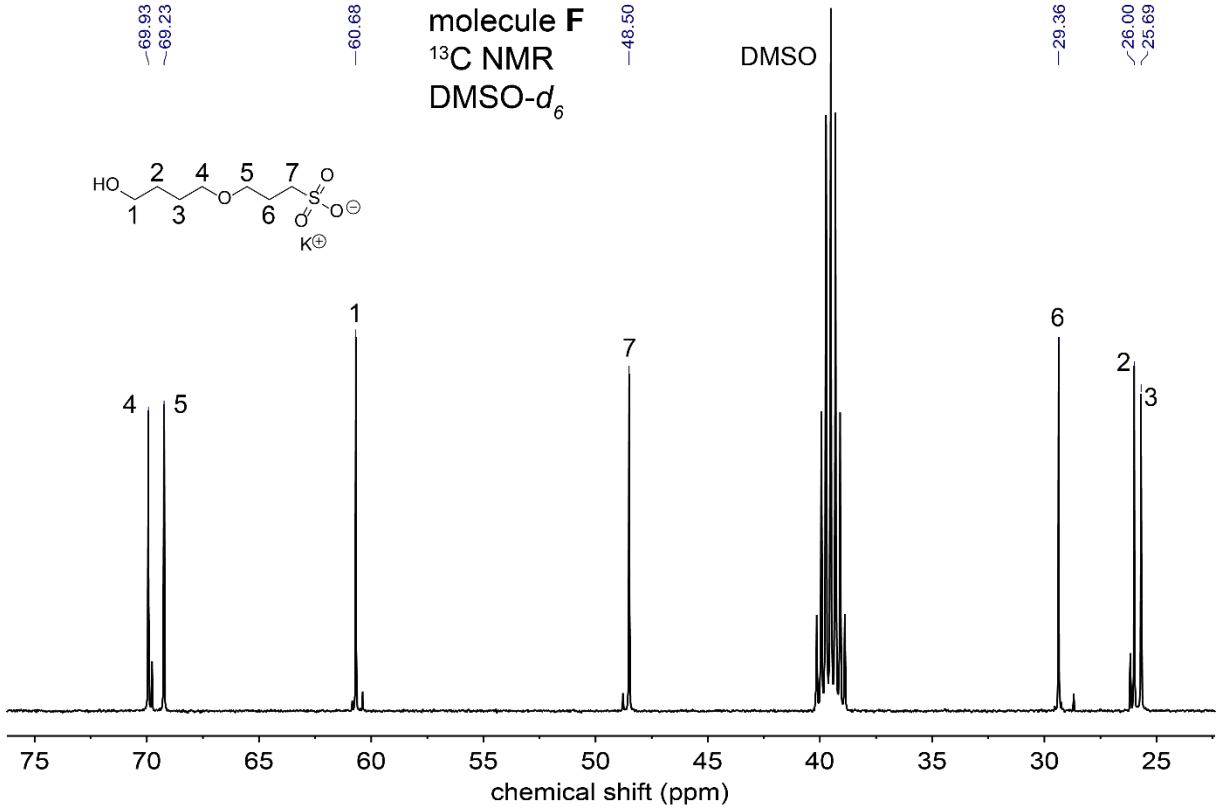
molecule **F**
^{13}C NMR
DMSO-d_6
69.93
69.23
60.68
48.50
DMSO
29.36
26.00
25.69
4
5
1
7
6
2
3
75
70
65
60
55
50
45
40
35
30
25
chemical shift (ppm)

Molecule **G**

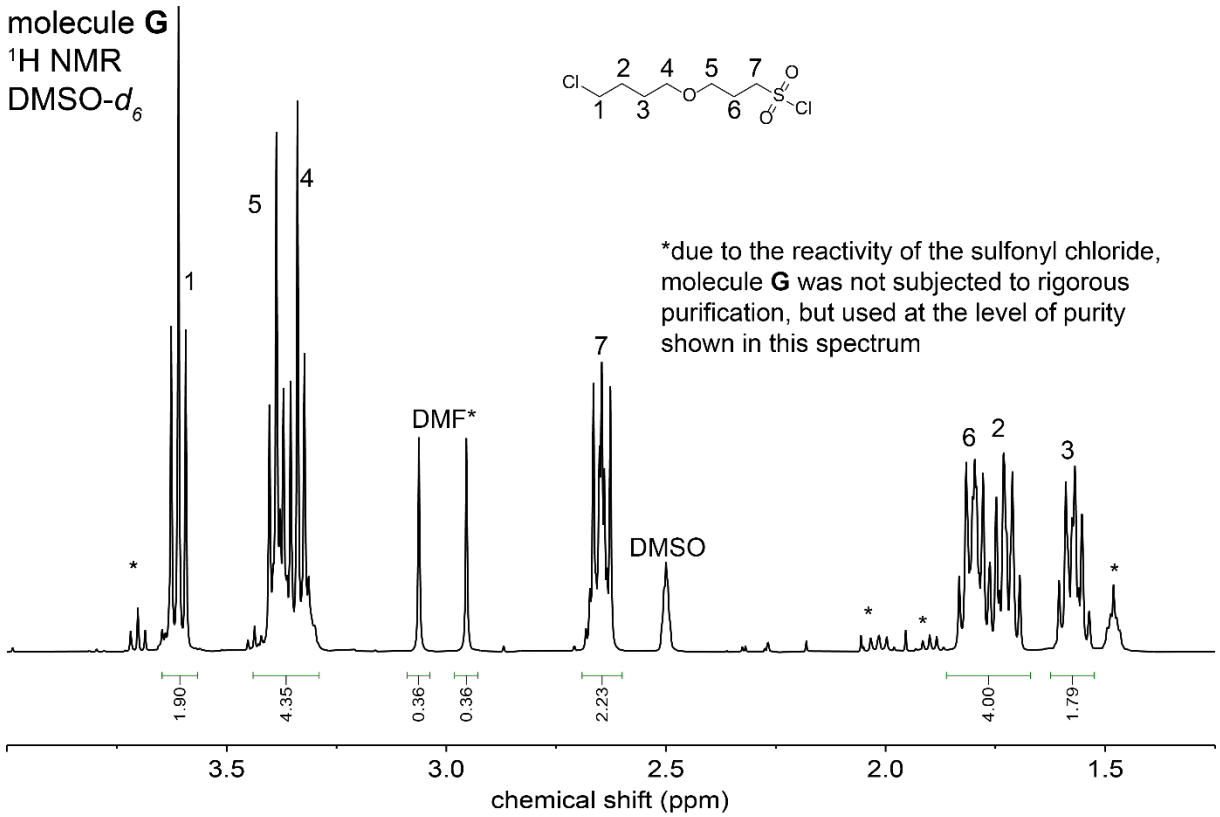
molecule **G**
^{1}H NMR
DMSO-d_6
*due to the reactivity of the sulfonyl chloride, molecule **G** was not subjected to rigorous purification, but used at the level of purity shown in this spectrum
DMF*
DMSO
1.90
4.35
0.36
0.36
2.23
4.00
1.79
chemical shift (ppm)

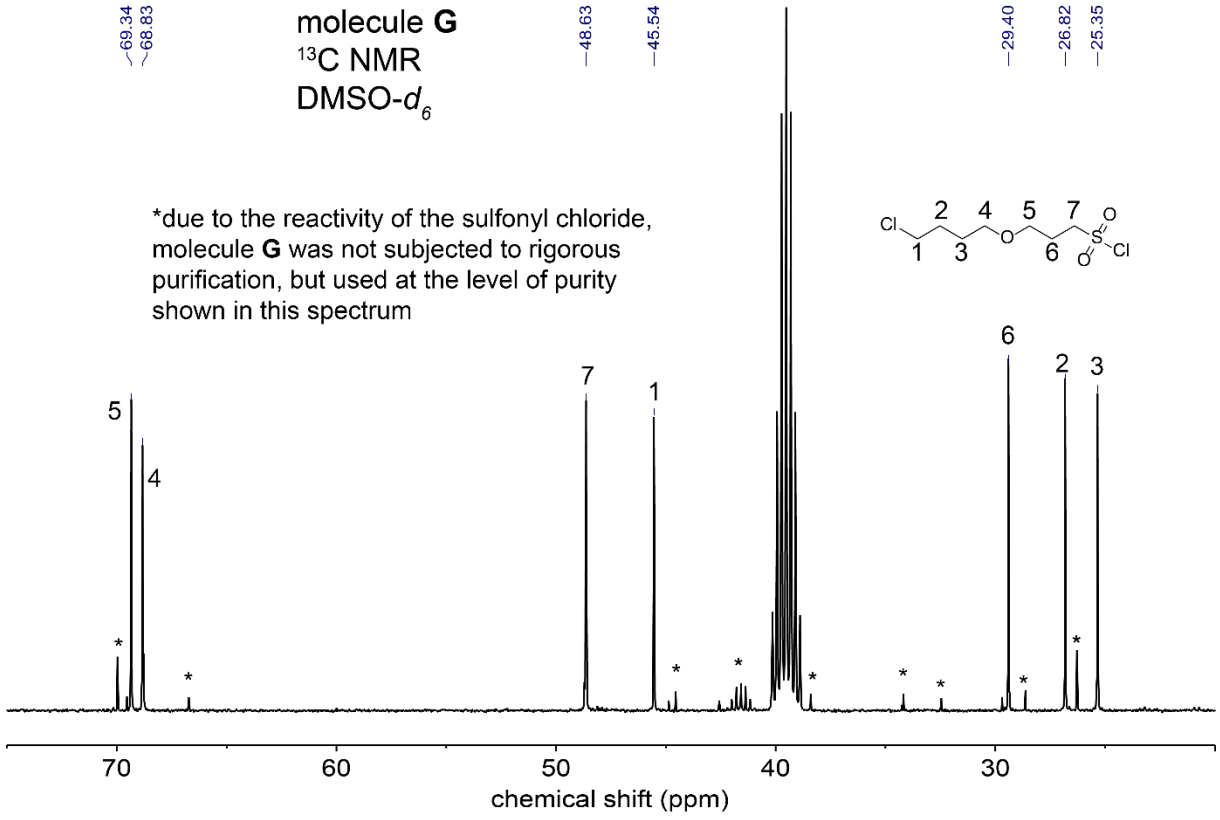
molecule **G**
^{13}C NMR
DMSO-d_6
69.34
68.83
48.63
45.54
29.40
26.82
25.35
*due to the reactivity of the sulfonyl chloride, molecule **G** was not subjected to rigorous purification, but used at the level of purity shown in this spectrum
chemical shift (ppm)

Molecule **H**

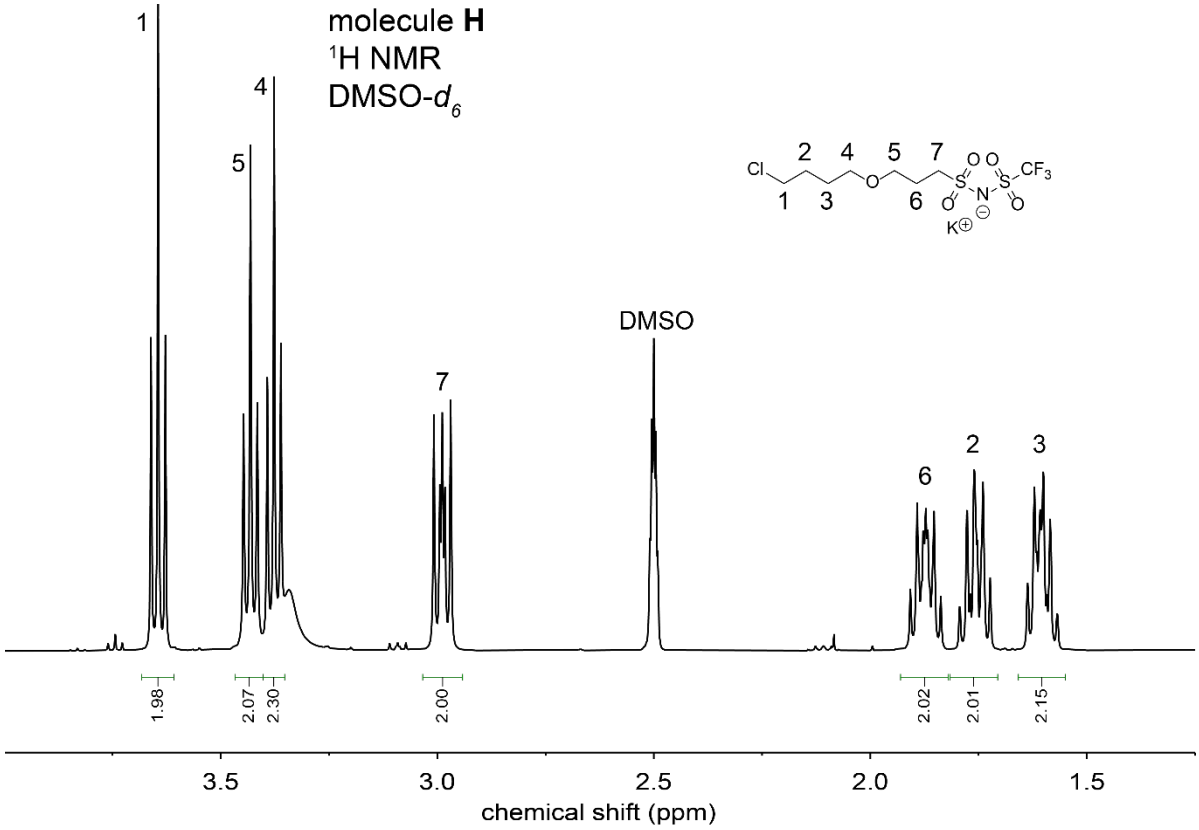
molecule **H**
^{1}H NMR
DMSO-d_6
1
4
5
7
DMSO
6
2
3
1.98
2.07
2.30
2.00
2.02
2.01
2.15
3.5
3.0
2.5
2.0
1.5
chemical shift (ppm)

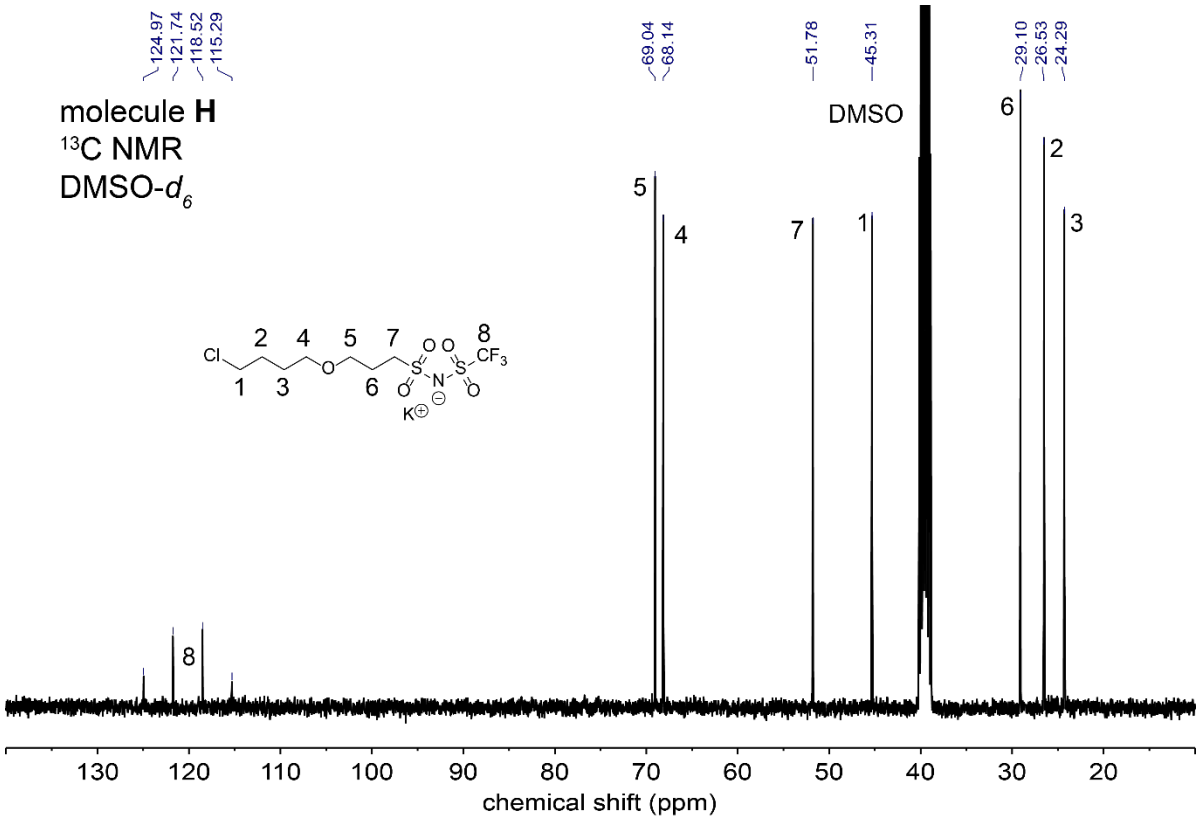
124.97
121.74
118.52
115.29
69.04
68.14
51.78
45.31
29.10
26.53
24.29
molecule **H**
^{13}C NMR
DMSO-d_6
DMSO
8
5
4
7
1
6
2
3
130
120
110
100
90
80
70
60
50
40
30
20
chemical shift (ppm)

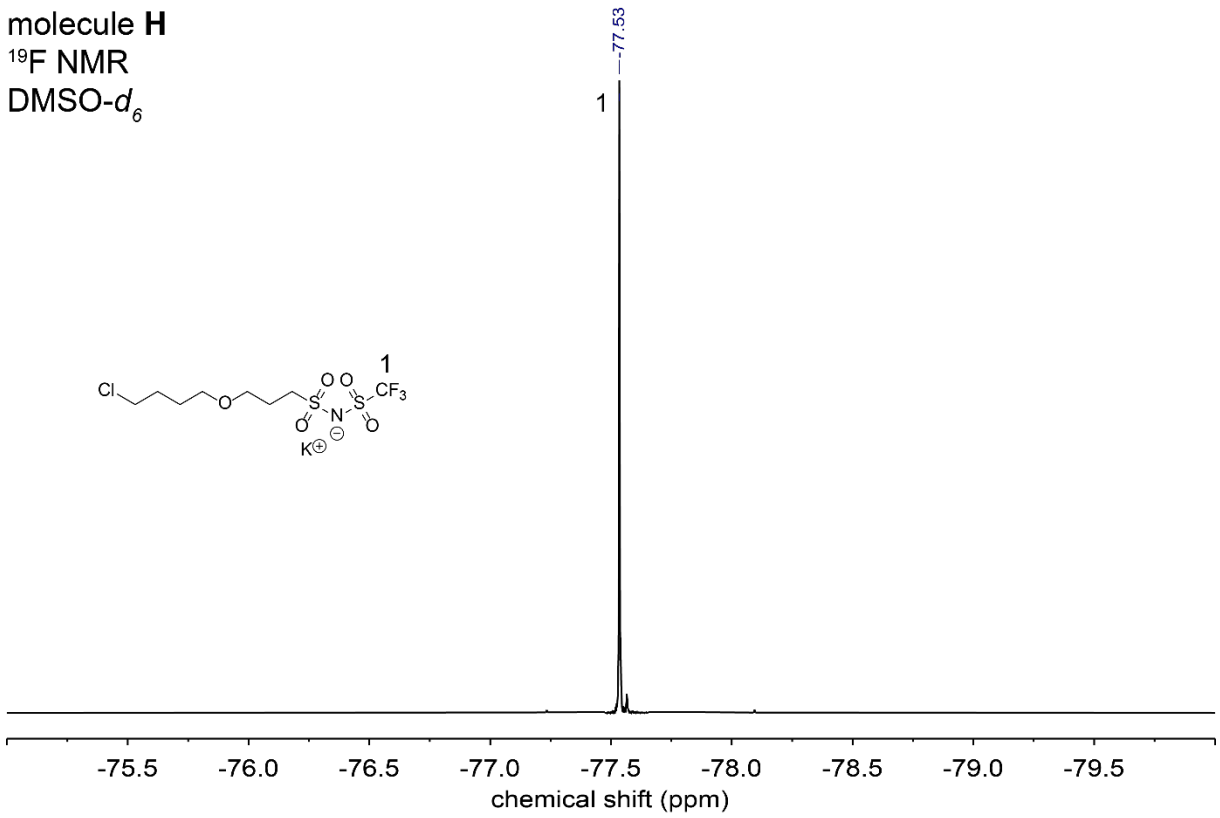
molecule **H**
^{19}F NMR
DMSO-d_6
-77.53
1
Cl
O
S
O
O
N
S
O
O
CF3
K
1
-75.5
-76.0
-76.5
-77.0
-77.5
-78.0
-78.5
-79.0
-79.5
chemical shift (ppm)

Molecule **I**

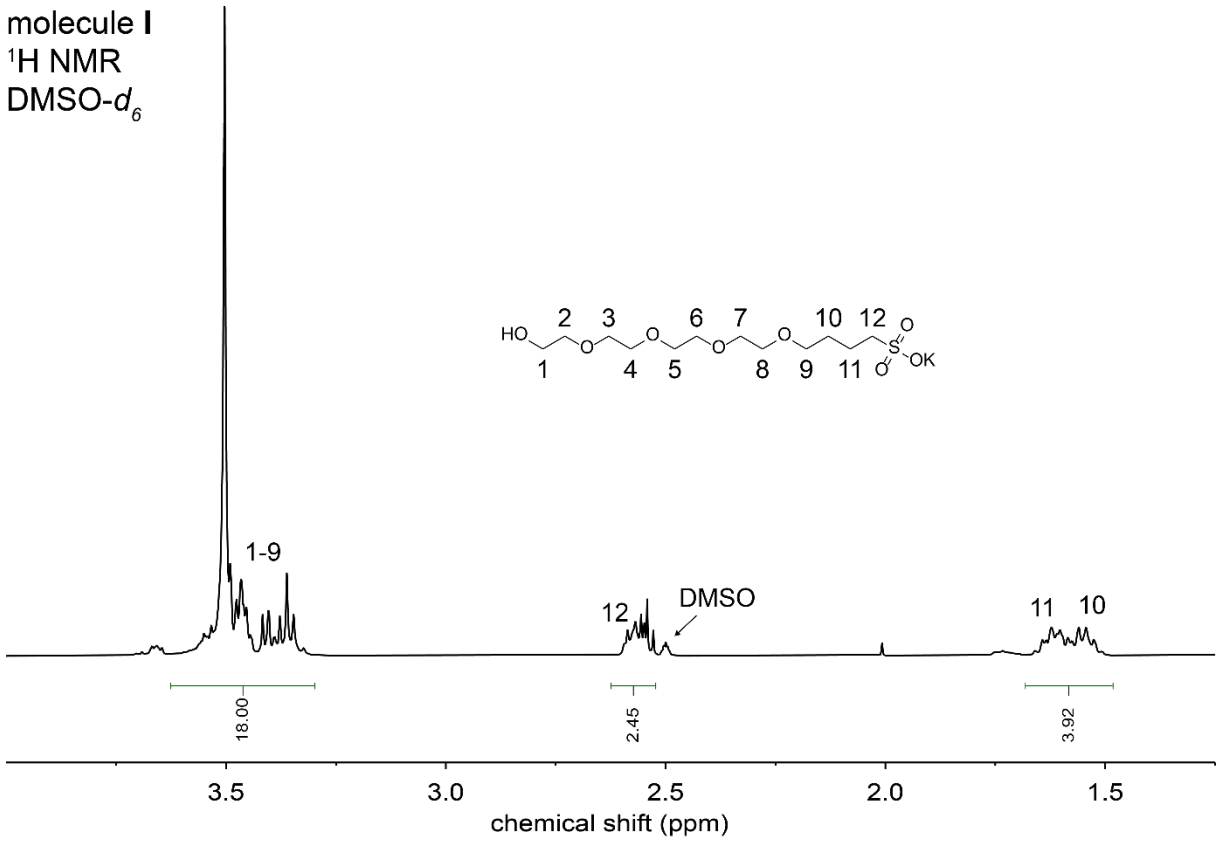
molecule **I**
^{1}H NMR
DMSO-d_6
HO
O
O
O
O
O
S
O
OK
2 3 6 7 10 12
1 4 5 8 9 11
1-9
12
DMSO
11 10
18.00
2.45
3.92
3.5
3.0
2.5
2.0
1.5
chemical shift (ppm)

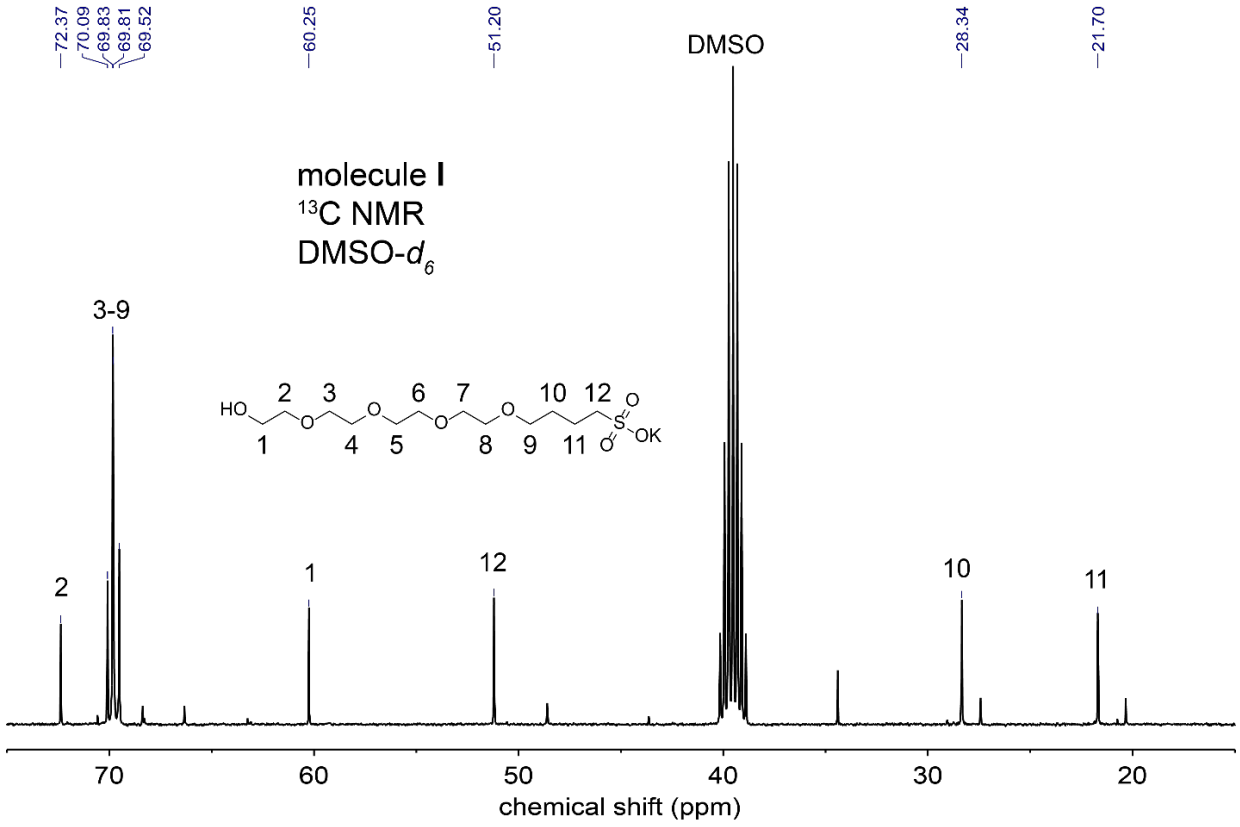
72.37
70.09
69.83
69.81
69.52
60.25
51.20
DMSO
28.34
21.70
molecule I
13C NMR
DMSO-d6
3-9
HO
OK
2
1
12
10
11
70
60
50
40
30
20
chemical shift (ppm)

Molecule **J**

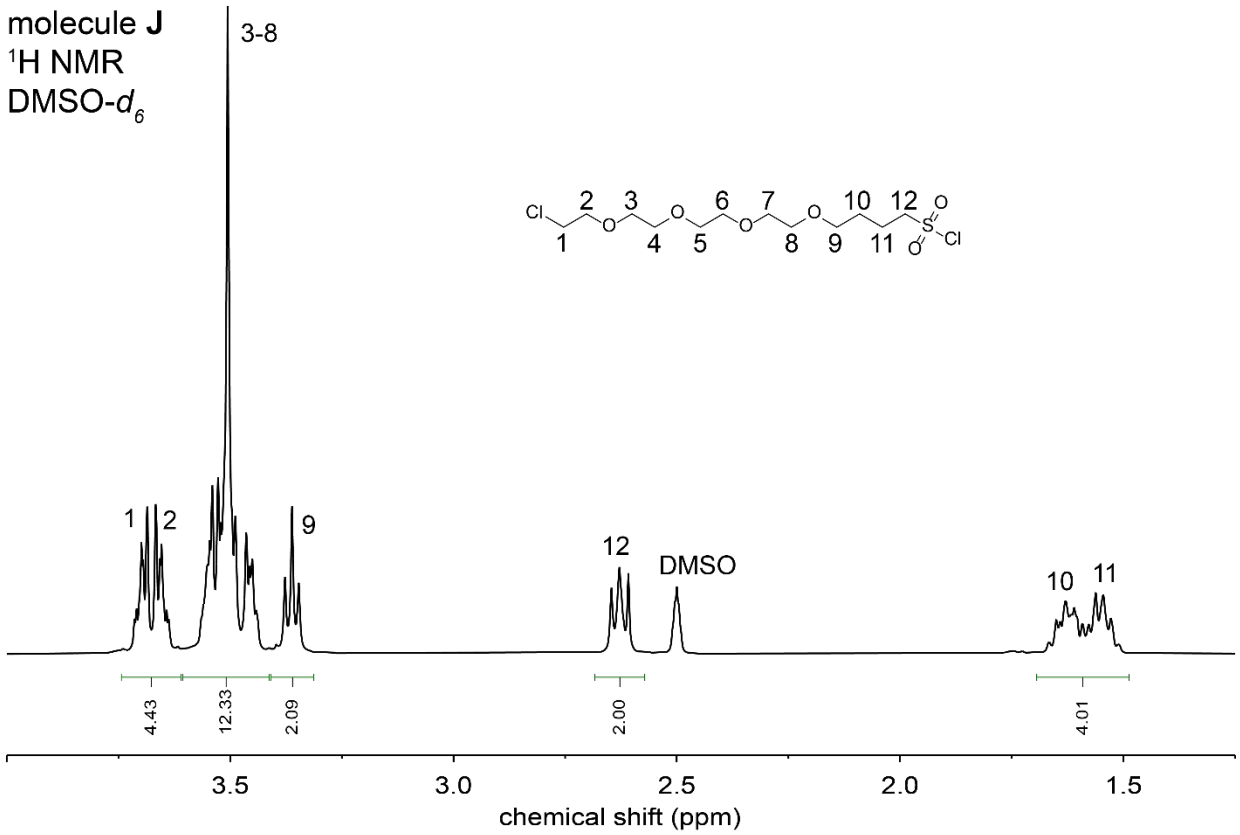
molecule J
1H NMR
DMSO-d6
3-8
Cl
Cl
1
2
9
12
DMSO
10
11
4.43
12.33
2.09
2.00
4.01
3.5
3.0
2.5
2.0
1.5
chemical shift (ppm)

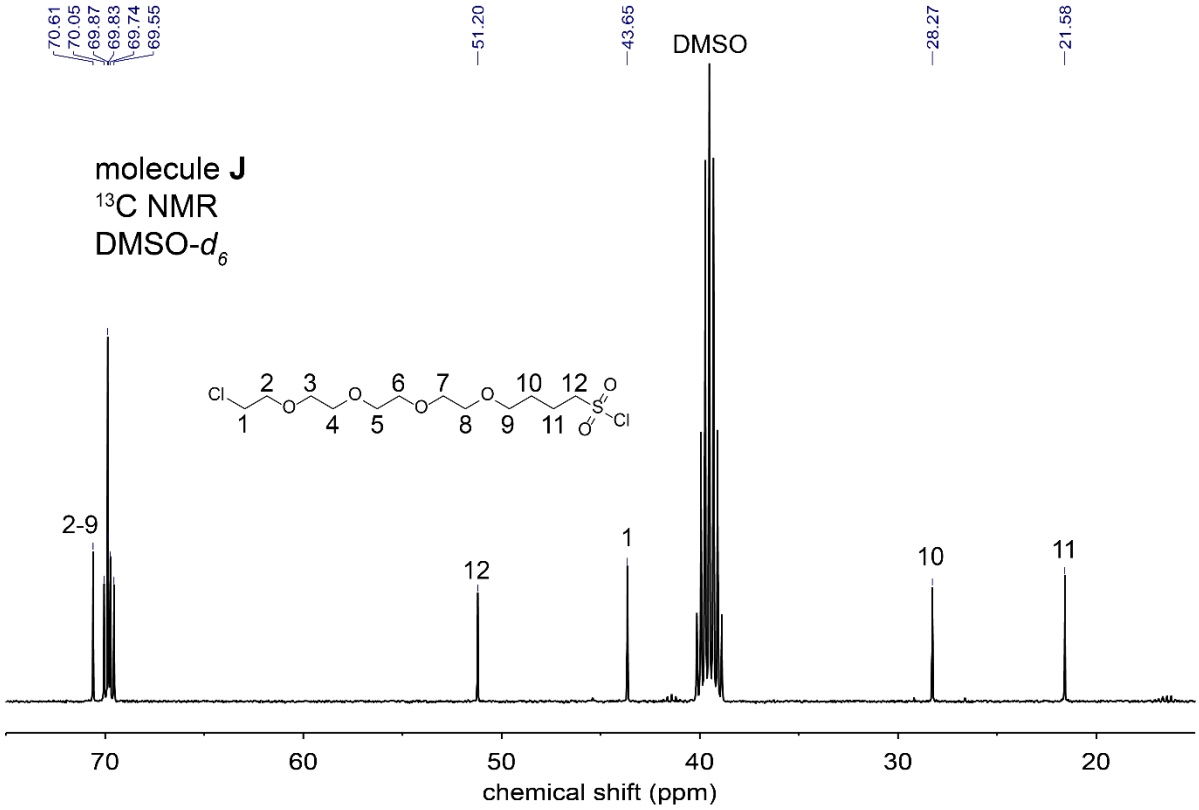
70.61
70.05
69.87
69.83
69.74
69.55
51.20
43.65
DMSO
28.27
21.58
molecule **J**
^{13}C NMR
DMSO-d_6
2-9
12
1
10
11
chemical shift (ppm)

Molecule **K**

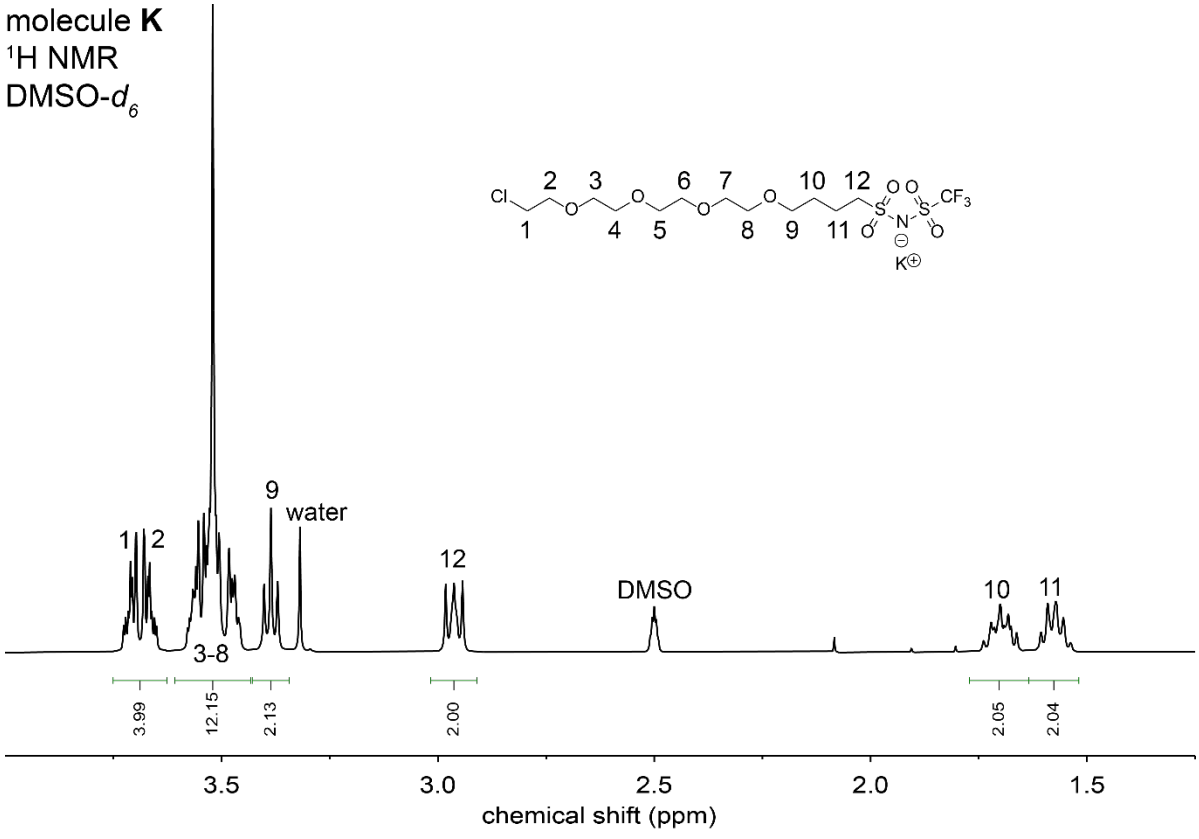
molecule **K**
^{1}H NMR
DMSO-d_6
1
2
3-8
9
water
12
DMSO
10
11
3.99
12.15
2.13
2.00
2.05
2.04
chemical shift (ppm)

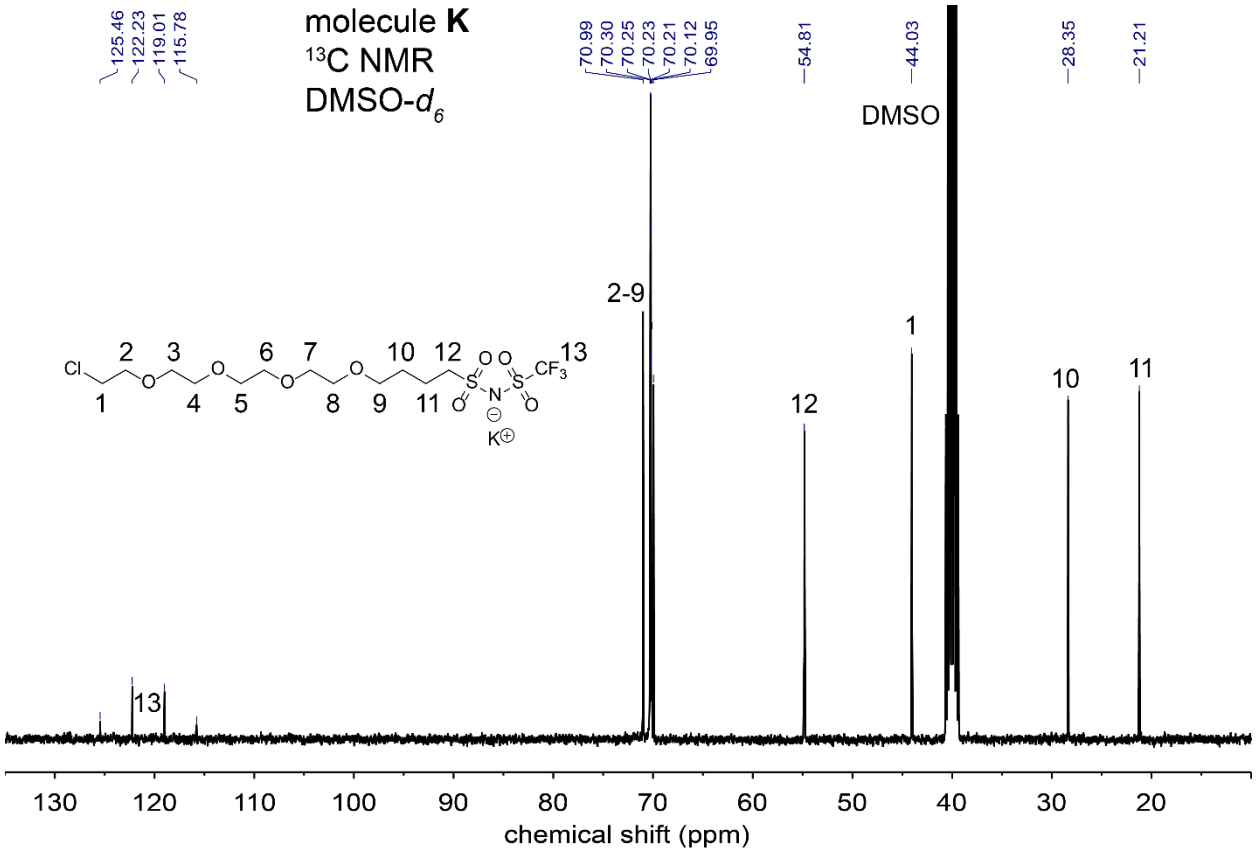
molecule **K**
^{13}C NMR
DMSO-d_6
125.46
122.23
119.01
115.78
70.99
70.30
70.25
70.23
70.21
70.12
69.95
54.81
44.03
28.35
21.21
DMSO
2-9
1
12
10
11
13
chemical shift (ppm)

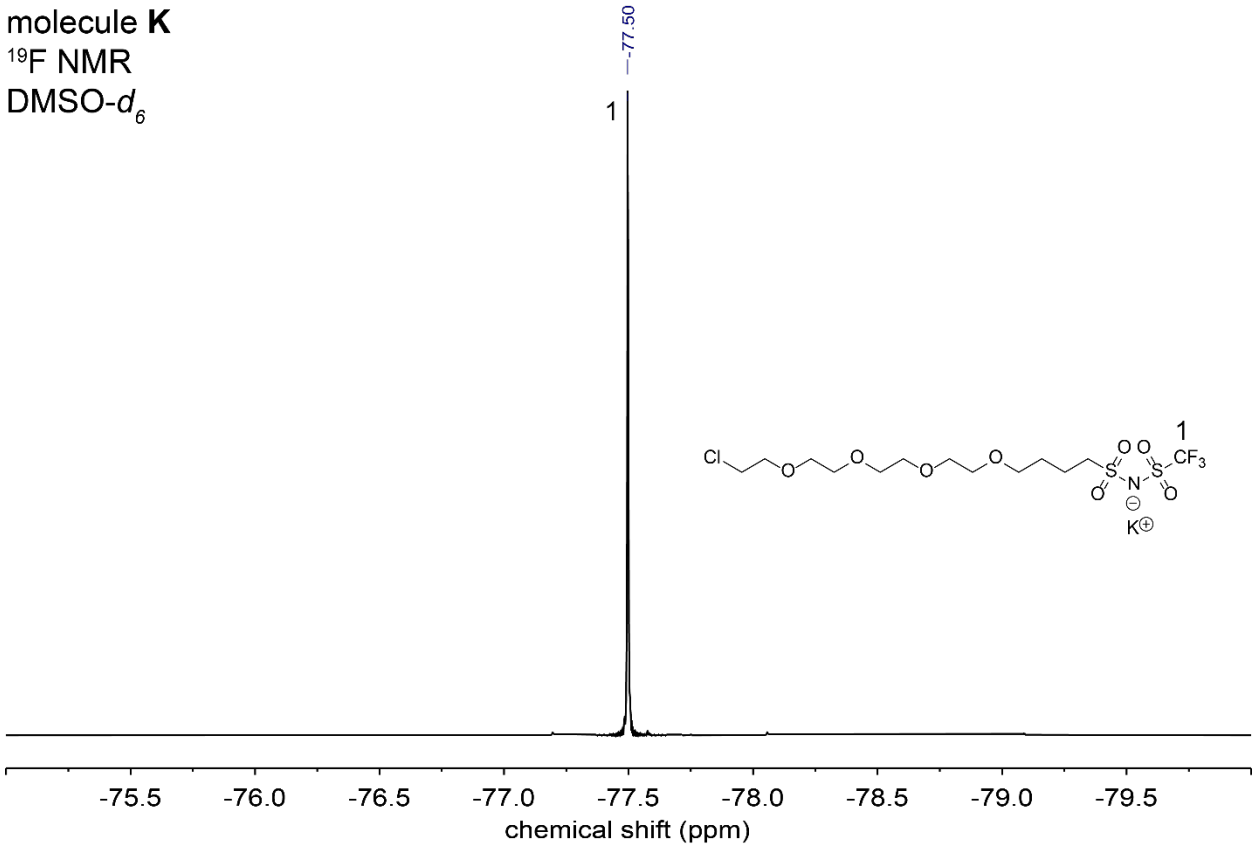
molecule **K**
^{19}F NMR
DMSO-d_6
-77.50
1
chemical shift (ppm)

Molecule **L**

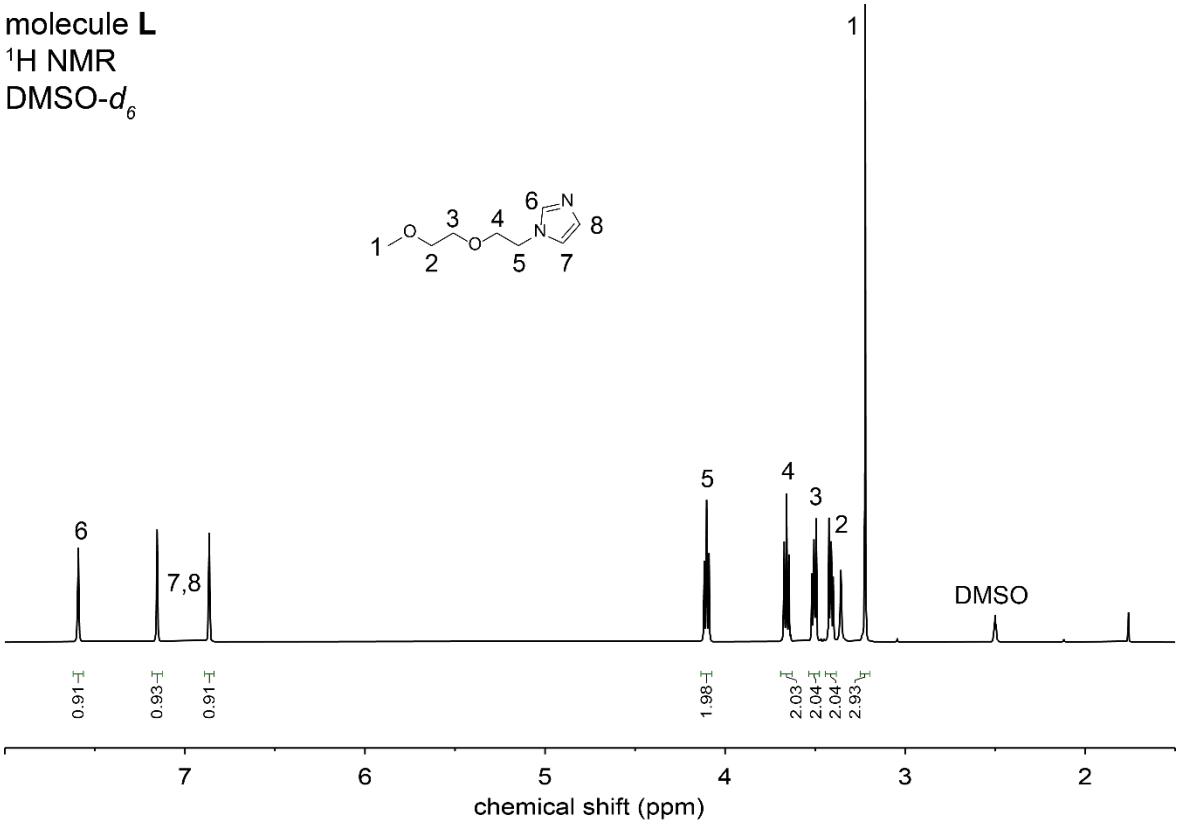
molecule **L**
^{1}H NMR
DMSO-d_6
1
6
7,8
5
4
3
2
DMSO
0.91
0.93
0.91
1.98
2.03
2.04
2.04
2.93
chemical shift (ppm)

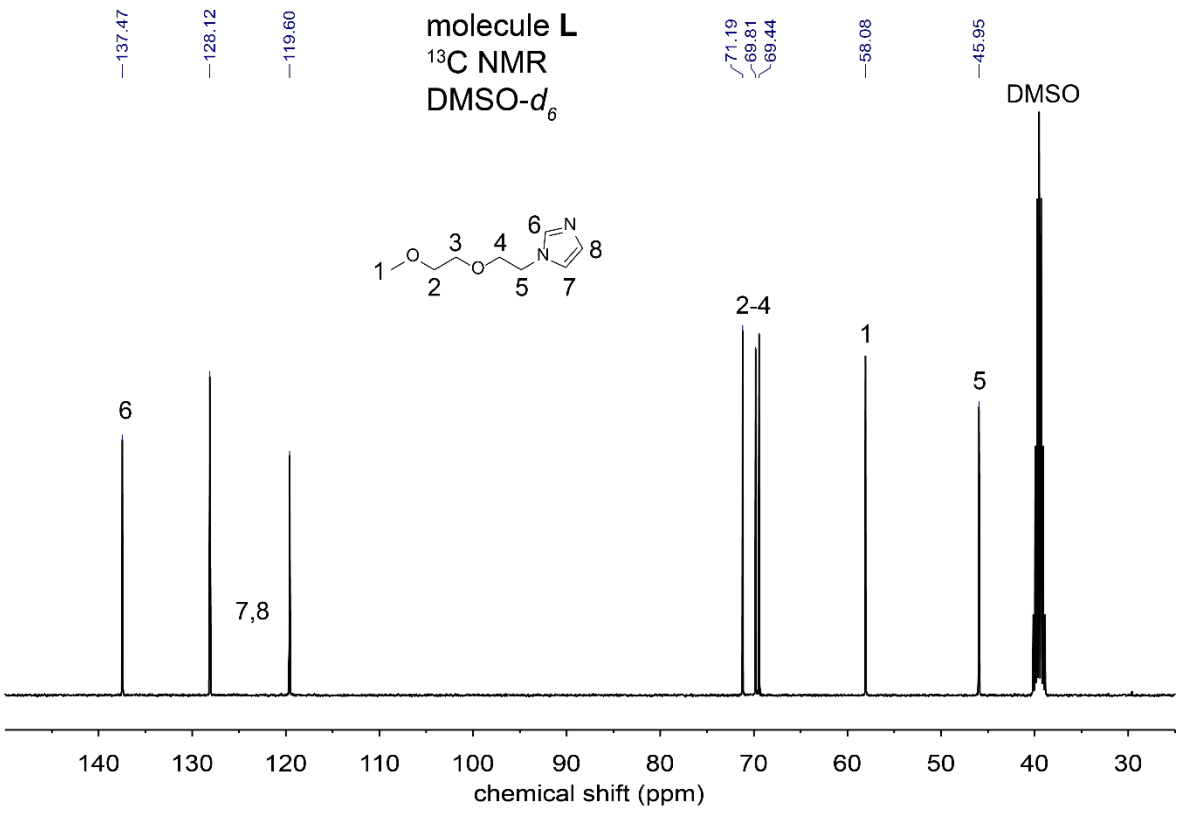
137.47
128.12
119.60
71.19
69.81
69.44
58.08
45.95
molecule **L**
^{13}C NMR
DMSO-d_6
DMSO
2-4
1
5
6
7,8
chemical shift (ppm)

Molecule **M**

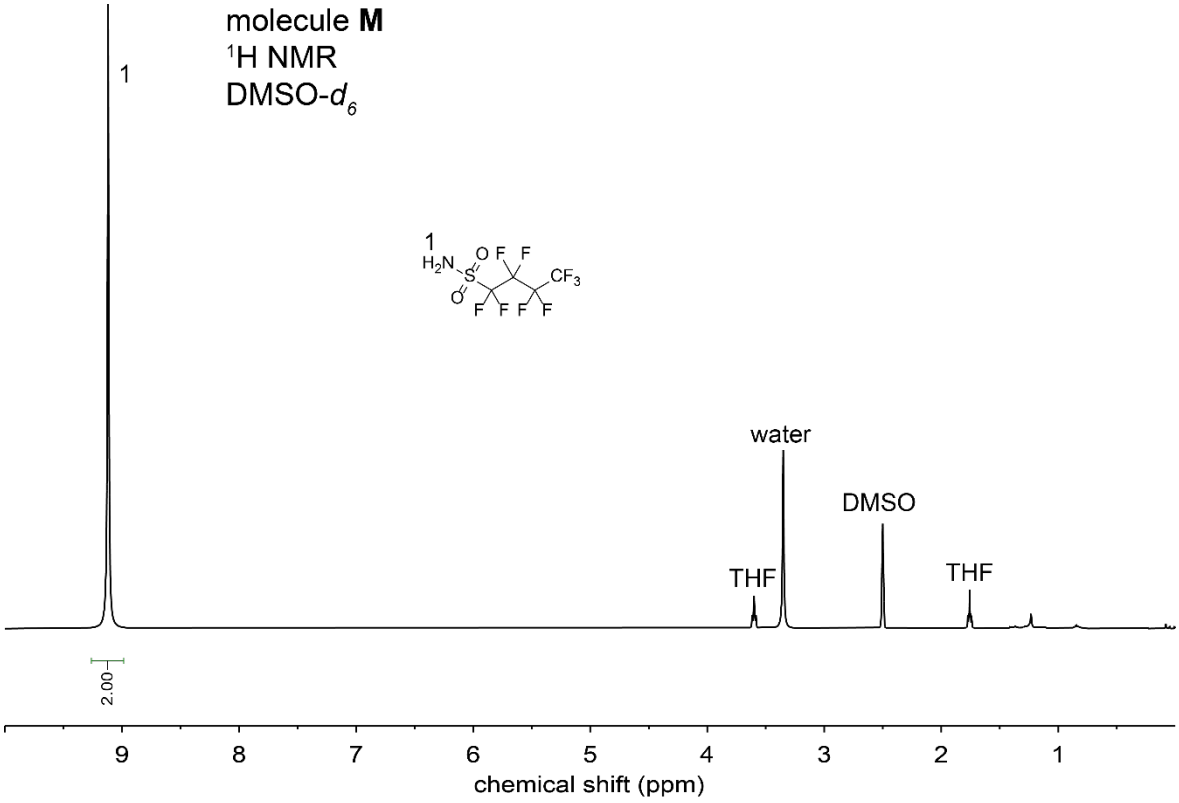
molecule **M**
^{1}H NMR
DMSO-d_6
1
water
DMSO
THF
THF
2.00
9
8
7
6
5
4
3
2
1
chemical shift (ppm)

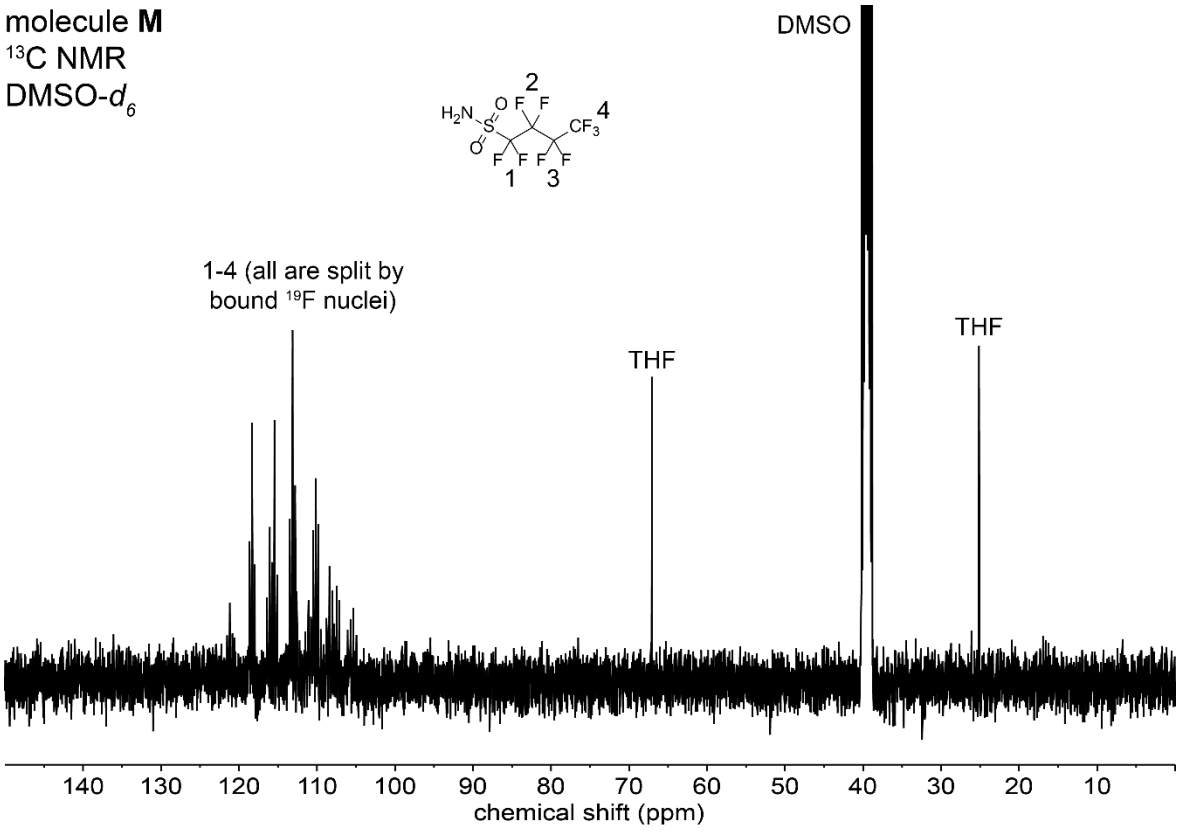
molecule **M**
^{13}C NMR
DMSO-d_6
DMSO
1-4 (all are split by bound ^{19}F nuclei)
THF
THF
140
130
120
110
100
90
80
70
60
50
40
30
20
10
chemical shift (ppm)

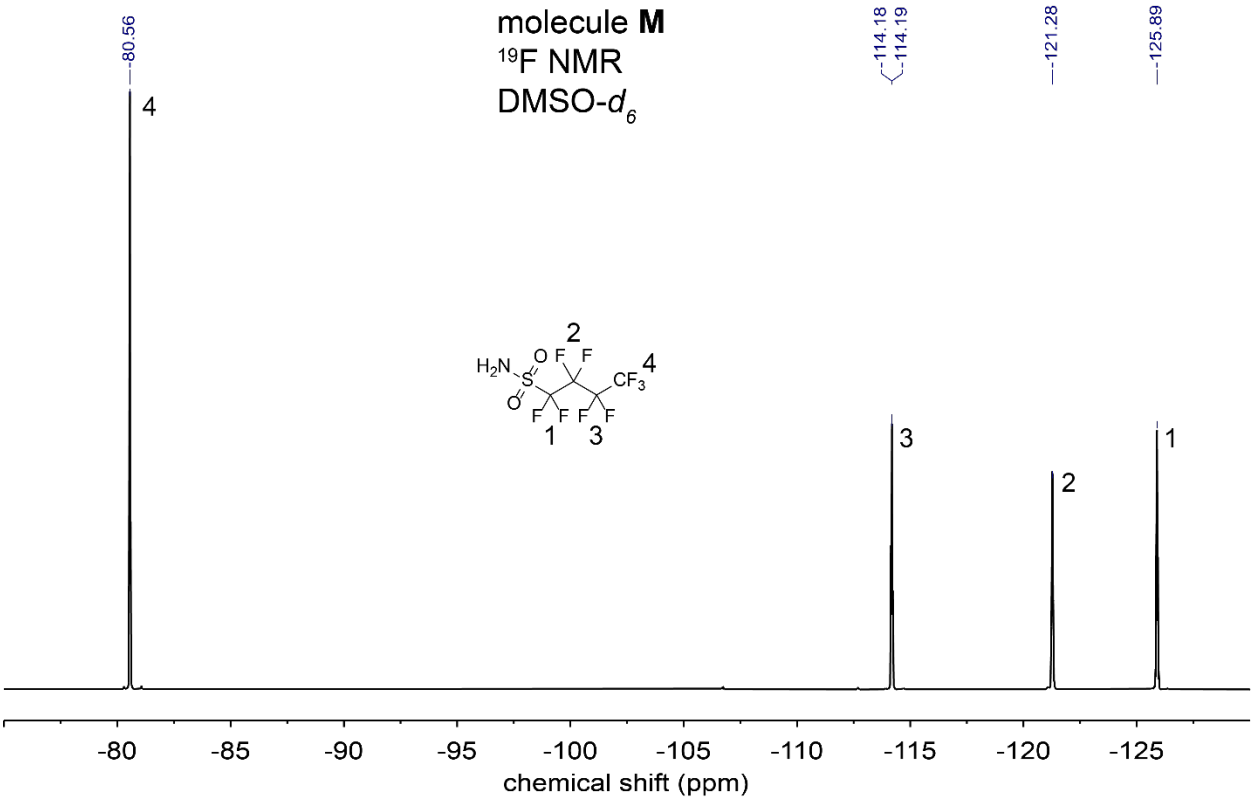
molecule **M**
^{19}F NMR
DMSO-d_6
-80.56
-114.18
-114.19
-121.28
-125.89
4
3
2
1
chemical shift (ppm)

Molecule **N**

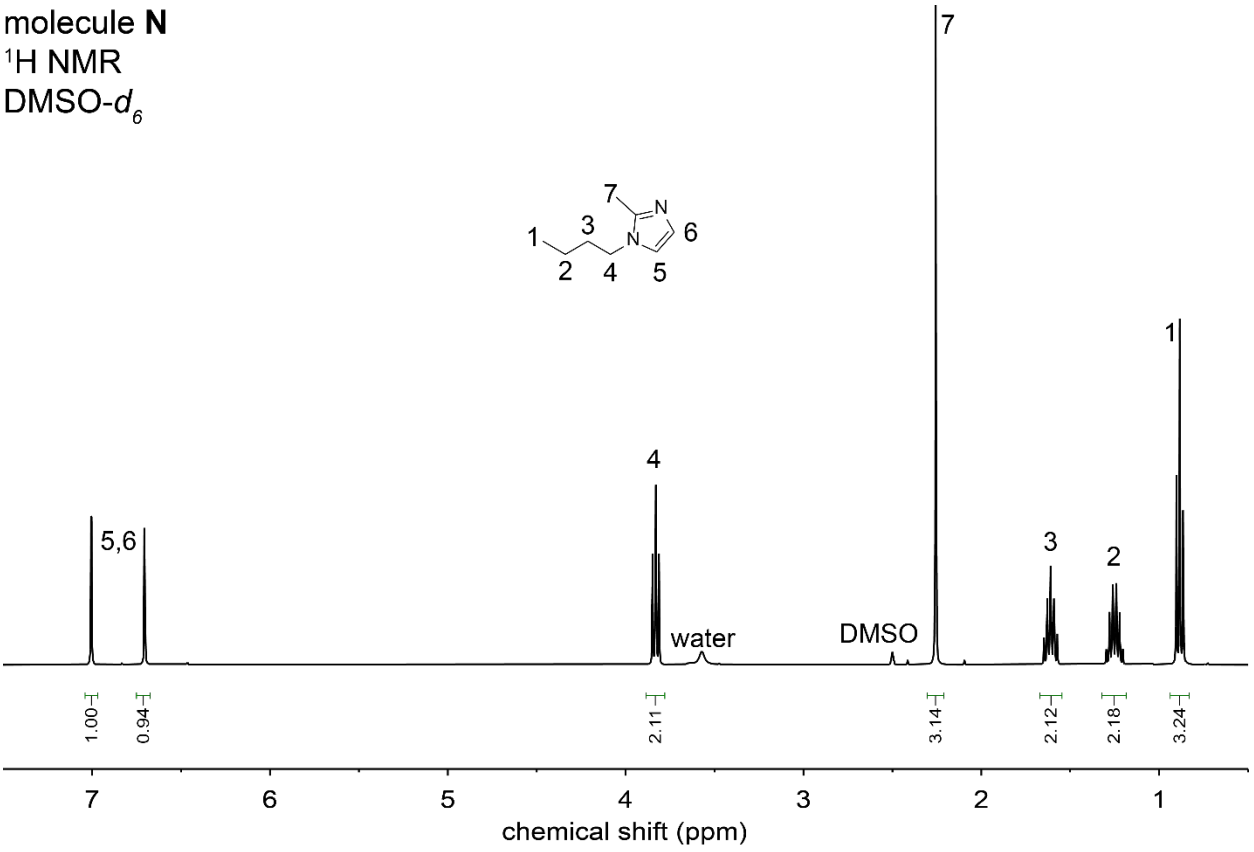
molecule **N**
^{1}H NMR
DMSO-d_6
5,6
4
water
DMSO
7
3
2
1
1.00
0.94
2.11
3.14
2.12
2.18
3.24
chemical shift (ppm)

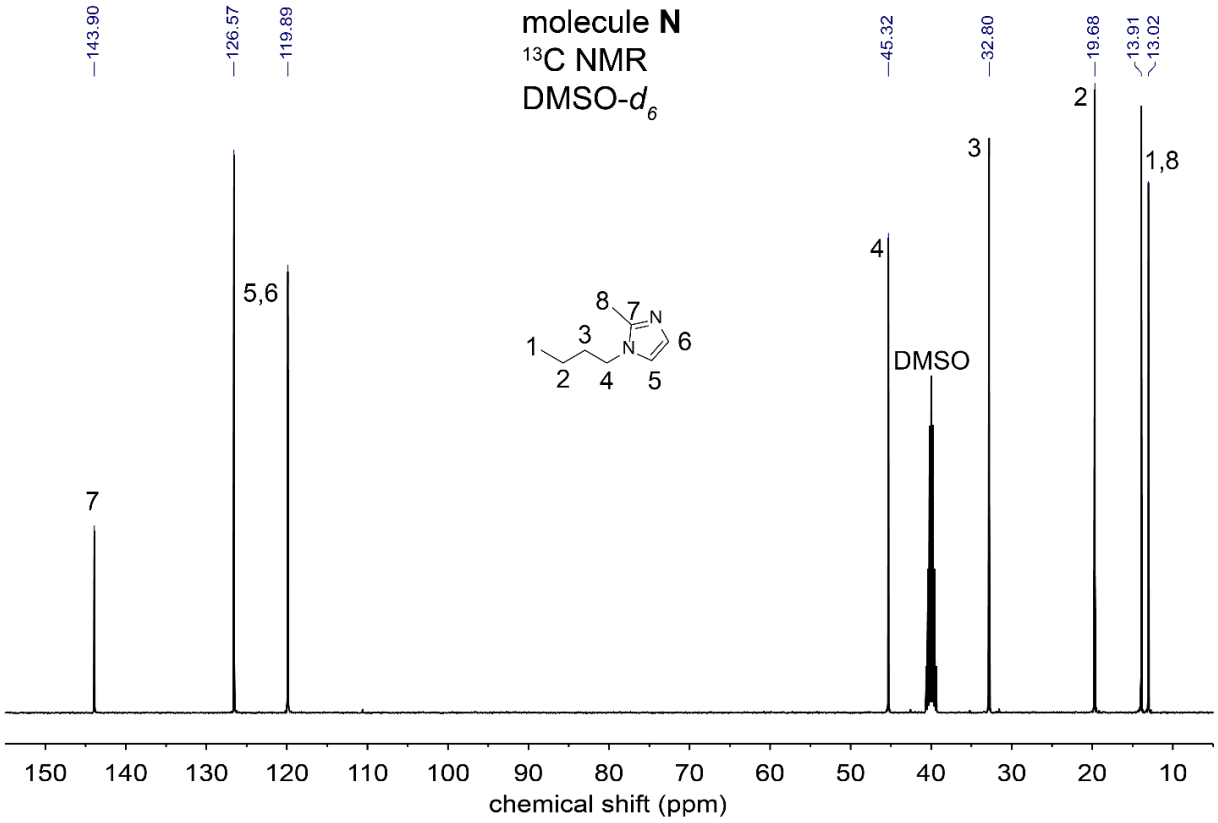
molecule **N**
^{13}C NMR
DMSO-d_6
143.90
126.57
119.89
45.32
32.80
19.68
13.91
13.02
7
5,6
4
DMSO
3
2
1,8
chemical shift (ppm)

Molecule **O**

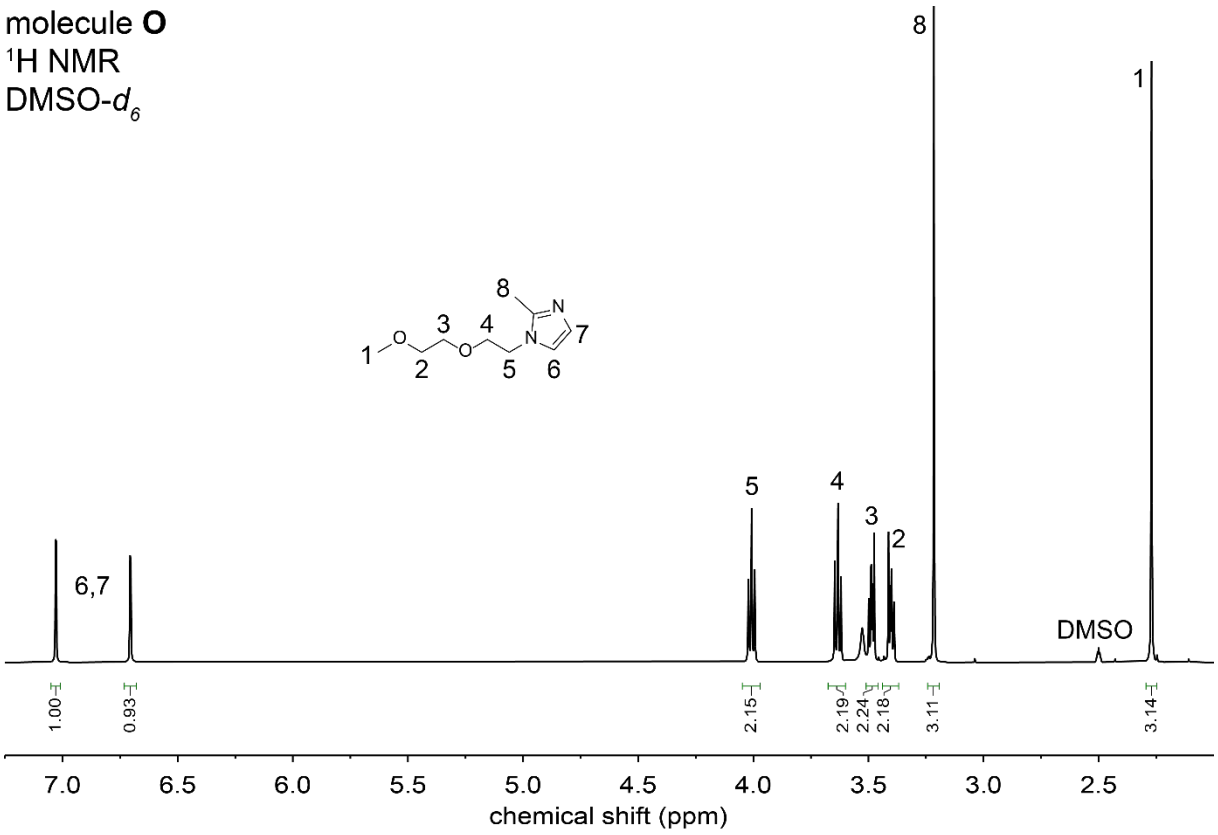
molecule **O**
^{1}H NMR
DMSO-d_6
8
1
6,7
5
4
3
2
DMSO
1.00
0.93
2.15
2.19
2.24
2.18
3.11
3.14
chemical shift (ppm)

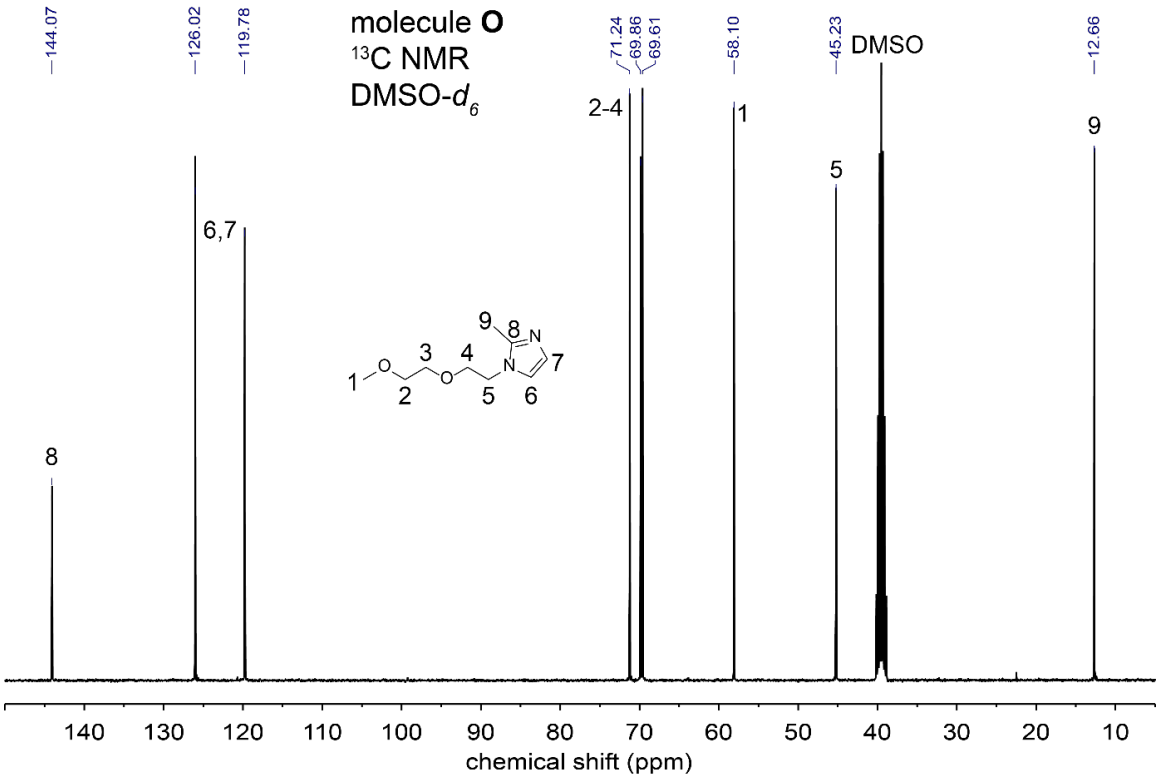
molecule O
13C NMR
DMSO-d6
144.07
126.02
119.78
71.24
69.86
69.61
58.10
45.23
DMSO
12.66
8
6,7
2-4
1
5
9
chemical shift (ppm)

Data S2: Mass spectrometry of zwitterions and intermediates

Molecule **1**

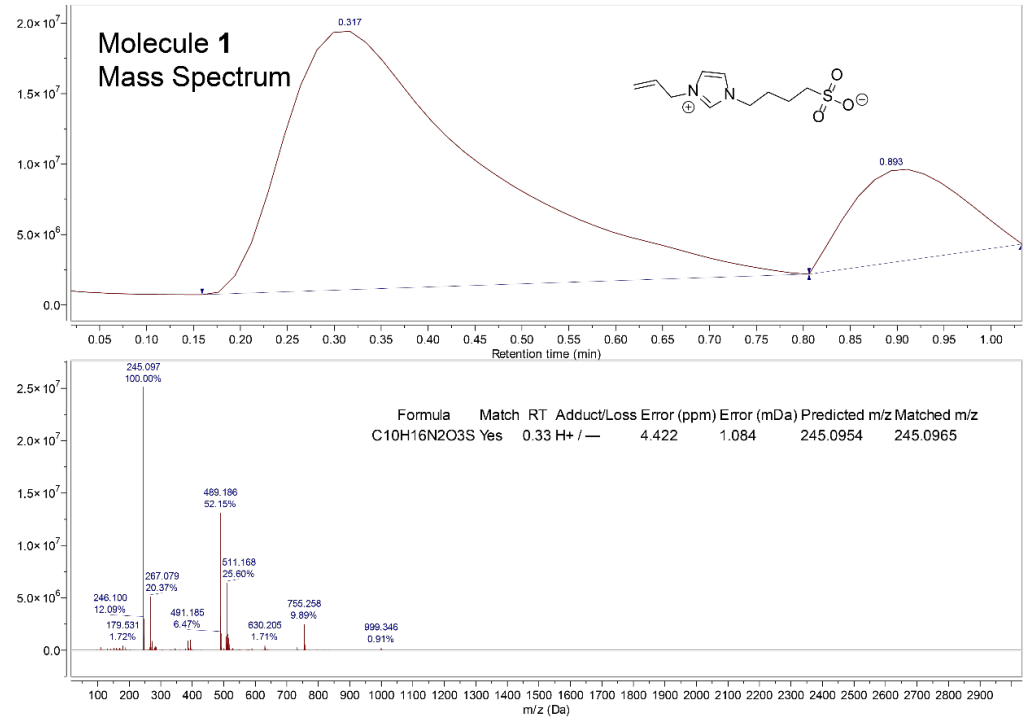

Molecule **2**

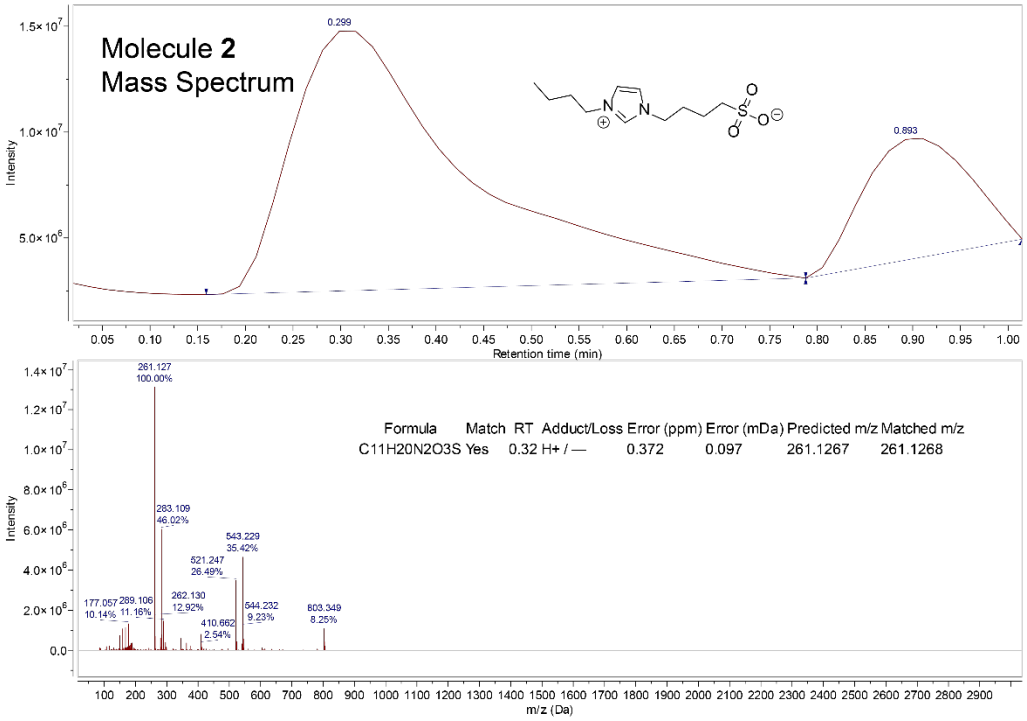

Molecule **3**

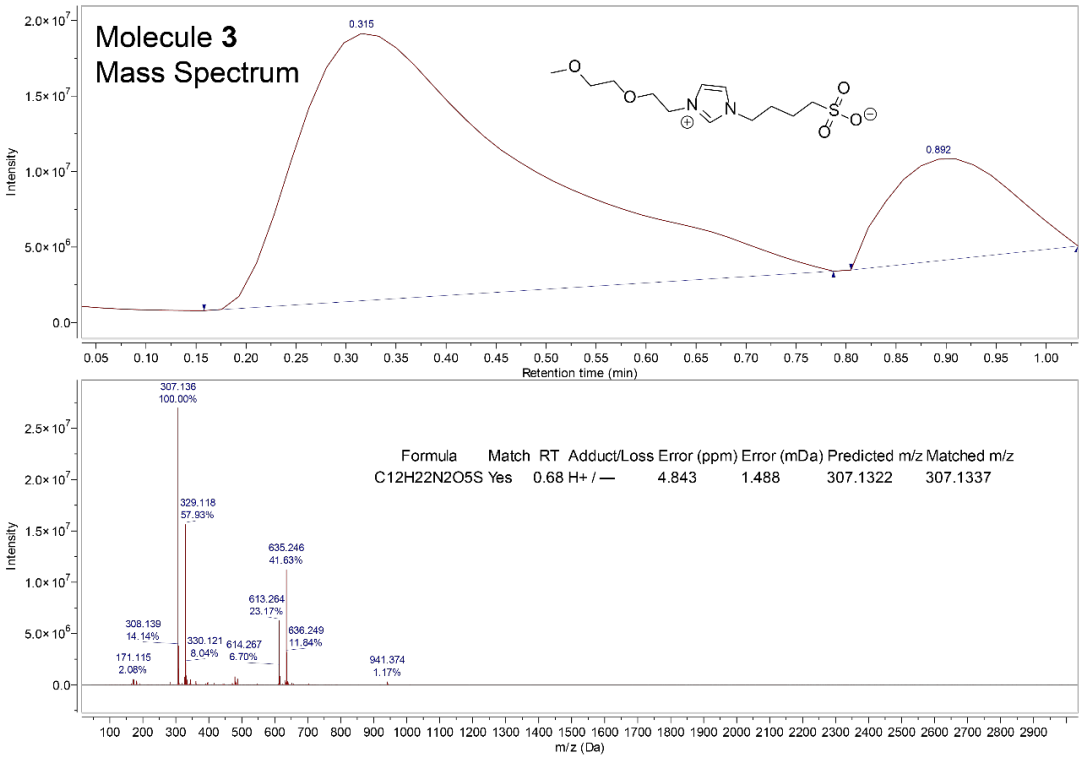

Formula	Match	RT	Adduct/Loss	Error (ppm)	Error (mDa)	Predicted m/z	Matched m/z
C12H22N2O5S	Yes	0.68	H+ / —	4.843	1.488	307.1322	307.1337

Molecule **4**

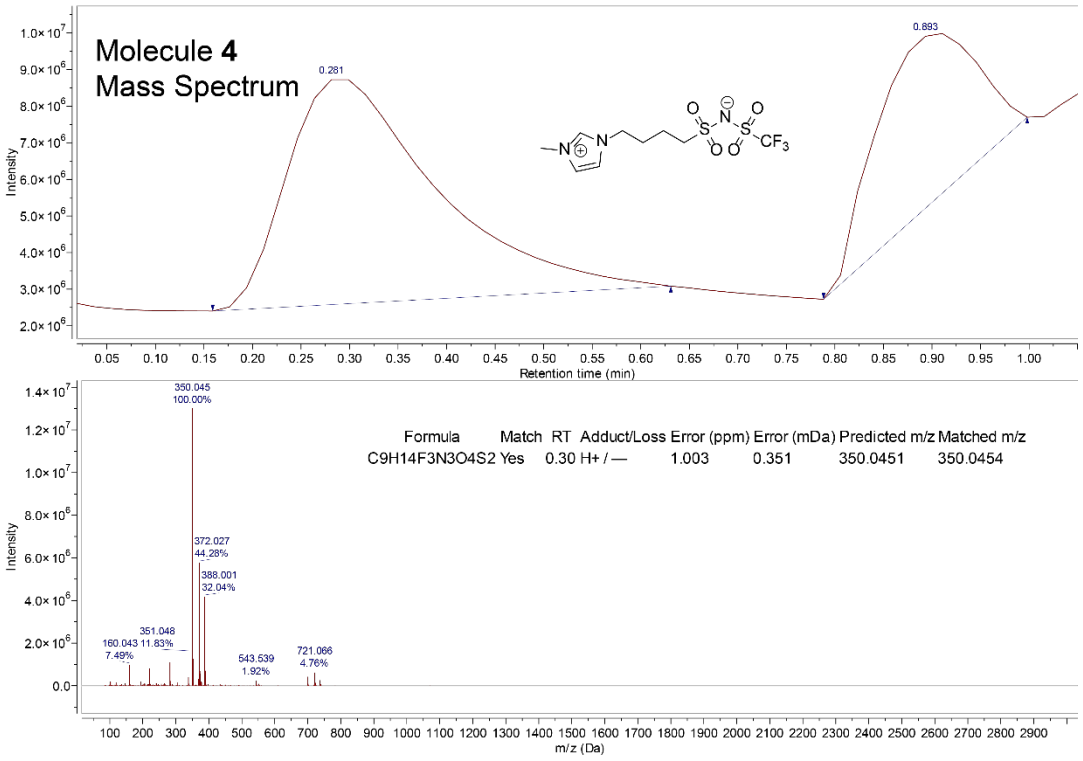

Formula	Match	RT	Adduct/Loss	Error (ppm)	Error (mDa)	Predicted m/z	Matched m/z
C9H14F3N3O4S2	Yes	0.30	H+ / —	1.003	0.351	350.0451	350.0454

Molecule **5**

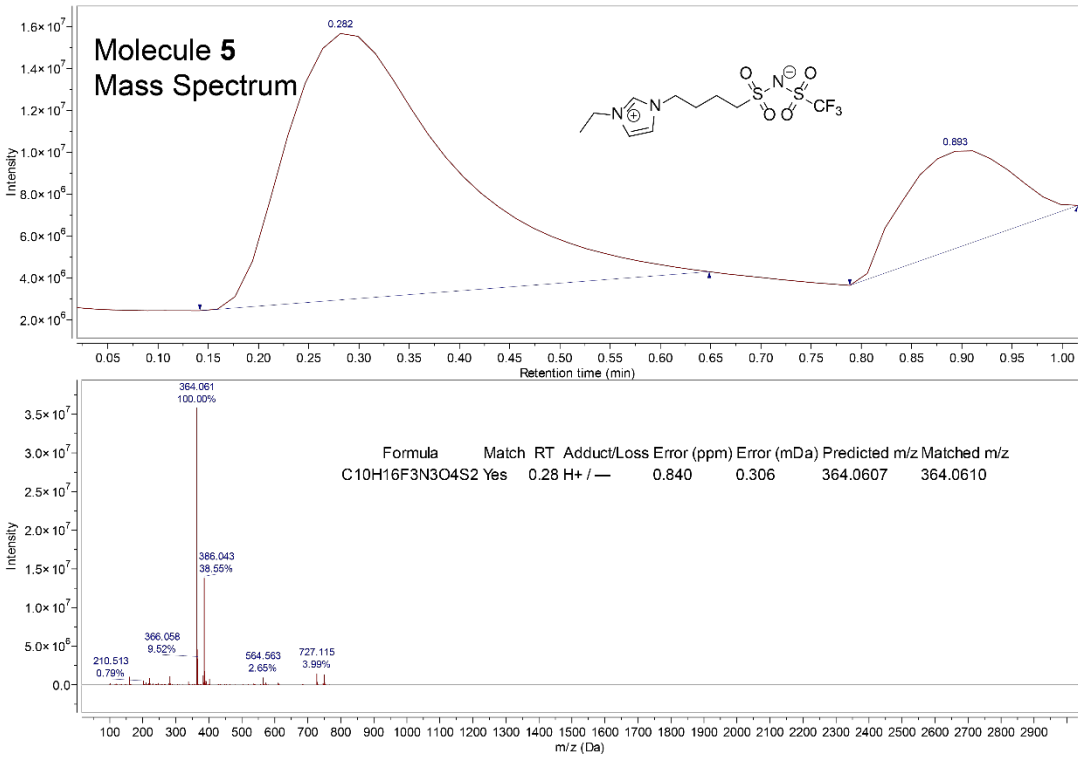

Formula	Match	RT	Adduct/Loss	Error (ppm)	Error (mDa)	Predicted m/z	Matched m/z
C10H16F3N3O4S2	Yes	0.28	H+ / —	0.840	0.306	364.0607	364.0610

Molecule **6**

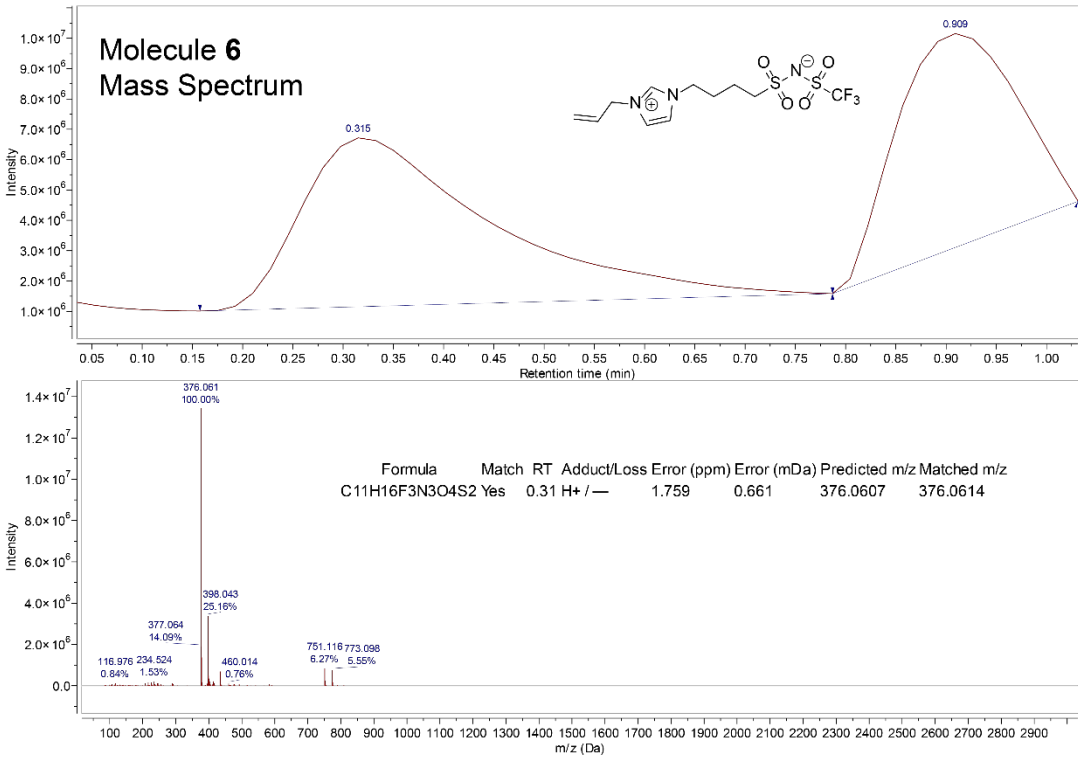

Formula	Match	RT	Adduct/Loss	Error (ppm)	Error (mDa)	Predicted m/z	Matched m/z
C11H16F3N3O4S2	Yes	0.31	H+ / —	1.759	0.661	376.0607	376.0614

Molecule **7**

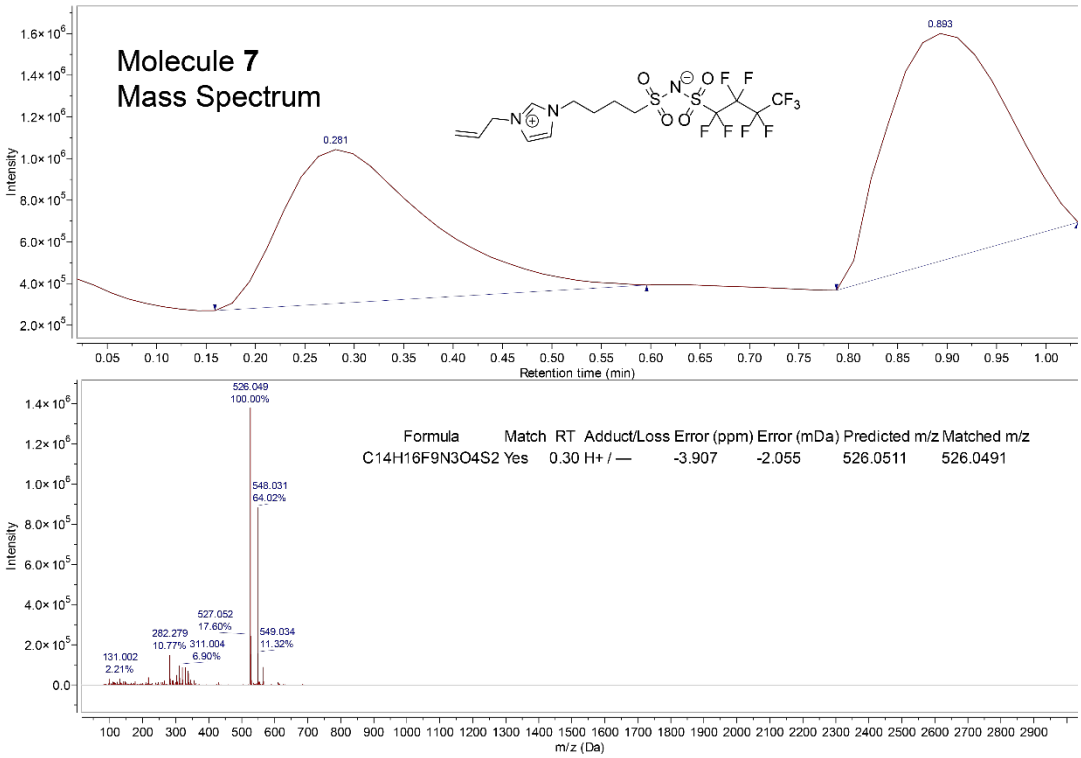

Molecule **8**

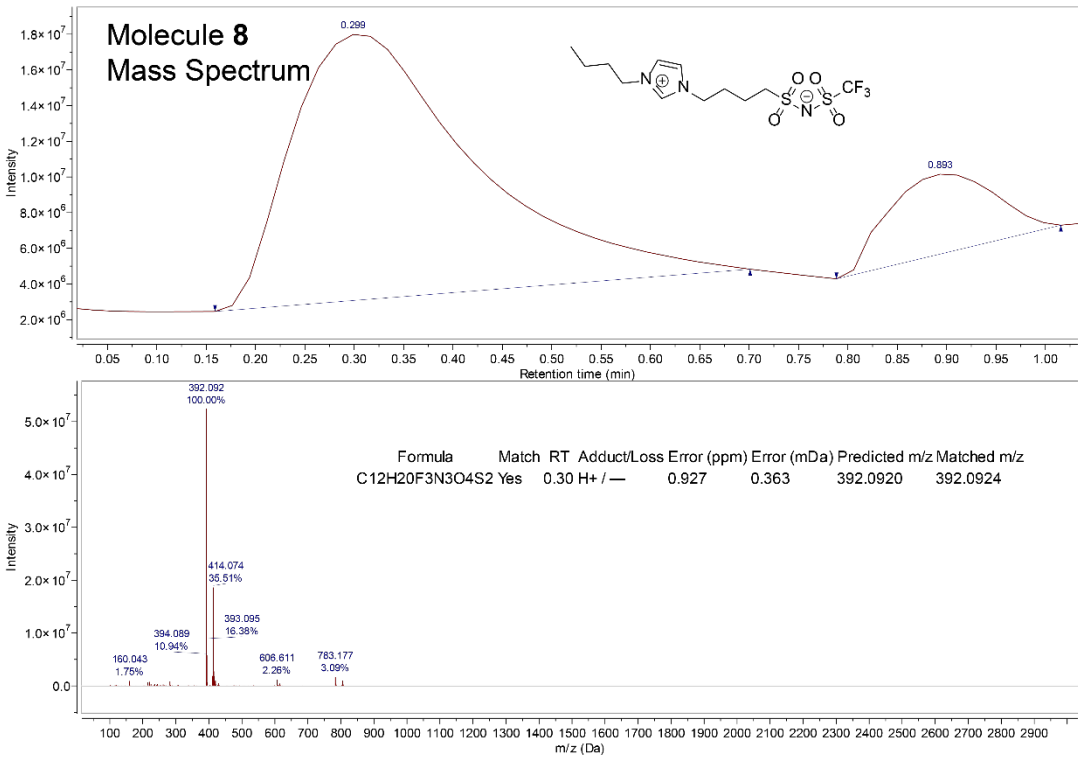

Molecule **9**

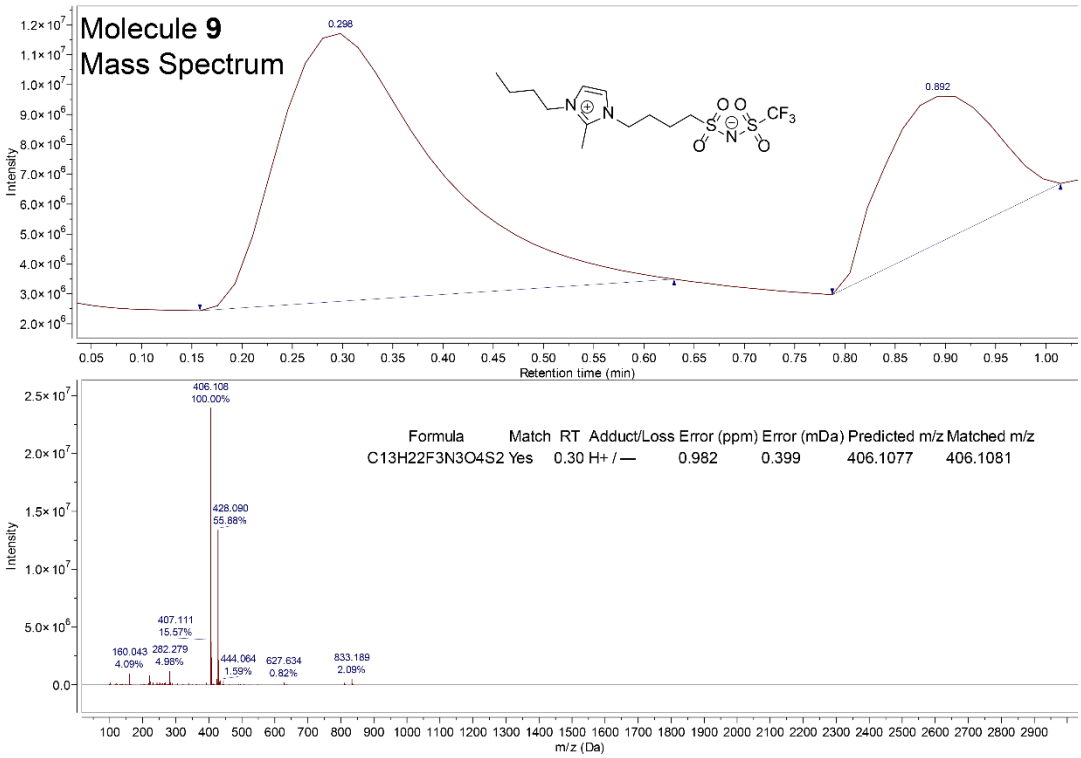

Molecule **10**

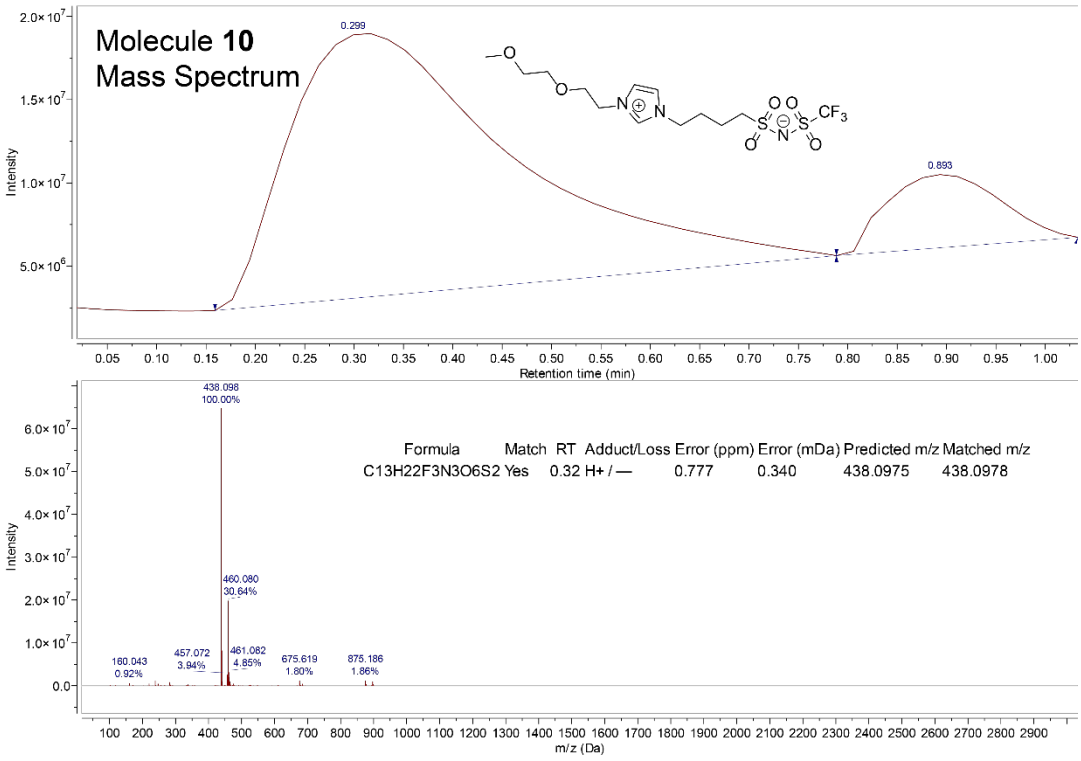

Molecule **11**

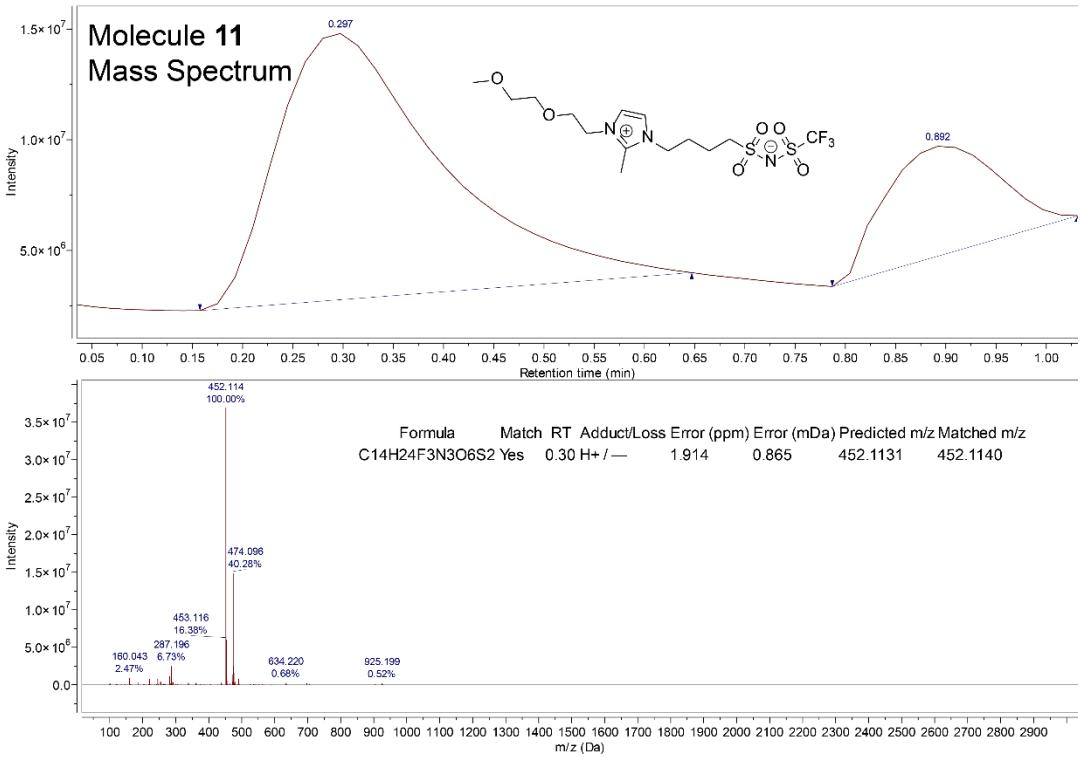

Molecule **12**

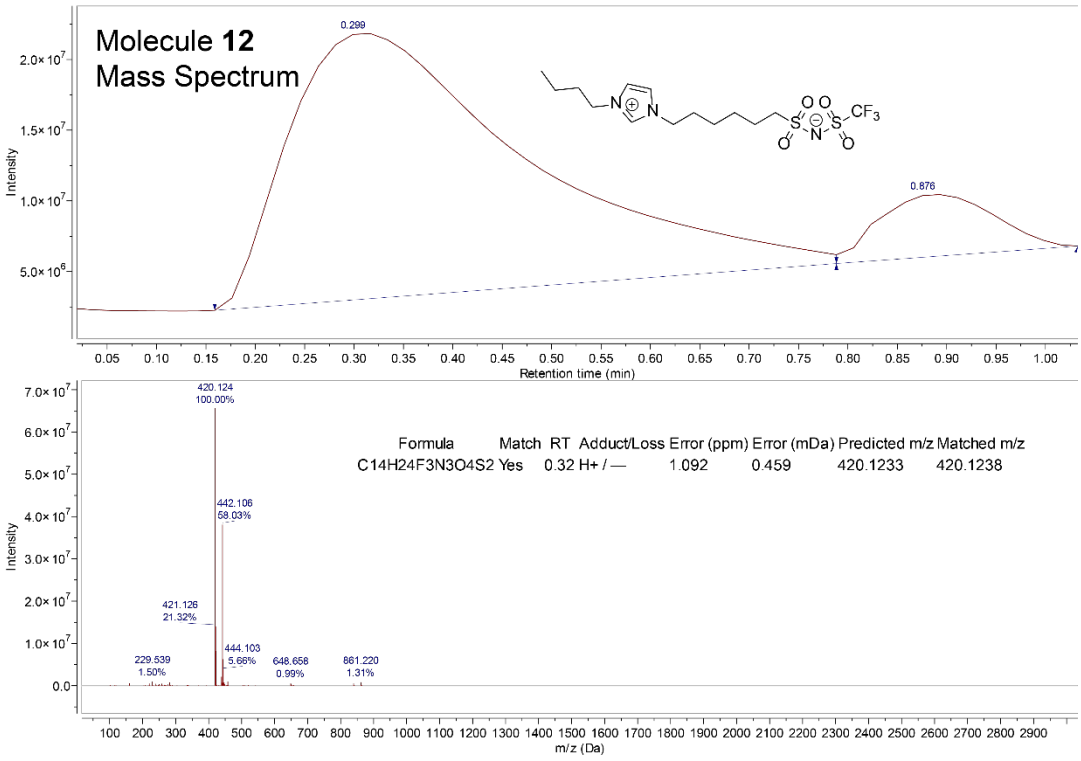

Molecule **13**

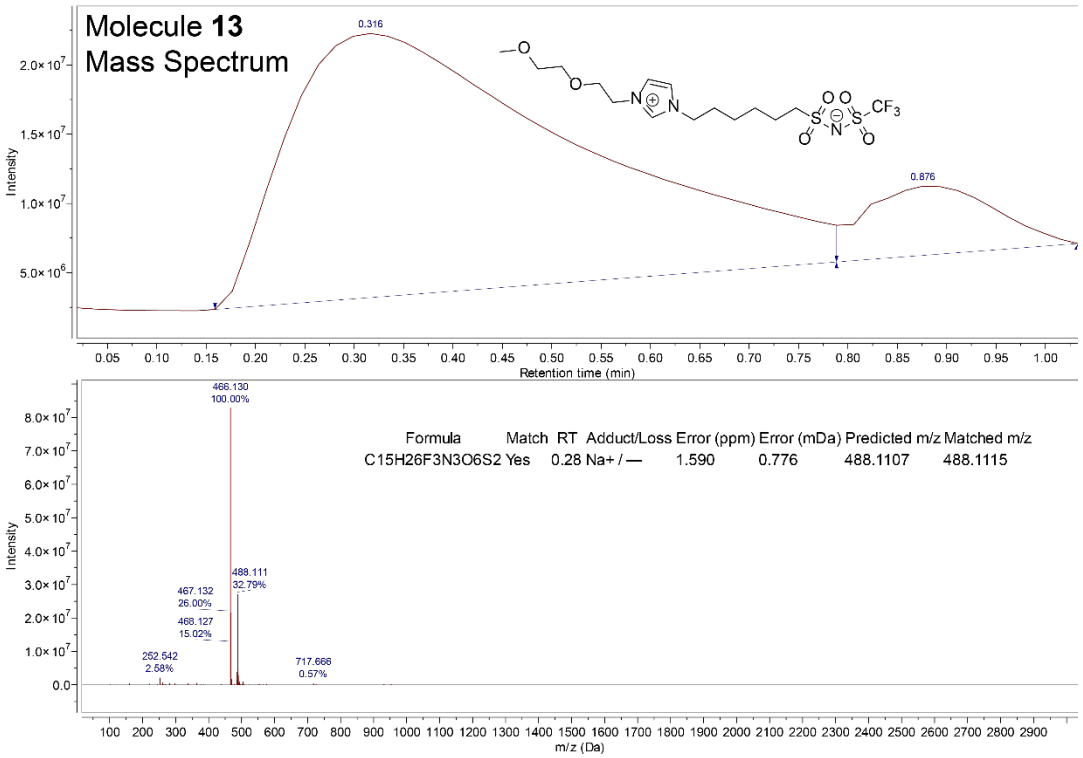

Formula	Match	RT	Adduct/Loss	Error (ppm)	Error (mDa)	Predicted m/z	Matched m/z
C15H26F3N3O6S2	Yes	0.28	Na+ / —	1.590	0.776	488.1107	488.1115

Molecule **14**

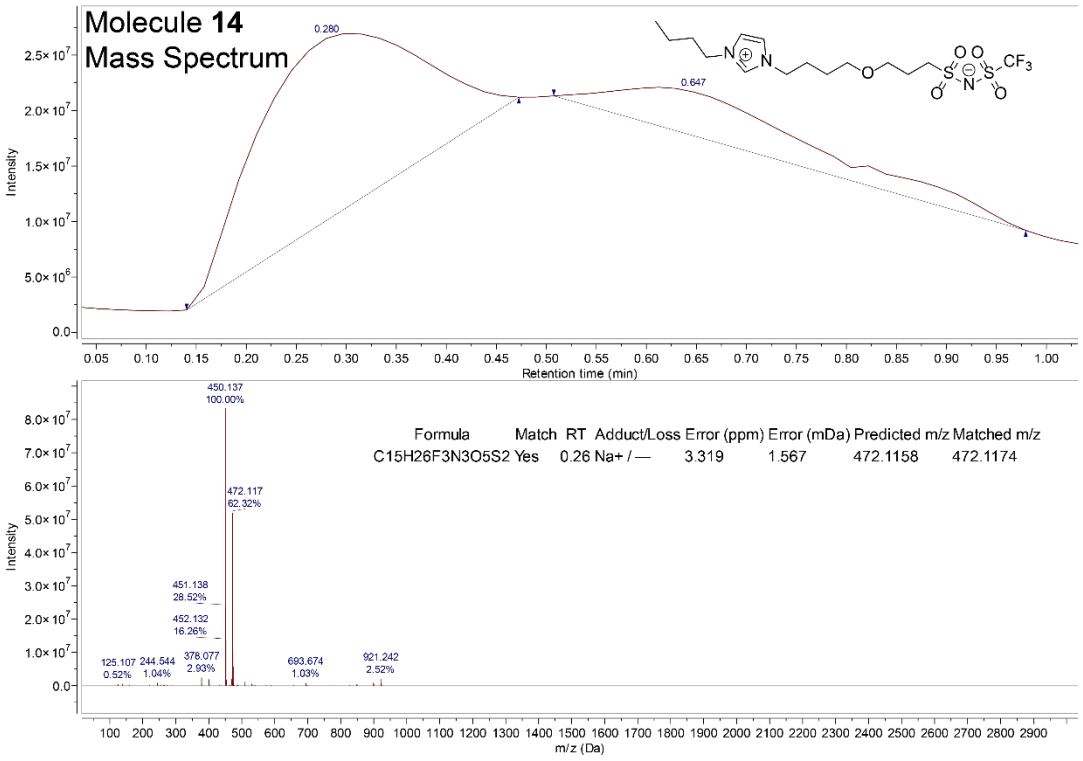

Formula	Match	RT	Adduct/Loss	Error (ppm)	Error (mDa)	Predicted m/z	Matched m/z
C15H26F3N3O5S2	Yes	0.26	Na+ / —	3.319	1.567	472.1158	472.1174

Molecule **15**

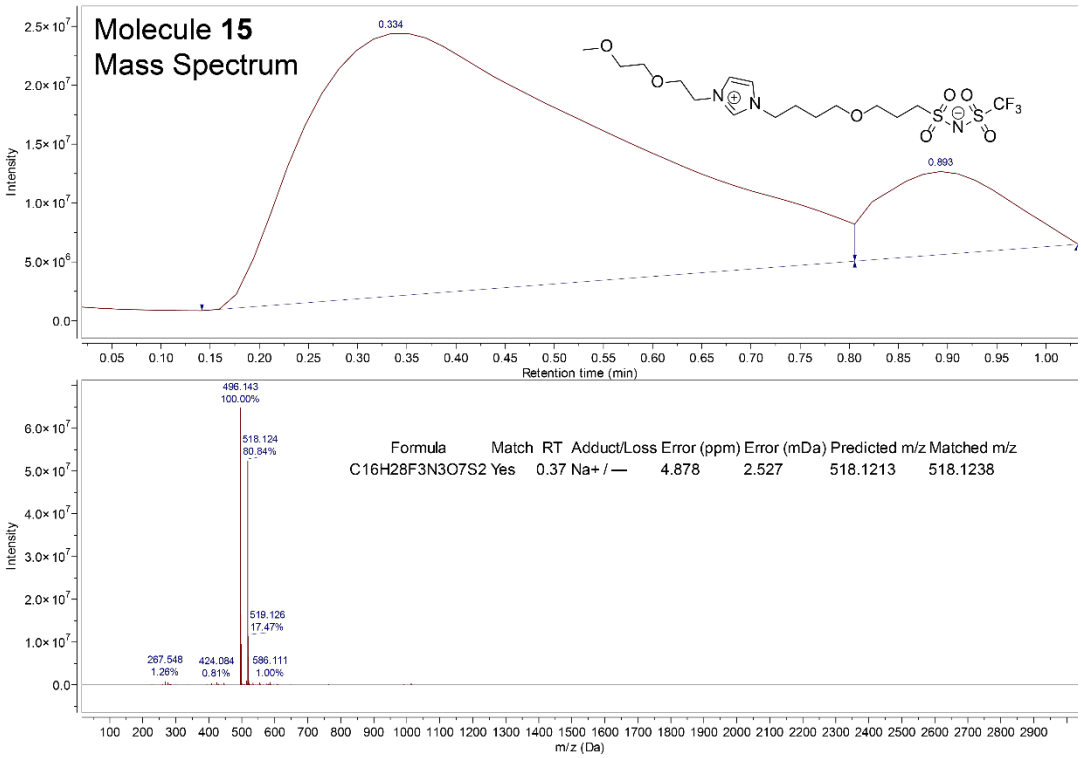

Formula	Match	RT	Adduct/Loss	Error (ppm)	Error (mDa)	Predicted m/z	Matched m/z
C16H28F3N3O7S2	Yes	0.37	Na+ / —	4.878	2.527	518.1213	518.1238

Molecule **16**

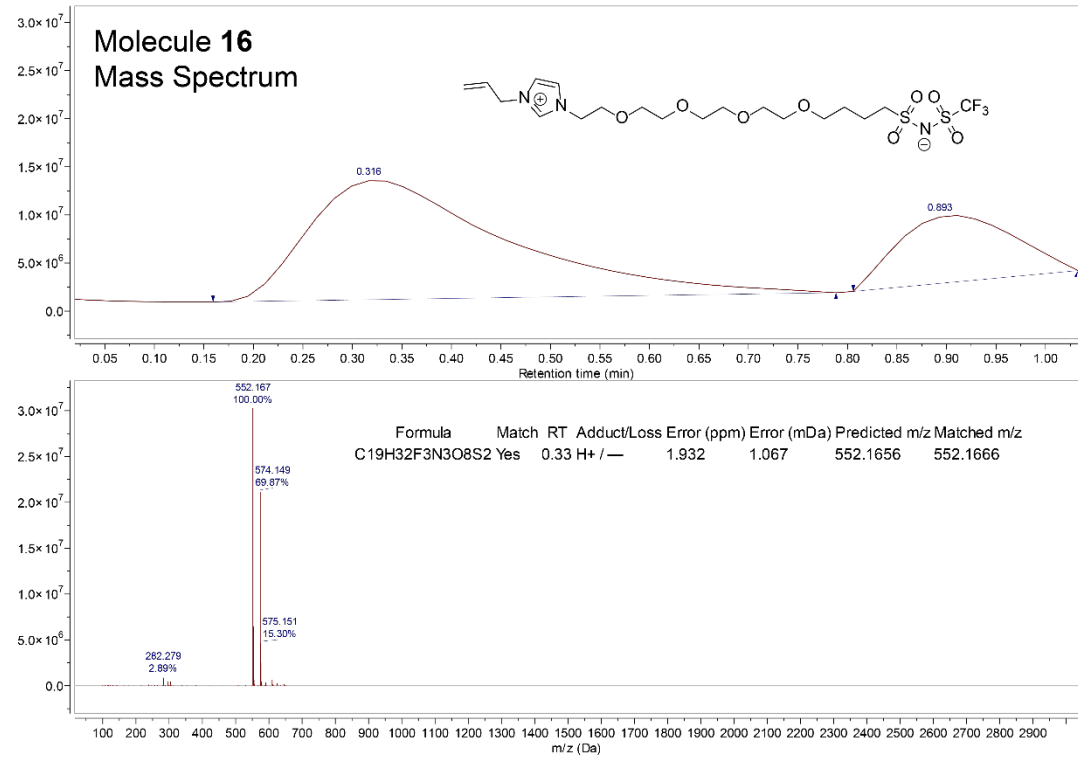

Formula	Match	RT	Adduct/Loss	Error (ppm)	Error (mDa)	Predicted m/z	Matched m/z
C19H32F3N3O8S2	Yes	0.33	H+ / —	1.932	1.067	552.1656	552.1666

Molecule **17**

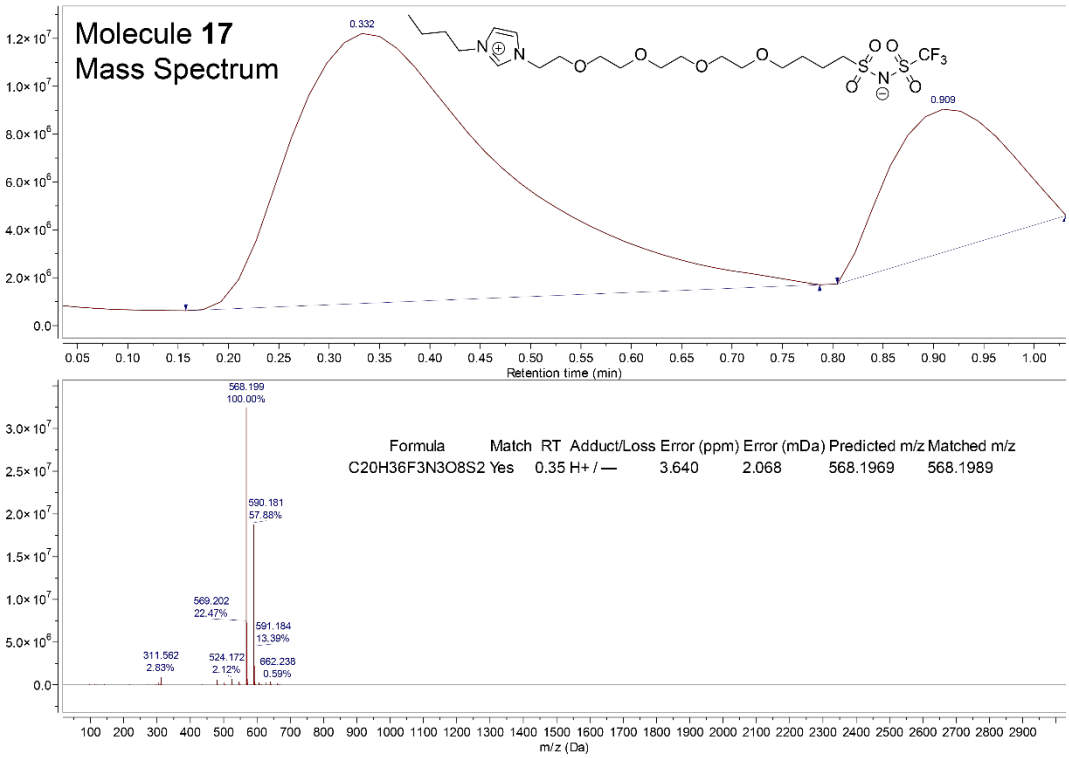

Formula	Match	RT	Adduct/Loss	Error (ppm)	Error (mDa)	Predicted m/z	Matched m/z
C20H36F3N3O8S2	Yes	0.35	H+ / —	3.640	2.068	568.1969	568.1989

Molecule **18**

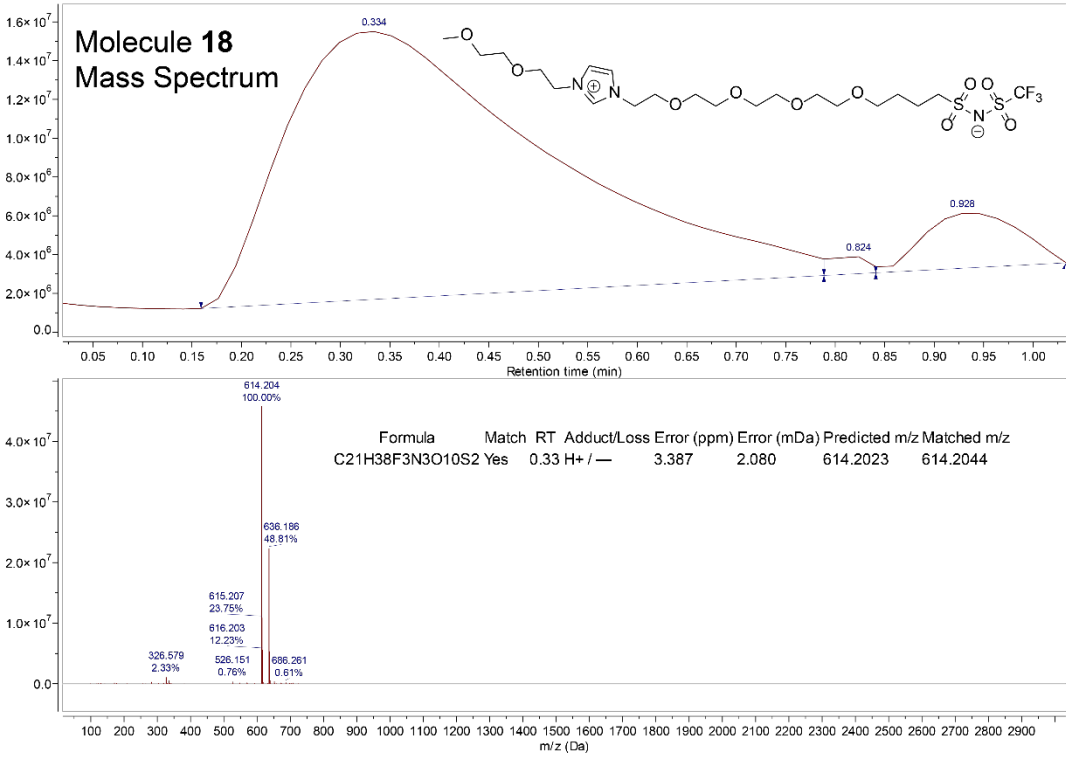

Formula	Match	RT	Adduct/Loss	Error (ppm)	Error (mDa)	Predicted m/z	Matched m/z
C21H38F3N3O10S2	Yes	0.33	H+ / —	3.387	2.080	614.2023	614.2044

Molecule **B-CF_3**

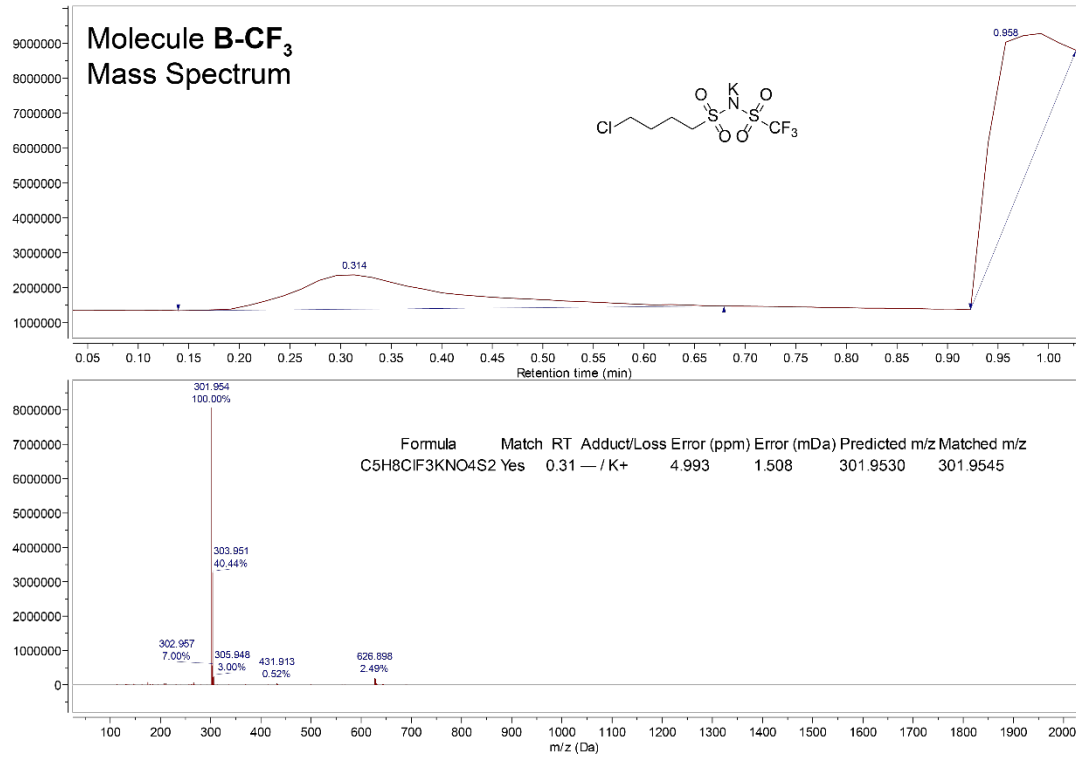

Molecule **B-$_4CF_9$**

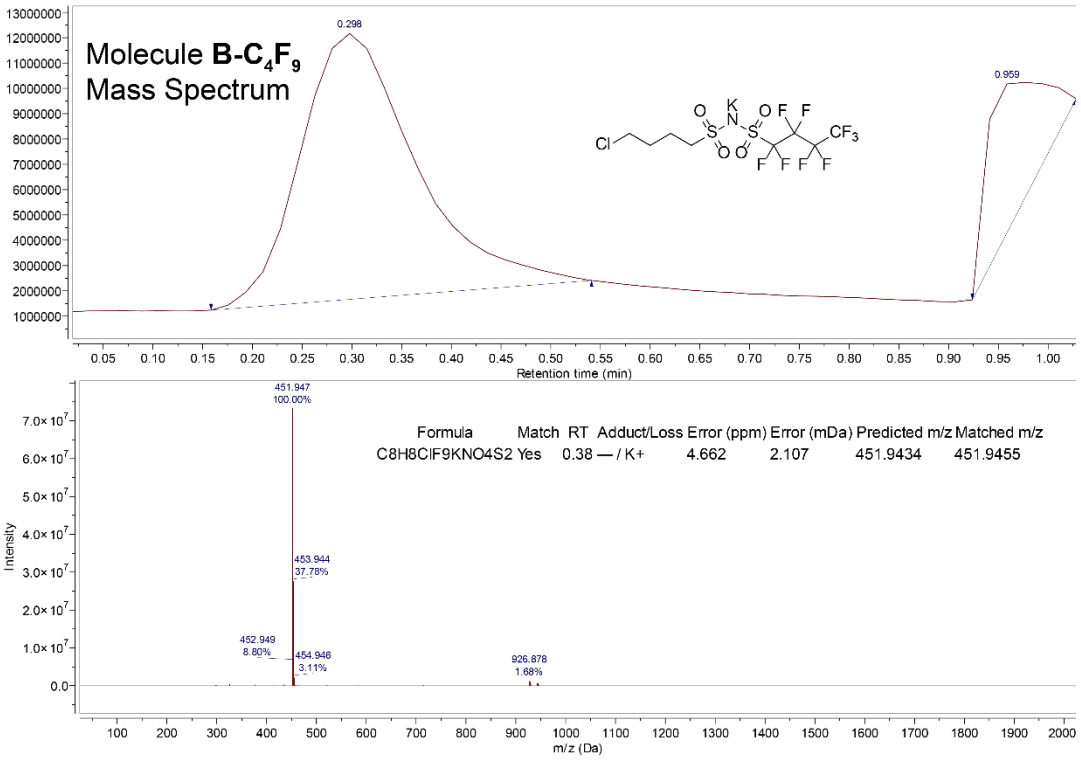

Molecule **C**

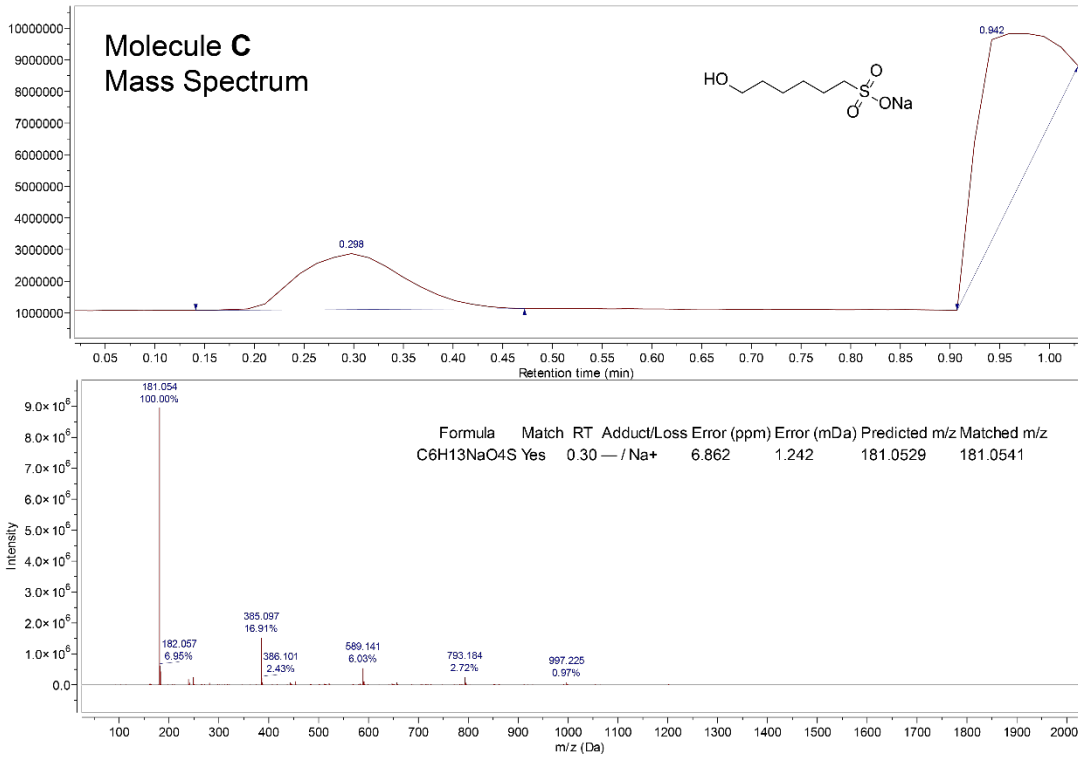

Molecule **E**

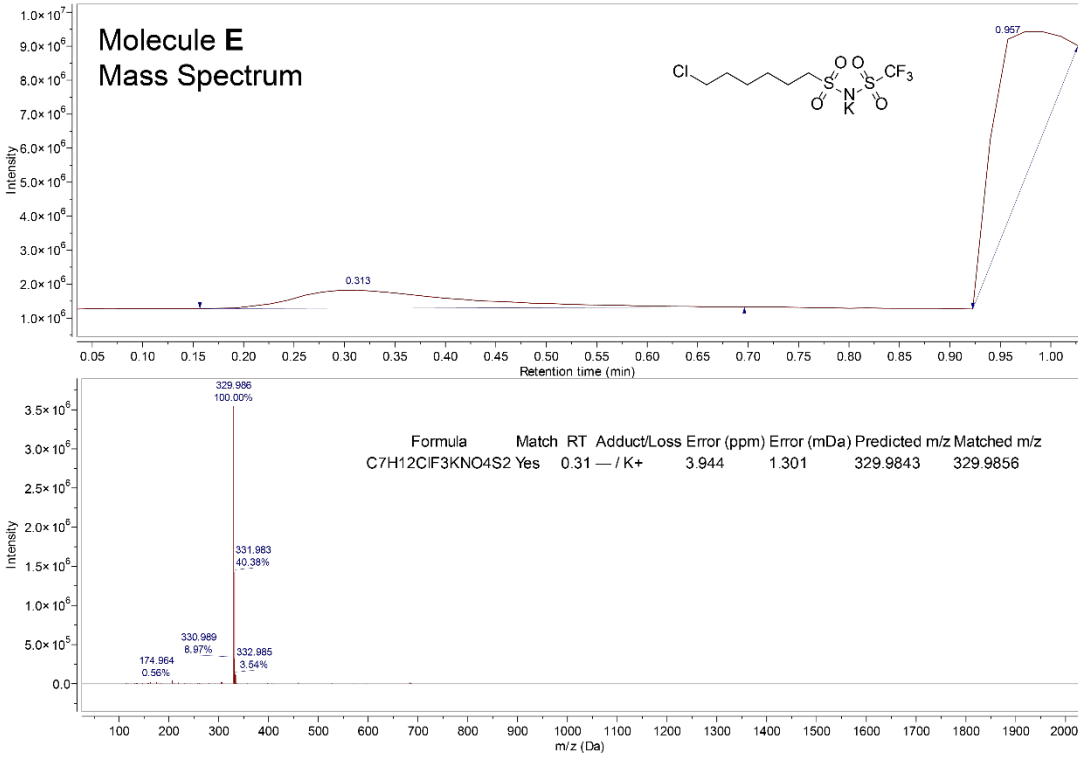

Molecule **F**

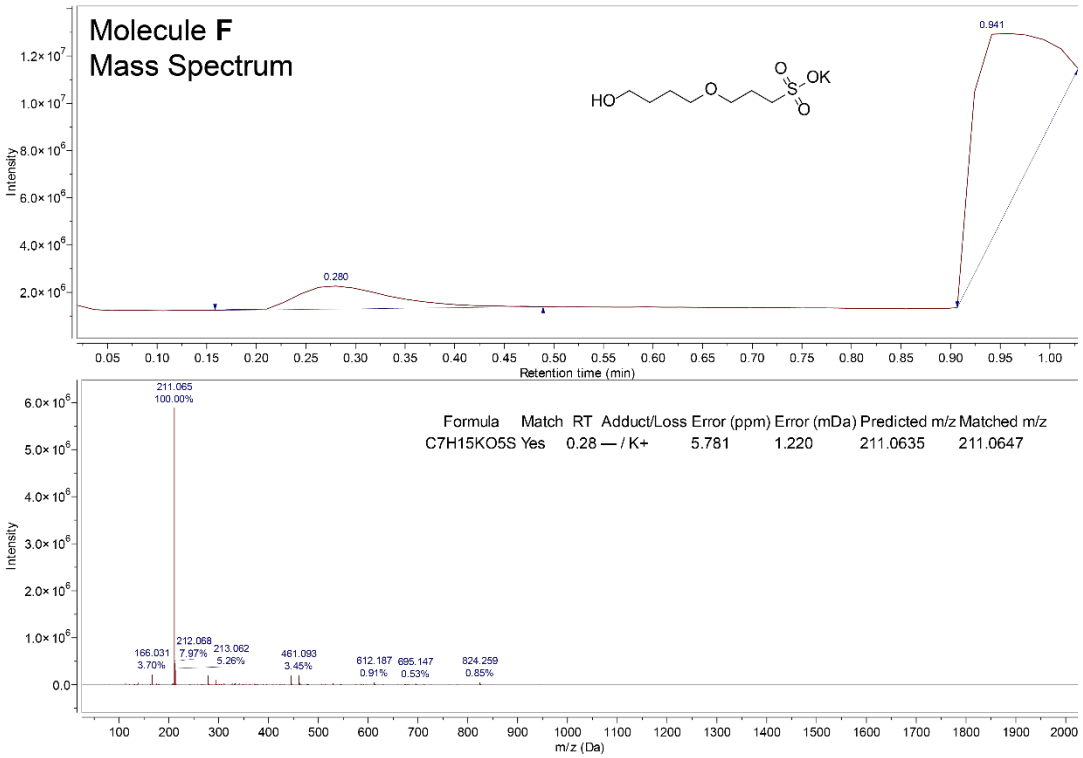

Molecule **H**

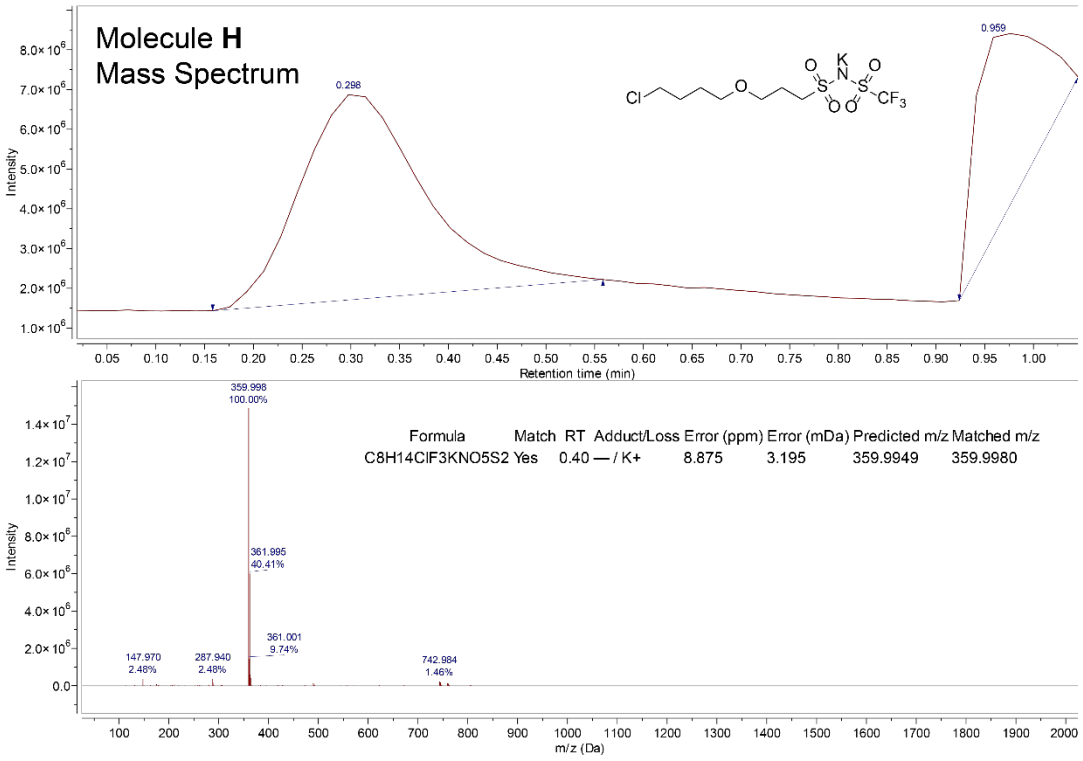

Molecule **I**

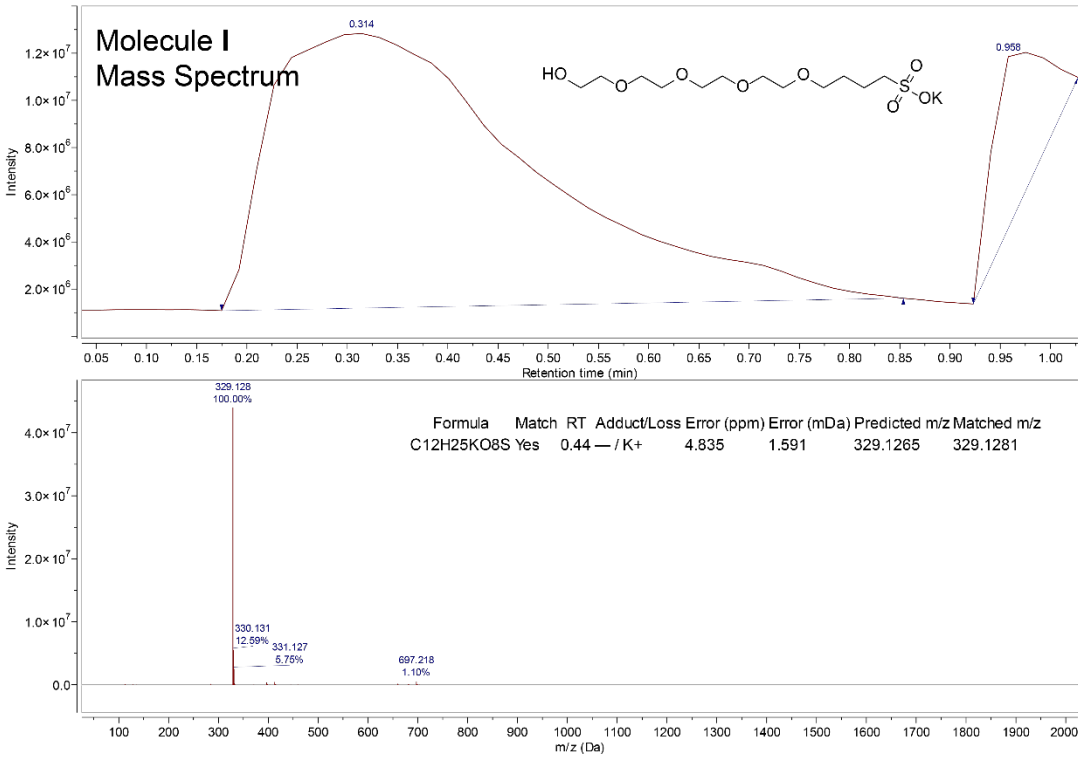

Molecule **K**

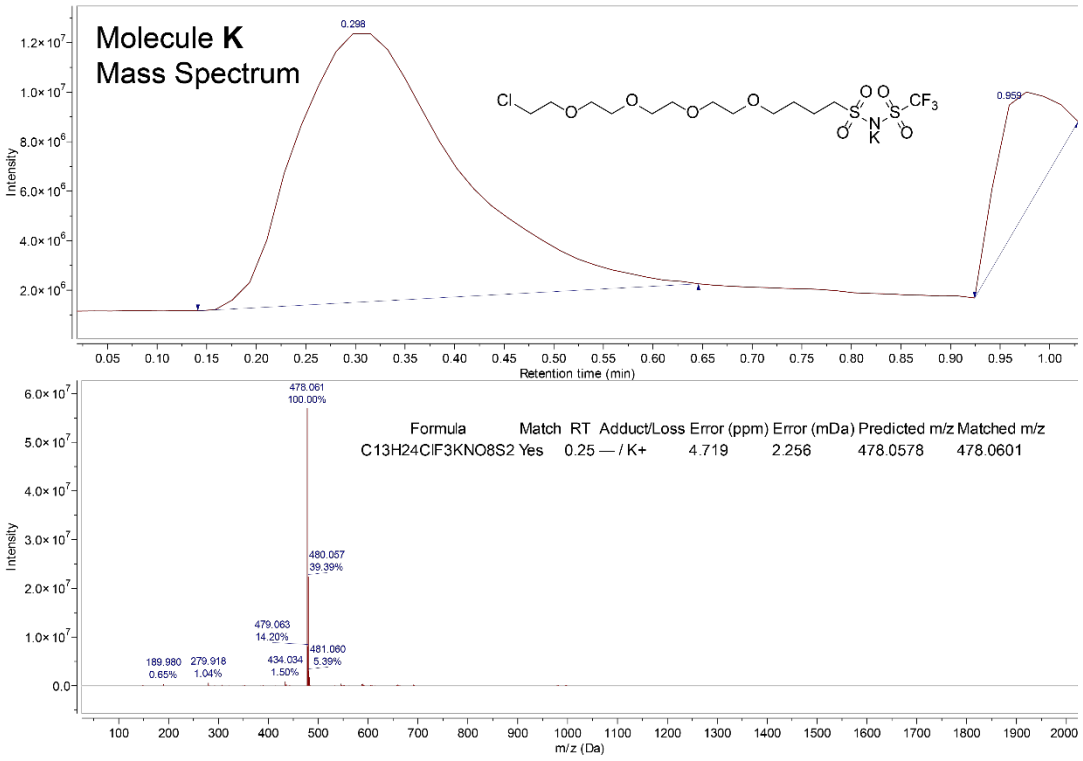

Molecule **L**

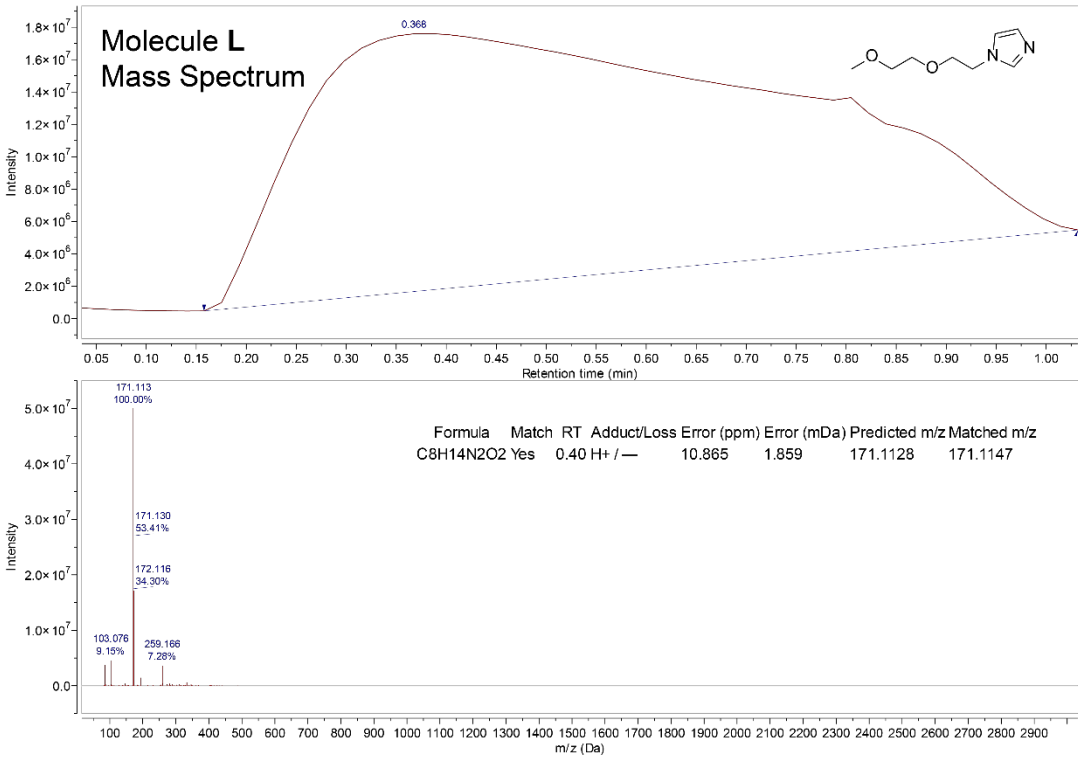

Molecule **M**

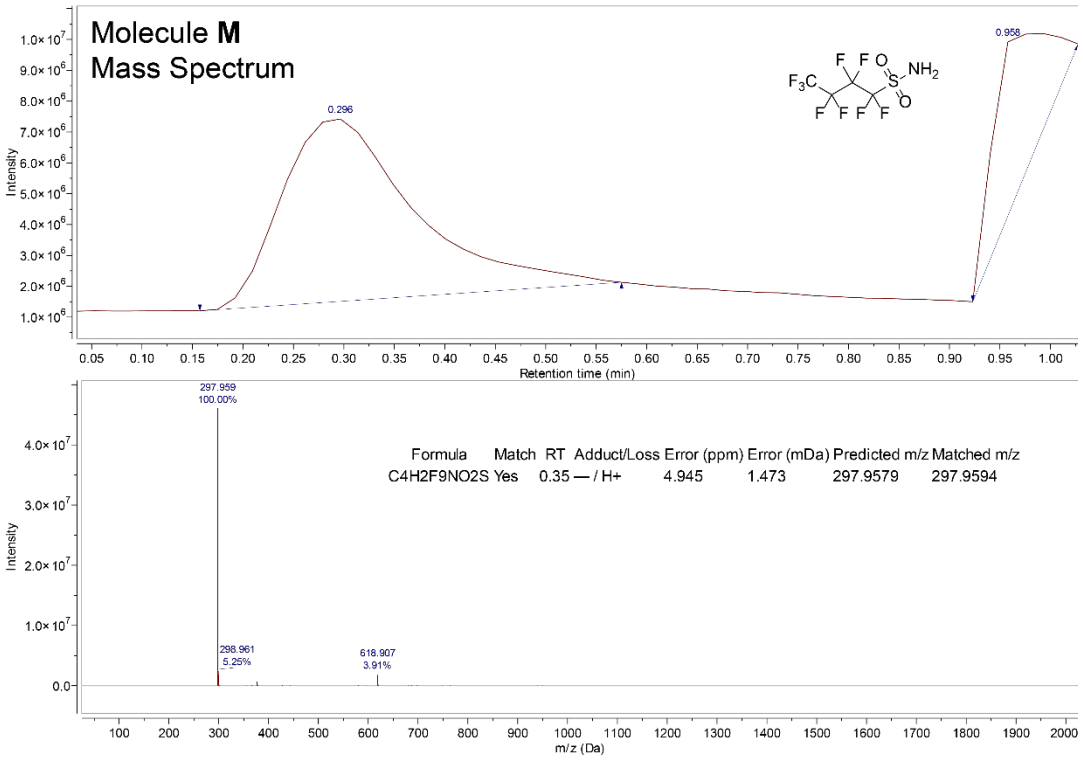

Molecule **N**

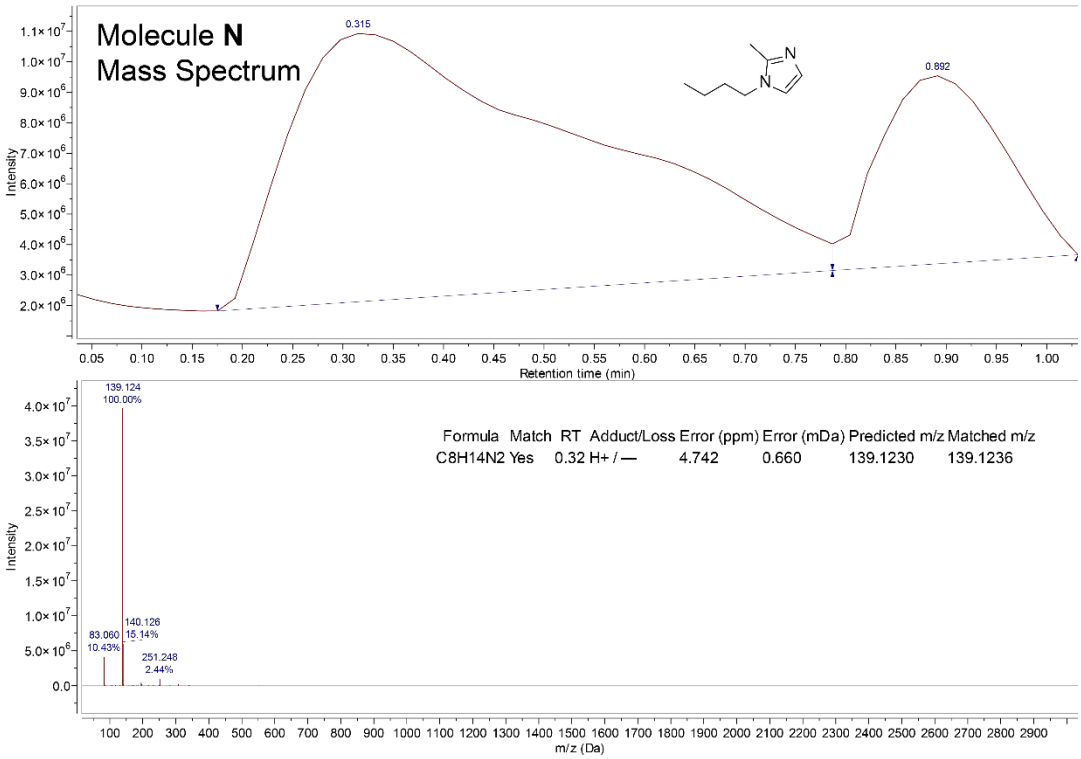

Formula	Match	RT	Adduct/Loss	Error (ppm)	Error (mDa)	Predicted m/z	Matched m/z
C8H14N2	Yes	0.32	H+ / —	4.742	0.660	139.1230	139.1236

Molecule **O**

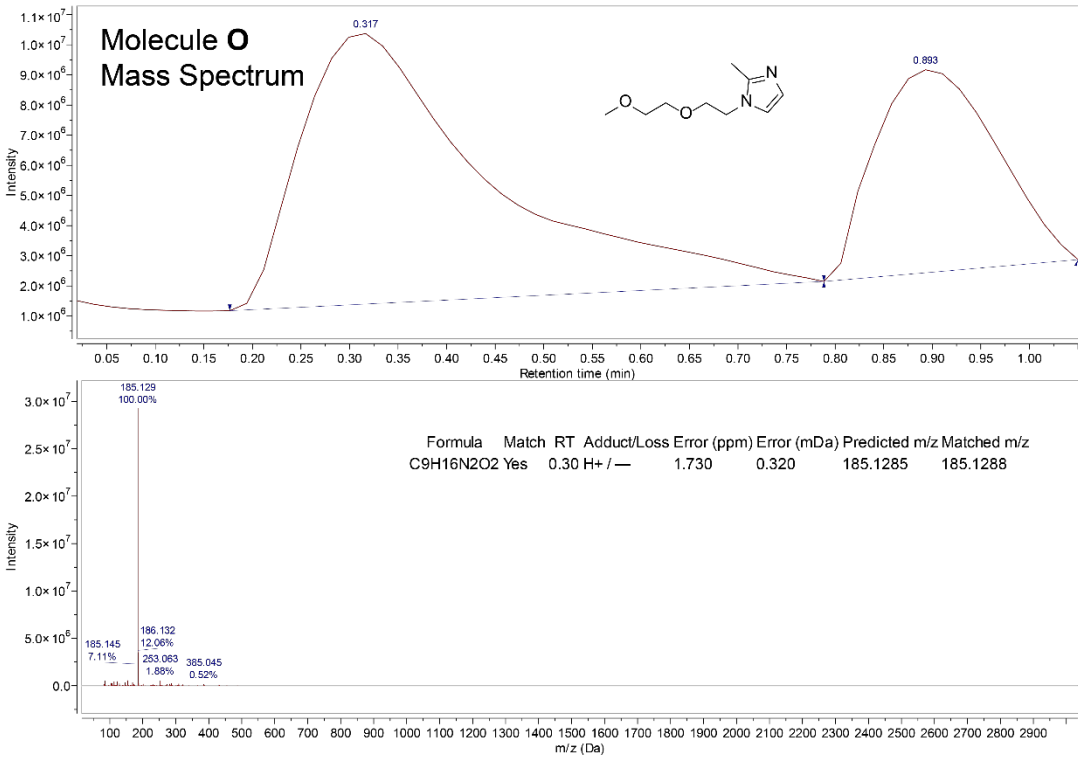

Formula	Match	RT	Adduct/Loss	Error (ppm)	Error (mDa)	Predicted m/z	Matched m/z
C9H16N2O2	Yes	0.30	H+ / —	1.730	0.320	185.1285	185.1288

Data S3: Differential scanning calorimetry (exo up) of zwitterions

Molecule **1**

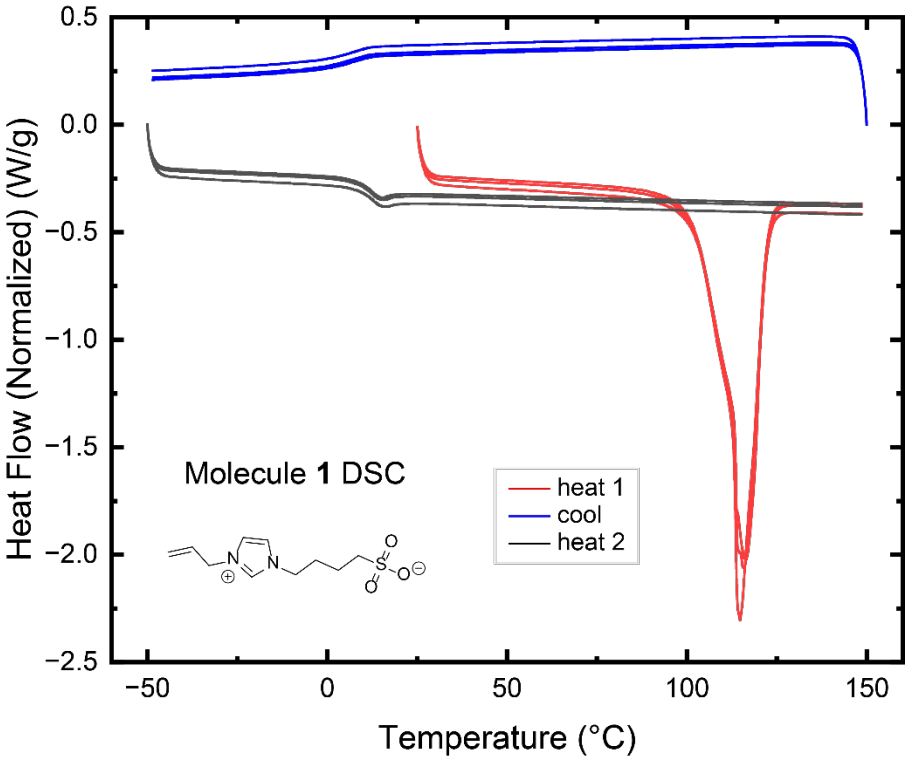

Molecule **2**

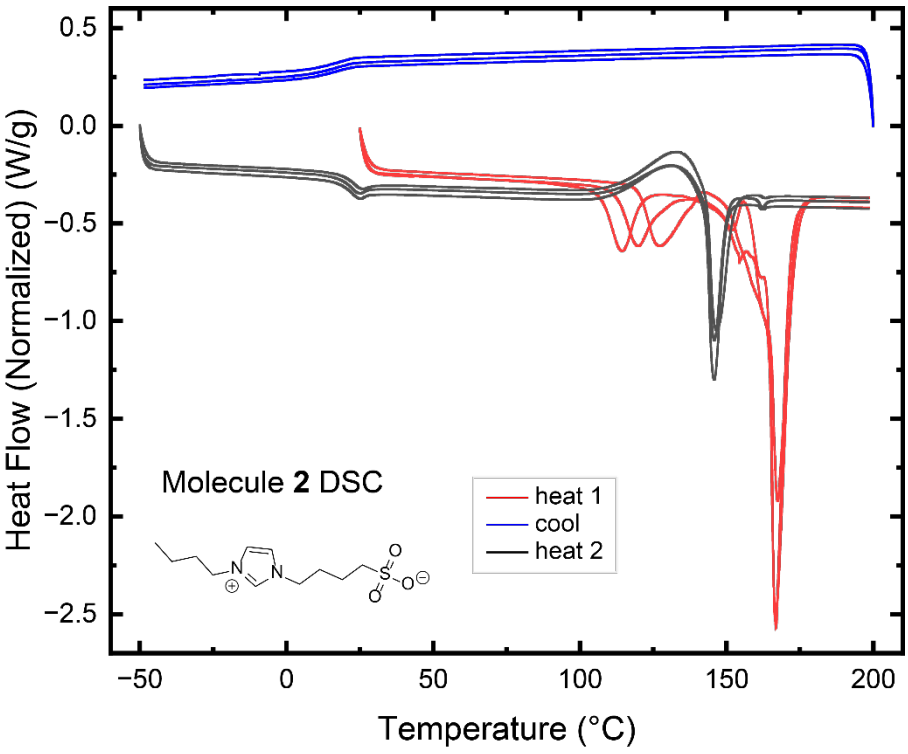

Molecule **3**

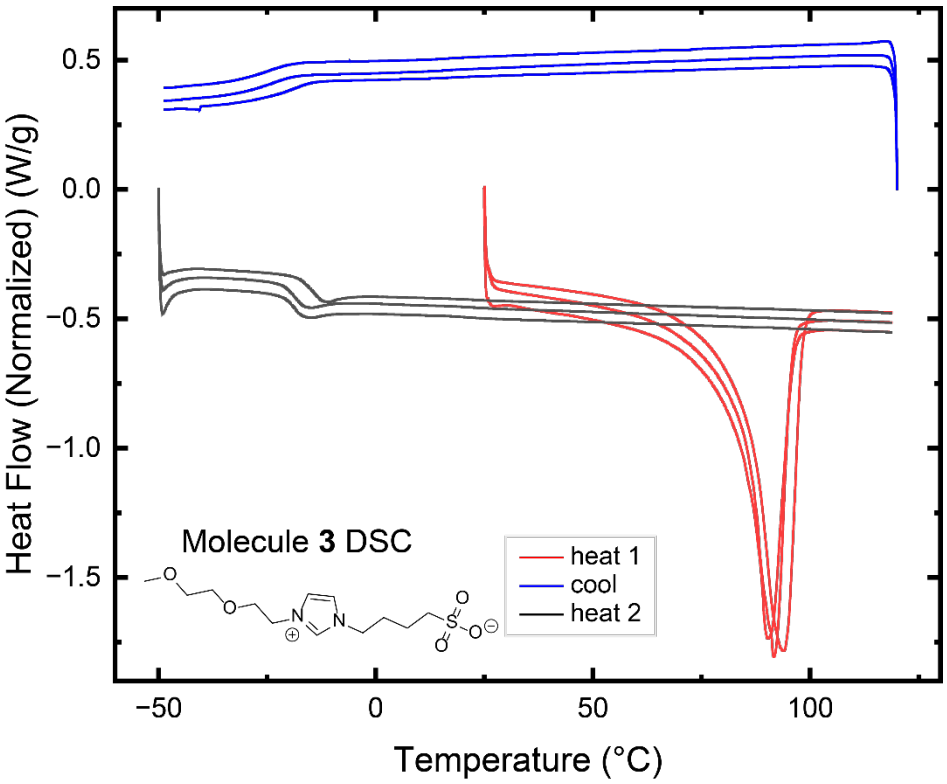

Molecule **4**

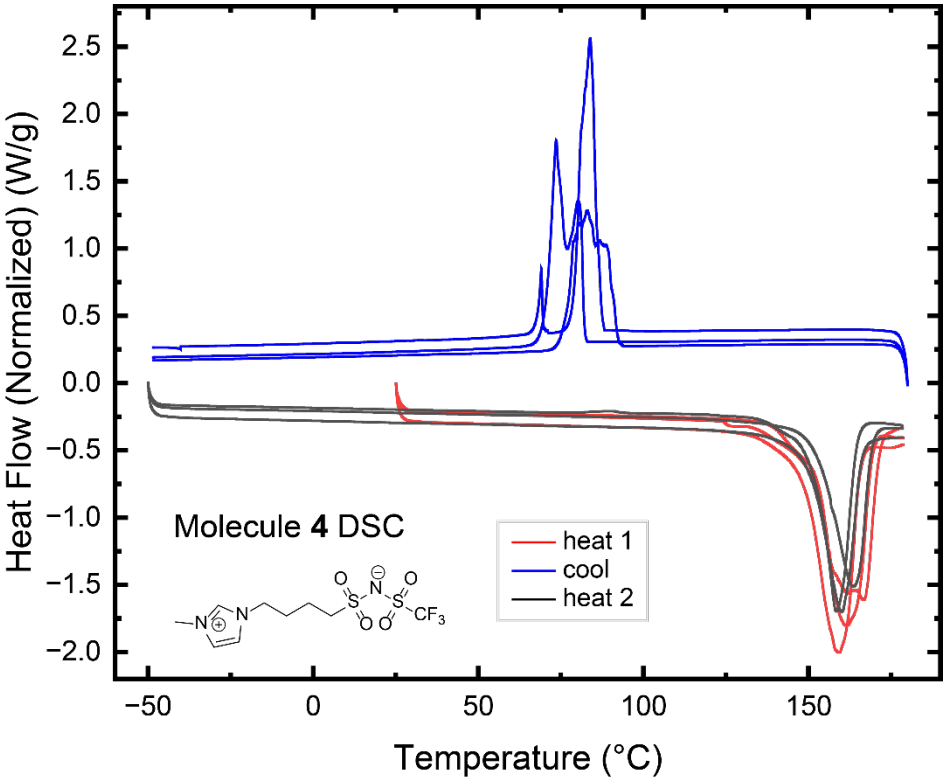

Molecule **5**

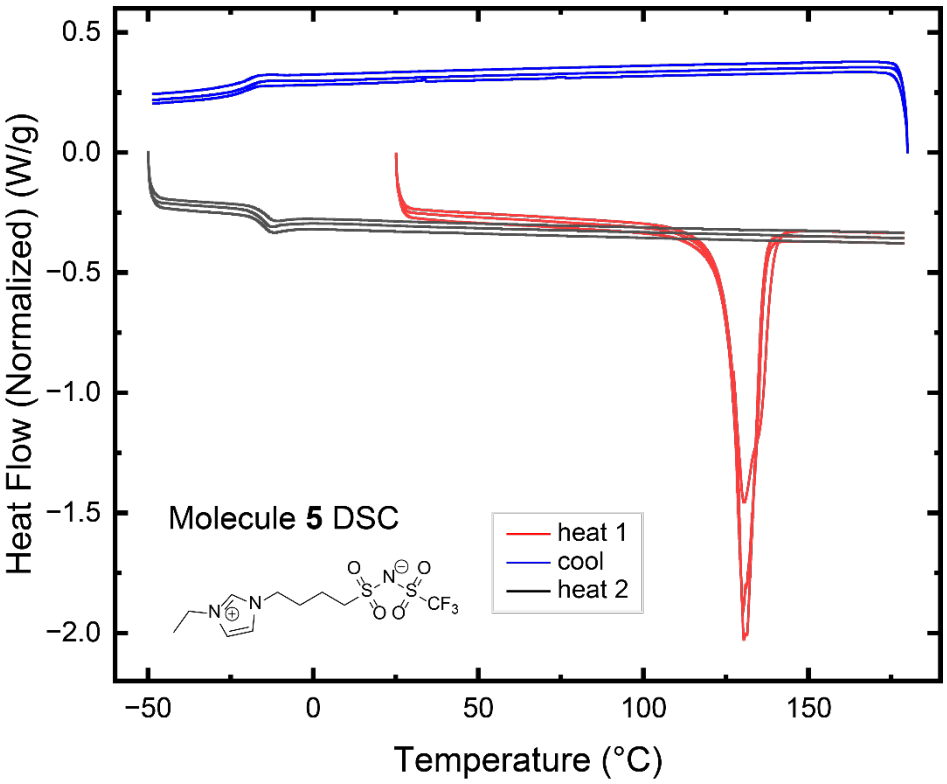

Molecule **6**

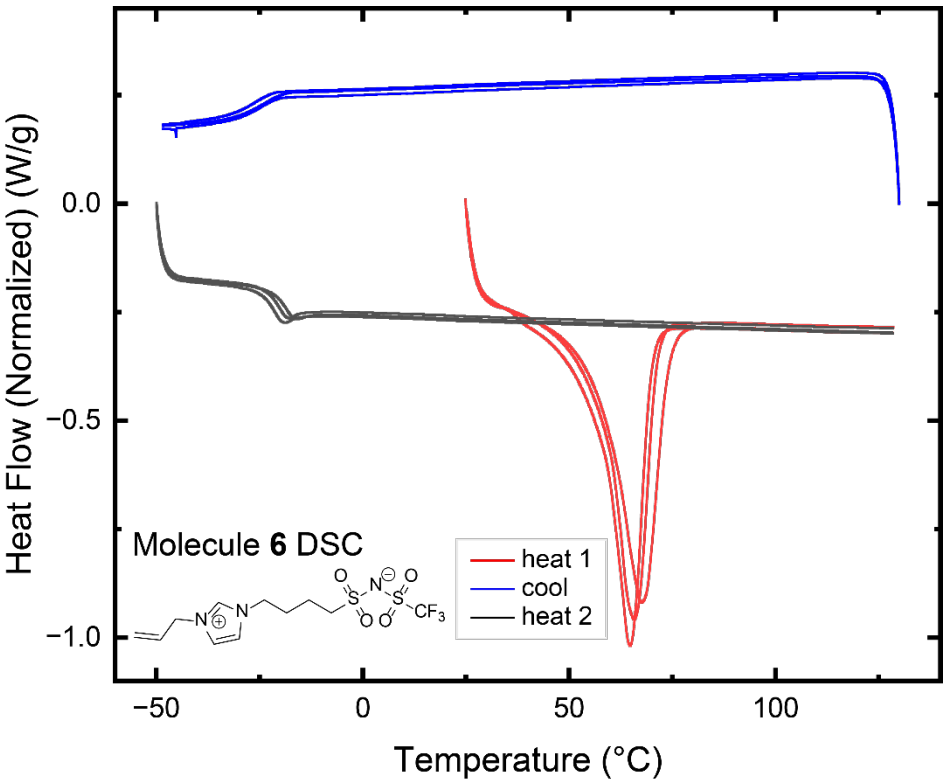

Molecule **7**

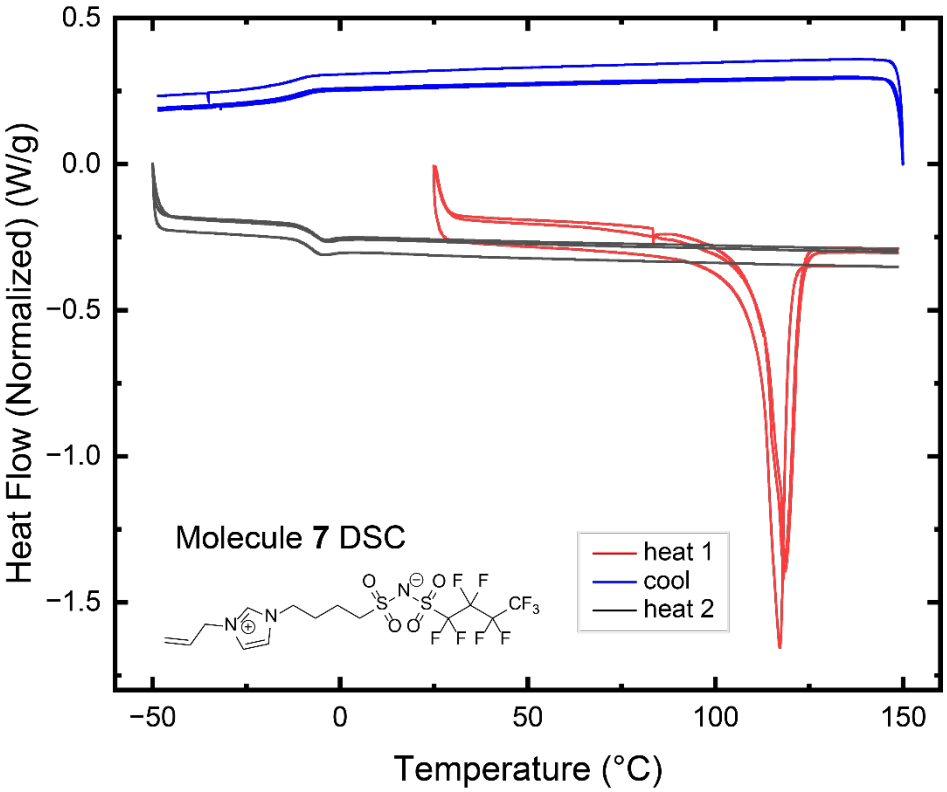

Molecule **8**

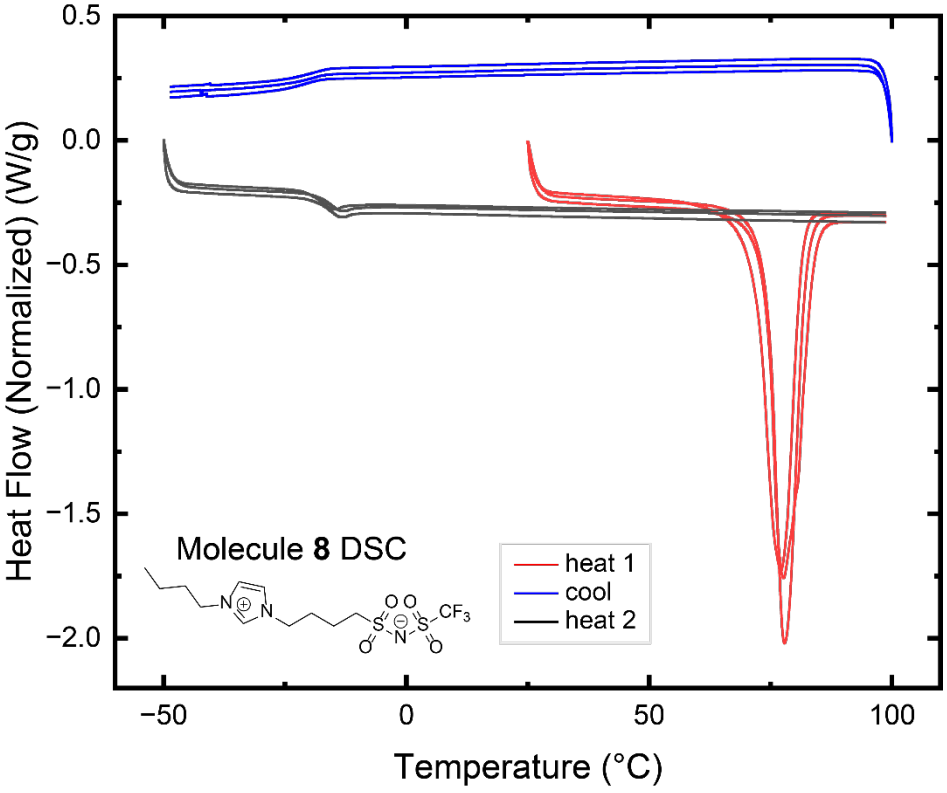

Molecule **9**

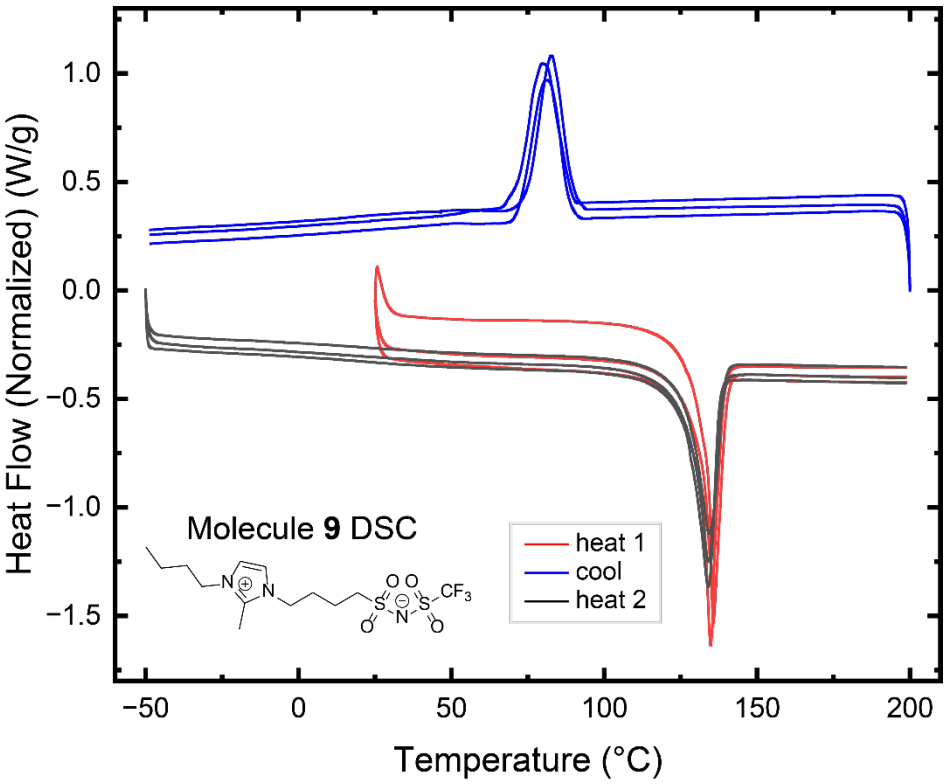

Molecule **10**

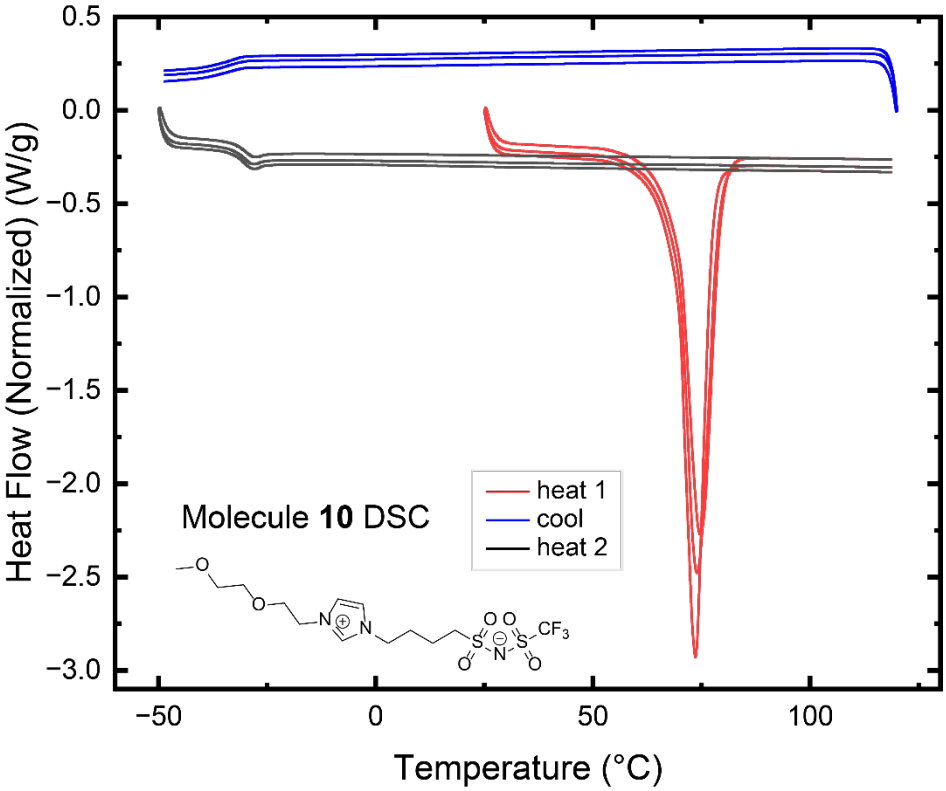

Molecule **11**

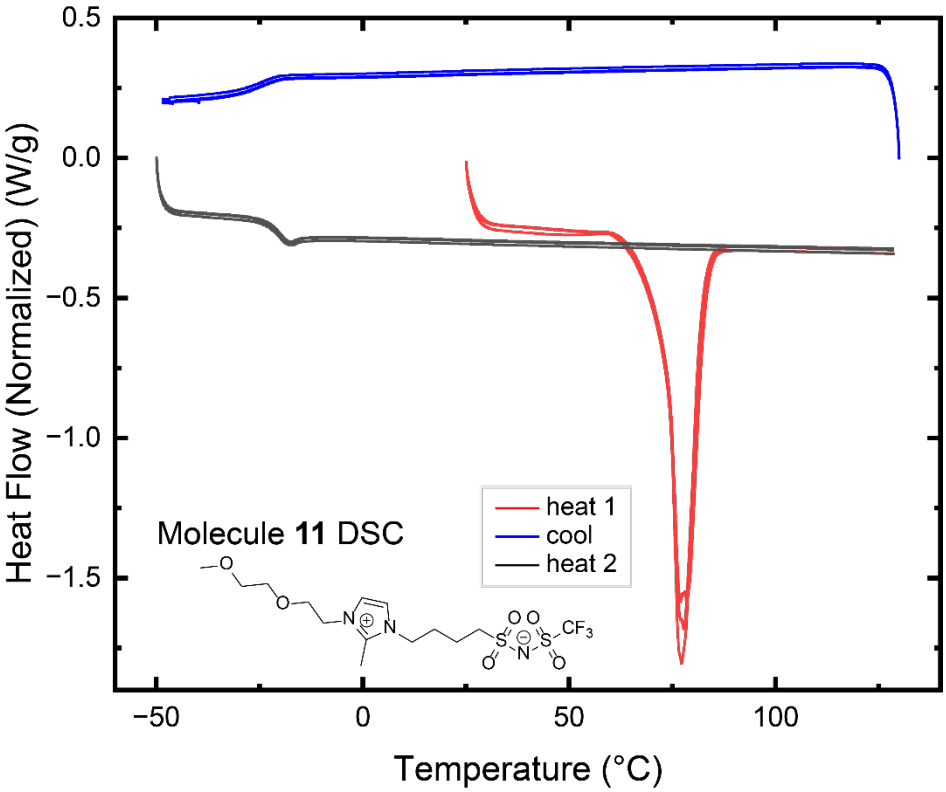

Molecule **12**

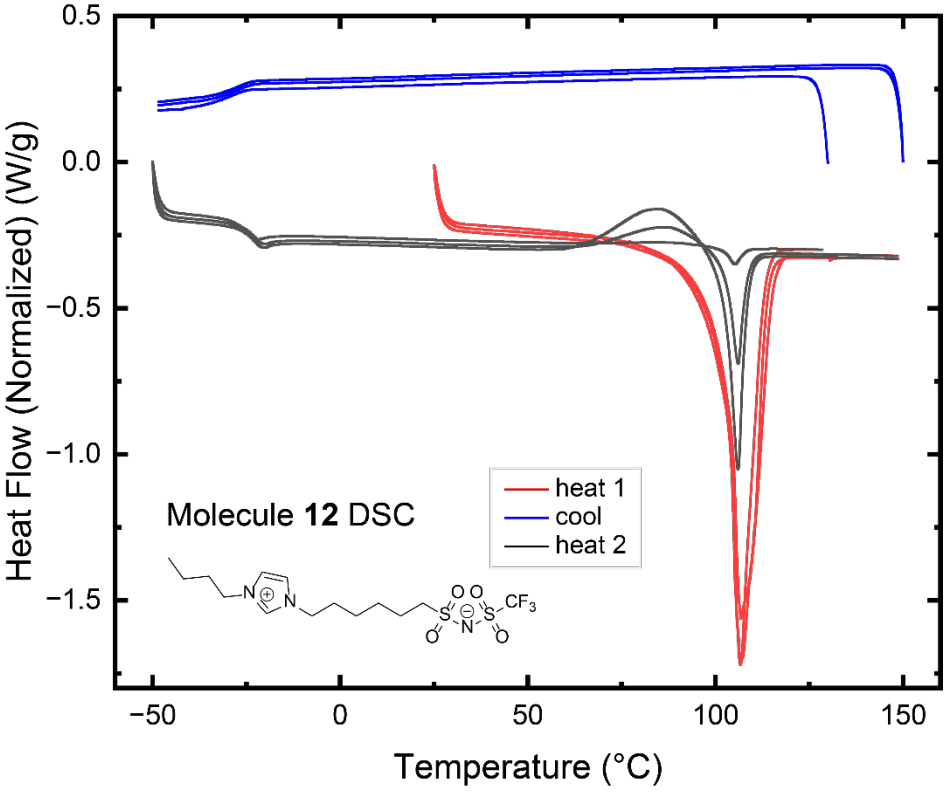

Molecule **13**

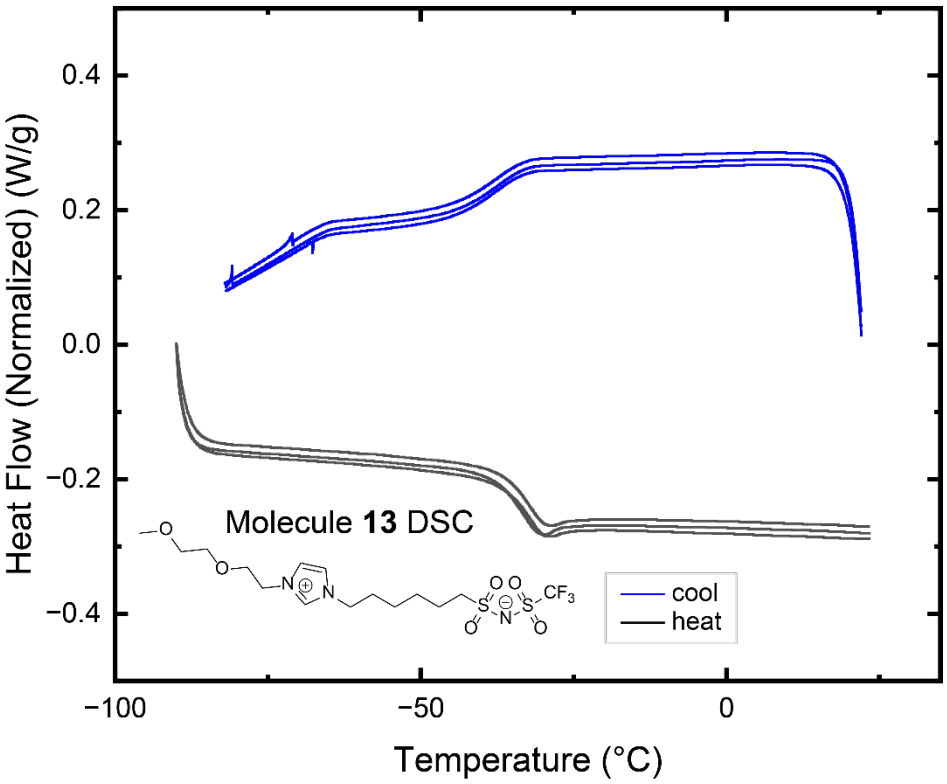

Molecule **14**

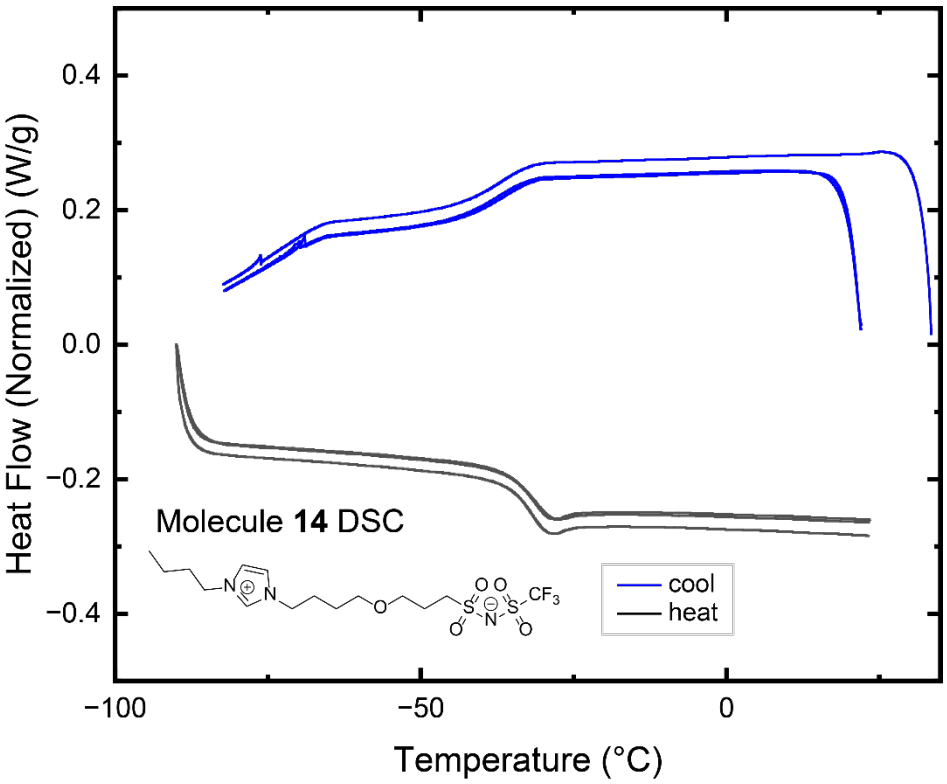

Molecule **15**

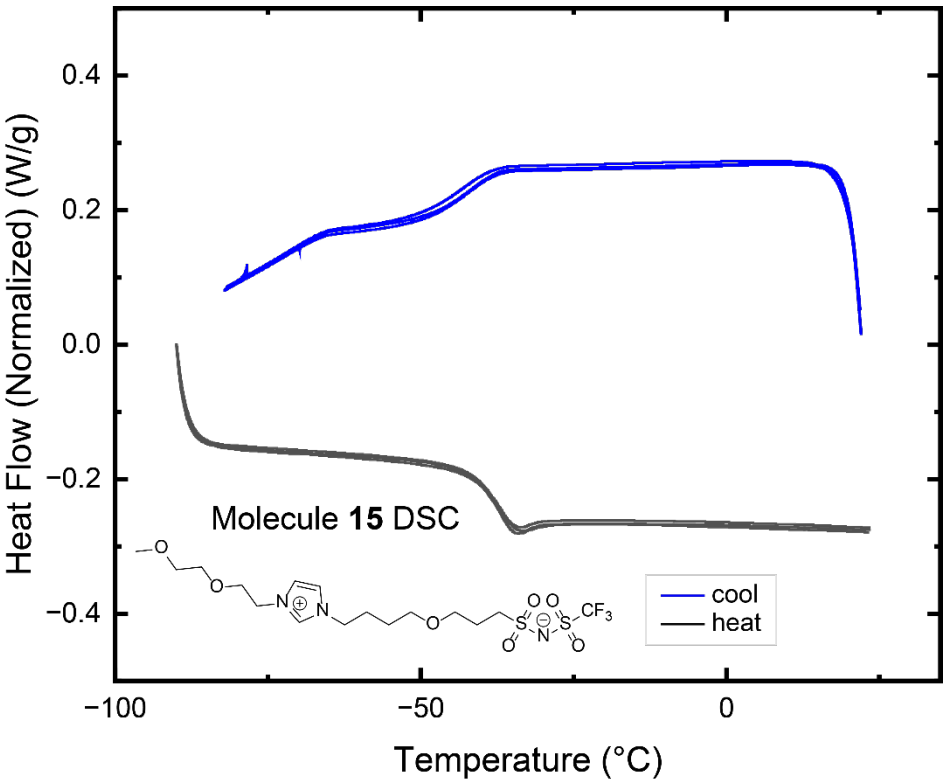

Molecule **16**

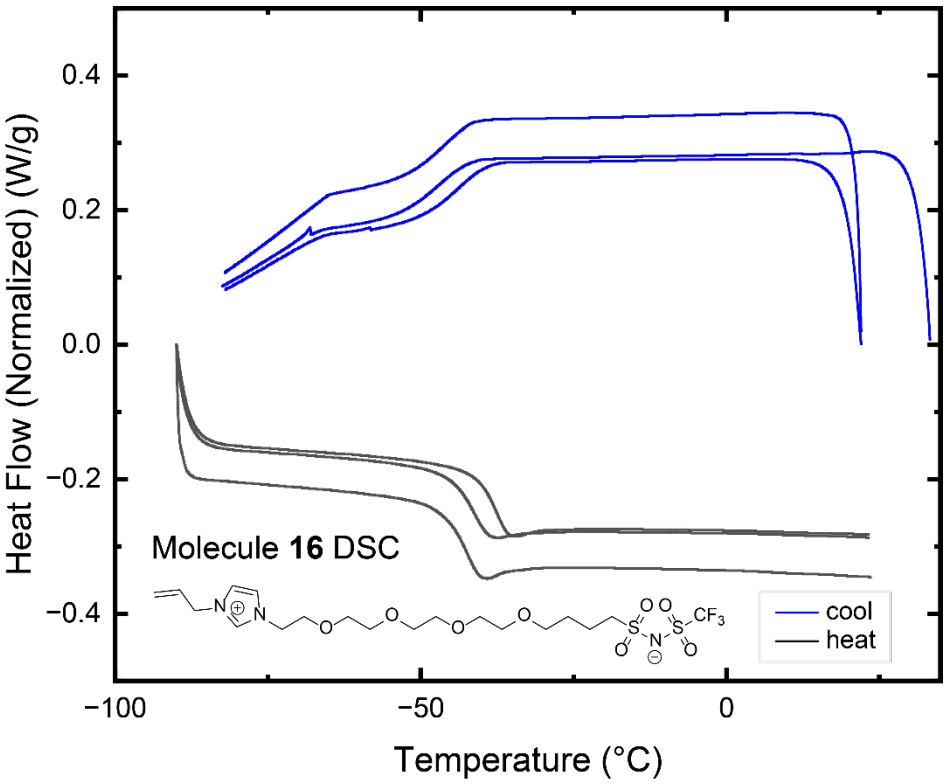

Molecule **17**

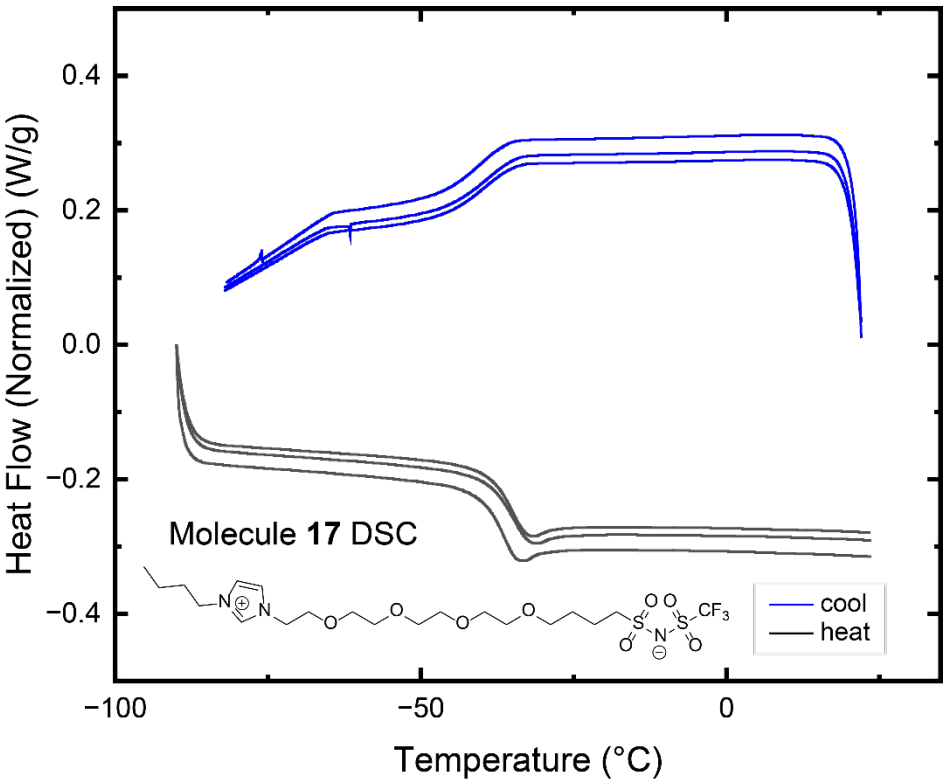

Molecule **18**